

Silicon Nanocrystals: from Solution to Solid State

by

Maryam Aghajamali

A thesis submitted in partial fulfillment of the requirements for the degree of

Doctor of Philosophy

Department of Chemistry

University of Alberta

© Maryam Aghajamali, 2018

Abstract

Silicon nanocrystals (SiNCs) are a class of quantum dots (QDs) exhibiting unique size- and surface-dependent optoelectronic properties. They have shown promise as a safe and viable alternative to traditional compound QDs, mainly because silicon is non-toxic and earth-abundant. These NCs are attractive for potential applications, ranging from optoelectronics (e.g., light-emitting diodes) to energy storage devices (e.g., lithium-ion batteries (LIBs)). To access the unique properties of SiNCs and expand the scope of their applications, they must be transferred to functional structures (e.g., optical media, conductive matrices, patterned substrates). Hence, this thesis focuses on two approaches to transfer SiNCs from solutions to a solid host/substrate: aerogel incorporation and patterned transfer.

Aerogel incorporation involves incorporating SiNCs into an aerogel host to improve NC properties. In Chapter 2, SiNCs were incorporated into a silica aerogel host to combine optical properties of SiNCs with optical transparency and low thermal conductivity of silica aerogels in order to accommodate their optoelectronic applications. SiNC/silica aerogel hybrids were synthesized by incorporating hydrophilic SiNCs of various sizes ($d \sim 3$ and 8 nm) and surface groups (i.e., carboxylic acid, polymer-coated alkyl, and polyethylene glycol (PEG)) into silica aerogels. The resulting hybrid materials retain the optical response of the SiNCs, while the optical transparency of the silica aerogel is only retained when 3 nm PEG-functionalized SiNCs are employed; this emphasizes the impact of NC size and surface chemistry on optical properties of hybrid aerogels. In Chapter 3, SiNCs were incorporated into a graphene aerogel host to combine the high specific capacity of SiNCs with the high porosity and high electrical conductivity of graphene aerogels in order to facilitate their LIB applications. SiNC/graphene aerogel hybrids were synthesized by incorporating hydrophilic SiNCs ($d \sim 3, 5, 8,$ and 15 nm) into graphene aerogel hosts. The electrochemical characterization performed on the SiNCs and

their corresponding SiNC/graphene aerogel hybrids indicate improved cycling stabilities and high specific capacities for the hybrid aerogels. When the size of entrained SiNCs decreased, a significant improvement on the cycling performance was observed; this highlights the role of SiNC size on their electrochemical performance.

Patterned transfer involves transferring and positioning NCs on areas of interest on a solid substrate, opening the door to advanced optoelectronic applications (e.g., flexible sensor arrays, curved displays). Chapter 4 introduces a straightforward and cost-effective water-based approach to transfer patterns of nanomaterials onto a variety of substrates, including non-planar surfaces at low temperatures. Water-assisted transfer patterning of nanomaterials uses an inexpensive water-soluble polymer film as a sacrificial carrier to transfer hydrophobic nanomaterials from a patterned source substrate onto a target substrate. Using this approach, nanomaterials are transferred readily from solutions onto surfaces of various shapes and compositions with good fidelity for feature sizes approaching 10 microns.

A brief introduction to materials and approaches investigated in this thesis is presented in Chapter 1, and a summary of the experimental Chapters, as well as future directions for these studies, are presented in Chapter 5.

Preface

This thesis is an original work by Maryam Aghajamali. The research was conducted under the supervision of Dr. Jonathan G. C. Veinot at the Department of Chemistry, University of Alberta.

A version of Chapter 2 has been published as Aghajamali, M.; Iqbal, M.; Purkait, T. K.; Hadidi, L.; Sinelnikov, R.; Veinot, J. G. C. Synthesis and Properties of Luminescent Silicon Nanocrystal/Silica Aerogel Hybrid Materials. *Chem. Mater.* **2016**, *28* (11), 3877–3886. I designed the project, performed the experiments, carried out the majority of material characterization and data analysis, and wrote the manuscript. Iqbal, M. and Purkait, T. K. assisted with material characterization and data analysis (e.g., TEM, XPS). Hadidi, L. assisted with BET measurements. Sinelnikov, R. assisted with PL measurements. Veinot, J. G. C. supervised the project and was involved with the manuscript composition.

Some of the data presented in Chapter 3 is part of a research collaboration with Dr. Jillian M. Buriak's group in the Department of Chemistry at the University of Alberta. Hezhen Xie and Dr. Peter Kalisvaart in Dr. Buriak's group performed electrochemical characterization and data analysis, as well as XRD measurements reported in Chapter 3.

A version of Chapter 4 has been submitted as Aghajamali, M.; Cheong, I T.; Veinot, J. G. C. Water-Assisted Transfer Patterning of Nanomaterials. *Langmuir*, March 2018. I designed the project, performed the experiments, carried out material characterization and data analysis, and wrote the manuscript. Cheong, I T. assisted with experiments. Veinot, J. G. C. supervised the project and was involved with the manuscript composition.

I dedicate this thesis to my family.

Acknowledgments

At the end of my PhD studies, I am so grateful to those who have contributed to my educational and professional development. First, I want to express my sincere gratitude to my supervisor, Dr. Jonathan G. C. Veinot, for supporting me and giving me the utmost freedom to explore new fields. Your guidance and encouragement always will be remembered and greatly appreciated.

I would like to thank my committee members, Drs. Arthur Mar, Michael Serpe, Al Meldrum, Charles Lucy, Jeff Stryker, and Mohamed Gamal El-Din for their valuable time and comments. I also thank Dr. Tricia Carmichael for serving as an external reader and for her invaluable input. I want to thank Drs. Jillian M. Buriak, Tom Nilges, Al Meldrum, Bernhard Rieger, Thomas Fässler, Greg Goss, and their team for useful discussions and excellent collaborations. I also thank Professor Nilges and his group members for hosting me at the Technical University of Munich.

I had the opportunity to work with amazing people in the Veinot group, who made this journey much easier and more enjoyable. I would like to thank Drs. Muhammad Iqbal and Tapas Purkait for being great mentors and friends, who were there for me whenever I needed assistance. I want to thank my best mentor/mentee (from day one), Regina Sinelnikov, who always supported me during hard times and improved my speaking and presentation skills. Christopher Jay T. Robidillo, my late night buddy, your presence and encouragement motivated me to stay longer and work harder; thanks Mon Amie! I Teng (Emily) Cheong, my first and last mentee in the PhD program, your questions and curiosity improved my teaching and mentoring skills; thank you, and I wish you a bright future! I want to thank all the past and present members of the Veinot group, especially Yi Zhai, Dr. Lida Hadidi, Dr. Morteza Javadi, Dr. Christina

Gonzalez, Dr. Md Hosnay Mobarok, Dr. Muhammad Amirul Islam, Dr. Angélique Faramus, Alyxandra Thiessen, and Xiyu (Zach) Zhang, for their support and assistance on various projects.

None of what is described in this thesis would have been possible without the technical expertise of Dr. Wayne Moffat, Dr. Nathan Gerein, Dr. Kai Cui, Greg Popowich, Pinzhang Gao, Dr. Aaron Hryciw, Peng Li, Dr. Dimitre Karpuzov, Dr. Shixiong Xu, Dr. Anqiang He, Jason Dibbs, and the staff at the Design and Manufacturing Centre; thank you for your assistance! I also want to thank my lab coordinators, Drs. Norman Gee and Jason Cooke, for making my teaching experience enjoyable and guiding me to be a better teacher. I thank the amazing staff members, especially Anita Weiler, for all their help from day one. Special thanks to lovely Dr. Anna Jordan for editing this thesis. Anna, I could not do this without your help and support.

I acknowledge the generous funding from the Natural Sciences and Engineering Research Council of Canada (NSERC) Discovery Grant Program, the NSERC CREATE supported Alberta/Technical University of Munich International Graduate School for Hybrid Functional Materials (ATUMS), and the Department of Chemistry at the University of Alberta. I would like to thank Leah Veinot and Dr. Sergei Vagin, ATUMS coordinators, for all their assistance. I also thank the ATUMS community, especially my amazing collaborators and friends, Kirsty Gardner, Hezhen Xie, Claudia Ott, Kerstin Mayer, Julian Kehrle, and Dr. Tobias Helbich.

During my stay at the University of Alberta and through my involvement in student associations and the ATUMS program, I met lots of people (500+ according to LinkedIn!) and made amazing friends. Here, I want to thank Regina Sinelnikov, Kate Powers, and Kimberly Hyson, my first friends in the PhD program, for introducing me to "North American" culture. Thanks to Dr. Abishek Iyer, Dr. Anton Oliynyk, Dr. Van Ortega, Dr. Olena Shynkaruk, Dr. John Washington, and Peyman Azad Khaneghah for their support and assistance.

I want to thank my family for their unconditional love and support. Words cannot express how grateful I am for everything you have done for me. Last but not least, I want to thank my love, Ahura Abtin. You are the exact definition of a supportive husband, and I could not come this far without having you by my side in all the ups and downs.

Table of Contents

Chapter 1: Introduction	1
1.1 Nanomaterials.....	2
1.2 Quantum Dots	2
1.3 Silicon Nanocrystals.....	4
1.3.1 Synthesis of Silicon Nanocrystals.....	4
1.3.2 Surface Functionalization of Silicon Nanocrystals.....	6
1.3.3 Optical Properties of Silicon Nanocrystals	7
1.3.4 Electrical Properties and Battery Application of Silicon Nanocrystals	8
1.4 Aerogels	11
1.4.1 Silica Aerogels	11
1.4.2 Graphene Aerogels.....	16
1.5 Patterned Transfer	17
1.6 Thesis Outline	20
1.7 References	22
Chapter 2: Synthesis and Properties of Luminescent Silicon Nanocrystal/Silica Aerogel Hybrid Materials	40
2.1 Introduction	41
2.2 Experimental	42
2.2.1 Reagents and Materials	42
2.2.2 Synthesis, Liberation, and Functionalization of SiNCs	43
2.2.3 Synthesis of NC-Free and SiNC-Containing Silica Aerogels.....	46
2.2.4 Photoluminescence Quenching of SiNC-Containing Silica Aerogel.....	47
2.2.5 Material Characterization.....	47

2.3	Results and Discussion.....	49
2.4	Conclusions	68
2.5	References	69
Chapter 3: Silicon Nanocrystal/Graphene Aerogel Hybrids as Anode Materials for Lithium-Ion Batteries		
		74
3.1	Introduction	75
3.2	Experimental	76
3.2.1	Reagents and Materials	76
3.2.2	Synthesis, Liberation, and Functionalization of SiNCs	77
3.2.3	Synthesis of SiNC/Graphene Aerogel Hybrids.....	78
3.2.4	Material Characterization.....	79
3.2.5	Electrochemical Characterization	81
3.3	Results and Discussion.....	82
3.4	Conclusions	97
3.5	References	98
Chapter 4: Water-Assisted Transfer Patterning of Nanomaterials		
		102
4.1	Introduction	103
4.2	Experimental	104
4.2.1	Reagents and Materials	104
4.2.2	Fabrication of Line-Patterned Silicon Substrates (Microplates).....	104
4.2.3	Synthesis and Functionalization of Nanomaterials.....	104
4.2.4	Water-Assisted Transfer Patterning (WTP) of Nanomaterials	105
4.2.5	Material Characterization.....	106
4.3	Results and Discussion.....	108
4.4	Conclusions	116

4.5	References	117
Chapter 5: Conclusions		120
5.1	Conclusions	121
5.2	Future Directions.....	125
5.2.1	SiNC/Silica Aerogel Hybrid Materials	125
5.2.2	Development of SiNC/Carbon-Based Anode Materials.....	126
5.2.3	Water-Assisted Transfer Patterning of Nanomaterials	127
5.3	References	128
Bibliography		130
Appendices.....		160
Appendix A: A Detailed Procedure of CO ₂ Supercritical Drying Presented in Experimental Sections of Chapters 2 and 3.....		161

List of Figures

- Figure 1-1.** a) A photograph showing size-dependent photoluminescence of CdSe/ZnS core-shell nanocrystals; the particles with the smallest (~1.7 nm) CdSe core emit blue; the particles with the largest (~5 nm) core emit red. Reprinted with permission from Reference 14. Copyright 2002 Wiley. b) A diagram indicating the relationship between QD size and band gap. Adapted by permission from Reference 16. 3
- Figure 1-2.** Schematic representation of band structure in a) bulk Si and b) silicon nanocrystal. 7
- Figure 1-3.** The shift in PL of SiNCs as a result of a) band gap (Reprinted (adapted) with permission from Reference 42. Copyright 2006 American Chemical Society), and b) surface state emissions (Reprinted with permission from Reference 43). 8
- Figure 1-4.** Schematic representation of a conventional LIB showing the device components. Reprinted with permission from Reference 97. Copyright 2009 Wiley. 9
- Figure 1-5.** Schematic representation of silica aerogel synthesis; sol-gel processing followed by CO₂ supercritical drying. Reprinted from Reference 134, with permission from Elsevier. 12
- Figure 1-6.** Schematic procedure of drying a gel by a) evaporation, b) supercritical drying, and c) freeze drying. 15
- Figure 1-7.** Representative examples of unique material constructs and devices fabricated by transfer printing techniques: a) Photograph of an epidermal electronic device, conformally laminated onto the surface of the skin (Reprinted with permission from Reference 172a. Copyright 2012 Wiley). b) Photograph of a flexible integrated circuit that uses printed networks of single-wall carbon nanotubes for the semiconductor (Reproduced with permission from Reference 172b. Copyright 2008 Nature Publishing Group). c) Photograph of a 4-inch, full-color QD-LED display (Reproduced with permission from Reference 172c. 17

Copyright 2011 Nature Publishing Group). d) Image of a mechanically flexed array of ultrathin, microscale, blue LEDs printed onto a thin strip of plastic (Reproduced with permission from Reference 172d. Copyright 2011 National Academy of Sciences).

Figure 1-8. Schematic illustration of a) three distinct transfer printing techniques (i.e., additive transfer, subtractive transfer, and deterministic assembly) (Reprinted with permission from Reference 172a. Copyright 2012 Wiley), b) PMMA-mediated transfer (Reprinted (adapted) with permission from Reference 176. Copyright 2008 American Chemical Society), and c) lift-off by etching (Reprinted (adapted) with permission from Reference 180. Copyright 2008 American Chemical Society). 19

Figure 1-9. a) Schematic illustration of water transfer printing process, and b) examples of applications in the automobile, household, and toy industry. Reprinted with permission from References 188 and 189. 20

Figure 2-1. The FTIR spectra of SiNCs with diameters a) 3 nm and b) 8 nm functionalized with indicated surface groups (C12: dodecyl, COOH: pentanoic acid, and PEG: polyethylene glycol). 53

Figure 2-2. The FTIR spectra of polymer-coated dodecyl functionalized SiNCs with diameters 3 and 8 nm. 53

Figure 2-3. High-resolution XP spectra of the Si 2p region of SiNCs with diameters a) 3 nm and b) 8 nm functionalized with indicated surface groups (C12: dodecyl, COOH: pentanoic acid, and PEG: polyethylene glycol). Please note, only Si 2p_{3/2} components are shown; Si 2p_{1/2} components are omitted for clarity. 54

Figure 2-4. Representative bright-field TEM images of SiNCs functionalized with indicated surface groups (C12: dodecyl, COOH: pentanoic acid, and PEG: polyethylene glycol) and diameters, 3C12: ($d = 3.2 \pm 0.4$ nm), 8C12: ($d = 8.1 \pm 0.9$ nm), 3COOH: ($d = 3.2 \pm 0.3$ nm), 8COOH: ($d = 7.5 \pm 0.7$ nm), 3PEG: ($d = 3.2 \pm 0.4$ nm), and 8PEG: ($d = 7.5 \pm 1.0$ nm). The corresponding HRTEM images showing characteristic Si (111) lattice spacing are presented as insets. 56

Figure 2-5. Size distributions of 3 and 8 nm SiNCs functionalized with indicated surface groups (C12: dodecyl, COOH: pentanoic acid, and PEG: polyethylene glycol).	57
Figure 2-6. Solvated diameters of 3 and 8 nm SiNCs functionalized with indicated surface groups (C12: dodecyl, C12/P: polymer-coated dodecyl, COOH: pentanoic acid, and PEG: polyethylene glycol).	58
Figure 2-7. Photographs of NC-free and SiNC-containing silica alcogels/aerogels with indicated sizes ($d \sim 3$ or 8 nm) and surface groups (PEG: polyethylene glycol, COOH: pentanoic acid, and C12/P: polymer-coated dodecyl) under (a, b) ambient and (c, d) UV light. The scale bar is 1 cm.	60
Figure 2-8. The PL spectra of solutions/dispersions containing SiNCs with diameters a) 3 nm and b) 8 nm functionalized with indicated surface groups (C12/P: polymer-coated dodecyl, COOH: pentanoic acid, and PEG: polyethylene glycol), and their corresponding SiO ₂ aerogel monoliths upon excitation at 405 nm.	61
Figure 2-9. Representative bright-field TEM images of NC-free and 8PEG-loaded silica aerogels. The corresponding HRTEM image showing characteristic Si (111) lattice spacing is presented as an inset.	62
Figure 2-10. Representative bright-field TEM images of silica aerogels containing 3 and 8 nm SiNCs functionalized with indicated surface groups (C12/P: polymer-coated dodecyl, COOH: pentanoic acid, and PEG: polyethylene glycol).	63
Figure 2-11. Nitrogen adsorption–desorption isotherm of NC-free silica aerogel.	64
Figure 2-12. Nitrogen adsorption–desorption isotherms of silica aerogels containing SiNCs with diameters a) 3 nm and b) 8 nm functionalized with indicated surface groups (C12/P: polymer-coated dodecyl, COOH: pentanoic acid, and PEG: polyethylene glycol).	65
Figure 2-13. 3PEG-loaded silica aerogel a) before, b) partial, and c) complete exposure to nitrobenzene.	67

- Figure 3-1.** a) FTIR and b) HRXP spectra of the Si 2p region of undecanoic acid-functionalized SiNCs ($d \sim 3, 5, 8,$ and 15 nm). Please note, only Si $2p_{3/2}$ components are shown; Si $2p_{1/2}$ components are omitted for clarity. 84
- Figure 3-2.** HRXP spectra of a) the Si 2p region and b) the C 1s region of graphene oxide and graphene aerogels containing undecanoic acid-functionalized SiNCs ($d \sim 3, 5, 8,$ and 15 nm). Please note, only Si $2p_{3/2}$ components are shown; Si $2p_{1/2}$ components are omitted for clarity. 85
- Figure 3-3.** a) Bright-field TEM images of undecanoic acid-functionalized SiNCs ($d \sim 3, 5, 8,$ and 15 nm), b) their size distributions, and c) bright-field TEM images of SiNC/graphene aerogel hybrids. 86
- Figure 3-4.** a) XRD patterns and b) Raman spectra of graphene aerogels containing undecanoic acid-functionalized SiNCs ($d \sim 3, 5, 8,$ and 15 nm). 87
- Figure 3-5.** a) Secondary electron images, b) EDX spectra, and c) EDX mapping of graphene aerogels containing undecanoic acid-functionalized SiNCs ($d \sim 3, 5, 8,$ and 15 nm). 89
- Figure 3-6.** a) Secondary electron images and b) N_2 adsorption–desorption isotherms of graphene aerogels containing undecanoic acid-functionalized SiNCs ($d \sim 3, 5, 8,$ and 15 nm). The specific surface area (SSA), total pore volume (PV), and average pore size (PS) are presented as insets. 90
- Figure 3-7.** TGA of a) undecanoic acid-functionalized SiNCs ($d \sim 3, 5, 8,$ and 15 nm), and b) their corresponding SiNC/graphene aerogel hybrids. 92
- Figure 3-8.** Cycling performance of a) undecanoic acid-functionalized SiNCs ($d \sim 3, 5, 8,$ and 15 nm) and b) their corresponding SiNC/graphene aerogel hybrids. 94
- Figure 3-9.** a) Cycling performance of annealed SiNC/GA hybrids at the current density of 200 mA/g, b) cycling performance and Coulombic efficiency of Si3/GA hybrid at the current density of 400 mA/g, c) differential capacity (dQ/dV) plots of annealed SiNC/GA hybrids at the second cycle, and d) capacity retention of annealed SiNC/GA hybrids at various rates ranging from 200 mA/g to 8000 mA/g. 95

Figure 4-1. (a) An illustration of WTP of nanomaterials: (i) A poly (vinyl alcohol) film is formed on a substrate bearing a preformed nanomaterial pattern. (ii) The patterned film is peeled from the source substrate and framed with tape. (iii) The tape-framed film is attached to a transfer vessel partially filled with water. (iv) The water level is raised to expose the film to water and dissolve it. (v) A target substrate is immersed into the water to transfer the pattern. (b) WTP of dodecyl-functionalized SiNCs ($d \sim 3$ nm). Photographs of (i) SiNCs deposited on a commercial patterned stainless steel substrate under ambient light. (ii) A PVA film patterned with SiNCs under UV light. (iii) A tape-framed PVA film bearing a SiNC pattern attached to a transfer vessel under UV light. (iv) A non-planar quartz substrate patterned with photoluminescent SiNCs under UV light. 109

Figure 4-2. PL spectrum of a toluene solution containing dodecyl-functionalized SiNCs ($d \sim 3$ nm) upon excitation at 405 nm. The insets show a SiNC solution (a) before and (b) after exposure to UV light ($\lambda \sim 350$ nm). 110

Figure 4-3. Characterization of dodecanethiol-capped AuNPs (a) HRXP spectrum of Au 4f region, (b) HRXP spectrum of S 2p region, (c) bright-field TEM image, and (d) size distribution. 111

Figure 4-4. (a) Photograph of a 2×2 cm line-patterned silicon substrate (i.e., W200 μ -P600 μ). (b,c) Schematic representation of a microplate defining width (W) and pitch (P); (b) top view and (c) cross-sectional view (blue arrow for when NPs deposit in the troughs and red arrow for when they are on the area between the troughs). 112

Figure 4-5. BSE images of AuNPs on PVA films (FW10 μ -P100 μ) obtained from AuNP depositions at (a) 500, (b) 1000, and (c) 2000 rpm. The brighter areas correspond to AuNPs. 113

Figure 4-6. BSE images of AuNPs on (a) PVA film (FW2 μ -P50 μ) and (b) aluminum substrate (SW2 μ -P50 μ). The brighter areas correspond to AuNPs. 113

Figure 4-7. BSE images of AuNPs on PVA films (FW10 μ -100 μ) obtained from 114

AuNP suspensions of concentrations (a) 5, (b) 10, and (c) 20 mg/mL containing 0.6 M diethyl succinate. The brighter areas correspond to AuNPs.

Figure 4-8. (a) BSE images of AuNPs on PVA films, (b) BSE images of AuNPs on aluminum substrates, (c) EDX mapping of AuNPs on aluminum substrates, and (d) EDX line scans of AuNPs on aluminum substrates. 115

Figure 5-1. Photographs of NC-free and SiNC-containing silica aerogels with indicated sizes and surface groups under ambient (top) and UV (bottom) light (for details see Chapter 2). 122

Figure 5-2. a) Photographs of a graphene aerogel containing 3 nm undecanoic acid-functionalized SiNCs under ambient and UV light and b) cycling performance of an annealed 3 nm SiNC/graphene aerogel hybrid at the current density of 400 mA/g (for details see Chapter 3). 123

Figure 5-3. A simplified illustration and examples of patterned transfer of nanomaterials (e.g., SiNCs, AuNPs) from PVA films onto solid substrates (for details see Chapter 4). 124

Figure 5-4. Schematic representation of a modified pattern layer; nanomaterials are sandwiched between the PVA layer and the protective layer. 127

Figure A-1. Photographs of a) a home-built CO₂ supercritical dryer with a 1-inch diameter opening, b) the front view, and c) the side view. 161

Figure A-2. Photographs of a) a CO₂ supercritical dryer indicating main components, b) loading a gel, and c) tightening the pipe plug. 162

List of Tables

List of Tables	Page
Table 2-1. The BET specific surface area (SSA), total pore volume (PV), average pore size (PS), and bulk density (ρ) of NC-free and SiNC-containing silica aerogels with indicated sizes ($d \sim 3$ or 8 nm) and surface groups (C12/P: polymer-coated dodecyl, COOH: pentanoic acid, and PEG: polyethylene glycol).	67
Table 3-1. CHNS data of undecanoic acid-functionalized SiNCs ($d \sim 3, 5, 8,$ and 15 nm) and their corresponding hybrid aerogel.	93
Table 4-1. Widths (W) and pitches (P) of line-patterned silicon substrates (microplates).	112

List of Schemes

- Scheme 1-1.** Synthesis of SiNCs via the disproportionation of hydrogen silsesquioxane (HSQ). 5
- Scheme 1-2.** General mechanisms of hydrolysis and condensation of silicon alkoxide precursors in the presence of a) acid and b) base catalysts. Reproduced (Adapted) from Reference 136 with permission of The Royal Society of Chemistry. 13
- Scheme 2-1.** Synthesis of dodecyl, pentanoic acid, and polyethylene glycol functionalized SiNCs with diameters 3 and 8 nm. 51
- Scheme 2-2.** Coating of dodecyl functionalized SiNCs with the amphiphilic polymer. 51
- Scheme 3-1.** Synthesis of a) 3 nm undecanoic acid-functionalized SiNCs (Si₃-COOH), and b) a graphene aerogel containing Si₃-COOH (Si₃-COOH/GA). Photograph of Si₃-COOH/GA under UV light is shown as inset. The scale bar is 1 cm. 83
- Scheme 5-1.** Synthesis of a SiNC–RGO hybrid material. 126

List of Symbols, Nomenclature, and Abbreviations

AIBN	Azobisisobutyronitrile
AuNP(s)	Gold nanoparticle(s)
a.u.	Arbitrary unit
BET	Brunauer–Emmett–Teller
BJH	Barrett–Joyner–Halenda
BSE	Backscattered electron
CB	Conduction band
<i>d</i>	Diameter
DI	Deionized
DLS	Dynamic light scattering
EDX	Energy-dispersive X-ray
FTIR	Fourier transform infrared
FW2 μ -P50 μ	Film with patterns reproduced from W2 μ -P50 μ
FW10 μ -P100 μ	Film with patterns reproduced from W10 μ -P100 μ
FW50 μ -P200 μ	Film with patterns reproduced from W50 μ -P200 μ
FW100 μ -P400 μ	Film with patterns reproduced from W100 μ -P400 μ
FW200 μ -P600 μ	Film with patterns reproduced from W200 μ -P600 μ
GA(s)	Graphene aerogel(s)
GO	Graphene oxide
HRTEM	High-resolution transmission electron microscopy

HRXPS	High-resolution X-ray photoelectron spectroscopy
HSQ	Hydrogen silsesquioxane
H-SiNC(s)	Hydride-terminated silicon nanocrystal(s)
L-AA	L-ascorbic acid
LED(s)	Light-emitting diode(s)
LIB(s)	lithium-ion batterie(s)
M_w	Weight-average molecular weight
μ	Micron
μm	Micrometer
NC(s)	Nanocrystal(s)
NM(s)	Nanomaterial(s)
NP(s)	Nanoparticle(s)
n-Si	Nanoscale silicon
NMP	<i>N</i> -Methyl-2-pyrrolidone
P	Pitch
PEG	Polyethylene glycol
PDMS	Poly (dimethylsiloxane)
PMMA	Poly (methyl methacrylate)
PMT	PMMA-Mediated Transfer
PVA	Poly (vinyl alcohol)
PVDF	Poly (vinylidene fluoride)
PL	Photoluminescence

PS	Average pore size
PV	Total pore volume
QD(s)	Quantum dot(s)
RGO	Reduced graphene oxide
SEM	Scanning electron microscopy
SEI	Solid electrolyte interphase
SiNC(s)	Silicon nanocrystal(s)
SiNC/SiO ₂	Silicon nanocrystals embedded in a silica matrix
SiO ₂ -3COOH	Silica aerogel containing pentanoic acid functionalized SiNCs (<i>d</i> ~ 3 nm)
SiO ₂ -8COOH	Silica aerogel containing pentanoic acid functionalized SiNCs (<i>d</i> ~ 8 nm)
SiO ₂ -3C12/P	Silica aerogel containing 3 nm polymer-coated dodecyl functionalized SiNCs
SiO ₂ -8C12/P	Silica aerogel containing 8 nm polymer-coated dodecyl functionalized SiNCs
SiO ₂ -3PEG	Silica aerogel containing 3 nm polyethylene glycol functionalized SiNCs
SiO ₂ -8PEG	Silica aerogel containing 8 nm polyethylene glycol functionalized SiNCs
Si3-COOH	3 nm undecanoic acid-functionalized SiNCs
Si3-COOH/GA	Graphene aerogel containing Si3-COOH
Si3/GA	Annealed Si3-COOH/GA
Si5-COOH	5 nm undecanoic acid-functionalized SiNCs
Si5-COOH/GA	Graphene aerogel containing Si5-COOH
Si5/GA	Annealed Si5-COOH/GA
Si8-COOH	8 nm undecanoic acid-functionalized SiNCs
Si8-COOH/GA	Graphene aerogel containing Si8-COOH

Si8/GA	Annealed Si8-COOH/GA
Si15-COOH	15 nm undecanoic acid-functionalized SiNCs
Si15-COOH/GA	Graphene aerogel containing Si15-COOH
Si15/GA	Annealed Si15-COOH/GA
SSA	Specific surface area
SW2 μ -P50 μ	Substrate with patterns reproduced from FW2 μ -P50 μ
SW10 μ -P100 μ	Substrate with patterns reproduced from FW10 μ -P100 μ
SW50 μ -P200 μ	Substrate with patterns reproduced from FW50 μ -P200 μ
SW100 μ -P400 μ	Substrate with patterns reproduced from FW100 μ -P400 μ
SW200 μ -P600 μ	Substrate with patterns reproduced from FW200 μ -P600 μ
TGA	Thermogravimetric analysis
TEM	Transmission electron microscopy
TEOS	Tetraethyl orthosilicate
TMOS	Tetramethyl orthosilicate
TP	Transfer Printing
UV	Ultraviolet
VB	Valence band
W	Width
W2 μ -P50 μ	Microplate with 2 μ width and 50 μ pitch
W10 μ -P100 μ	Microplate with 10 μ width and 100 μ pitch
W50 μ -P200 μ	Microplate with 50 μ width and 200 μ pitch
W100 μ -P400 μ	Microplate with 100 μ width and 400 μ pitch

W200 μ -P600 μ	Microplate with 200 μ width and 600 μ pitch
WTP	Water-Assisted Transfer Patterning
XPS	X-ray photoelectron spectroscopy
XRD	X-ray diffraction
3COOH	Pentanoic acid functionalized SiNCs ($d \sim 3$ nm)
8COOH	Pentanoic acid functionalized SiNCs ($d \sim 8$ nm)
3C12	Dodecyl functionalized SiNCs ($d \sim 3$ nm)
8C12	Dodecyl functionalized SiNCs ($d \sim 8$ nm)
3C12/P	Polymer-coated dodecyl functionalized SiNCs ($d \sim 3$ nm)
8C12/P	Polymer-coated dodecyl functionalized SiNCs ($d \sim 8$ nm)
3PEG	Polyethylene glycol functionalized SiNCs ($d \sim 3$ nm)
8PEG	Polyethylene glycol functionalized SiNCs ($d \sim 8$ nm)

Chapter 1:

Introduction

1.1 Nanomaterials

Nanomaterials have attracted great attention since the discovery of fullerenes and colloidal nanoparticles.¹⁻³ They include any manufactured materials with at least one characteristic dimension at the nanoscale (1–100 nm) exhibiting one or more dimension-dependent properties/phenomena.⁴ The characteristic dimension could be the particle diameter, layer thickness, or even the size of a pore, and many interesting dimension-dependent properties (e.g., optical, electrical, thermal, etc.) emerge at the nanoscale, mainly due to the large surface to volume ratio and quantum confinement effects.⁵⁻⁸ There are many different geometries of nanomaterials (e.g., nanoparticles, nanowires, nanosheets, etc.), and they are classified into three main categories: zero- (e.g., nanoparticles), one- (e.g., nanowires), and two- (e.g., nanosheets) dimensional nanomaterials.⁹

1.2 Quantum Dots

Quantum dots (QDs) are zero-dimensional semiconductor nanomaterials exhibiting unique size-dependent optoelectronic properties upon reducing their size below the Bohr exciton (electrostatically bound electron–hole pair) radius.¹⁰ One of the most explored optoelectronic properties is size-dependent photoluminescence (PL). As the QD size decreases, the density of electronic energy states decreases, leading to an increase in the band gap and a decrease in PL emission wavelength; this results in the PL emission spectrum ranging from infrared to blue light.¹¹⁻¹³ A prototypical example of QDs (e.g., CdSe/ZnS core-shell nanocrystals) and their size-dependent PL emission colors is shown in **Figure 1-1a**.^{14,15} The size-dependent PL is governed by quantum confinement, which is the confinement of excitons within the QDs (**Figure 1-1b**).¹⁶

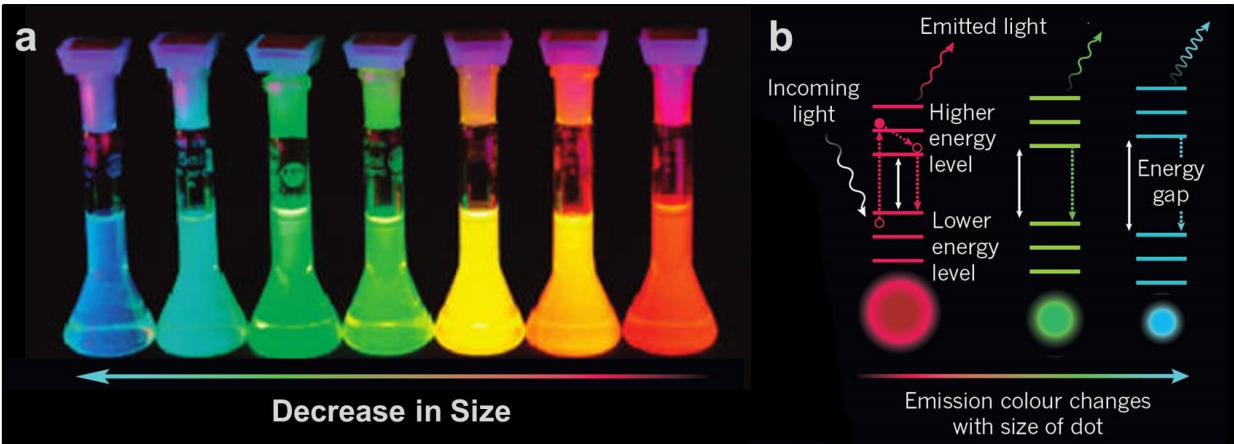


Figure 1-1. a) A photograph showing size-dependent photoluminescence of CdSe/ZnS core-shell nanocrystals; the particles with the smallest (~ 1.7 nm) CdSe core emit blue; the particles with the largest (~ 5 nm) core emit red. Reprinted with permission from Reference 14. Copyright 2002 Wiley. **b)** A diagram indicating the relationship between QD size and band gap. Adapted by permission from Reference 16.

Group II-VI¹⁷⁻²⁰ (e.g., CdSe, CdS, ZnSe, ZnS, etc.) and III-V²¹⁻²⁵ (e.g., GaAs, InAs, InP, etc.) QDs are the most widely explored QDs. These QDs have been studied for potential applications, including light-emitting diodes (LEDs),^{26,27} solar cells,^{28,29} sensors,^{30,31} lasers,^{32,33} and bioimaging;^{34,35} however, the toxicity of heavy metals (e.g., Cd, As)^{36,37} and limited resources for some elements (e.g., Ga, In, and Se)^{38,39} prevents their commercialization.

1.3 Silicon Nanocrystals

Silicon (Si) is non-toxic, earth-abundant, and the workhorse material in electronic devices.^{40,41} While bulk Si has dominated the microelectronic industry for decades, its optical application is limited. When the dimensions of silicon particles are decreased and approach the Bohr exciton radius for Si (~5 nm), quantum confinement effects emerge, and PL shifts into the visible spectrum.⁴⁰ Silicon nanocrystals (SiNCs) are heavy-metal-free QDs whose optical response may be tuned through the variations of NC size and surface chemistry.^{42,43} These NCs have been investigated for potential applications in LEDs, sensors, bioimaging, and lithium-ion batteries (LIBs), and they are considered as a viable replacement for traditional compound QDs.⁴⁴⁻⁴⁸ In this Section, the synthesis, surface functionalization, properties, and some applications of SiNCs will be discussed.

1.3.1 Synthesis of Silicon Nanocrystals

Many methods have been developed for the synthesis of SiNCs since the discovery of photoluminescent porous silicon by Canham in the early 1990s.^{49,50} These methods are based on two general approaches: top-down, in which bulk Si is broken down into nanoscale particles, and bottom-up, in which silicon-based precursors are processed thermally or chemically oxidized/reduced to produce SiNCs.^{41,51}

Top-down approaches include ball milling,^{52,53} chemical etching,^{54,55} electrochemical etching,^{56,57} and laser ablation.^{58,59} Reduction of silicon halides or alkoxides,⁶⁰⁻⁶³ metathesis reactions of Zintl salts (ASi: A = Na, K, Mg),⁶⁴⁻⁶⁶ decomposition of silane precursors,⁶⁷⁻⁷¹ and disproportionation of silicon-rich oxides^{42,72-75} are examples of bottom-up approaches. The disproportionation of silicon-rich oxides is one of the effective approaches to synthesize size-

1.3.2 Surface Functionalization of Silicon Nanocrystals

Hydride-terminated SiNCs (H-SiNCs), obtained from HF-etching of SiNC/SiO₂ composites, are susceptible to oxidation; hence, surface functionalization is required for passivating their surface and preventing oxidation, tuning and enhancing the PL response, inducing colloidal stability, and tailoring the surface chemistry for targeted applications. Surface functionalization of SiNCs is achieved commonly via reactions of surface hydrides or halides with appropriate ligands.³⁹⁻⁴¹

Hydrosilylation is the most common approach for the surface functionalization of H-SiNCs. Formally, it involves the insertion of unsaturated bonds (e.g., alkene, alkyne) across the Si-H bonds to form stable Si-C bonds,⁷⁶ and it can be achieved via thermal,^{77,78} radical,^{79,80} photochemical,^{69,81} and catalytic processes.⁸²⁻⁸⁴ Thermal hydrosilylation is the most widely employed and straightforward approach for the surface functionalization of H-SiNCs; it is performed at elevated temperatures (100–190 °C) in neat alkene/alkyne, which minimizes the surface oxidation and provides high surface coverage.^{77,85} The thermal hydrosilylation leads to the formation of surface bonded ligand oligomers, which potentially hinders many optoelectronic applications due to the insulating nature of oligomeric surface groups.^{77,86} Moreover, it is not applicable to low boiling short chain alkenes/alkynes because of the temperature requirements of the reaction.⁸⁰ Radical-initiated hydrosilylation is an alternative approach that uses reagents (e.g., 2,2'-azobis(2-methylpropionitrile), benzoyl peroxide) to facilitate the reaction at relatively low temperatures (e.g., 60–85 °C) and provides monolayer surface coverage after short reaction times.⁸⁰ In the studies, described in Chapters 2–4, radical-initiated hydrosilylation was used for monolayer surface coverage and thermal hydrosilylation for oligomeric surface coverage.

1.3.3 Optical Properties of Silicon Nanocrystals

The electronic properties and applications of bulk Si have been explored extensively, and it is the workhorse material of the microelectronic industry.⁸⁷ However, its optical applications are limited due to its band structure. Silicon has an indirect band gap in which the highest point of the valence band (VB) and the lowest point of the conduction band (CB) appear at different wavevectors in reciprocal space; hence, the vertical band gap optical transition is forbidden (**Figure 1-2a**).^{40,88,89} This transition can occur only with the involvement of a phonon (i.e., lattice vibration). The possibility of a phonon-assisted transition in bulk Si is low, therefore, the PL yield is near zero at room temperature.⁹⁰

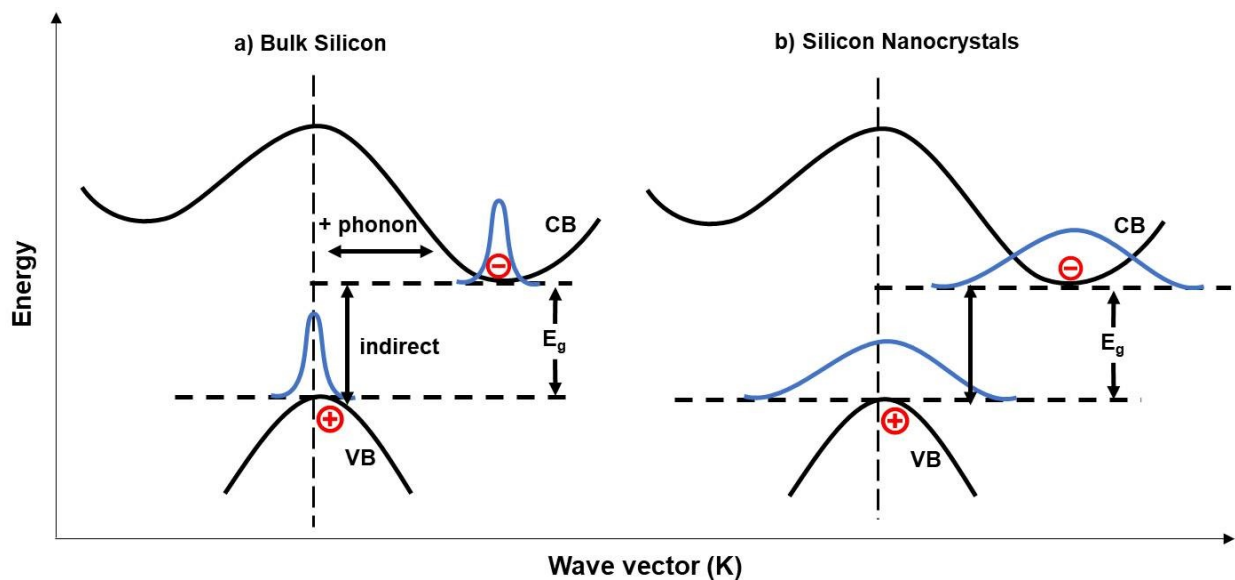


Figure 1-2. Schematic representation of band structure in a) bulk Si and b) silicon nanocrystal.

When the size of the Si particle decreases and reaches below its Bohr exciton radius (~ 5 nm), quantum confinement occurs, and excitons become confined within the NCs spatially. Confining excitons results in the broadening of their wave function according to the Heisenberg uncertainty principle.^{90,91} This leads to an increased possibility of overlap between the VB and

CB wave functions and, consequently, an increased probability of radiative recombination rendering SiNCs luminescent (**Figure 1-2b**).⁹¹ Although this discussion provides an explanation for the observed photoluminescence in SiNCs, the specific origin of SiNC PL is almost certainly more complex and could involve band gap and/or surface state emissions (**Figure 1-3**).^{42,43,92-95}

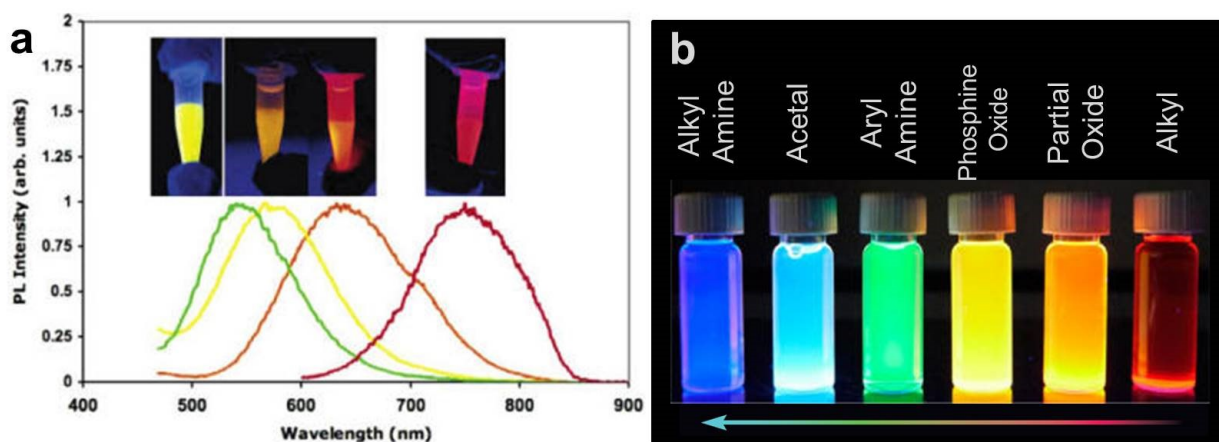


Figure 1-3. The shift in PL of SiNCs as a result of **a**) band gap (Reprinted (adapted) with permission from Reference 42. Copyright 2006 American Chemical Society), and **b**) surface state emissions (Reprinted with permission from Reference 43).

The band gap emission model states that decreasing the NC size leads to an increase in band gap energy, resulting in a blue-shift in PL emission (**Figure 1-3a**).^{42,49,50} The surface state emission model suggests that surface species (i.e., ligands, oxides) influence PL emission (**Figure 1-3b**).^{43,92,93} Regardless of origin of the PL, the PL response of SiNCs opens the door to numerous optical applications (e.g., LEDs, sensors, bioimaging, etc.).^{44,47,48}

1.3.4 Electrical Properties and Battery Application of Silicon Nanocrystals

In addition to their promise in optoelectronic applications, SiNCs are also promising anode materials for high-performance lithium-ion batteries (LIBs). LIBs have been employed widely in

portable electronics, such as cell phones, laptops, and medical devices, due to their high energy density and long cycle life.⁹⁶⁻⁹⁸ These batteries consist of one or more electrochemical cells composed of three main components: an anode, a cathode, and a non-aqueous liquid electrolyte (Figure 1-4).⁹⁷ During charging, Li ions are deintercalated from the cathode, pass through the electrolyte, and are intercalated into the anode; the reverse process happens during discharge.

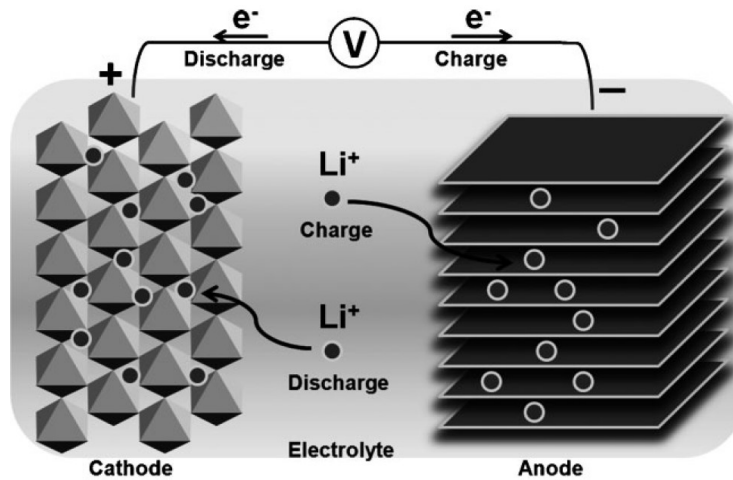


Figure 1-4. Schematic representation of a conventional LIB showing the device components. Reprinted with permission from Reference 97. Copyright 2009 Wiley.

The total cell capacity (mAhg^{-1}) of a battery depends on the theoretical specific capacities of the anode (C_A) and cathode (C_C), and the specific mass of other cell components ($1/Q_M$), as shown in eq 1-1:⁹⁹

$$\text{Total Cell Capacity} = \frac{1}{\left(\frac{1}{C_A}\right) + \left(\frac{1}{C_C}\right) + \left(\frac{1}{Q_M}\right)} \quad (1 - 1)$$

In commercial LIBs, the anode and cathode materials are made of graphite and lithium metal oxides (lithium cobalt oxide and lithium manganese oxide) or lithium iron phosphate; they exhibit theoretical specific capacities of $\sim 372 \text{ mAhg}^{-1}$ and $\sim 200 \text{ mAhg}^{-1}$, respectively.^{97,100,101}

To improve LIBs and extend their scope of application to stationary energy storage and electric vehicles, electrodes with higher specific capacities are being investigated aggressively; air- and sulfur-based cathodes as well as alloy-based anodes are of particular interest.¹⁰²⁻¹⁰⁵ Among alloy-type anodes, silicon-based materials are among the most promising due to their high theoretical specific capacity, which can be as much as 10 times higher than that of existing commercial graphite anodes (*vide infra*).¹⁰⁵ Alloying silicon with lithium leads to the formation of $\text{Li}_{12}\text{Si}_7$, $\text{Li}_{14}\text{Si}_6$, $\text{Li}_{13}\text{Si}_4$, and $\text{Li}_{22}\text{Si}_5$,¹⁰⁶ and the theoretical specific capacity of the fully lithiated alloy (i.e., $\text{Li}_{22}\text{Si}_5$ or $\text{Li}_{4.4}\text{Si}$) is 4200 mAhg^{-1} .^{99,100} Adding to the appeal of silicon is its abundance, non-toxicity, and its low discharge potential (0.4 V against Li/Li^+).⁹⁸⁻¹⁰¹

The practical application of Si anodes is hindered by the low diffusion rate of lithium in Si (diffusion coefficient between 10^{-14} and $10^{-13} \text{ cm}^2\text{s}^{-1}$),¹⁰⁷ low electrical conductivity of Si ($\sim 10^{-3} \text{ Scm}^{-1}$),¹⁰⁸ and large volume changes during the lithiation and delithiation cycling ($>300\%$).⁹⁸⁻¹⁰¹ In addition, these large volume changes result in pulverization of the Si anode, and a complex unstable solid electrolyte interphase (SEI) forms, resulting in a loss of electrical contact, rapid capacity fading, and poor cyclability.⁹⁸⁻¹⁰¹ One approach to address these issues is to employ nanoscale Si. Moving from bulk to nanoscale Si provides a high surface to volume ratio, leading to shorter lithium diffusion lengths within the electrode and the possibility of increased charging and discharging rates.¹⁰⁹ Si-based nanomaterials also limit the material pulverization resulting from lithiation and delithiation cycling by minimizing the stress/strain arising from volume changes, and they improve the cycling performance of Si anodes.¹⁰⁹ In this regard, Si nanostructures of varied morphologies (*e.g.*, nanoparticles,¹¹⁰ nanowires,^{111,112} nanotubes,^{113,114} hollow nanospheres,¹¹⁵ and nanoporous Si^{116,117}) have been investigated; in all cases, improvements in the initial capacity and volume changes of the Si anodes were observed.

Another effective approach that could solve the issues facing Si electrodes related to the low electrical conductivity of Si is to incorporate nanoscale Si into conductive carbon matrices;¹¹⁸⁻¹²³ this will be discussed in detail in Chapter 3.

1.4 Aerogels

Aerogels are nanoporous materials with pore sizes in the range of 1–100 nm, exhibiting high porosity, low density, and high specific surface area.^{124,125} According to the International Union of Pure and Applied Chemistry (IUPAC), nanoporous materials are classified into three categories based on their pore size: microporous ($d < 2$ nm), mesoporous ($2 \text{ nm} < d < 50$ nm), and macroporous ($d > 50$ nm).¹²⁶ The term aerogel was introduced by Kistler in 1931 to describe gels in which the liquid was replaced by air without collapsing the gel solid network.¹²⁷ After Kistler, many efforts have been expended to develop and exploit aerogels based on metal oxides (e.g., silica, alumina, and titania) or, recently, carbon materials (e.g., graphene, carbon nanotube).^{128,129} In this Section, the synthesis, properties, and some applications of silica and graphene aerogels will be discussed.

1.4.1 Silica Aerogels

Silica aerogels are the first and most widely investigated aerogels. They exhibit intriguing properties such as high specific surface area (500–1200 m²/g), low density (~0.1 g/cm³), low thermal conductivity (<0.02 W/mK), and optical transparency.^{130,131} Some applications that benefit directly from these characteristics include catalysts, thermal insulators, and sensors.^{132,133} There are a number of methods to synthesize silica aerogels; all include sol–gel processing of silicon-containing precursors, followed by the application of various drying techniques (e.g., supercritical drying) (**Figure 1-5**).^{130,134}

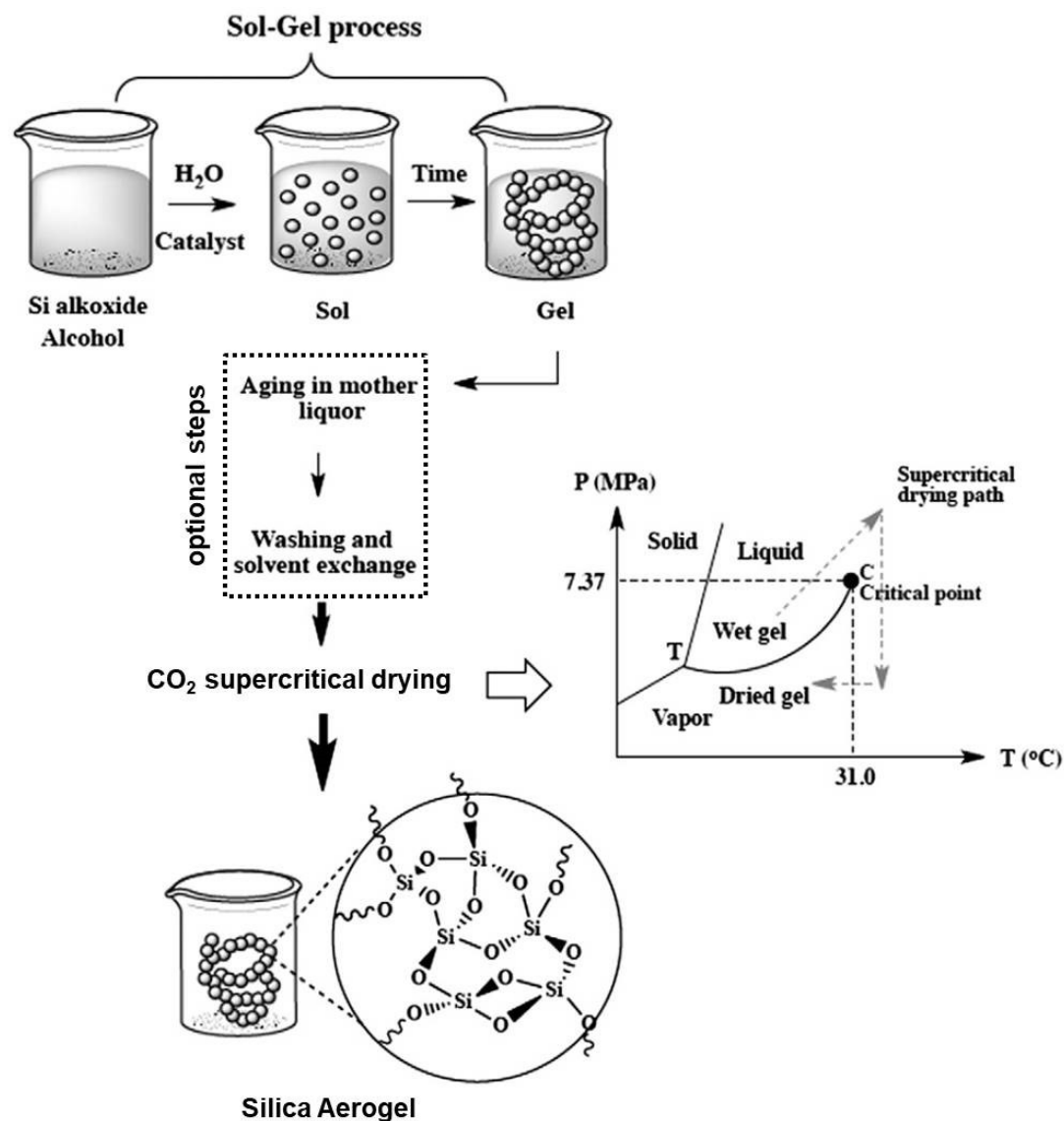
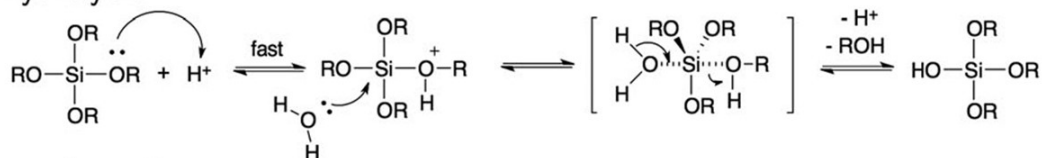


Figure 1-5. Schematic representation of silica aerogel synthesis; sol-gel processing followed by CO₂ supercritical drying. Reprinted from Reference 134, with permission from Elsevier.

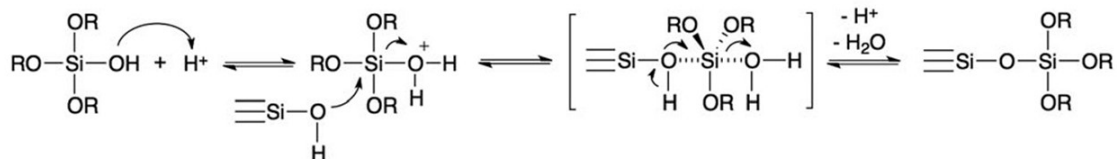
Sol-gel processing involves the hydrolysis and condensation of silicon-containing precursors in the presence of acid (e.g., hydrochloric acid) or base (e.g., ammonium hydroxide) catalyst (**Scheme 1-2**).^{135,136} Silicon alkoxides (e.g., tetramethyl orthosilicate (TMOS), tetraethyl orthosilicate (TEOS)) are the most common silicon-containing precursors.^{130,134} Since silicon

alkoxides are immiscible with water, additional solvent (e.g., methanol, ethanol) is required to homogenize the mixture.

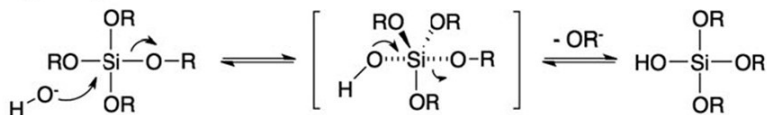
a) hydrolysis



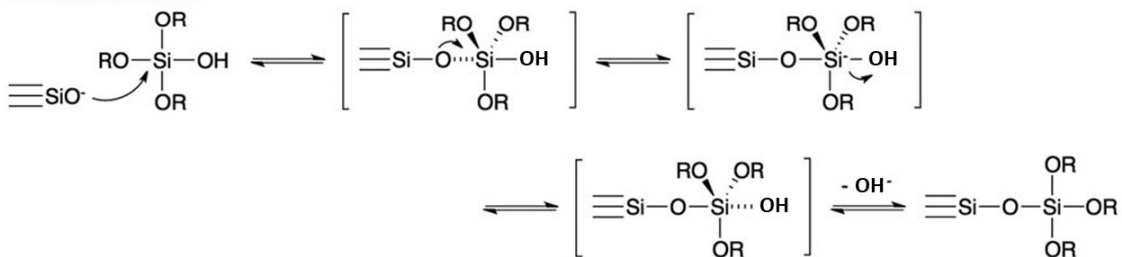
condensation



b) hydrolysis



condensation



Scheme 1-2. General mechanisms of hydrolysis and condensation of silicon alkoxide precursors in the presence of **a)** acid and **b)** base catalysts. Reproduced (Adapted) from Reference 136 with permission of The Royal Society of Chemistry.

The hydrolysis and condensation of silicon alkoxide precursors creates siloxane bridges (Si–O–Si) between Si atoms and leads to the formation of chain-like or branched structures

depending on the catalyst type. For acid-catalyzed sol–gel processing, the electron density of the Si atom should be high to stabilize the positive charge of the transition state (**Scheme 1-2a**); this leads to a chain-like and microporous structure.^{130,137} However, for base-catalyzed sol–gel processing, a negatively charged transition state should be stabilized (**Scheme 1-2a**), leading to a branched structure with decreased microporosity.^{130,137} The acid- or base-catalyzed sol–gel processing results in a mixture that is initially in a liquid phase and, subsequently, forms a gel known as alcogel. The precursor mixture is poured into a mold to form a gel, and the resulting gel may undergo aging and solvent exchange processes before the drying step (**Figure 1-5**).

Drying a gel is a critical step to obtain an aerogel; it is governed by capillary pressure, which depends on the surface tension at the liquid–vapor interface.¹³⁸ As a result of capillary forces, a gel dried under ambient conditions results in a material with a collapsed pore structure called a xerogel (**Figure 1-6a**). To obtain an aerogel, one can avoid crossing the liquid–vapor phase boundary by supercritical drying or freeze drying. Supercritical drying was introduced by Kistler and involves increasing the temperature and pressure of the pore liquid above its critical point and then removing it from a gel in the supercritical phase, where there is no liquid–vapor interface, therefore, no capillary pressure (**Figure 1-6b**).¹²⁷ There are different methods of supercritical drying¹³⁰ (e.g., high temperature, low temperature), and CO₂ supercritical drying is the most practical one due to the low temperature (<40 °C) and moderate pressure (<80 bar) required for drying a gel.¹³⁹ Freeze drying is another approach to avoid liquid–vapor surface tension, which involves freezing the pore liquid, followed by sublimation under vacuum (**Figure 1-6c**); a material produced by this method is called a cryogel.¹⁴⁰ It has been shown that freeze-dried gels lead to more macroporous aerogels compared to those obtained via supercritical drying.¹⁴¹

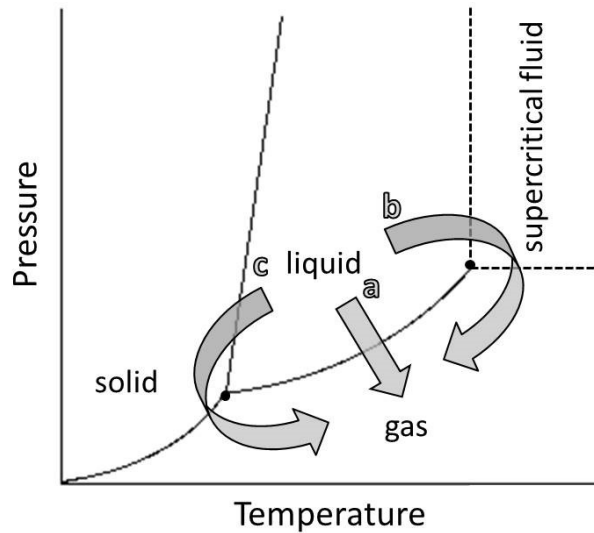


Figure 1-6. Schematic procedure of drying a gel by **a)** evaporation, **b)** supercritical drying, and **c)** freeze drying.

One of the most interesting properties of silica aerogels is their very low thermal conductivity (<0.02 W/mK), even lower than that of air (0.025 W/mK).^{142,143} Silica aerogels are composed of an insulating (i.e., electrical, thermal) silica matrix (~1–10%) and air (~90–99%). Gases are able to transport thermal energy, but the nanoporosity of aerogels prevents gas movement, leading to their very low thermal conductivity; as a result, silica aerogels are among the best thermal insulating materials.^{143,144} Another interesting feature of silica aerogels is their optical transparency, which is an unusual property for a porous material.^{130,135} Aerogels are nanoporous materials, and the pore structure in silica aerogels is small compared to the wavelength of light; this leads to less light scattering and optical transparency in the visible region. Due to their very high thermal insulation properties and optical transparency, silica aerogels could be excellent optical media for SiNCs; this is the focus of Chapter 2.

1.4.2 Graphene Aerogels

Graphene aerogels are carbon-based aerogels, exhibiting interesting properties, such as high specific surface area ($\sim 500 \text{ m}^2/\text{g}$), low density ($\sim 0.1 \text{ g/cm}^3$), high electrical conductivity ($\sim 100 \text{ S/m}$), and good mechanical strength.¹⁴⁵⁻¹⁴⁷ Because of their unique physical, electrical, and mechanical properties, graphene aerogels have demonstrated prototype applications as active materials in batteries, supercapacitors, fuel cells, oil sorbents, and catalysts.¹⁴⁸⁻¹⁵⁵

Since the first report on graphene aerogel in 2009,¹⁵⁶ many methods have been developed to synthesize this class of aerogels, including chemical reduction,^{157,158} electrochemical reduction,^{159,160} hydrothermal reduction,^{161,162} template-directed reduction,^{163,164} and a variety of cross-linking approaches.¹⁶⁵⁻¹⁶⁷ All involve the gelation of a graphene oxide (GO) precursor through the physical or chemical cross-links, followed by different drying methods. GO is a hydrophilic carbon material prepared by the oxidation of graphite using strong oxidizing agents and following the well-established Hummers' method.¹⁶⁸ Although the exact structure of GO is difficult to determine, it is clear that in GO the contiguous aromatic structure of graphene is interrupted by epoxides, alcohols, ketone carbonyls, and carboxylic groups.^{169,170}

Chemical reduction is a common and straightforward approach to synthesize graphene aerogels. A reducing agent (e.g., vitamin C, sodium ascorbate) is added to an aqueous suspension of GO, and the mixture is heated at a moderate temperature ($<100 \text{ }^\circ\text{C}$) for a certain period of time.^{157,158,171} After the chemical reduction of GO, hydrogels form as a result of hydrophobic interactions and π - π stacking between the reduced GO sheets (physical cross-links). Next, they are dried (i.e., supercritical drying or freeze drying) to obtain a graphene aerogel. Graphene aerogels are conductive mesoporous carbon materials and could be an excellent host for SiNCs

for LIB application since they can improve their electrical conductivity and accommodate their volume changes during the lithiation and delithiation cycling; this will be discussed in Chapter 3.

1.5 Patterned Transfer

Transfer of nanomaterials (NMs) from one substrate to another is important for large-scale integration of nanoscale materials into functional devices, and **Figure 1-7** demonstrates the unique material constructs and devices fabricated by advanced forms of transfer printing techniques.^{172a}

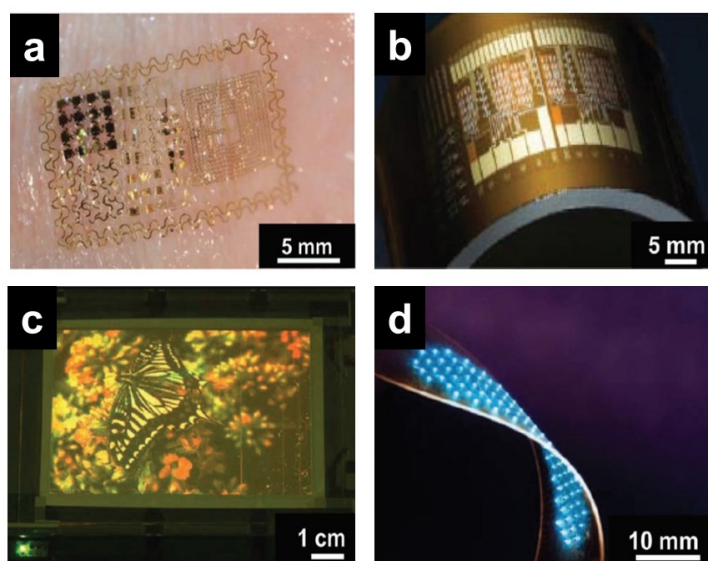


Figure 1-7. Representative examples of unique material constructs and devices fabricated by transfer printing techniques: **a)** Photograph of an epidermal electronic device, conformally laminated onto the surface of the skin (Reprinted with permission from Reference 172a. Copyright 2012 Wiley). **b)** Photograph of a flexible integrated circuit that uses printed networks of single-wall carbon nanotubes for the semiconductor (Reproduced with permission from Reference 172b. Copyright 2008 Nature Publishing Group). **c)** Photograph of a 4-inch, full-color QD-LED display (Reproduced with permission from Reference 172c. Copyright 2011 Nature Publishing Group). **d)** Image of a mechanically flexed array of ultrathin, microscale, blue LEDs printed onto a thin strip of plastic (Reproduced with permission from Reference 172d. Copyright 2011 National Academy of Sciences).

Despite impressive advances,¹⁷³⁻¹⁸⁶ there is no single approach that allows NM transfer on all substrates, and every method brings with it process-specific challenges/limitations. Transfer printing, PMMA-mediated transfer, and lift-off by etching are some examples of transfer techniques (**Figure 1-8**).^{173-178,180,181}

Transfer printing^{172a,173-175} is the most common transfer method and utilizes a structured elastomeric poly(dimethylsiloxane) (PDMS) stamp to achieve NM patterning (**Figure 1-8a**); while effective, it can be complicated by the necessity to control the adhesion forces at the many interfaces involved (i.e., ink/donor, stamp/ink, and ink/receiver). PMMA-mediated¹⁷⁶⁻¹⁷⁸ transfer uses a thin poly(methyl methacrylate) (PMMA) film to transfer NM patterns (**Figure 1-8b**); unfortunately, high temperatures are required when peeling the PMMA film from the source substrate (e.g., 80 °C) and removing the PMMA residues from the target substrate (e.g., 300 °C). Lift-off by etching^{180,181} employs reactive chemicals (e.g., NaOH, HCl) to etch the source substrate partially and release the patterned NM film, which requires NM tolerance to the chemical etchant (**Figure 1-8c**). Hence, developing a general and robust NM transfer method is an active area of research.

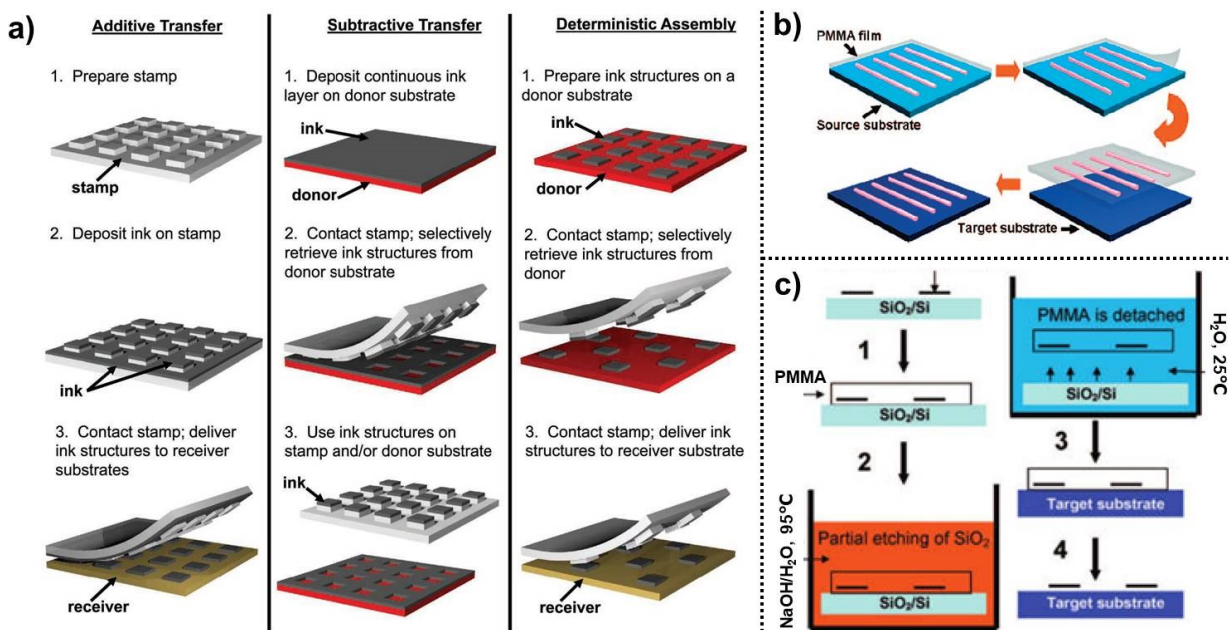


Figure 1-8. Schematic illustration of **a)** three distinct transfer printing techniques (i.e., additive transfer, subtractive transfer, and deterministic assembly) (Reprinted with permission from Reference 172a. Copyright 2012 Wiley), **b)** PMMA-mediated transfer (Reprinted (adapted) with permission from Reference 176. Copyright 2008 American Chemical Society), and **c)** lift-off by etching (Reprinted (adapted) with permission from Reference 180. Copyright 2008 American Chemical Society).

Water transfer printing is an industrial method introduced in 1980 and developed to transfer decorative patterns printed on a polymer film to the surfaces of various shapes and compositions using water pressure.¹⁸⁷ To transfer decorative patterns onto three-dimensional (3D) objects, an inexpensive water-soluble or water-swelling film (e.g., starch, poly(vinyl alcohol) (PVA)) with a printed pattern on top, which has been activated by spraying a solvent mixture (e.g., aliphatic hydrocarbons, aromatic hydrocarbons, monohydric alcohols, ketones, etc.), is made to float on the water surface with the patterned side facing up. Then the 3D object is pressed onto the

pattern, after partial dissolution of the polymer film, to transfer the pattern onto the object (**Figure 1-9a**).^{187,188} This method is straightforward, fast, and cost-effective; it has been employed extensively in the automobile, household, and toy industry (**Figure 1-9b**). A NM transfer method based on water transfer printing could facilitate large-scale transfer of NMs onto various substrates; this will be discussed in Chapter 4. This method does not require a delicate control over the adhesion forces to lift off nanomaterials from the source substrate or high temperatures for removing the polymer residues from the target substrate, and the whole process is carried out in water at low temperatures.

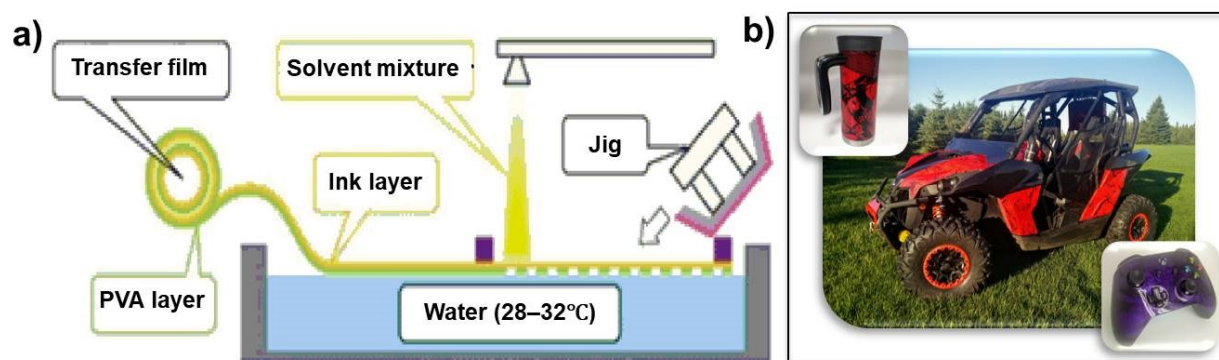


Figure 1-9. a) Schematic illustration of water transfer printing process, and b) examples of applications in the automobile, household, and toy industry. Reprinted with permission from References 188 and 189.

1.6 Thesis Outline

As discussed in this Chapter, silicon nanocrystals are promising nanomaterials for potential optical (e.g., LEDs, sensors) as well as energy (e.g., LIBs) applications. The present thesis focuses on the approaches to transfer SiNCs from solutions to a solid host/substrate to facilitate their practical applications.

One approach to transfer SiNCs from solutions to a solid phase is their incorporation into an aerogel host; this will be discussed in Chapters 2 and 3. The synthesis of luminescent SiNC/silica aerogels of varied transparency is presented in Chapter 2. These hybrid materials are prepared by incorporating hydrophilic SiNCs ($d \sim 3$ or 8 nm) into silica aerogels by exploiting base-catalyzed sol-gel processing and CO₂ supercritical drying. The role of NC size and surface chemistry on the optical properties of the resultant hybrid materials is studied.

Incorporating SiNCs into a conductive mesoporous graphene aerogel could improve their electrical conductivity and accommodate their volume changes during the charging and discharging processes, opening the door to high-performance LIBs. Hence, Chapter 3 focuses on the synthesis and electrochemical characterization of SiNC/graphene aerogel hybrids. Hydrophilic SiNCs of various sizes ($d \sim 3, 5, 8,$ and 15 nm) were synthesized and incorporated into graphene aerogels; the effect of their size and surface chemistry on the electrochemical performance of the hybrid aerogels is investigated.

Patterned transfer is another approach to transfer and position nanomaterials in areas of interest on a solid substrate. A transfer method based on the principles of water transfer printing is developed to transfer hydrophobic nanomaterials from solutions to planar and non-planar substrates and will be discussed in Chapter 4. A summary of main findings of Chapters 2–4 and relevant future directions will be presented in Chapter 5.

1.7 References

1. Kroto, H. W.; Heath, J. R.; O'Brien, S. C.; Curl, R. F.; Smalley R. E. C60: Buckminsterfullerene. *Nature* **1985**, *318*, 162–163.
2. Schmid, G. Large Clusters and Colloids. Metals in the Embryonic State. *Chem. Rev.* **1992**, *92* (8), 1709–1727.
3. Lu, Z.; Yin, Y. Colloidal Nanoparticle Clusters: Functional Materials by Design. *Chem. Soc. Rev.* **2012**, *41* (21), 6874.
4. www.hc-sc.gc.ca/sr-sr/pubs/nano/pol-eng.php (accessed April 1, 2018)
5. Alivisatos, A. P. Perspectives on the Physical Chemistry of Semiconductor Nanocrystals. *J. Phys. Chem.* **1996**, *100* (31), 13226–13239.
6. Eustis, S.; El-Sayed, M. A. Why Gold Nanoparticles Are More Precious than Pretty Gold: Noble Metal Surface Plasmon Resonance and Its Enhancement of the Radiative and Nonradiative Properties of Nanocrystals of Different Shapes. *Chem. Soc. Rev.* **2006**, *35* (3), 209–217.
7. Henglein, A. Small-Particle Research: Physicochemical Properties of Extremely Small Colloidal Metal and Semiconductor Particles. *Chem. Rev.* **1989**, *89* (8), 1861–1873.
8. Zhang, G.; Li, B. Impacts of Doping on Thermal and Thermoelectric Properties of Nanomaterials. *Nanoscale* **2010**, *2* (7), 1058–68.
9. G. Cao, Nanostructures and Nanomaterials, Imperial College Press, London, UK, 2004.
10. Reed, M. A.; Randall, J. N.; Aggarwal, R. J.; Matyi, R. J.; Moore, T. M.; Wetsel, A. E. Observation of Discrete Electronic States in A Zero-Dimensional Semiconductor Nanostructure. *Phys. Rev. Lett.* **1988**, *60* (6), 535–537.
11. Lim, S. J.; Zahid, M. U.; Le, P.; Ma, L.; Entenberg, D.; Harney, A. S.; Condeelis, J.; Smith, A. M. Brightness-Equalized Quantum Dots. *Nat. Commun.* **2015**, *6*, 1–10.
12. Yang, Z.; Voznyy, O.; Liu, M.; Yuan, M.; Ip, A. H.; Ahmed, O. S.; Levina, L.; Kinge, S.; Hoogland, S.; Sargent, E. H. All-Quantum-Dot Infrared Light-Emitting Diodes. *ACS Nano* **2015**, *9* (12), 12327–12333.

13. Jeong, K. S.; Guyot-Sionnest, P. Mid-Infrared Photoluminescence of CdS and CdSe Colloidal Quantum Dots. *ACS Nano* **2016**, *10* (2), 2225–2231.
14. Rogach, B. A. L.; Talapin, D. V; Shevchenko, E. V; Kornowski, A.; Haase, M.; Weller, H. Organization of Matter on Different Size Scales: Monodisperse Nanocrystals and Their Superstructures. *Adv. Funct. Mater.* **2002**, *12* (10), 653–664.
15. Talapin, D. V; Lee, J.; Kovalenko, M. V; Shevchenko, E. V. Prospects of Colloidal Nanocrystals for Electronic and Optoelectronic Applications. *Chem. Rev.* **2010**, *110* (1), **2010**, 389–458.
16. Lim, X. The nanolight revolution is coming *Nature* **2016**, *531*, 26–28.
17. Murray, C. B.; Norris, D. J.; Bawendi, M. G. Synthesis and Characterization of Nearly Monodisperse CdE (E = S, Se, Te) Semiconductor Nanocrystallites. *J. Am. Chem. Soc.* **1993**, *115* (19), 8706–8715.
18. Jun, Y.; Choi, C.-S.; Cheon, J. Size and Shape Controlled ZnTe Nanocrystals with Quantum Confinement Effect. *Chem. Commun.* **2001**, *5769* (1), 101–102.
19. Shim, M.; Guyot-Sionnest, P. Organic-Capped ZnO Nanocrystals: Synthesis and N-Type Character. *J. Am. Chem. Soc.* **2001**, *123* (47), 11651–11654.
20. Yang, Y. A.; Wu, H.; Williams, K. R.; Cao, Y. C. Synthesis of CdSe and CdTe Nanocrystals without Precursor Injection. *Angew. Chemie - Int. Ed.* **2005**, *44* (41), 6712–6715.
21. Battaglia, D.; Peng, X. Formation of High Quality InP and InAs Nanocrystals in a Noncoordinating Solvent. *Nano Lett.* **2002**, *2* (9), 1027–1030.
22. Xie, R.; Battaglia, D.; Peng, X. Colloidal InP Nanocrystals as Efficient Emitters Covering Blue to near-Infrared. *J. Am. Chem. Soc.* **2007**, *129* (50), 15432–15433.
23. Harris, D. K.; Bawendi, M. G. Improved Precursor Chemistry for the Synthesis of III-V Quantum Dots. *J. Am. Chem. Soc.* **2012**, *134* (50), 20211–20213.
24. Marzin, J.-Y.; Gérard, J.-M.; Izraël, A.; Barrier, D.; Bastard, G. Photoluminescence of Single InAs Quantum Dots Obtained by Self-Organized Growth on GaAs. *Phys. Rev. Lett.*

- 1994**, 73, 716–719.
25. Mičić, O. I.; Ahrenkiel, S. P.; Bertram, D.; Nozik, A. J. Synthesis, Structure, and Optical Properties of Colloidal GaN Quantum Dots. *Appl. Phys. Lett.* **1999**, 75 (4), 478–480.
 26. Coe, S.; Woo, M.; Bawendi, W. K.; Bulović, V. Electroluminescence from Single Monolayers of Nanocrystals in Molecular Organic Devices. *Nature* **2002**, 420, 800–803.
 27. Rogach, A. L.; Gaponik, N.; Lupton, J. M.; Bertoni, C.; Gallardo, D. E.; Dunn, S.; Li Pira, N.; Paderi, M.; Repetto, P.; Romanov, S. G.; et al. Light-Emitting Diodes with Semiconductor Nanocrystals. *Angew. Chemie - Int. Ed.* **2008**, 47 (35), 6538–6549.
 28. Chuang, C.-H. M.; Brown, P. R.; Bulović, V.; Bawendi, M. G. Improved Performance and Stability in Quantum Dot Solar Cells through Band Alignment Engineering. *Nat. Mater.* **2014**, 13 (8), 796–801.
 29. Carey, G. H.; Abdelhady, A. L.; Ning, Z.; Thon, S. M.; Bakr, O. M.; Sargent, E. H. Colloidal Quantum Dot Solar Cells. *Chem. Rev.* **2015**, 115 (23), 12732–12763.
 30. Medintz, I. L.; Uyeda, H. T.; Goldman, E. R.; Mattoussi, H. Quantum Dot Bioconjugates for Imaging, Labelling and Sensing. *Nat. Mater.* **2005**, 4 (6), 435–446.
 31. Freeman, R.; Willner, I. Optical Molecular Sensing with Semiconductor Quantum Dots (QDs). *Chem. Soc. Rev.* **2012**, 41 (10), 4067.
 32. Huffaker, D. L.; Park, G.; Zou, Z.; Shchekin, O. B.; Deppe, D. G. 1.3 Mm Room-Temperature GaAs-Based Quantum-Dot Laser. *Appl. Phys. Lett.* **1998**, 73 (18), 2564–2566.
 33. Bimberg, D.; Grundmann, M.; Heinrichsdorff, F.; Ledentsov, N. N.; Ustinov, V. M.; Zhukov, A. E.; Kovsh, A. R.; Maximov, M. V.; Shernyakov, Y. M.; Volovik, B. V.; et al. Quantum Dot Lasers: Breakthrough in Optoelectronics. *Thin Solid Films* **2000**, 367 (1–2), 235–249.
 34. Michalet, X.; Pinaud, F. F.; Bentolila, L. A.; Tsay, J. M.; Doose, S.; Li, J. J.; Sundaresan, G.; Wu, A. M.; Gambhir, S. S.; Weiss, S. Quantum Dots for Live Cells, in Vivo Imaging, and Diagnostics. *Science* **2005**, 307, 538–544.
 35. Wegner, K. D.; Hildebrandt, N. Quantum Dots: Bright and Versatile in Vitro and in Vivo

- Fluorescence Imaging Biosensors. *Chem. Soc. Rev.* **2015**, *44*, 4792–4834.
36. Graeme, K.; Pollack, C. Heavy Metal Toxicity, Part 1: Arsenic and Mercury. *J. Emerg. Med.* **1998**, *16* (1), 46–56.
 37. Houston, M. C. The Role of Mercury and Cadmium Heavy Metals in Vascular Disease, Hypertension, Coronary Heart Disease, and Myocardial Infarction. *Altern. Ther. Health Med.* **2007**, *13* (2), 128–33.
 38. Gordon, R. B.; Bertram, M.; Graedel, T. E. Metal Stocks and Sustainability. *Proc. Natl. Acad. Sci.* **2006**, *103* (5), 1209–1214.
 39. Dasog, M.; Kehrle, J.; Rieger, B.; Veinot, J. G. C. Silicon Nanocrystals and Silicon-Polymer Hybrids: Synthesis, Surface Engineering, and Applications. *Angew. Chemie Int. Ed.* **2016**, *55* (7), 2322–2339.
 40. Veinot, J. G. C. Synthesis, Surface Functionalization, and Properties of Freestanding Silicon Nanocrystals. *Chem. Commun.* **2006**, 4160–4168.
 41. Cheng, X.; Lowe, S. B.; Reece, P. J.; Gooding, J. J. Colloidal Silicon Quantum Dots: From Preparation to the Modification of Self-Assembled Monolayers (SAMs) for Bio-Applications. *Chem. Soc. Rev.* **2014**, *43* (8), 2680–2700.
 42. Hessel, C. M.; Henderson, E. J.; Veinot, J. G. C. Hydrogen Silsesquioxane: A Molecular Precursor for Nanocrystalline Si-SiO₂ Composites and Freestanding Hydride-Surface-Terminated Silicon Nanoparticles. *Chem. Mater.* **2006**, *18* (26), 6139–6146.
 43. Dasog, M.; De Los Reyes, G. B.; Titova, L. V.; Hegmann, F. A.; Veinot, J. G. C. Size vs Surface: Tuning the Photoluminescence of Freestanding Silicon Nanocrystals Across the Visible Spectrum via Surface Groups. *ACS Nano* **2014**, *8* (9), 9636–9648.
 44. Maier-Flaig, F.; Rinck, J.; Stephan, M.; Bocksrocker, T.; Bruns, M.; Kübel, C.; Powell, A. K.; Ozin, G. A.; Lemmer, U. Multicolor Silicon Light-Emitting Diodes (SiLEDs). *Nano Lett.* **2013**, *13* (2), 475–480.
 45. Liu, X. H.; Zhong, L.; Huang, S.; Mao, S. X.; Zhu, T.; Huang, J. Y. Size-Dependent Fracture of Silicon Nanoparticles during Lithiation. *ACS Nano* **2012**, *6* (2), 1522–1531.

46. Liu, C.-Y.; Holman, Z. C.; Kortshagen, U. R. Hybrid Solar Cells from P3HT and Silicon Nanocrystals. *Nano Lett.* **2009**, *9* (1), 449–452.
47. Gonzalez, C. M.; Iqbal, M.; Dasog, M.; Piercey, D. G.; Lockwood, R.; Klapötke, T. M.; Veinot, J. G. C. Detection of High-Energy Compounds Using Photoluminescent Silicon Nanocrystal Paper Based Sensors. *Nanoscale* **2014**, *6* (5), 2608–2612.
48. Erogbogbo, F.; Yong, K.-T.; Roy, I.; Hu, R.; Law, W.-C.; Zhao, W.; Ding, H.; Wu, F.; Kumar, R.; Swihart, M. T.; Prasad, P. N. *In Vivo* Targeted Cancer Imaging, Sentinel Lymph Node Mapping and Multi-Channel Imaging with Biocompatible Silicon Nanocrystals. *ACS Nano* **2011**, *5* (1), 413–423.
49. Canham, L. T. Silicon Quantum Wire Array Fabrication by Electrochemical and Chemical Dissolution of Wafers. *Appl. Phys. Lett.* **1990**, *57*, 1046–48.
50. Cullis, A. G.; Canham, L. T. Visible Light Emission due to Quantum Size Effects in Highly Porous Crystalline Silicon. *Nature* **1991**, *353*, 335–338.
51. Ghosh, B.; Shirahata, N. Colloidal Silicon Quantum Dots: Synthesis and Luminescence Tuning from the near-UV to the near-IR Range. *Sci. Technol. Adv. Mater.* **2014**, *15* (1), 14207.
52. Heintz, A. S.; Fink, M. J.; Mitchell, B. S. Mechanochemical Synthesis of Blue Luminescent Alkyl/alkenyl-Passivated Silicon Nanoparticles. *Adv. Mater.* **2007**, *19* (22), 3984–3988.
53. Chaudhary, A.-L.; Sheppard, D. A.; Paskevicius, M.; Saunders, M.; Buckley, C. E. Mechanochemical Synthesis of Amorphous Silicon Nanoparticles. *RSC Adv.* **2014**, *4* (42), 21979–21983.
54. Kelly, M. T.; Chun, J. K. M.; Bocarsly, A. B. High Efficiency Chemical Etchant for the Formation of Luminescent Porous Silicon. *Appl. Phys. Lett.* **1994**, *64* (13), 1693–1695.
55. Sato, K.; Tsuji, H.; Hirakuri, K.; Fukata, N.; Yamauchi, Y. Controlled Chemical Etching for Silicon Nanocrystals with Wavelength-Tunable Photoluminescence. *Chem. Commun.* **2009**, No. 25, 3759–3761.
56. Bley, R. A.; Kauzlarich, S. M.; Davis, J. E.; Lee, H. W. H. Characterization of Silicon

- Nanoparticles Prepared from Porous Silicon. *Chem. Mater.* **1996**, 8 (8), 1881–1888.
57. Anglin, E. J.; Cheng, L.; Freeman, W. R.; Sailor, M. J. Porous Silicon in Drug Delivery Devices and Materials. *Adv. Drug Deliv. Rev.* **2008**, 60 (11), 1266–1277.
 58. Okada, R.; Iijima, S. Oxidation Property of Silicon Small Particles. *Appl. Phys. Lett.* **1991**, 58 (15), 1662–1663.
 59. Shirahata, N.; Linford, M. R.; Furumi, S.; Pei, L.; Sakka, Y.; Gates, R. J.; Asplund, M. C. Laser-Derived One-Pot Synthesis of Silicon Nanocrystals Terminated with Organic Monolayers. *Chem. Commun.* **2009**, No. 31, 4684–4686.
 60. Heath, J. R. A Liquid-Solution-Phase Synthesis of Crystalline Silicon. *Science* **1992**, 258, 1131–1133.
 61. Arul Dhas, N.; Raj, C. P.; Gedanken, A. Preparation of Luminescent Silicon Nanoparticles: A Novel Sonochemical Approach. *Chem. Mater.* **1998**, 10 (11), 3278–3281.
 62. Warner, J. H.; Hoshino, A.; Yamamoto, K.; Tilley, R. D. Water-Soluble Photoluminescent Silicon Quantum Dots. *Angew. Chemie - Int. Ed.* **2005**, 44 (29), 4550–4554.
 63. Shavel, A.; Guerrini, L.; Alvarez-Puebla, R. A. Colloidal Synthesis of Silicon Nanoparticles in Molten Salts. *Nanoscale* **2017**, 9 (24), 8157–8163.
 64. Bley, R. A.; Kauzlarich, S. M. A Low-Temperature Solution Phase Route for the Synthesis of Silicon Nanoclusters. *J. Am. Chem. Soc.* **1996**, 118 (49), 12461–12462.
 65. Yang, C. S.; Bley, R. A.; Kauzlarich, S. M.; Lee, H. W. H.; Delgado, G. R. Synthesis of Alkyl-Terminated Silicon Nanoclusters by a Solution Route. *J. Am. Chem. Soc.* **1999**, 121 (22), 5191–5195.
 66. Wang, L.; Lin, N.; Zhou, J.; Zhu, Y.; Qian, Y. Silicon Nanoparticles Obtained via a Low Temperature Chemical “metathesis” Synthesis Route and Their Lithium-Ion Battery Properties. *Chem. Commun.* **2015**, 51 (12), 2345–2348.
 67. Huisken, F.; Kohn, B.; Paillard, V. Structured Films of Light-Emitting Silicon Nanoparticles Produced by Cluster Beam Deposition. *Appl. Phys. Lett.* **1999**, 74 (25), 3776–3778.
 68. Li, X.; He, Y.; Talukdar, S. S.; Swihart, M. T. Process for Preparing Macroscopic Quantities

- of Brightly Photoluminescent Silicon Nanoparticles with Emission Spanning the Visible Spectrum. *Langmuir* **2003**, *19* (20), 8490–8496.
69. Hua, F.; Swihart, M. T.; Ruckenstein, E. Efficient Surface Grafting of Luminescent Silicon Quantum Dots by Photoinitiated Hydrosilylation. *Langmuir* **2005**, *21* (13), 6054–6062.
70. Mangolini, L.; Thimsen, E.; Kortshagen, U. High-Yield Plasma Synthesis of Luminescent Silicon Nanocrystals. *Nano Lett.* **2005**, *5* (4), 655–659.
71. Holmes, J. D.; Ziegler, K. J.; Doty, R. C.; Pell, L. E.; Johnston, K. P.; Korgel, B. A. Highly Luminescent Silicon Nanocrystals with Discrete Optical Transitions. *J. Am. Chem. Soc.* **2001**, *123* (16), 3743–3748.
72. Hessel, C. M.; Henderson, E. J.; Veinot, J. G. C. An Investigation of the Formation and Growth of Oxide-Embedded Silicon Nanocrystals in Hydrogen Silsesquioxane-Derived Nanocomposites. *J. Phys. Chem. C* **2007**, *111* (19), 6956–6961.
73. Hessel, C. M.; Reid, D.; Panthani, M. G.; Rasch, M. R.; Goodfellow, B. W.; Wei, J.; Fujii, H.; Akhavan, V.; Korgel, B. A. Synthesis of Ligand-Stabilized Silicon Nanocrystals with Size-Dependent Photoluminescence Spanning Visible to near-Infrared Wavelengths. *Chem. Mater.* **2012**, *24* (2), 393–401.
74. Mastronardi, M. L.; Hennrich, F.; Henderson, E. J.; Maier-Flaig, F.; Blum, C.; Reichenbach, J.; Lemmer, U.; Kübel, C.; Wang, D.; Kappes, M. M.; et al. Preparation of Monodisperse Silicon Nanocrystals Using Density Gradient Ultracentrifugation. *J. Am. Chem. Soc.* **2011**, *133* (31), 11928–11931.
75. Sun, W.; Qian, C.; Cui, X. S.; Wang, L.; Wei, M.; Casillas, G.; Helmy, A. S.; Ozin, G. A. Silicon Monoxide – a Convenient Precursor for Large Scale Synthesis of near Infrared Emitting Monodisperse Silicon Nanocrystals. *Nanoscale* **2016**, *8* (6), 3678–3684.
76. Buriak, J. M. Illuminating Silicon Surface Hydrosilylation: An Unexpected Plurality of Mechanisms. *Chem. Mater.* **2014**, *26* (1), 763–772.
77. Yang, Z.; Iqbal, M.; Dobbie, A. R.; Veinot, J. G. C. Surface-Induced Alkene Oligomerization: Does Thermal Hydrosilylation Really Lead to Monolayer Protected Silicon Nanocrystals? *J. Am. Chem. Soc.* **2013**, *135* (46), 17595–17601.

78. Yang, Z.; Dasog, M.; Dobbie, A. R.; Lockwood, R.; Zhi, Y.; Meldrum, A.; Veinot, J. G. C. Highly Luminescent Covalently Linked Silicon Nanocrystal/polystyrene Hybrid Functional Materials: Synthesis, Properties, and Processability. *Adv. Funct. Mater.* **2014**, *24* (10), 1345–1353.
79. Kehrle, J.; Höhle, I. M. D.; Yang, Z.; Jochem, A. R.; Helbich, T.; Kraus, T.; Veinot, J. G. C.; Rieger, B. Thermoresponsive and Photoluminescent Hybrid Silicon Nanoparticles by Surface-Initiated Group Transfer Polymerization of Diethyl Vinylphosphonate. *Angew. Chemie. Int. Ed.* **2014**, *53*, 12494–12497.
80. Yang, Z.; Gonzalez, C. M.; Purkait, T. K.; Iqbal, M.; Meldrum, A.; Veinot, J. G. C. Radical Initiated Hydrosilylation on Silicon Nanocrystal Surfaces: An Evaluation of Functional Group Tolerance and Mechanistic Study. *Langmuir* **2015**, *31*, 10540–10548.
81. Kelly, J. A.; Shukaliak, A. M.; Fleischauer, M. D.; Veinot, J. G. C. Size-Dependent Reactivity in Hydrosilylation of Silicon Nanocrystals. *J. Am. Chem. Soc.* **2011**, *133* (24), 9564–9571.
82. Purkait, T. K.; Iqbal, M.; Wahl, M. H.; Gottschling, K.; Gonzalez, C. M.; Islam, M. A.; Veinot, J. G. C. Borane-Catalyzed Room-Temperature Hydrosilylation of Alkenes/alkynes on Silicon Nanocrystal Surfaces. *J. Am. Chem. Soc.* **2014**, *136* (52), 17914–17917.
83. Mobarok, M. H.; Purkait, T. K.; Islam, M. A.; Miskolzie, M.; Veinot, J. G. C. Instantaneous Functionalization of Chemically Etched Silicon Nanocrystal Surfaces. *Angew. Chemie - Int. Ed.* **2017**, *56* (22), 6073–6077.
84. Islam, M. A.; Mobarok, M. H.; Sinelnikov, R.; Purkait, T. K.; Veinot, J. G. C. Phosphorus Pentachloride Initiated Functionalization of Silicon Nanocrystals. *Langmuir* **2017**, *33* (35), 8766–8773.
85. Thissen, P.; Seitz, O.; Chabal, Y. J. Wet Chemical Surface Functionalization of Oxide-Free Silicon. *Prog. Surf. Sci.* **2012**, *87* (9–12), 272–290.
86. Hirschman, K. D.; Tsybeskov, L.; Dutta Gupta, S. P.; Fauchet, P. M. Silicon-Based Visible Light-Emitting Devices Integrated into Microelectronic Circuits. *Nature* **1996**, *384*, 338–341.

87. Clemens, J. T. Silicon Microelectronics Technology. *Bell Labs Tech. J.* **2002**, 2 (4), 76–102.
88. Liang, D.; Bowers, J. E. Recent Progress in Lasers on Silicon. *Nat. Photonics* **2010**, 4, 511–517.
89. Hill, N. A.; Whaley, K. B. A Theoretical Study of Light Emission from Nanoscale Silicon. *J. Electron. Mater.* **1996**, 25 (2), 269–285.
90. Daldosso, N.; Pavesi, L. Nanosilicon Photonics. *Laser Photonics Rev.* **2009**, 3 (6), 508–534.
91. Hybertsen, M. S. Absorption and Emission of Light in Nanoscale Silicon Structures. *Phys. Rev. Lett.* **1994**, 72 (10), 1514–1517.
92. Wolkin, M. V.; Jorne, J.; Fauchet, P. M.; Allan, G.; Delerue, C. Electronic States and Luminescence in Porous Silicon Quantum Dots: The Role of Oxygen. *Phys. Rev. Lett.* **1999**, 82 (1), 197–200.
93. Godefroo, S.; Hayne, M.; Jivanescu, M.; Stesmans, A.; Zacharias, M.; Lebedev, O. I.; Van Tendeloo, G.; Moshchalkov, V. V. Classification and Control of the Origin of Photoluminescence from Si Nanocrystals. *Nat. Nanotechnol.* **2008**, 3 (3), 174–178.
94. Sun, W.; Qian, C.; Chen, K. K.; Ozin, G. A. Silicon Nanocrystals: It's Simply a Matter of Size. *ChemNanoMat* **2016**, 2 (9), 847–855.
95. Sinelnikov, R.; Dasog, M.; Beamish, J.; Meldrum, A.; Veinot, J. G. C. Revisiting an Ongoing Debate: What Role Do Surface Groups Play in Silicon Nanocrystal Photoluminescence? *ACS Photonics* **2017**, 4 (8), 1920–1929.
96. Bruce, P. G.; Scrosati, B.; Tarascon, J. M. Nanomaterials for Rechargeable Lithium Batteries. *Angew. Chemie - Int. Ed.* **2008**, 47 (16), 2930–2946.
97. Teki, R.; Krishnan, R.; Parker, T. C.; Lu, T. M.; Datta, M. K.; Kumta, P. N.; Koratkar, N. Nanostructured Silicon Anodes for Lithium Ion Rechargeable Batteries. *Small* **2009**, 5 (20), 2236–2242.
98. Su, X.; Wu, Q.; Li, J.; Xiao, X.; Lott, A.; Lu, W.; Sheldon, B. W.; Wu, J. Silicon-Based Nanomaterials for Lithium-Ion Batteries: A Review. *Adv. Energy Mater.* **2014**, 4, 1300882.
99. Kasavajjula, U.; Wang, C.; Appleby, A. J. Nano- and Bulk-Silicon-Based Insertion Anodes

- for Lithium-Ion Secondary Cells. *J. Power Sources* **2007**, *163* (2), 1003–1039.
100. Wu, H.; Cui, Y. Designing Nanostructured Si Anodes for High Energy Lithium Ion Batteries. *Nano Today* **2012**, *7* (5), 414–429.
101. Zamfir, M. R.; Nguyen, H. T.; Moyen, E.; Lee, Y. H.; Pribat, D. Silicon Nanowires for Li-Based Battery Anodes: A Review. *J. Mater. Chem. A* **2013**, *1* (34), 9566.
102. Bruce, P. G.; Freunberger, S. A.; Hardwick, L. J.; Tarascon, J.-M. Li–O₂ and Li–S Batteries with High Energy Storage. *Nat. Mater.* **2012**, *11* (1), 19–29.
103. Christensen, J.; Albertus, P.; Sanchez-Carrera, R. S.; Lohmann, T.; Kozinsky, B.; Liedtke, R.; Ahmed, J.; Kojic, A. A Critical Review of Li/Air Batteries. *J. Electrochem. Soc.* **2012**, *159* (2), R1.
104. Park, C.-M.; Kim, J.-H.; Kim, H.; Sohn, H.-J. Li-Alloy Based Anode Materials for Li Secondary Batteries. *Chem. Soc. Rev.* **2010**, *39* (8), 3115.
105. Zhang, W. J. A Review of the Electrochemical Performance of Alloy Anodes for Lithium-Ion Batteries. *J. Power Sources* **2011**, *196* (1), 13–24.
106. Boukamp, B. A.; Lesh, G. C.; Huggins, R. A. All-Solid Lithium Electrodes with Mixed-Conductor Matrix. *J. Electrochem. Soc.* **1981**, *128* (4), 725–729.
107. Kulova, T. L.; Skundin, A. M.; Pleskov, Y. V.; Terukov, E. I.; Kon'kov, O. I. Lithium Insertion into Amorphous Silicon Thin-Film Electrodes. *J. Electroanal. Chem.* **2007**, *600* (1), 217–225.
108. Pollak, E.; Salitra, G.; Baranchugov, V.; Aurbach, D. In Situ Conductivity, Impedance Spectroscopy, and Ex Situ Raman Spectra of Amorphous Silicon during the Insertion/extraction of Lithium. *J. Phys. Chem. C* **2007**, *111* (30), 11437–11444.
109. Szczech, J. R.; Jin, S. Nanostructured Silicon for High Capacity Lithium Battery Anodes. *Energy Environ. Sci.* **2011**, *4* (1), 56–72.
110. Liu, X. H.; Zhong, L.; Huang, S.; Mao, S. X.; Zhu, T.; Huang, J. Y. Size-Dependent Fracture of Silicon Nanoparticles during Lithiation. *ACS Nano* **2012**, *6* (2), 1522–1531.
111. Chockla, A. M.; Harris, J. T.; Akhavan, V. A.; Bogart, T. D.; Holmberg, V. C.; Steinhausen,

- C.; Mullins, C. B.; Stevenson, K. J.; Korgel, B. A. Silicon Nanowire Fabric as a Lithium Ion Battery Electrode Material. *J. Am. Chem. Soc.* **2011**, *133* (51), 20914–20921.
112. Nguyen, H. T.; Yao, F.; Zamfir, M. R.; Biswas, C.; So, K. P.; Lee, Y. H.; Kim, S. M.; Cha, S. N.; Kim, J. M.; Pribat, D. Highly Interconnected Si Nanowires for Improved Stability Li-Ion Battery Anodes. *Adv. Energy Mater.* **2011**, *1* (6), 1154–1161.
113. Park, M.; Kim, M. G.; Joo, J.; Kim, K.; Kim, J.; Ahn, S.; Cui, Y.; Cho, J. Silicon Nanotube Battery Anodes. *Nano Lett.* **2009**, *9* (11), 3844–3847.
114. Wu, H.; Chan, G.; Choi, J. W.; Ryu, I.; Yao, Y.; McDowell, M. T.; Lee, S. W.; Jackson, A.; Yang, Y.; Hu, L.; et al. Stable Cycling of Double-Walled Silicon Nanotube Battery Anodes through Solid-Electrolyte Interphase Control. *Nat. Nanotechnol.* **2012**, *7* (5), 310–315.
115. Yao, Y.; McDowell, M. T.; Ryu, I.; Wu, H.; Liu, N.; Hu, L.; Nix, W. D.; Cui, Y. Interconnected Silicon Hollow Nanospheres for Lithium-Ion Battery Anodes with Long Cycle Life. *Nano Lett.* **2011**, *11* (7), 2949–2954.
116. Zhao, Y.; Liu, X.; Li, H.; Zhai, T.; Zhou, H. Hierarchical Micro/nano Porous Silicon Li-Ion Battery Anodes. *Chem. Commun.* **2012**, *48* (42), 5079.
117. Zhu, J.; Gladden, C.; Liu, N.; Cui, Y.; Zhang, X. Nanoporous Silicon Networks as Anodes for Lithium Ion Batteries. *Phys. Chem. Chem. Phys.* **2013**, *15* (2), 440–443.
118. Wang, B.; Li, X.; Zhang, X.; Luo, B.; Jin, M.; Liang, M.; Dayeh, S. A.; Picraux, S. T.; Zhi, L. Adaptable Silicon-Carbon Nanocables Sandwiched between Reduced Graphene Oxide Sheets as Lithium Ion Battery Anodes. *ACS Nano* **2013**, *7* (2), 1437–1445.
119. Liu, N.; Lu, Z.; Zhao, J.; McDowell, M. T.; Lee, H. W.; Zhao, W.; Cui, Y. A Pomegranate-Inspired Nanoscale Design for Large-Volume-Change Lithium Battery Anodes. *Nat. Nanotechnol.* **2014**, *9* (3), 187–192.
120. Chang, J.; Huang, X.; Zhou, G.; Cui, S.; Hallac, P. B.; Jiang, J.; Hurley, P. T.; Chen, J. Multilayered Si Nanoparticle/reduced Graphene Oxide Hybrid as a High-Performance Lithium-Ion Battery Anode. *Adv. Mater.* **2014**, *26* (5), 758–764.
121. Lu, Z.; Liu, N.; Lee, H. W.; Zhao, J.; Li, W.; Li, Y.; Cui, Y. Nonfilling Carbon Coating of

- Porous Silicon Micrometer-Sized Particles for High-Performance Lithium Battery Anodes. *ACS Nano* **2015**, *9* (3), 2540–2547.
122. Xu, Q.; Li, J. Y.; Sun, J. K.; Yin, Y. X.; Wan, L. J.; Guo, Y. G. Watermelon-Inspired Si/C Microspheres with Hierarchical Buffer Structures for Densely Compacted Lithium-Ion Battery Anodes. *Adv. Energy Mater.* **2017**, *7* (3), 1–6.
123. Chen, S.; Shen, L.; van Aken, P. A.; Maier, J.; Yu, Y. Dual-Functionalized Double Carbon Shells Coated Silicon Nanoparticles for High Performance Lithium-Ion Batteries. *Adv. Mater.* **2017**, *29* (21).
124. Heinrich, T.; Klett, U.; Fricke, J. Aerogels-Nanoporous Materials Part I: Sol-Gel Process and Drying of Gels. *J. Porous Mater.* **1995**, *1* (1), 7–17.
125. Fricke, J. Aerogels — Highly Tenuous Solids with Fascinating Properties. *J. Non. Cryst. Solids* **1988**, *100* (1–3), 169–173.
126. Hu, Z.; Srinivasan, M. P.; Ni, Y. Preparation of Mesoporous High-Surface-Area Activated Carbon. *Adv. Mater.* **2000**, *12* (1), 62–65.
127. Kistler, S. S. Coherent Expanded-Aerogels. *J. Phys. Chem.* **1931**, *36* (1), 52–64.
128. Teichner, S. J.; Nicolaon, G. A.; Vicarini, M. A.; Gardes, G. E. E. Inorganic Oxide Aerogels. *Adv. Colloid Interface Sci.* **1976**, *5* (3), 245–273.
129. Du, A.; Zhou, B.; Zhang, Z.; Shen, J. A Special Material or a New State of Matter: A Review and Reconsideration of the Aerogel. *Materials* **2013**, *6* (3), 941–968.
130. Soleimani Dorcheh, A.; Abbasi, M. H. Silica Aerogel; Synthesis, Properties and Characterization. *J. Mater. Process. Technol.* **2008**, *199* (1–3), 10–26.
131. Gurav, J. L.; Jung, I.-K.; Park, H.-H.; Kang, E. S.; Nadargi, D. Y. Silica Aerogel: Synthesis and Applications. *J. Nanomater.* **2010**, *2010*, 1–11.
132. Schmidt, M.; Schwertfeger, F. Applications for Silica Aerogel Products. *J. Non. Cryst. Solids* **1998**, *225*, 364–368.
133. Pajonk, G. M. Some Applications of Silica Aerogels. *Colloid Polym. Sci.* **2003**, *281* (7), 637–651.

134. Maleki, H.; Durães, L.; Portugal, A. An Overview on Silica Aerogels Synthesis and Different Mechanical Reinforcing Strategies. *J. Non. Cryst. Solids* **2014**, *385*, 55–74.
135. Pierre, A. C.; Pajonk, G. M. Chemistry of Aerogels and Their Applications. *Chem. Rev.* **2002**, *102*, 4243–4265.
136. Lofgreen, J. E.; Ozin, G. A. Controlling Morphology and Porosity to Improve Performance of Molecularly Imprinted Sol–gel Silica. *Chem. Soc. Rev.* **2014**, *43* (3), 911–933.
137. Schubert, U.; Hüsing, N. *Synthesis of Inorganic Materials*, Second, Revised and Updated Edition. Wiley-VCH: Germany, 2005, 205–206.
138. Bisson, A.; Rigacci, A.; Lecomte, D.; Rodier, E.; Achard, P. Drying of Silica Gels to Obtain Aerogels: Phenomenology and Basic Techniques. *Dry. Technol.* **2003**, *21* (4), 593–628.
139. Tewari, P. H.; Hunt, A. J.; Lofftus, K. D. Ambient-Temperature Supercritical Drying of Transparent Silica Aerogels. *Mater. Lett.* **1985**, *3* (9–10), 363–367.
140. Scherer, G. W. Freezing Gels. *J. Non. Cryst. Solids* **1993**, *155* (1), 1–25.
141. Kalinin, S. V.; Kheifets, L. I.; Mamchik, A. I.; Knot'ko, A. G.; Vertegel, A. A. Influence of the Drying Technique on the Structure of Silica Gels. *J. Sol-Gel Sci. Technol.* **1999**, *15* (1), 31–35.
142. Hrubesh, L. W.; Pekala, R. W. Thermal Properties of Organic and Inorganic Aerogels. *J. Mater. Res.* **1994**, *9* (3), 731–738.
143. Yoldas, B. E.; Annen, M. J.; Bostaph, J. Chemical Engineering of Aerogel Morphology Formed under Nonsupercritical Conditions for Thermal Insulation. *Chem. Mater.* **2000**, *12* (8), 2475–2484.
144. Thapliyal, P. C.; Singh, K. Aerogels as Promising Thermal Insulating Materials: An Overview. *J. Mater.* **2014**, *2014*, 10.
145. Nardecchia, S.; Carriazo, D.; Ferrer, M. L.; Gutiérrez, M. C.; del Monte, F. Three Dimensional Macroporous Architectures and Aerogels Built of Carbon Nanotubes and/or Graphene: Synthesis and Applications. *Chem. Soc. Rev.* **2013**, *42* (2), 794–830.
146. Ma, Y.; Chen, Y. Three-Dimensional Graphene Networks: Synthesis, Properties and

- Applications. *Natl. Sci. Rev.* **2015**, *2* (1), 40–53.
147. Gorgolis, G.; Galiotis, C. Graphene Aerogels: A Review. *2D Mater.* **2017**, *4* (3), 032001.
148. Mao, J.; Iocozzia, J.; Huang, J.; Meng, K.; Lai, Y.; Lin, Z. Graphene Aerogels for Efficient Energy Storage and Conversion. *Energy Environ. Sci.* **2018**, *11*, 772–799.
149. Chen, Z.; Li, H.; Tian, R.; Duan, H.; Guo, Y.; Chen, Y.; Zhou, J.; Zhang, C.; Dugnani, R.; Liu, H. Three Dimensional Graphene Aerogels as Binder-Less, Freestanding, Elastic and High-Performance Electrodes for Lithium-Ion Batteries. *Sci. Rep.* **2016**, *6*, 1–9.
150. Yu, Z.; McInnis, M.; Calderon, J.; Seal, S.; Zhai, L.; Thomas, J. Functionalized Graphene Aerogel Composites for High-Performance Asymmetric Supercapacitors. *Nano Energy* **2015**, *11*, 611–620.
151. Zhu, C.; Liu, T.; Qian, F.; Han, T. Y. J.; Duoss, E. B.; Kuntz, J. D.; Spadaccini, C. M.; Worsley, M. A.; Li, Y. Supercapacitors Based on Three-Dimensional Hierarchical Graphene Aerogels with Periodic Macropores. *Nano Lett.* **2016**, *16* (6), 3448–3456.
152. Ren, L.; Hui, K. S.; Hui, K. N. Self-Assembled Free-Standing Three-Dimensional Nickel Nanoparticle/graphene Aerogel for Direct Ethanol Fuel Cells. *J. Mater. Chem. A* **2013**, *1* (18), 5689.
153. Bi, H.; Xie, X.; Yin, K.; Zhou, Y.; Wan, S.; He, L.; Xu, F.; Banhart, F.; Sun, L.; Ruoff, R. S. Spongy Graphene as a Highly Efficient and Recyclable Sorbent for Oils and Organic Solvents. *Adv. Funct. Mater.* **2012**, *22* (21), 4421–4425.
154. Wu, Z.; Yang, S.; Sun, Y.; Parvez, K.; Feng, X.; Müllen, K. 3D Nitrogen-Doped Graphene Aerogel-Supported Fe₃O₄ Nanoparticles as Efficient Electrocatalysts for the Oxygen Reduction Reaction. *J. Am. Chem. Soc.* **2012**, *134* (22), 9082–9085.
155. Yin, H.; Zhang, C.; Liu, F.; Hou, Y. Hybrid of Iron Nitride and Nitrogen-Doped Graphene Aerogel as Synergistic Catalyst for Oxygen Reduction Reaction. *Adv. Funct. Mater.* **2014**, *24* (20), 2930–2937.
156. Wang, J.; Ellsworth, M. W. Graphene Aerogels. *ECS Trans.* **2009**, *19* (5), 241–247.
157. Sheng, K. X.; Xu, Y. X.; Li, C.; Shi, G. Q. High-Performance Self-Assembled Graphene

- Hydrogels Prepared by Chemical Reduction of Graphene Oxide. *New Carbon Mater.* **2011**, *26* (1), 9–15.
158. Chen, W.; Yan, L. In Situ Self-Assembly of Mild Chemical Reduction Graphene for Three-Dimensional Architectures. *Nanoscale* **2011**, *3* (8), 3132.
159. Sheng, K.; Sun, Y.; Li, C.; Yuan, W.; Shi, G. Ultrahigh-Rate Supercapacitors Based on Electrochemically Reduced Graphene Oxide for AC Line-Filtering. *Sci. Rep.* **2012**, *2*, 3–7.
160. Li, Y.; Sheng, K.; Yuan, W.; Shi, G. A High-Performance Flexible Fibre-Shaped Electrochemical Capacitor Based on Electrochemically Reduced Graphene Oxide. *Chem. Commun.* **2013**, *49* (3), 291–293.
161. Yuxi Xu, Kaixuan Sheng, C. L.; Shi, G. Self-Assembled Graphene Hydrogel. *ACS Nano* **2010**, *4* (7), 4324–4330.
162. Han, Z.; Tang, Z.; Li, P.; Yang, G.; Zheng, Q.; Yang, J. Ammonia Solution Strengthened Three-Dimensional Macro-Porous Graphene Aerogel. *Nanoscale* **2013**, *5* (12), 5462.
163. Choi, B. G.; Yang, M.; Hong, W. H.; Choi, J. W.; Huh, Y. S. 3D Macroporous Graphene Frameworks for Supercapacitors with High Energy and Power Densities. *ACS Nano* **2012**, *6* (5), 4020–4028.
164. Wang, Z.; Shen, X.; Han, N. M.; Liu, X.; Wu, Y.; Ye, W.; Kim, J. K. Ultralow Electrical Percolation in Graphene Aerogel/Epoxy Composites. *Chem. Mater.* **2016**, *28* (18), 6731–6741.
165. Hu, H.; Zhao, Z.; Wan, W.; Gogotsi, Y.; Qiu, J. Ultralight and Highly Compressible Graphene Aerogels. *Adv. Mater.* **2013**, *25* (15), 2219–2223.
166. Cong, H. P.; Ren, X. C.; Wang, P.; Yu, S. H. Macroscopic Multifunctional Graphene-Based Hydrogels and Aerogels by a Metal Ion Induced Self-Assembly Process. *ACS Nano* **2012**, *6* (3), 2693–2703.
167. Worsley, M. a; Pauzauskie, P. J.; Olson, T. Y.; Biener, J.; Satcher Jr., J. H.; Baumann, T. F. Synthesis of Graphene Aerogel with High Electrical Conductivity. *J. Am. Chem. Soc.* **2010**, *132*, 14067–14069.

168. Hummers, W. S.; Offeman, R. E. Preparation of Graphitic Oxide. *J. Am. Chem. Soc.* **1958**, *80* (6), 1339.
169. Dreyer, D. R.; Park, S.; Bielawski, C. W.; Ruoff, R. S. Graphite Oxide. *Chem. Soc. Rev.* **2010**, *39* (1), 228–240.
170. Marcano, D. C.; Kosynkin, D. V.; Berlin, J. M.; Sinitskii, A.; Sun, Z. Z.; Slesarev, A.; Alemany, L. B.; Lu, W.; Tour, J. M. Improved Synthesis of Graphene Oxide. *ACS Nano* **2010**, *4* (8), 4806–4814.
171. Zhang, X.; Sui, Z.; Xu, B.; Yue, S.; Luo, Y.; Zhan, W.; Liu, B. Mechanically Strong and Highly Conductive Graphene Aerogel and Its Use as Electrodes for Electrochemical Power Sources. *J. Mater. Chem.* **2011**, *21* (18), 6494.
172. **a)** Carlson, A.; Bowen, A. M.; Huang, Y.; Nuzzo, R. G.; Rogers, J. A. Transfer Printing Techniques for Materials Assembly and Micro/Nanodevice Fabrication. *Adv. Mater.* **2012**, *24* (39), 5284–5318. **b)** Cao, Q.; Kim, H. S.; Pimparkar, N.; Kulkarni, J. P.; Wang, C.; Shim, M.; Roy, K.; Alam, M. A.; Rogers, J. A. Medium-Scale Carbon Nanotube Thin-Film Integrated Circuits on Flexible Plastic Substrates. *Nature* **2008**, *454* (7203), 495–500. **c)** Kim, T. H.; Cho, K. S.; Lee, E. K.; Lee, S. J.; Chae, J.; Kim, J. W.; Kim, D. H.; Kwon, J. Y.; Amaratunga, G.; Lee, S. Y.; et al. Full-Colour Quantum Dot Displays Fabricated by Transfer Printing. *Nat. Photonics* **2011**, *5* (3), 176–182. **d)** Kim, H.; Brueckner, E.; Song, J.; Li, Y.; Kim, S.; Lu, C.; Sulkin, J.; Choquette, K.; Huang, Y.; Nuzzo, R. G.; Rogers, J. A. Unusual Strategies for Using Indium Gallium Nitride Grown on Silicon (111) for Solid-State Lighting. *Proc. Natl. Acad. Sci.* **2011**, *108* (25), 10072.
173. Meitl, M. A.; Zhu, Z.-T.; Kumar, V.; Lee, K. J.; Feng, X.; Huang, Y. Y.; Adesida, I.; Nuzzo, R. G.; Rogers, J. A. Transfer Printing by Kinetic Control of Adhesion to an Elastomeric Stamp. *Nat. Mater.* **2006**, *5* (1), 33–38.
174. Allen, M. J.; Tung, V. C.; Gomez, L.; Xu, Z.; Chen, L. M.; Nelson, K. S.; Zhou, C.; Kaner, R. B.; Yang, Y. Soft Transfer Printing of Chemically Converted Graphene. *Adv. Mater.* **2009**, *21* (20), 2098–2102.
175. Kim, B. H.; Nam, S.; Oh, N.; Cho, S. Y.; Yu, K. J.; Lee, C. H.; Zhang, J.; Deshpande, K.;

- Trefonas, P.; Kim, J. H.; et al. Multilayer Transfer Printing for Pixelated, Multicolor Quantum Dot Light-Emitting Diodes. *ACS Nano* **2016**, *10* (5), 4920–4925.
176. Jiao, L.; Fan, B.; Xian, X.; Wu, Z.; Zhang, J.; Liu, Z. Creation of Nanostructures with Poly(methyl Methacrylate)-Mediated Nanotransfer Printing. *J. Am. Chem. Soc.* **2008**, *130* (38), 12612–12613.
177. Suk, J. W.; Kitt, A.; Magnuson, C. W.; Hao, Y.; Ahmed, S.; An, J.; Swan, A. K.; Goldberg, B. B.; Ruoff, R. S. Transfer of CVD-Grown Monolayer Graphene onto Arbitrary Substrates. *ACS Nano* **2011**, *5* (9), 6916–6924.
178. Liu, Y.; Cheng, R.; Liao, L.; Zhou, H.; Bai, J.; Liu, G.; Liu, L.; Huang, Y.; Duan, X. Plasmon Resonance Enhanced Multicolour Photodetection by Graphene. *Nat. Commun.* **2011**, *2* (1), 577–579.
179. Xu, Q.; Rioux, R. M.; Dickey, M. D.; Whitesides, G. M. Nanoskiving: A New Method to Produce Arrays of Nanostructures. *Acc. Chem. Res.* **2008**, *41* (12), 1566–1577.
180. Reina, A.; Son, H.; Jiao, L.; Fan, B.; Dresselhaus, M. S.; Liu, Z.; Kong, J. Transferring and Identification of Single- and Few-Layer Graphene on Arbitrary Substrates. *J. Phys. Chem. C* **2008**, *112* (46), 17741–17744.
181. Reina, A., Jia, X., Ho, J., Nezich, D., Son, H., Bulovic, V., Dresselhaus, M.S. and Kong, J. Large Area, Few-Layer Graphene Films on Arbitrary Substrates by Chemical Vapor Deposition. *Nano Lett.* **2008**, *9* (1), 30–35.
182. Schneider, G. F.; Calado, V. E.; Zandbergen, H.; Vandersypen, L. M. K.; Dekker, C. Wedging Transfer of Nanostructures. *Nano Lett.* **2010**, *10* (5), 1912–1916.
183. Lee, C. H.; Kim, D. R.; Cho, I. S.; William, N.; Wang, Q.; Zheng, X. Peel-and-Stick: Fabricating Thin Film Solar Cell on Universal Substrates. *Sci. Rep.* **2012**, *2*, 2–5.
184. Li, H.; Wu, J.; Huang, X.; Yin, Z.; Liu, J.; Zhang, H. A Universal, Rapid Method for Clean Transfer of Nanostructures onto Various Substrates. *ACS Nano* **2014**, *8* (7), 6563–6570.
185. Choi, M. K.; Yang, J.; Kang, K.; Kim, D. C.; Choi, C.; Park, C.; Kim, S. J.; Chae, S. I.; Kim, T. H.; Kim, J. H.; et al. Wearable Red-Green-Blue Quantum Dot Light-Emitting Diode

- Array Using High-Resolution Intaglio Transfer Printing. *Nat. Commun.* **2015**, *6*, 1–8.
186. Ma, X.; Liu, Q.; Xu, D.; Zhu, Y.; Kim, S.; Cui, Y.; Zhong, L.; Liu, M. Capillary-Force-Assisted Clean-Stamp Transfer of Two-Dimensional Materials. *Nano Lett.* **2017**, *17* (11), 6961–6967.
187. Arai, E.; Kamei, K.; Kawasaki, A.; Takagi, F.; Shirai, K.; Orihara, Y. Patent US 4229239, 1980.
188. Water Transfer Printing Films - DIC Corporation
http://www.dic-global.com/us/en/products/decorative_materials/transcript.html.
189. <http://www.liquidcustoms.ca/gallery>

Chapter 2:

Synthesis and Properties of Luminescent Silicon Nanocrystal/Silica Aerogel Hybrid Materials

A version of this Chapter has been published:

Aghajamali, M.; Iqbal, M.; Purkait, T. K.; Hadidi, L.; Sinelnikov, R.; Veinot, J. G. C., *Chem. Mater.* **2016**, *28*, 3877–3886.

Copyright © 2016 American Chemical Society.

2.1 Introduction

Aerogels are intriguing materials that possess high specific surface area and porosity, low density, and exhibit unique thermal, optical, as well as chemical properties.^{1,2} Some aerogel applications that benefit directly from these characteristics include sensors,³⁻⁵ catalysts,⁶⁻⁹ thermal insulators,¹⁰⁻¹² and energy storage electrodes.^{13,14} To date, much effort has been expended to develop and exploit aerogels based upon metal oxides (e.g., silica (SiO₂), alumina, and titania).¹⁵ Silica aerogels have attracted substantial interest because of the relative ease with which they may be fabricated; they are prepared readily by exploiting the well-established principles of silicon sol-gel chemistry (i.e., the hydrolysis and condensation of silicon alkoxide precursors) and various drying procedures (e.g., supercritical drying, freeze drying). Aerogels prepared in this way are transparent and possess specific surface areas approaching 500–1200 m²/g, porosities of 80–99.8%, and low densities (0.003–0.35 g/cm³).^{16,17} Reaching beyond basic systems, hybrids made up of a host aerogel and nanoscale guest hold promise of combining the unique physical, chemical, and optical properties of both components to yield composite characteristics that could expand the scope of the applications of aerogel systems.^{18,19}

Silicon nanocrystals (SiNCs) are non-toxic quantum dots whose optical response may be tuned through variations of NC size and surface chemistry.²⁰⁻²³ Because of their exquisitely tunable electronic, optical, and chemical properties, SiNCs have demonstrated prototype applications as active materials in sensors,^{24,25} batteries,^{26,27} bioimaging,^{28,29} drug delivery,^{22,30} optoelectronic structures,^{31,32} and photovoltaics.³³⁻³⁵ Surprisingly, despite their chemical compatibility with silica and associated aerogels, only a small number of reports aim to combine the properties of these two important classes of materials.³⁶⁻³⁸ Early SiNC-SiO₂ aerogel composites were prepared by either sol-gel processing of a mixture containing nanoscale Si and

silicon alkoxide precursors^{36,37} or by pressing powders of porous silicon and silica aerogels.³⁸ The SiNC-SiO₂ aerogel hybrids prepared using sol-gel processing were limited to comparatively large SiNCs ($d > 10$ nm)³⁶ or ill-defined porous silicon grains.³⁷ Silicon nanoparticles of these dimensions do not exhibit tunable photoluminescence (PL); quantum confinement only impacts the properties of much smaller ($d < 5$ nm) nano-silicon particles.²⁰ In addition, the SiNC properties (e.g., size and surface chemistry) and nanocomposite aerogel characteristics (e.g., optical transparency and physical properties) were not explored. Furthermore, there are no reports of transparent luminescent SiNC-loaded SiO₂ aerogels with high loading of SiNCs, which opens the door to potential applications ranging from sensors to optoelectronics. In this Chapter, a detailed investigation aimed at interfacing the complementary properties of luminescent SiNCs with transparent high surface area silica aerogels is described. We have investigated the role of NC size and surface chemistry on the properties of the resultant nanocomposites, methodically.

2.2 Experimental

2.2.1 Reagents and Materials

Commercial hydrogen silsesquioxane (HSQ, trade name Fox-17) was obtained as a solution in methyl isobutyl ketone from Dow Corning Corporation; the solvent was removed under vacuum, and the resulting white solid was used without further purification. Electronics grade hydrofluoric acid (HF, 49% aqueous solution) was purchased from J. T. Baker. Tetramethyl orthosilicate (TMOS) (98%), 1-dodecene (95%), azobisisobutyronitrile (AIBN) (98%), methanol (reagent grade), toluene (reagent grade), and chloroform (reagent grade) were obtained from Sigma-Aldrich. 4-pentenoic acid (98%, Alfa Aesar), allyloxy (polyethylene oxide) methyl ether ($M_w \sim 450-455$, Gelest Inc.), anhydrous diethyl ether (reagent grade, Fisher Scientific),

ammonium hydroxide (28–30%, Caledon Laboratory Chemicals), nitrobenzene (99%, Alfa Aesar), and low viscosity embedding media Spurr's kit (Electron Microscopy Sciences) were used as received unless otherwise specified.

2.2.2 Synthesis, Liberation, and Functionalization of SiNCs

Preparation of oxide-embedded SiNCs: Oxide-embedded SiNCs were synthesized using well-established procedures developed in the Veinot laboratory.^{39,40} An appropriate amount of HSQ (i.e., 5 g) was transferred to a quartz boat, placed in a Lindberg Blue tube furnace, and thermally processed at 1100 °C for 1 h in 5% H₂/95% Ar. This procedure yielded an amber solid that consisted of SiNCs ($d \sim 3$ nm) encapsulated in a SiO₂-like matrix. This solid was ground using an agate mortar and pestle. To achieve larger SiNCs ($d \sim 8$ nm), the manually ground amber solid containing 3 nm SiNCs was placed in a high-temperature furnace (Sentro Tech Corp.) for further thermal processing at 1300 °C for 1 h in argon. The resulting 8 nm SiNC/SiO₂ composite was ground following the procedures described above and stored in standard glass vials until needed.

Preparation of hydride-terminated SiNCs (H-SiNCs): Hydride-terminated SiNCs ($d \sim 3$ or 8 nm) were freed from the oxide matrix via HF etching.^{39,40} Briefly, 0.5 g of the ground SiNC/SiO₂ composite was etched using 18 mL of a solution containing 100% ethanol: deionized (DI) water: 49% HF in a ratio of 1: 1: 1 (v: v: v). (**Caution!** HF must be handled with extreme care.) The mixture was stirred for 1 h under ambient conditions, and the resulting H-SiNCs (ca. 50 mg) were collected by multiple extractions with toluene (i.e., 3×10 mL) and centrifugation at 3000 rpm for 10 minutes.

Synthesis of pentanoic acid functionalized SiNCs (3COOH, 8COOH): Pentanoic acid functionalized SiNCs were prepared using a radical induced hydrosilylation.²⁸ H-SiNCs ($d \sim 3$ or 8 nm), obtained from etching 0.5 g SiNC/SiO₂ composite, were dispersed in dry toluene (15 mL) in a Schlenk flask equipped with a magnetic stir bar. 4-pentenoic acid (7 mL) and AIBN (75 mg) were added to the flask and the mixture was subjected to three freeze/pump/thaw cycles using an Ar charged Schlenk line. After stirring at 65 °C for 15 h, the resulting particles were isolated by centrifugation (12000 rpm, 25 min) and purified by three successive cycles of dispersion/precipitation using methanol/toluene as the solvent/antisolvent mixture. Acid functionalized SiNCs (3COOH and 8COOH) were dispersible in common polar solvents (e.g., methanol).

Synthesis of polyethylene glycol functionalized SiNCs (3PEG, 8PEG): Radical induced hydrosilylation was used to prepare polyethylene glycol functionalized SiNCs. Allyloxy (polyethylene oxide) methyl ether ($M_w \sim 450\text{--}455$) (1 mL) was transferred to a Schlenk flask equipped with a magnetic stir bar, degassed in vacuum (12 mTorr) at 75 °C for about 1 h, and mixed with a dispersion of H-SiNCs ($d \sim 3$ or 8 nm, obtained from 0.5 g composite) in dry toluene (10 mL) containing AIBN (50 mg). After performing three freeze/pump/thaw cycles, the mixture was stirred for 15 h at 75 °C in argon. PEG functionalized SiNCs were recovered following centrifugation (12000 rpm, 25 min) and purified by three dispersion/precipitation cycles using toluene/diethyl ether as the solvent/antisolvent system. 3PEG samples were soluble in hydrophilic (i.e., methanol) and hydrophobic (i.e., toluene) solvents. Cloudy suspensions were obtained for 8PEG samples.

Synthesis of dodecyl functionalized SiNCs (3C12, 8C12): Dodecyl functionalized SiNCs were synthesized using thermally initiated hydrosilylation.^{40,41} After etching of SiNC/SiO₂ composite (0.5 g), H-SiNCs were collected by centrifugation (3000 rpm, 10 min) and redispersed in 1-dodecene (15 mL) in a Schlenk flask equipped with a magnetic stir bar. The flask was evacuated and backfilled with argon three times prior to stirring the mixture for 15 h at 190 °C in an argon atmosphere. On completion of the reaction, the starting cloudy brown suspension of H-SiNCs (*d* ~ 3 or 8 nm) became transparent. Functionalized SiNCs were separated by centrifugation (12000 rpm, 25 min) and purified following standard procedures using toluene/methanol as the solvent/antisolvent mixture. Dodecyl functionalized SiNCs (3C12 and 8C12) were soluble in common non-polar solvents (e.g., toluene).

Preparation of polymer-coated dodecyl functionalized SiNCs (3C12/P, 8C12/P): To render dodecyl functionalized SiNCs hydrophilic, they were coated with an amphiphilic polymer. The amphiphilic polymer possessing a hydrophilic poly (maleic anhydride) backbone and hydrophobic dodecylamine side chains was synthesized following procedures reported by Parak et al.⁴² Polymer coated SiNCs were prepared by combining dodecyl functionalized SiNCs (3C12 or 8C12) (5 mg) and the amphiphilic polymer in a 1: 1 (w: w) ratio in a capped single neck flask containing anhydrous chloroform (5 mL). The solution was stirred for 30 min under ambient conditions, followed by evaporation of the solvent using a rotary evaporator to obtain a SiNC-containing polymer film. Aqueous sodium borate buffer (50 mM borate, 5 mL, pH 12) was added to the flask, and the mixture was stirred for 15 min. Next, DI water (10 mL) was added to the mixture to dilute the NCs, and the mixture was transferred to the ultracentrifugation filter (Amicon Ultra, regenerated cellulose membrane, 50 kDa molecular weight cut-off) and

centrifuged at 5000 rpm for 10 min. The dilution and centrifugation steps were repeated two more times using DI water. The resulting polymer coated dodecyl functionalized SiNCs (3C12/P and 8C12/P) were dispersible in common polar solvents (e.g., methanol).

2.2.3 Synthesis of NC-Free and SiNC-Containing Silica Aerogels

Preparation of NC-free silica aerogel: NC-free silica aerogels were prepared via base-catalyzed sol-gel processing using a minor variant of a literature procedure.^{43,44} Appropriate amounts of TMOS, methanol, and DI water with volume ratios 2.6: 5.9: 1, respectively, were mixed and sonicated for 1 min, after which a catalytic amount of ammonium hydroxide (3.4 μ L) was added to the as-prepared solution (9.5 mL). This silica sol (600 μ L) was transferred to plastic syringes (12 \times 60 mm), covered with Parafilm, and aged for 24 h. The resulting alcogel was placed in a capped glass vial, and the solvent was exchanged with anhydrous ethanol (every 4 h over a 24-hour period) to remove the ammonium hydroxide catalyst. Subsequently, the ethanol was exchanged with acetone, refreshing the acetone bath every 6 h over the period of 3 days. The acetone-exchanged gel was placed in a home-built CO₂ supercritical dryer (See Appendix A for a detailed instruction as well as photos of this equipment), and the acetone was exchanged with liquid CO₂ over a time period of at least 12 h prior to the final drying procedure. Finally, the temperature and pressure of the dryer assembly were raised to 40 °C and 8.3 MPa (above the critical point of liquid CO₂; T_c = 31 °C and P_c = 7.4 MPa), and the liquid CO₂-exchanged gel was dried for 1 h to yield a transparent silica aerogel monolith.

Preparation of SiNC-containing silica aerogels: SiNC-loaded silica aerogels were prepared by incorporating functionalized SiNCs into the silica sol, followed by CO₂ supercritical drying. Briefly, an appropriate amount of silica sol (solution containing TMOS, methanol, DI water, and

ammonium hydroxide) was added into a glass vial containing functionalized SiNCs (3COOH, 8COOH, 3PEG, 8PEG, 3C12/P, or 8C12/P) and sonicated to produce a uniform solution/dispersion of SiNCs in silica sol (5 mg/mL). The resulting solution/dispersion (600 μ L) was transferred to the cylindrical molds and treated as described for NC-free silica aerogel (vide supra). Silica aerogel containing 3PEG was transparent, while all other aerogels were opaque.

2.2.4 Photoluminescence Quenching of SiNC-Containing Silica Aerogel

The chemical accessibility of SiNCs within silica aerogel was studied by photoluminescence (PL) quenching using nitrobenzene. Briefly, an appropriate amount of nitrobenzene (300 μ L) was added stepwise to a watch glass containing luminescent 3PEG-loaded silica aerogel. PL of areas of 3PEG-containing silica aerogel exposed to nitrobenzene was quenched immediately, while unexposed areas remained luminescent.

2.2.5 Material Characterization

Fourier Transform Infrared (FTIR) spectra of functionalized SiNCs were acquired using a Nicolet Magna 750 IR spectrometer. X-ray photoelectron spectroscopy (XPS) analyses were performed using a Kratos Axis Ultra instrument operating in energy spectrum mode at 210 W. Samples were prepared by depositing a solution of functionalized SiNCs onto a copper foil substrate and drying in air to yield thin films. The base and operating chamber pressure were maintained at 10^{-7} Pa. A monochromatic Al K α source ($\lambda = 8.34$ Å) was used to irradiate the samples, and the spectra were obtained with an electron take-off angle of 90°. To minimize sample charging, the charge neutralizer filament was used when required. Survey spectra were collected using an elliptical spot with major and minor axis lengths of 2 and 1 mm, respectively, and 160 eV pass energy with a step of 0.33 eV. CasaXPS software (VAMAS) was used to interpret high-resolution spectra. All spectra were internally calibrated to the C 1s emission

(284.8 eV). After calibration, a Shirley-type background was applied to remove most of the extrinsic loss of structure. The high-resolution Si 2p region was fitted to Si 2p_{3/2} and Si 2p_{1/2} components, with spin-orbit splitting fixed at 0.6 eV, and the Si 2p_{3/2} / Si 2p_{1/2} intensity ratio set to 2/1.

Transmission electron microscopy (TEM) images were acquired using a JOEL 2010 TEM with LaB₆ filament at an accelerating voltage of 200 kV. TEM samples of SiNCs were prepared by depositing a droplet of dilute solutions of functionalized SiNCs onto a holey carbon coated copper grid. The NC size was averaged for 200 particles using Image J software (version 1.45). To prepare aerogel samples for TEM analysis, aerogel monoliths were broken into small pieces and dehydrated with anhydrous acetone for 1 h. Aerogel pieces were sequentially impregnated with commercial Spurr's mixture in anhydrous acetone with concentrations 25% (24 h), 50% (24 h), 75% (24 h), and 100% (48 h). 100% Spurr's mixture containing aerogel pieces was polymerized at 65 °C for 24 h, sliced into 70 nm thin films using a Leica EM UC6 ultramicrotome, and mounted on a holey carbon coated copper grid. High-resolution (HR) TEM images were obtained from a Hitachi-9500 electron microscope with an accelerating voltage of 300 kV. The HRTEM images were processed using Gatan Digital Micrograph software (Version 2.02.800.0). Dynamic light scattering (DLS) was performed using a Malvern Zetasizer Nano S series equipped with a 633 nm laser. Diluted solutions of dodecyl and PEG functionalized SiNCs were filtered using 0.45 μm PTFE syringe filters, then all diluted samples were equilibrated to 25 °C prior to data acquisition and scanned three times.

Photoluminescence (PL) spectra were recorded by exciting SiNC solutions/dispersions or SiNC-containing aerogel monoliths with a 405 nm LED light source equipped with a 500 nm

long pass interference filter. The emitted photons were collected using an optic fiber connected to an Ocean Optics USB2000 spectrometer that was normalized by a black body radiator. Hydrophilic solutions/dispersions of 3COOH, 8COOH, 3PEG, and 8PEG in methanol, as well as hydrophobic solutions of 3C12 and 8C12 in toluene, were used for PL measurements.

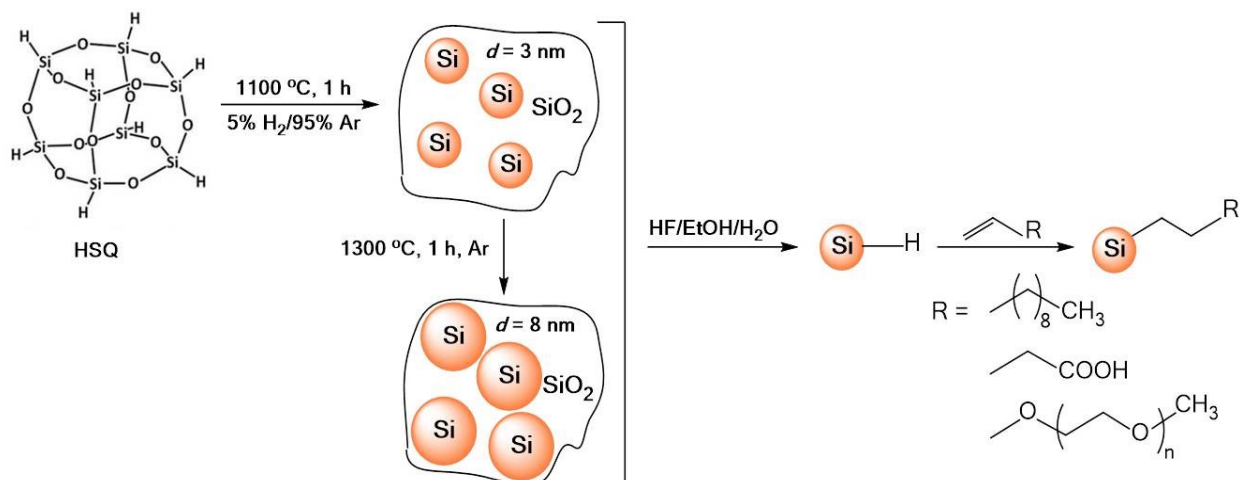
Nitrogen adsorption-desorption isotherms were measured at 77 K using a Quantachrome ASiQwin surface area and porosimetry analyzer available at the University of Alberta NanoFab facility. Fine aerogel powders were degassed under vacuum at 150 °C for 24 h prior to the analysis. The isotherm data were fitted using Brunauer–Emmett–Teller (BET) theory to determine the specific surface area. The average pore sizes and total pore volumes were calculated by applying the Barrett–Joyner–Halenda (BJH) model to desorption branches of the isotherms. Bulk densities of aerogels were determined by measuring the weight and volume of aerogel monoliths. The weight of aerogels was measured with a Sartorius analytical balance, and aerogel dimensions were measured with a digital caliper.

2.3 Results and Discussion

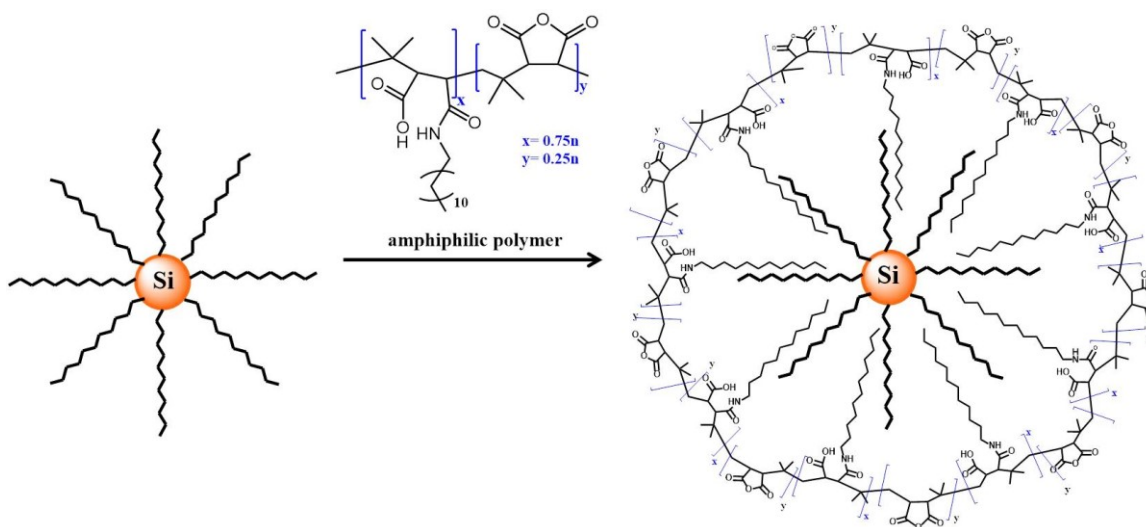
Oxide-embedded and hydride-terminated SiNCs ($d \sim 3$ and 8 nm) (H-SiNCs) were synthesized following well-established procedures developed in the Veinot laboratory.^{39,40} Briefly, a SiNC/SiO₂ composite obtained from thermal processing of hydrogen silsesquioxane (HSQ) was etched using hydrofluoric acid solution to remove the oxide and liberate SiNCs. Hydride-terminated SiNCs are susceptible to oxidation, and their surfaces must be passivated to prevent undesirable reactions and afford stable properties. To date, the most common approach to modify H-SiNC surfaces involves introducing long chain alkyl/alkenyl groups via various hydrosilylation strategies; this process renders the SiNCs hydrophobic and compatible with

common organic solvents.^{40,45} Silicon alkoxide precursors, such as tetramethyl orthosilicate (TMOS) used in silica aerogel synthesis, are soluble in polar solvents.^{43,44} If transparent SiNC-containing silica aerogels appropriate for optical applications are to be realized, hydrophilic SiNCs compatible with the aerogel synthetic method are needed.

In the present study, a series of methods were used to render SiNCs hydrophilic, and the resulting NCs were used in the preparation of SiNC-SiO₂ aerogel hybrids. General approaches to prepare hydrophilic SiNCs used here include direct surface functionalization of H-SiNCs with polar hydrophilic groups (i.e., 4-pentenoic acid and allyloxy (polyethylene oxide) methyl ether) or post-functionalization modification of hydrophobic SiNCs (i.e., dodecyl functionalized SiNCs) with an amphiphilic polymer. The 3 and 8 nm diameter pentanoic acid (i.e., 3COOH, 8COOH) and polyethylene glycol (i.e., 3PEG, 8PEG) functionalized SiNCs were synthesized via a radical induced hydrosilylation (Scheme 2-1).²⁸ Dodecyl terminated SiNCs with diameters of 3 and 8 nm (i.e., 3C12, 8C12) were prepared using thermally initiated hydrosilylation (Scheme 2-1).⁴⁰ To render dodecyl functionalized SiNCs hydrophilic, these NCs were coated with an amphiphilic polymer bearing a hydrophilic poly(maleic anhydride) backbone grafted with hydrophobic dodecylamine side chains (Scheme 2-2).^{41,42} A solution of 3PEG in methanol (5 mg/ml) was transparent, and cloudy suspensions were obtained for 8PEG and other modified SiNCs.



Scheme 2-1. Synthesis of dodecyl, pentanoic acid, and polyethylene glycol functionalized SiNCs with diameters 3 and 8 nm.



Scheme 2-2. Coating of dodecyl functionalized SiNCs with the amphiphilic polymer.

NC surface chemistry and size are the key to the properties of the present aerogels. Fourier Transform Infrared spectroscopy provides insight into the nature of SiNC surface functionalization. Representative FTIR spectra of the functionalized SiNCs investigated here

show expected features corresponding to the target functional groups (Figure 2-1). The H-SiNCs exhibit an absorption at $\sim 2100\text{ cm}^{-1}$ in FTIR that is routinely attributed to Si-H_x (x = 1–3) stretching.^{39,40} Following hydrosilylation with 1-dodecene, the Si-H absorption is replaced by intense absorptions at 2850–3000 and 1365–1475 cm^{-1} attributed to C-H stretching and bending, respectively (Figure 2-1, 3C12 and 8C12).^{40,45} Representative FTIR spectra of pentanoic acid functionalized SiNCs possess a sharp absorption at 1700–1725 cm^{-1} related to C=O stretching, as well as a broad feature associated with O-H stretching centered at $\sim 3300\text{ cm}^{-1}$ (Figure 2-1, 3COOH and 8COOH).²⁸ Symmetric and asymmetric stretching of C-O-C moieties are evident in the spectra of PEG functionalized SiNCs at 1100 and 1300 cm^{-1} , respectively (Figure 2-1, 3PEG and 8PEG). Features associated with -CH₂- also appear at 2869 and 2960 cm^{-1} . The FTIR spectra of polymer coated dodecyl functionalized SiNPs show spectral features corresponding to C-H stretching (2850–3000 cm^{-1}), C-H bending (1365–1475 cm^{-1}), N-H stretching (centered at $\sim 3300\text{ cm}^{-1}$), N-H bending (centered at $\sim 1575\text{ cm}^{-1}$), and C=O stretching (centered at $\sim 1705\text{ cm}^{-1}$) (Figure 2-2, 3C12/P and 8C12/P). Broad silicon oxide related features are at $\sim 1000\text{--}1130\text{ cm}^{-1}$, as well as weak absorptions at $\sim 2100\text{ cm}^{-1}$ (residual Si-H_x) are noted in the spectra of all functionalized SiNCs.

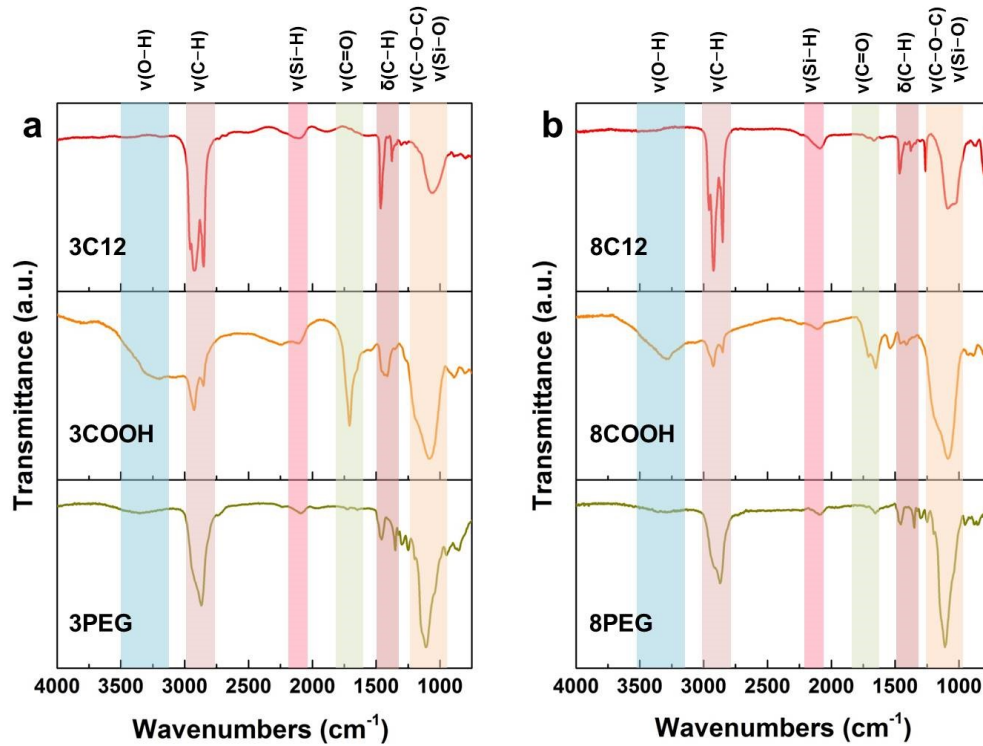


Figure 2-1. The FTIR spectra of SiNCs with diameters a) 3 nm and b) 8 nm functionalized with indicated surface groups (C12: dodecyl, COOH: pentanoic acid, and PEG: polyethylene glycol).

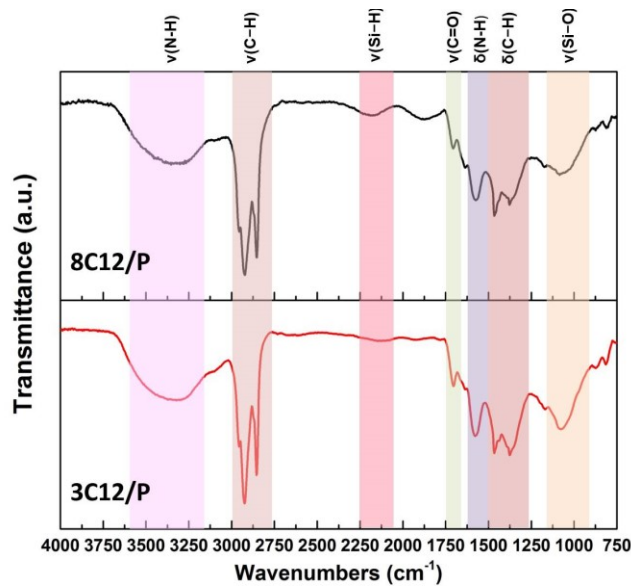


Figure 2-2. The FTIR spectra of polymer-coated dodecyl functionalized SiNCs with diameters 3 and 8 nm.

Survey X-ray photoelectron spectroscopy (XPS) confirms that the functionalized SiNCs contain Si, C, and trace quantities of O at the sensitivity of the techniques. High-resolution XP spectra of the Si 2p region show an intense emission at 99.34 eV characteristic of the Si core (i.e., Si(0)) (Figure 2-3). Higher binding energy features in this region are attributed to Si suboxides and surface functionalized Si atoms. We note that the features associated with silicon suboxides are more intense for SiNCs bearing hydrophilic surface groups, such as pentanoic acid and polyethylene glycol; this is attributed to a higher degree of surface oxidation resulting from the greater accessibility of water to the surface that is facilitated by the surface functionalities. This is also evident in FTIR spectra of the functionalized SiNCs (vide supra).

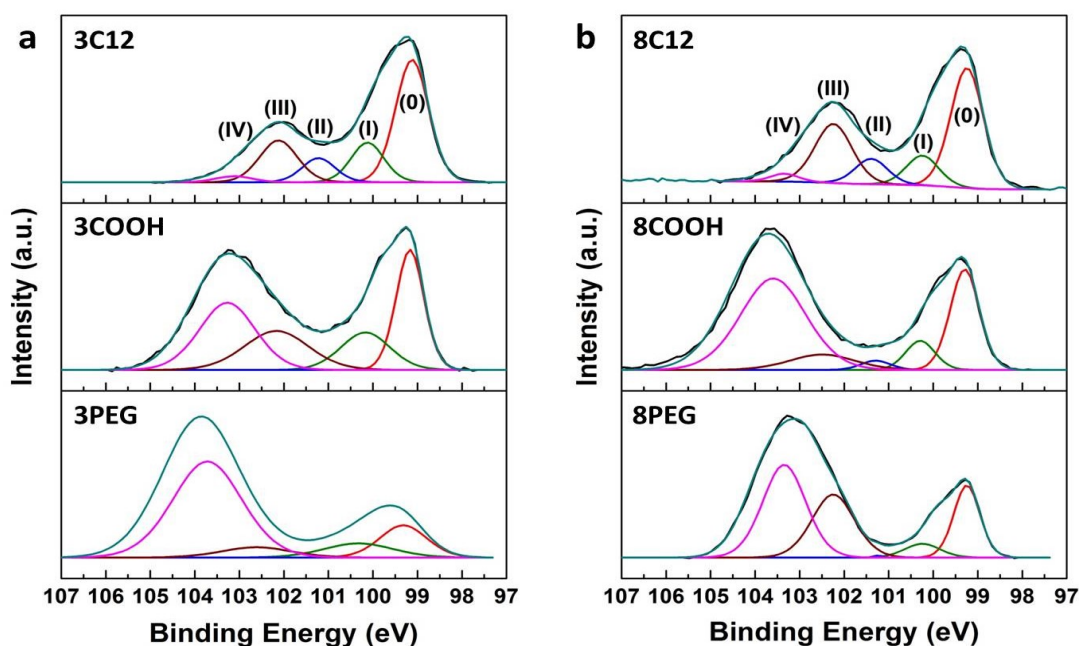


Figure 2-3. High-resolution XP spectra of the Si 2p region of SiNCs with diameters a) 3 nm and b) 8 nm functionalized with indicated surface groups (C12: dodecyl, COOH: pentanoic acid, and PEG: polyethylene glycol). Please note, only Si 2p_{3/2} components are shown; Si 2p_{1/2} components are omitted for clarity.

Representative transmission electron microscopy (TEM) and High-resolution (HR) TEM images of functionalized SiNCs are presented in Figure 2-4 and illustrate how surface chemistry dramatically influences NC assembly; their size distributions are indicated in Figure 2-5. Hydrophobic C12 functionalized SiNCs ($d = 3.2 \pm 0.4$ nm and $d = 8.1 \pm 0.9$ nm) as well as PEG functionalized SiNCs ($d = 3.2 \pm 0.4$ nm and $d = 7.5 \pm 1.0$ nm) are separated well, consistent with their ready dispersibility in their host solvents. In contrast, COOH functionalized SiNCs ($d = 3.2 \pm 0.3$ nm and $d = 7.5 \pm 0.7$ nm) appear as large assemblies, suggesting that particles interact strongly, leading to assemblies in various media. As expected, HRTEM images of SiNCs investigated here show lattice fringes spaced by 0.32 nm characteristic of a Si (111) lattice plane (Figure 2-4, insets).⁴⁶

Dynamic light scattering (DLS) measurements indicate that all functionalized SiNCs investigated here exhibit solvated dimensions exceeding those measured using transmission electron microscopy (Figure 2-6). Dodecyl functionalized SiNCs (3C12 and 8C12) show solvated diameters of 6.4 and 10.1 nm, respectively, in toluene. Similarly, polyethylene glycol functionalized SiNCs (3PEG and 8PEG) possess hydrodynamic diameters of 6.9 and 15.7 nm, respectively, in toluene, while pentanoic acid functionalized SiNCs (3COOH and 8COOH) have hydrodynamic diameters of 296.5 and 335.5 nm, respectively, in methanol, consistent with the large assemblies of particles observed in TEM images of these NCs (vide supra). Figure 2-6 also shows that introducing an amphiphilic polymer coating onto dodecyl functionalized SiNCs leads to a notable increase in hydrodynamic diameters (i.e., 235.2 and 332.8 nm for 3C12/P and 8C12/P, respectively).

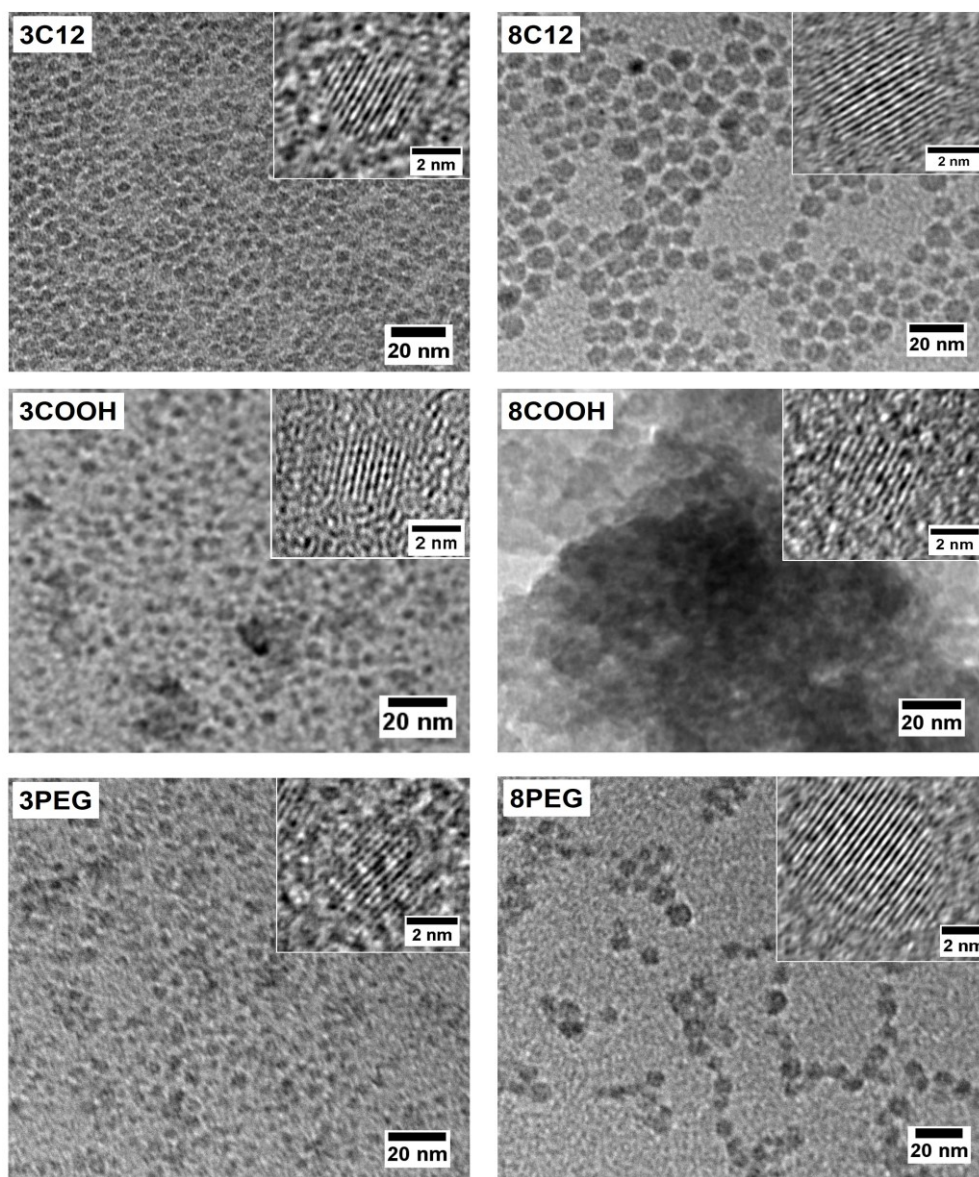


Figure 2-4. Representative bright-field TEM images of SiNCs functionalized with indicated surface groups (C12: dodecyl, COOH: pentanoic acid, and PEG: polyethylene glycol) and diameters, **3C12**: ($d = 3.2 \pm 0.4$ nm), **8C12**: ($d = 8.1 \pm 0.9$ nm), **3COOH**: ($d = 3.2 \pm 0.3$ nm), **8COOH**: ($d = 7.5 \pm 0.7$ nm), **3PEG**: ($d = 3.2 \pm 0.4$ nm), and **8PEG**: ($d = 7.5 \pm 1.0$ nm). The corresponding HRTEM images showing characteristic Si (111) lattice spacing are presented as insets.

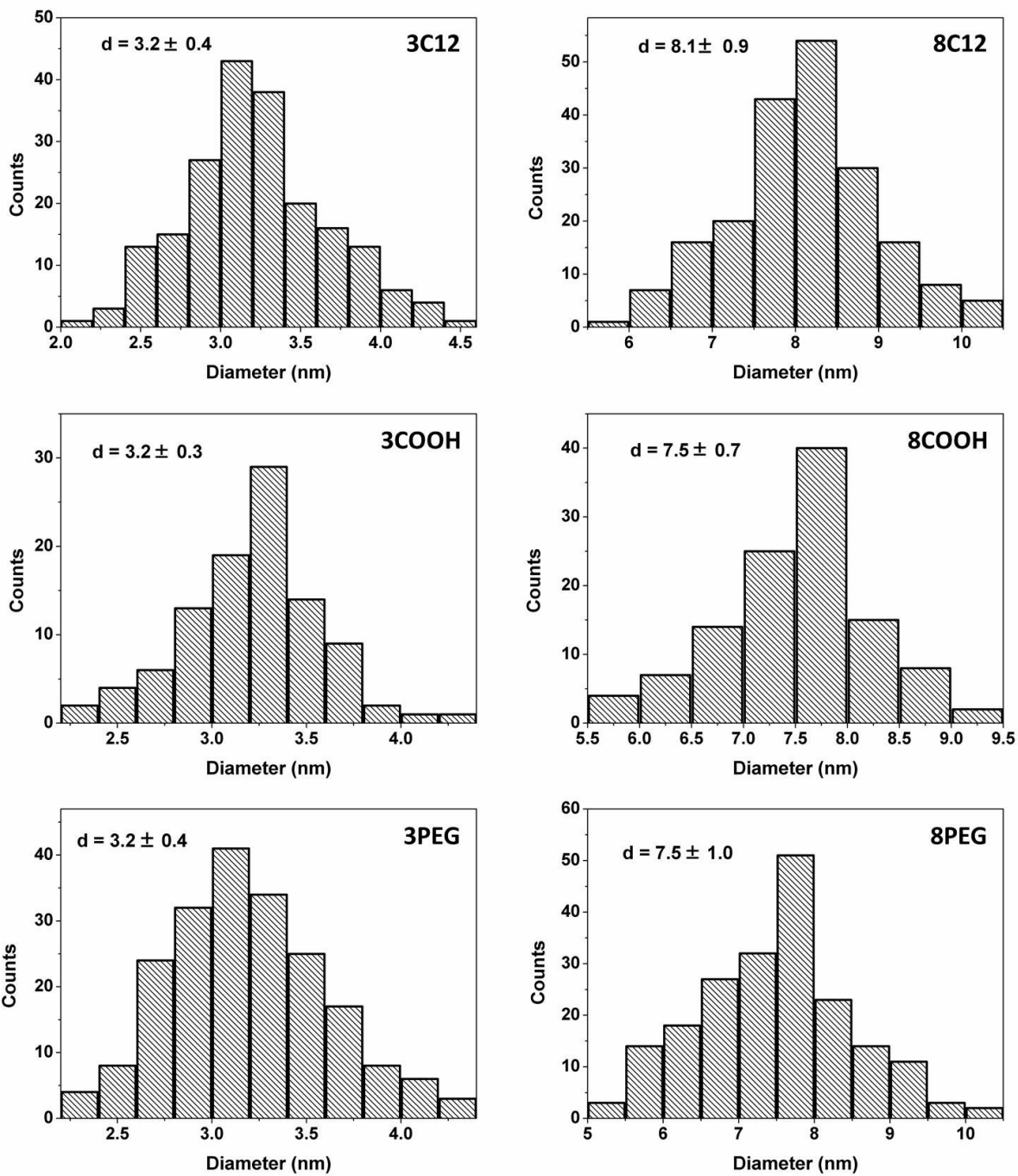


Figure 2-5. Size distributions of 3 and 8 nm SiNCs functionalized with indicated surface groups (C12: dodecyl, COOH: pentanoic acid, and PEG: polyethylene glycol).

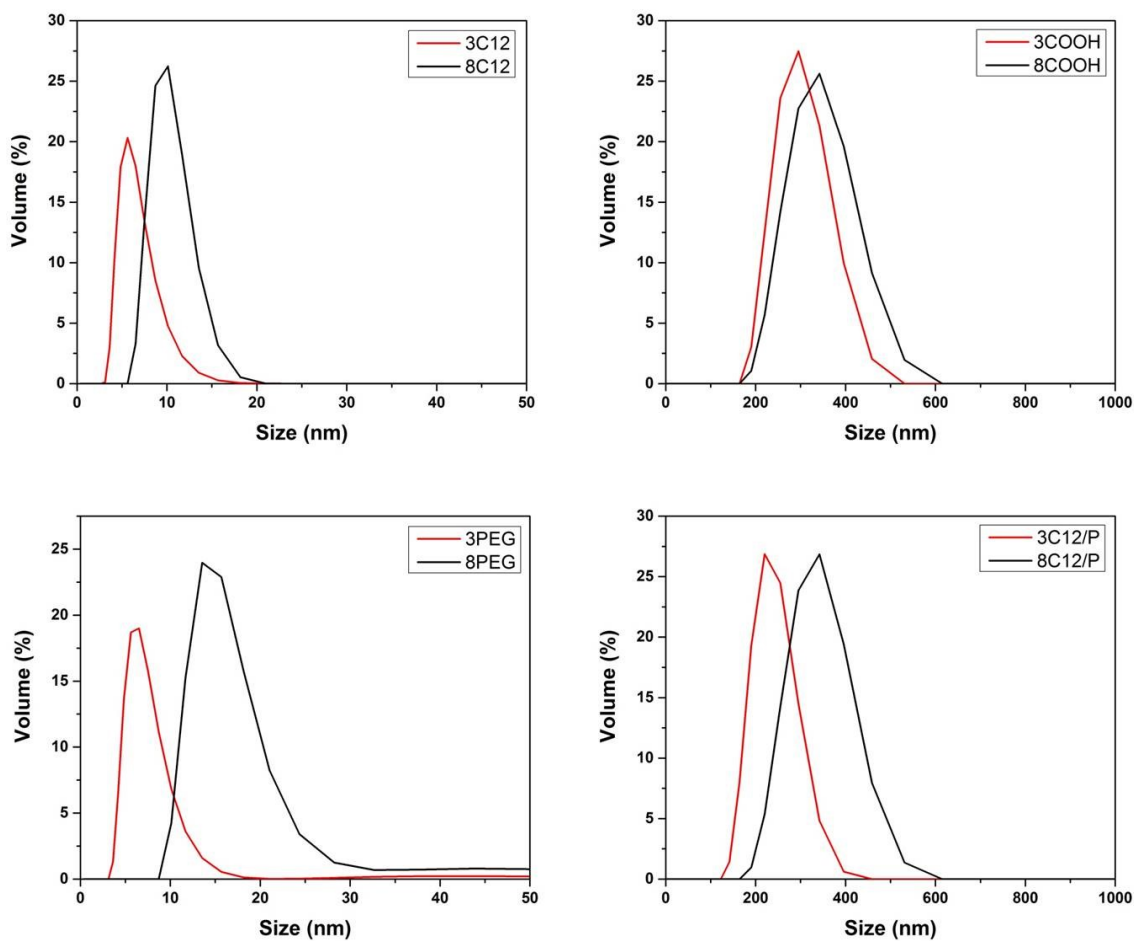


Figure 2-6. Solvated diameters of 3 and 8 nm SiNCs functionalized with indicated surface groups (C12: dodecyl, C12/P: polymer-coated dodecyl, COOH: pentanoic acid, and PEG: polyethylene glycol).

SiNCs bearing various surface modifications (i.e., polymer coated alkyl (C12/P), polyethylene glycol (PEG), and carboxylic acid (COOH)) were introduced to a TMOS containing basic solution. Following base-catalyzed cross-linking, alcogels were obtained that were dried subsequently using a CO₂ supercritical dryer to yield aerogel monoliths. Visual inspection of NC-containing systems reveals that surface chemistry and size appear to impact the optical transparency of aerogel monoliths, dramatically; these observations presumably relate to the uniformity of the dispersion of SiNCs throughout the aerogels (Figures 2-7a and 2-7b). The 3PEG-containing structure was similar to the NC-free aerogel, with the only obvious difference of being slightly yellow. Reflecting the limited solubility of other functionalized NCs in the sol-gel reaction media, opaque aerogels were obtained for 3 nm diameter SiNCs bearing other surface modifications (i.e., 3COOH, 3C12/P) and all larger SiNCs investigated (i.e., 8PEG, 8COOH, 8C12/P). Figures 2-7c and 2-7d qualitatively illustrate the photoluminescent response of the SiNC-silica alcogel and aerogel pairs upon exposure to UV light (i.e., 350 nm). In all cases, SiNC optical properties were preserved, indicating that the base catalyst required to promote the sol-gel reaction did not compromise the NC integrity. It is reasonable to attribute the blue appearance of the NC-free silica aerogel under UV lamp to Rayleigh scattering (Figure 2-7d).¹⁶

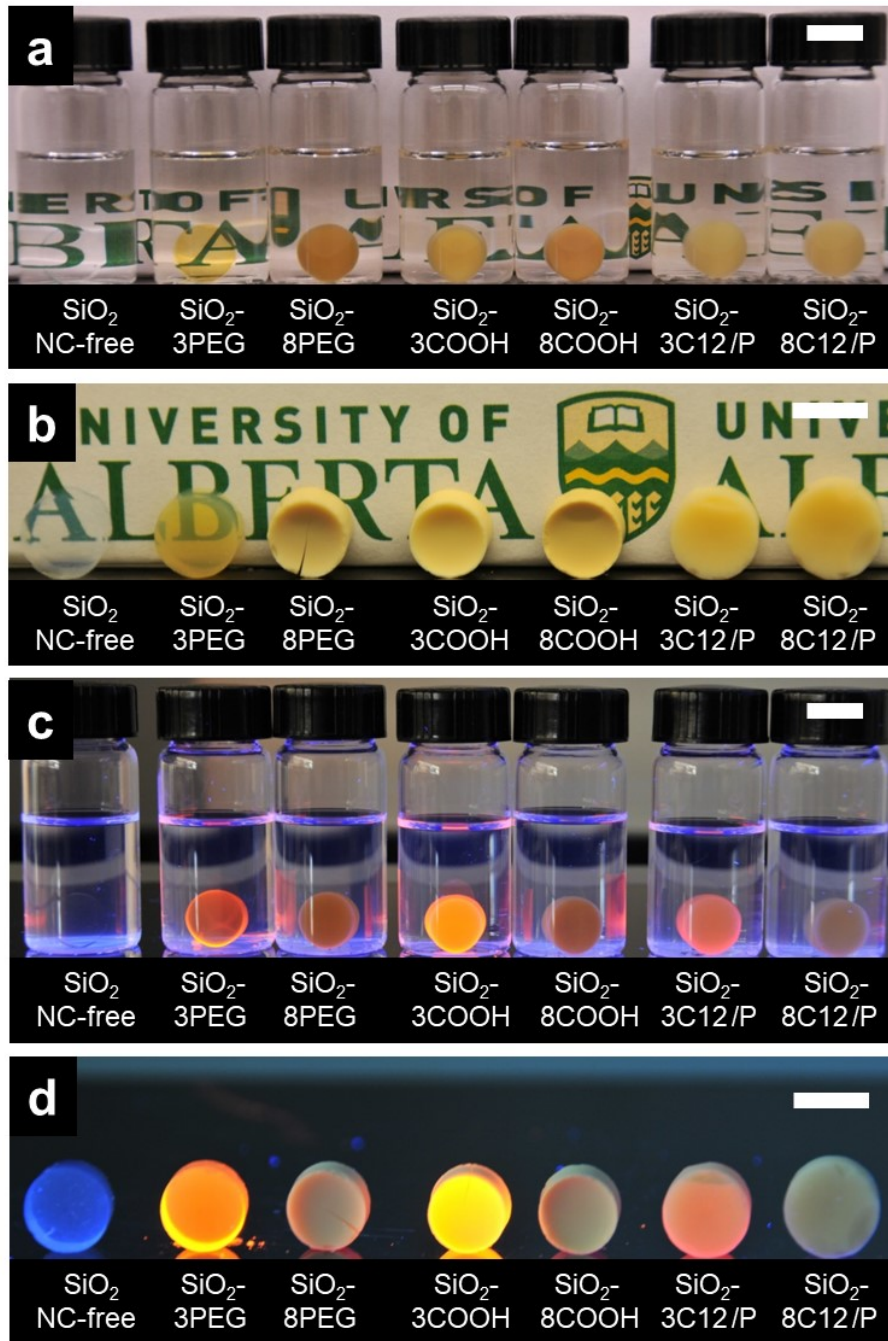


Figure 2-7. Photographs of NC-free and SiNC-containing silica alcogels/aerogels with indicated sizes ($d \sim 3$ or 8 nm) and surface groups (PEG: polyethylene glycol, COOH: pentanoic acid, and C12/P: polymer-coated dodecyl) under (a, b) ambient and (c, d) UV light. The scale bar is 1 cm.

Figure 2-8 shows the PL spectra of functionalized SiNCs investigated here and their corresponding SiNC-SiO₂ aerogel hybrids upon excitation at 405 nm; 3C12 exhibit PL centered at 749 nm, while 3COOH and 3PEG show emissions centered at 683 and 665 nm, respectively. Similar blue-shifts in PL maxima have been attributed previously to the influences of surface oxidation (e.g., reduced particle size and/or surface emitting species) noted in the present FTIR and XP spectra of 3COOH and 3PEG (vide supra).^{40,47} Similarly, the PL arising from 8COOH and 8PEG were blue-shifted compared to that of 8C12. In all cases, the optical response of the SiNCs remained intact following their incorporation into aerogels; however, a small blue-shift (ca. 70 nm) is noted for 8PEG functionalized SiNCs; the origin of this spectral shift is complex and might be due to the aggregation of the functionalized SiNCs.

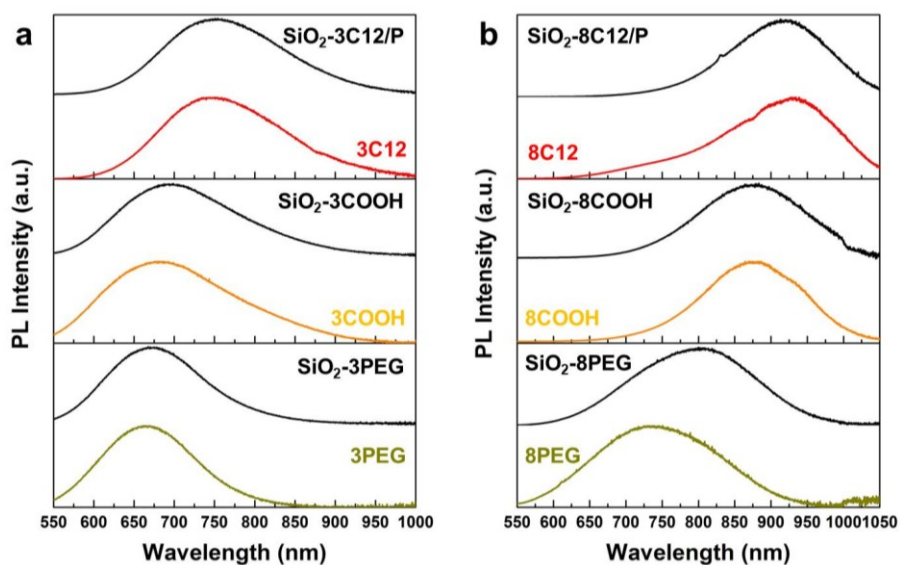


Figure 2-8. The PL spectra of solutions/dispersions containing SiNCs with diameters a) 3 nm and b) 8 nm functionalized with indicated surface groups (C12/P: polymer-coated dodecyl, COOH: pentanoic acid, and PEG: polyethylene glycol), and their corresponding SiO₂ aerogel monoliths upon excitation at 405 nm.

Representative TEM images of NC-free and SiNC-containing silica aerogels are presented in Figures 2-9 and 2-10, respectively. It is difficult to observe the distribution of SiNCs throughout the silica aerogel network using bright-field transmission electron microscopy. However, the HRTEM image of aerogel containing PEG functionalized SiNCs ($d \sim 8$ nm) indicates lattice fringes spaced by 0.32 nm, characteristic of Si (111) lattice plane, and verifies that the incorporation does not compromise the NC integrity.⁴⁶

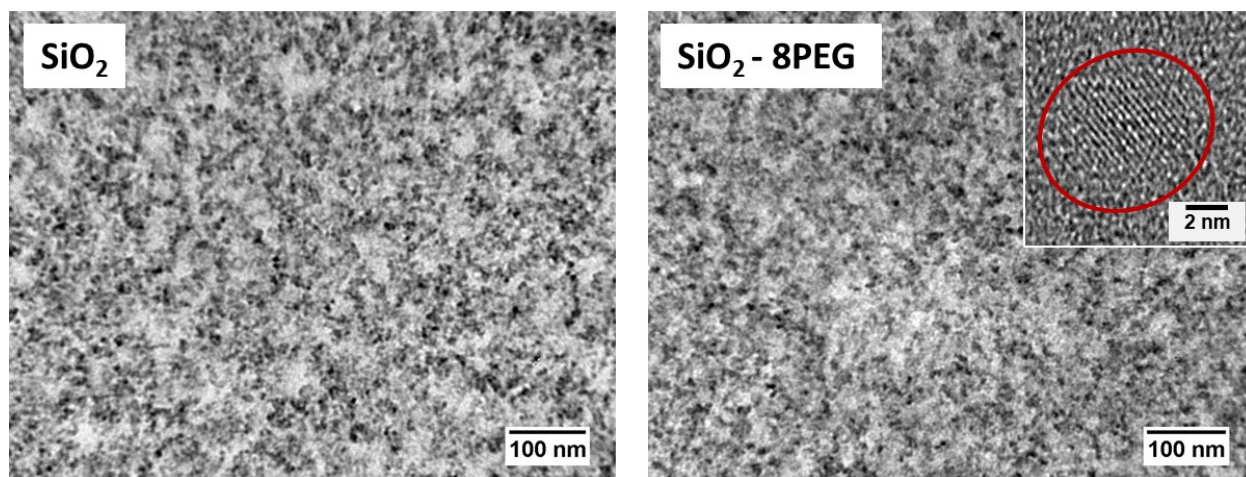


Figure 2-9. Representative bright-field TEM images of NC-free and 8PEG-loaded silica aerogels. The corresponding HRTEM image showing characteristic Si (111) lattice spacing is presented as an inset.

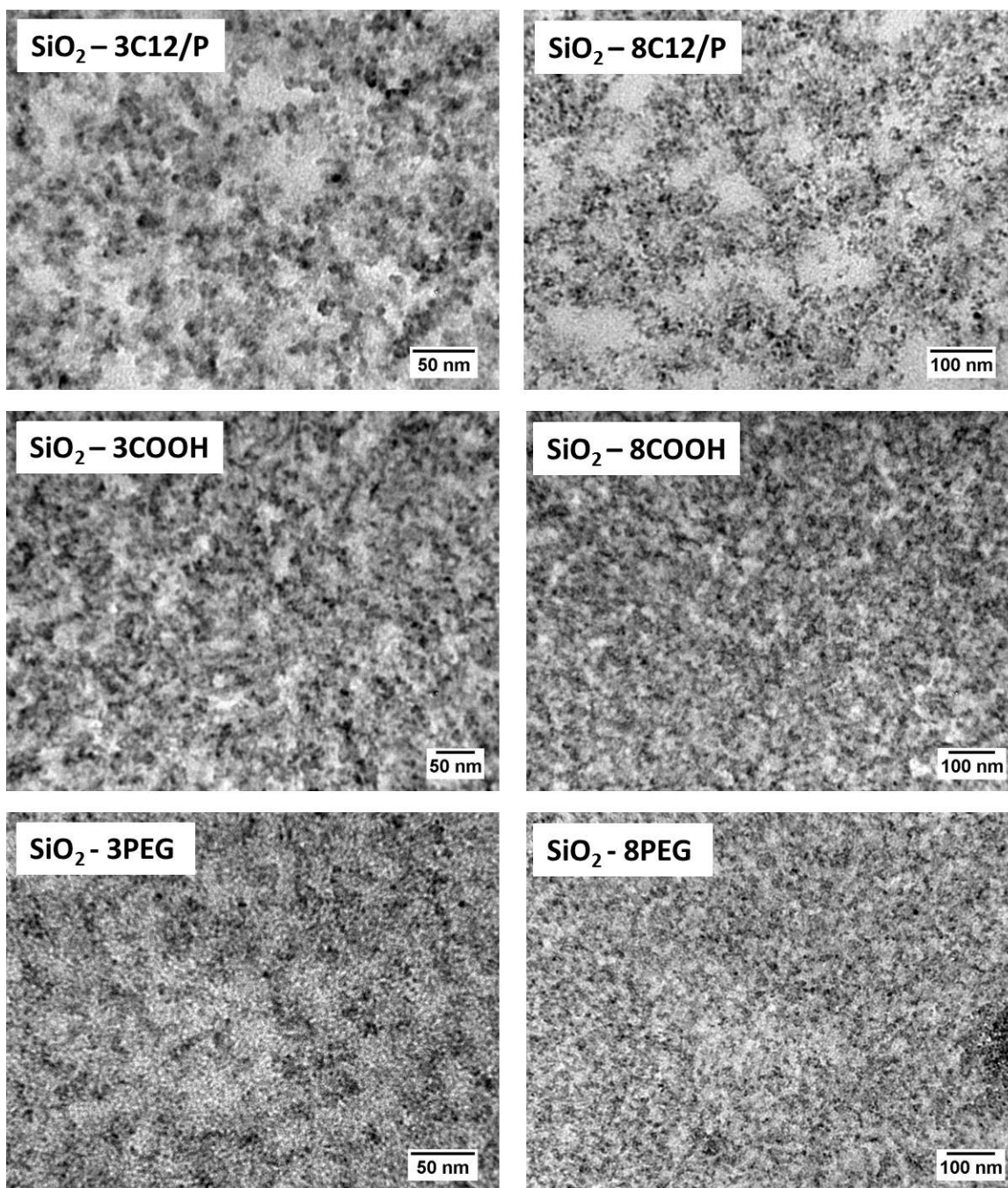


Figure 2-10. Representative bright-field TEM images of silica aerogels containing 3 and 8 nm SiNCs functionalized with indicated surface groups (C12/P: polymer-coated dodecyl, COOH: pentanoic acid, and PEG: polyethylene glycol).

Nitrogen adsorption–desorption isotherms of aerogels with and without SiNCs are shown in Figures 2-11 and 2-12, respectively. Each exhibited a Type-IV isotherm with distinct capillary condensation and evaporation steps characteristic of mesoporous materials ($d = 2\text{--}50\text{ nm}$).⁴⁸ The absence of a plateau at high relative pressures in the isotherm of NC-free silica aerogels (Figure 2-11) suggests some degree of macroporosity ($d > 50\text{ nm}$).⁴⁸ Similarly, the isotherms of C12/P containing aerogels indicate the presence of some larger pores, while distinct plateaus at high relative pressures in the isotherms of COOH and PEG containing aerogels suggest a decrease in the degree of macroporosity (Figure 2-12). The shapes of the hysteresis loops noted for all aerogel systems indicate a Type-H1 profile, characterized by parallel and nearly vertical branches, suggesting the presence of cylindrical pores with narrow pore size distribution.⁴⁸

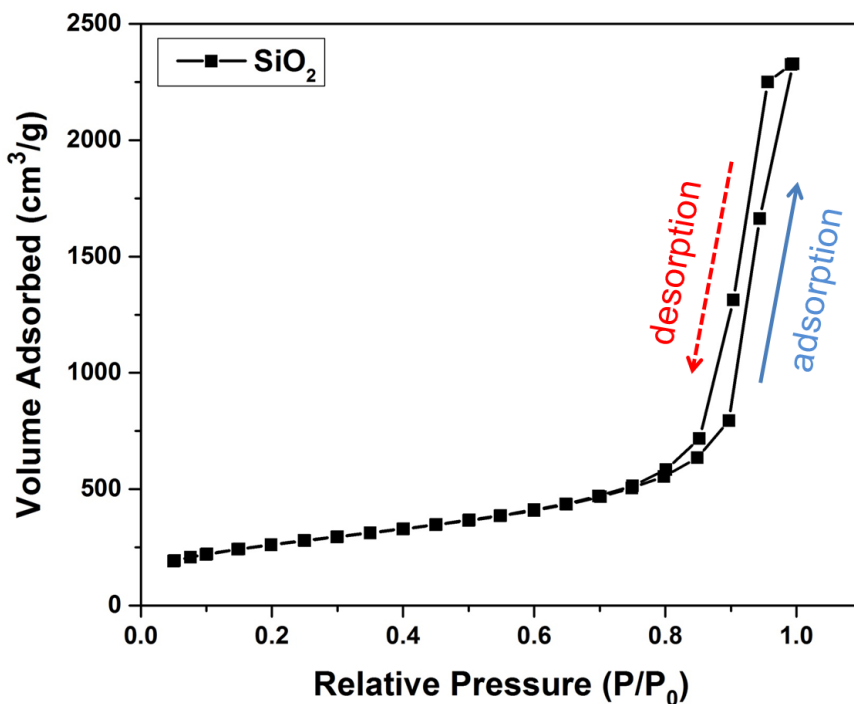


Figure 2-11. Nitrogen adsorption–desorption isotherm of NC-free silica aerogel.

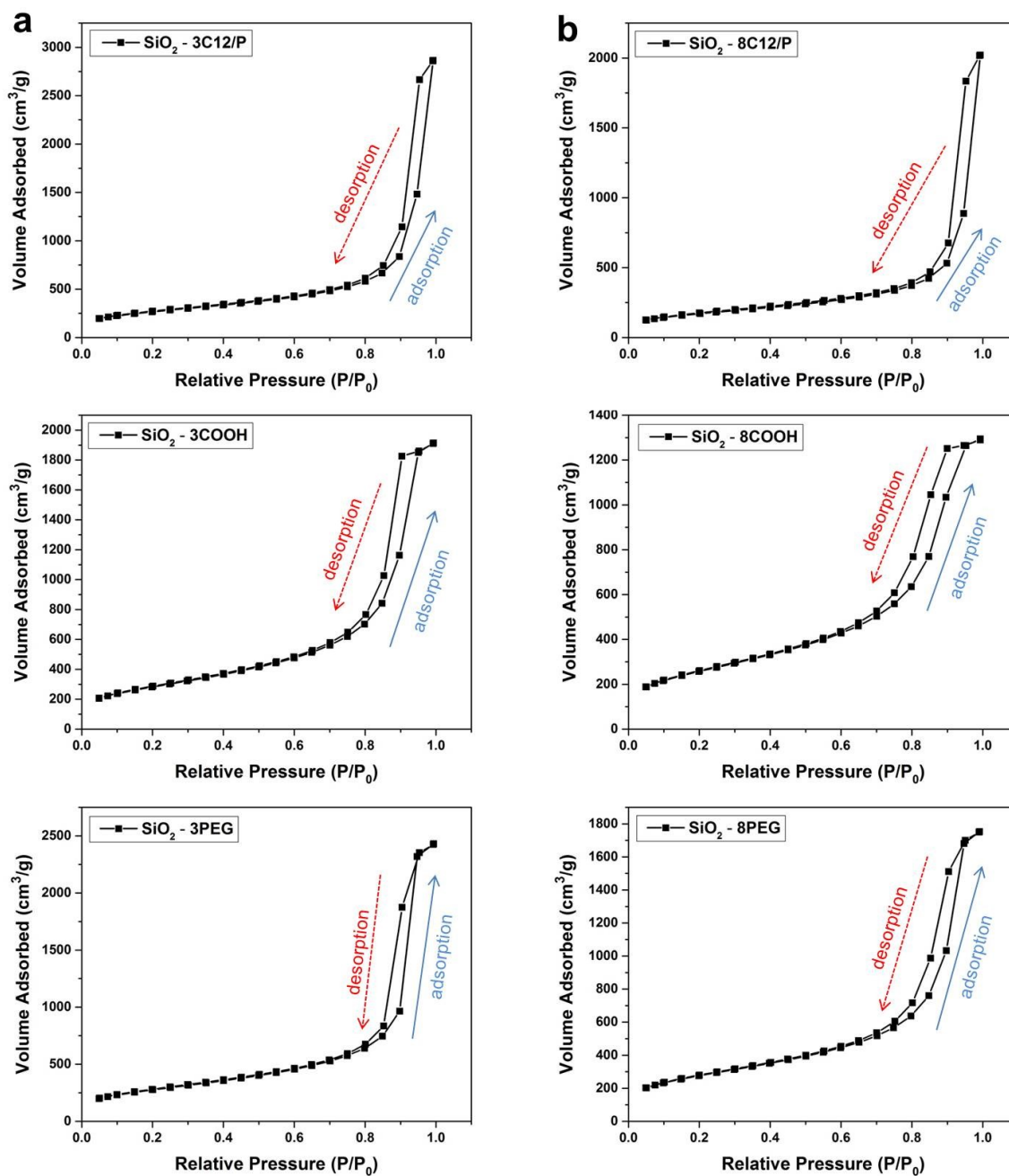


Figure 2-12. Nitrogen adsorption–desorption isotherms of silica aerogels containing SiNCs with diameters a) 3 nm and b) 8 nm functionalized with indicated surface groups (C12/P: polymer-coated dodecyl, COOH: pentanoic acid, and PEG: polyethylene glycol).

The specific surface area (SSA) of the present aerogels was calculated using the Brunauer–Emmett–Teller (BET) model (Table 2-1).⁴⁸ The BET specific surface area obtained for NC-free silica aerogels is 947 ± 25 m²/g, consistent with those reported for aerogels prepared using similar procedures.^{43,44} The incorporation of SiNCs into aerogels does not show a significant effect on SSA values of COOH and PEG containing aerogels, but lower SSA values are obtained for aerogels containing C12/Ps, consistent with increased macroporosity observed in the isotherms of these aerogels. A lower SSA value for 8C12/P loaded aerogel compared to that of aerogel containing 3C12/P is noted; this reveals that both surface chemistry and particle size play roles in the incorporation of C12/Ps in aerogels.

The total pore volume and average pore sizes of the present aerogels were determined using the desorption branches of the nitrogen adsorption–desorption isotherms by applying the Barrett–Joyner–Halenda (BJH) model.⁴⁸ The effects of SiNC size and surface chemistry on total pore volume and average pore sizes of the aerogels are summarized in Table 2-1. The total pore volume and average pore radius of 3.50 ± 0.05 and 8.9 ± 0.1 , respectively, were obtained for NC-free silica aerogels. The incorporation of SiNCs into the aerogels shows minimal effect on the average pore sizes of COOH and PEG loaded aerogels, although a slight reduction in total pore volume of these hybrid aerogels is observed. Surprisingly, C12/P containing aerogels show significantly larger average pore sizes, consistent with the more open structures observed in the TEM images of these systems (Figure 2-10). The 3C12/P loaded aerogels also show higher total pore volume compared to that of their 8 nm counterparts. Although the influence of surface chemistry and size on the average pore size and total pore volume of aerogels is complex, it is apparent that the bulky amphiphilic polymer plays a role. The bulk density of aerogels is

presented in Table 2-1; as expected, C12/P loaded aerogels possess lower bulk densities compared to NC-free aerogels.

Table 2-1. The BET specific surface area (SSA), total pore volume (PV), average pore size (PS), and bulk density (ρ) of NC-free and SiNC-containing silica aerogels with indicated sizes ($d \sim 3$ or 8 nm) and surface groups (C12/P: polymer-coated dodecyl, COOH: pentanoic acid, and PEG: polyethylene glycol).

Sample	SiO ₂	SiO ₂ - 3C12/P	SiO ₂ - 8C12/P	SiO ₂ - 3COOH	SiO ₂ - 8COOH	SiO ₂ - 3PEG	SiO ₂ - 8PEG
SSA ^a (m ² /g)	947±25	909±40	644±40	1025±30	1026±20	1014±25	1001±40
PV ^a (cm ³ /g)	3.50±0.05	4.14±0.16	3.09±0.05	2.77±0.08	2.97±0.07	3.41±0.25	3.18±0.11
PS ^a (nm)	8.9±0.1	16.1±0.1	15.9±0.1	8.9±0.1	8.9±0.1	8.9±0.1	8.9±0.1
ρ (g/cm ³)	0.176	0.147	0.142	0.209	0.220	0.210	0.214

^aThe SSA, PV, and PS values are presented as the average of high low values on two samples.

Many future applications of the present SiNC-SiO₂ aerogel hybrids (e.g., sensors, light emitting diodes, etc.) would benefit from the SiNCs being chemically accessible. Exposure to nitroaromatics is known to quench the PL of SiNCs via an electron transfer mechanism.²⁴ Figure 2-13 qualitatively shows the immediate quenching of the PL arising from 3PEG incorporated into silica aerogel upon exposure to nitrobenzene, confirming that the SiNCs are chemically accessible.

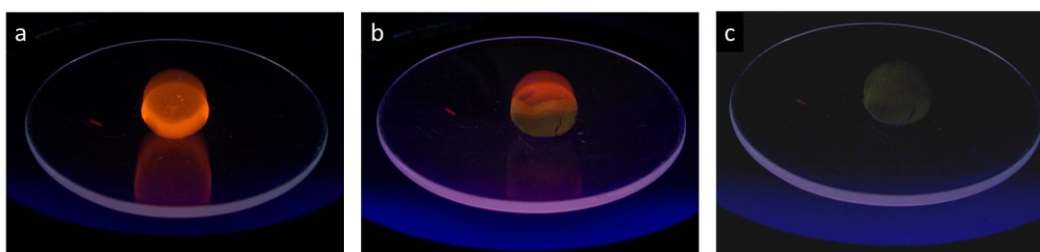


Figure 2-13. 3PEG-loaded silica aerogel a) before, b) partial, and c) complete exposure to nitrobenzene.

2.4 Conclusions

Hybrid materials consisting of hydrophilic SiNCs ($d \sim 3$ or 8 nm) and silica aerogels have been prepared by exploiting base-catalyzed sol-gel processing. The resulting hybrids retain the photoluminescent response of the entrained SiNCs, while the optical transparency of the parent aerogel is only retained when 3 nm SiNCs bearing polyethylene glycol surface group are employed. Nitrogen adsorption-desorption analysis indicates that the physical properties of the hybrid aerogels depend on the SiNC dimensions and surface chemistry. The quenching of the PL of the SiNC-loaded aerogel by molecular species confirms the chemical accessibility of the SiNCs within these high surface area optical materials and opens the door to unique advanced applications.

2.5 References

1. Hüsing, N.; Schubert, U. Aerogels—Airy Materials: Chemistry, Structure, and Properties. *Angew. Chem. Int. Ed.* **1998**, *37*, 22–45.
2. Pierre, A. C.; Pajonk, G. M. Chemistry of Aerogels and Their Applications. *Chem. Rev.* **2002**, *102*, 4243–4265.
3. Hrubesh, L. W. Aerogel Applications. *J. Non. Cryst. Solids* **1998**, *225*, 335–342.
4. Schmidt, M.; Schwertfeger, F. Applications for Silica Aerogel Products. *J. Non. Cryst. Solids* **1998**, *225*, 364–368.
5. Melde, B. J.; Johnson, B. J.; Charles, P. T. Mesoporous Silicate Materials in Sensing. *Sensors* **2008**, *8*, 5202–5228.
6. Pajonk, G. M. Aerogel Catalysts. *Appl. Catal.* **1991**, *72*, 217–266.
7. Pajonk, G. M. Catalytic Aerogels. *Catal. Today* **1997**, *35*, 319–337.
8. Rolison, D. R. Catalytic Nanoarchitectures: the Importance of Nothing and the Unimportance of Periodicity. *Science* **2003**, *299*, 1698–1701.
9. Wu, Z.; Yang, S.; Sun, Y.; Parvez, K.; Feng, X.; Müllen, K. 3D Nitrogen-Doped Graphene Aerogel-Supported Fe₃O₄ Nanoparticles as Efficient Electrocatalysts for the Oxygen Reduction Reaction. *J. Am. Chem. Soc.* **2012**, *134*, 9082–9085.
10. Hrubesh, L. W.; Poco, J. F. Thin Aerogel Films for Optical, Thermal, Acoustic and Electronic Applications. *J. Non. Cryst. Solids* **1995**, *188*, 46–53.
11. Fricke, J.; Tillotson, T. Aerogels: Production, Characterization, and Applications. *Thin Solid Films* **1997**, *297*, 212–223.
12. Akimov, Y. K. Fields of Application of Aerogels (Review). *Instrum. Exp. Tech.* **2003**, *46* (3), 287–299.
13. Frackowiak, E.; Béguin, F. Carbon Materials for the Electrochemical Storage of Energy in Capacitors. *Carbon* **2001**, *39*, 937–950.
14. Rolison, D. R.; Long, J. W.; Lytle, J. C.; Fischer, A. E.; Rhodes, C. P.; McEvoy, T. M.; Bourg, M. E.; Lubers, A. M. Multifunctional 3D Nanoarchitectures for Energy Storage and Conversion. *Chem. Soc. Rev.* **2009**, *38*, 226–252.
15. Teichner, S. J.; Nicolaon, G. A.; Vicarini, M. A.; Gardes, G. E. E. Inorganic Oxide Aerogels. *Adv. Colloid Interface Sci.* **1976**, *5*, 245–273.

16. Soleimani Dorcheh, A.; Abbasi, M. H. Silica Aerogel; Synthesis, Properties and Characterization. *J. Mater. Process. Technol.* **2008**, *199*, 10–26.
17. Fricke, J. Aerogels—Highly Tenuous Solids with Fascinating Properties. *J. Non. Cryst. Solids* **1988**, *100*, 169–173.
18. Morris, C. A.; Anderson, M. L.; Stroud, R. M.; Merzbacher, C. I.; Rolison, D. R. Silica Sol as A Nanoglue: Flexible Synthesis of Composite Aerogels. *Science* **1999**, *284*, 622–624.
19. Kim, J.; Nakanishi, H.; Pollanen, J.; Smoukov, S.; Halperin, W. P.; Grzybowski, B. A. Nanoparticle–Loaded Aerogels and Layered Aerogels Cast from Sol–Gel Mixtures. *Small* **2011**, *7* (18), 2568–2572.
20. Veinot, J. G. C. Synthesis, Surface Functionalization, and Properties of Freestanding Silicon Nanocrystals. *Chem. Commun.* **2006**, *40*, 4160–4168.
21. Dasog, M.; Reyes, G. B. D. L.; Titova, L. V.; Hegmann, F. A.; Veinot, J. G. C. Size vs Surface: Tuning the Photoluminescence of Freestanding Silicon Nanocrystals Across the Visible Spectrum *via* Surface Groups. *ACS Nano* **2014**, *8* (9), 9636–9648.
22. Park, J. H.; Gu, L.; von Maltzahn, G.; Ruoslahti, E.; Bhatia, S. N.; Sailor, M. J. Biodegradable Luminescent Porous Silicon Nanoparticles for *In Vivo* Applications. *Nat. Mater.* **2009**, *8* (4), 331–336.
23. Erogbogbo, F.; Yong, K. -T.; Roy, I.; Xu, G.; Prasad, P. N.; Swihart, M. T. Synthesis and Enhanced Light-Emission of Si Nanocrystals Embedded in Silicon Oxide Nanowires. *ACS Nano* **2008**, *2* (5), 873–878.
24. Gonzalez, C. M.; Iqbal, M.; Dasog, M.; Piercey, D. G.; Lockwood, R.; Klapötke, T. M.; Veinot, J. G. C. Detection of High-Energy Compounds Using Photoluminescent Silicon Nanocrystal Paper Based Sensors. *Nanoscale* **2014**, *6*, 2608–2612.
25. Lockwood, R.; Veinot, J. G. C.; Meldrum, A. Sensing Water and Alcohol Vapors with Freestanding Silicon Quantum Dots. *Sens. Lett.* **2013**, *11*, 1535–1540.
26. Kim, H.; Seo, M.; Park, M. H.; Cho, J. A Critical Size of Silicon Nano-Anodes for Lithium Rechargeable Batteries. *Angew. Chem. Int. Ed.* **2010**, *49*, 2146–2149.
27. Graetz, J.; Ahn, C. C.; Yazami, R.; Fultz, B. Highly Reversible Lithium Storage in Nanostructured Silicon. *Electrochem. Solid-State Lett.* **2003**, *6* (9), A194-A197.

28. Zhai, Y.; Dasog, M.; Snitynsky, R. B.; Purkait, T. K.; Aghajamali, M.; Hahn, A. H.; Sturdy, C. B.; Lowary, T. L.; Veinot, J. G. C. Water-Soluble Photoluminescent D-Mannose and L-Alanine Functionalized Silicon Nanocrystals and Their Application to Cancer Cell Imaging. *J. Mater. Chem. B* **2014**, *2*, 8427–8433.
29. Zhong, Y.; Peng, F.; Bao, F.; Wang, S.; Ji, X.; Yang, L.; Su, Y.; Lee, S. T.; He, Y. Large-Scale Aqueous Synthesis of Fluorescent and Biocompatible Silicon Nanoparticles and Their Use as Highly Photostable Biological Probes. *J. Am. Chem. Soc.* **2013**, *135*, 8350–8356.
30. Xu, Z.; Wang, D.; Guan, M.; Liu, X.; Yang, Y.; Wei, D.; Zhao, C.; Zhang, H. Photoluminescent Silicon Nanocrystal-Based Multifunctional Carrier for pH-Regulated Drug Delivery. *ACS Appl. Mater. Interfaces* **2012**, *4*, 3424 – 3431.
31. Kazes, M.; Lewis, D. Y.; Banin, U. Method for Preparation of Semiconductor Quantum-Rod Lasers in A Cylindrical Microcavity. *Adv. Funct. Mater.* **2004**, *14* (10), 957–962.
32. Maier-Flaig, F.; Rinck, J.; Stephan, M.; Bocksrocker, T.; Bruns, M.; Kübel, C.; Powell, A. K.; Ozin, G. A.; Lemmer, U. Multicolor Silicon Light-Emitting Diodes (SiLEDs). *Nano Lett.* **2013**, *13*, 475–480.
33. Conibeer, G.; Green, M.; Corkish, R.; Cho, Y.; Cho, E. C.; Jiang, C. W.; Fangsuwannarak, T.; Pink, E.; Huang, Y.; Puzzer, T.; Trupke, T.; Richards, B.; Shalav, A.; Lin, K. L. Silicon Nanostructures for Third Generation Photovoltaic Solar Cells. *Thin Solid Films* **2006**, *511-512*, 654–662.
34. Priolo, F.; Gregorkiewicz, T.; Galli, M.; Krauss, T. F. Silicon Nanostructures for Photonics and Photovoltaics. *Nat. Nanotechnol.* **2014**, *9*, 19–32.
35. Perez-Wurfl, I.; Hao, X.; Gentle, A.; Kim, D. H.; Conibeer, G.; Green, M. A. Si Nanocrystal p-i-n Diodes Fabricated on Quartz Substrates for Third Generation Solar Cell Applications. *Appl. Phys. Lett.* **2009**, *95*, 153506-3.
36. Borsella, E.; Falconieri, M.; Botti, S.; Martelli, S.; Bignoli, F.; Costa, L.; Grandi, S.; Sangaletti, L.; Allieri, B.; Depero, L. Optical and Morphological Characterization of Si Nanocrystals/Silica Composites Prepared by Sol–Gel Processing. *Mater. Sci. Eng. B* **2001**, *79*, 55–62.

37. Amonkosolpan, J.; Wolverson, D.; Goller, B.; Polisski, S.; Kovalev, D.; Rollings, M.; Grogan, M. D. W.; Birks, T. A. Porous Silicon Nanocrystals in A Silica Aerogel Matrix. *Nanoscale Res. Lett.* **2012**, *7*, 397-403.
38. Karlash, A. Y.; Skryshevsky, V. A.; Kuznetsov, G. V.; Kladko, V. P. Evolution of Visible Photoluminescence of Si Quantum Dots Embedded in Silicon Oxide Matrix. *J. Alloys Compd.* **2013**, *577*, 283–287.
39. Hessel, C. M.; Henderson, E. J.; Veinot, J. G. C. Hydrogen Silsesquioxane: A Molecular Precursor for Nanocrystalline Si-SiO₂ Composites and Freestanding Hydride-Surface-Terminated Silicon Nanoparticles. *Chem. Mater.* **2006**, *1*, 6139–6146.
40. Yang, Z.; Iqbal, M.; Dobbie, A. R.; Veinot, J. G. C. Surface-Induced Alkene Oligomerization: Does Thermal Hydrosilylation Really Lead to Monolayer Protected Silicon Nanocrystals?. *J. Am. Chem. Soc.* **2013**, *135*, 17595–17601.
41. Hessel, C. M.; Rasch, M. R.; Hueso, J. L.; Goodfellow, B. W.; Akhavan, V. A.; Puvanakrishnan, P.; Tunnel, J. W.; Korgel, B. A. Alkyl Passivation and Amphiphilic Polymer Coating of Silicon Nanocrystals for Diagnostic Imaging. *Small* **2010**, *6* (18), 2026–2034.
42. Lin, C. A. J.; Sperling, R. A.; Li, J. K.; Yang, T. Y.; Li, P. Y.; Zanella, M.; Chang, W. H.; Parak, W. J. Design of An Amphiphilic Polymer for Nanoparticle Coating and Functionalization. *Small* **2008**, *4* (3), 334–341.
43. Anderson, M. L.; Morris, C. A.; Stroud, R. M.; Merzbacher, C. I.; Rolison, D. R. Colloidal Gold Aerogels: Preparation, Properties, and Characterization. *Langmuir* **1999**, *15* (3), 674–681.
44. Russo, R. E.; Hunt, A. J. Comparison of Ethyl versus Methyl Sol-Gels for Silica Aerogels Using Polar Nephelometry. *J. Non-Cryst. Solids* **1986**, *86*, 219–230.
45. Purkait, T. K.; Iqbal, M.; Wahl, M. H.; Gottschling, K.; Gonzalez, C. M.; Islam, M. A.; Veinot, J. G. C. Borane-Catalyzed Room Temperature Hydrosilylation of Alkenes/Alkynes on Silicon Nanocrystal Surfaces. *J. Am. Chem. Soc.* **2014**, *136*, 17914–17917.
46. Liu, S.; Kobayashi, M.; Sato, S.; Kimura, K. Synthesis of Silicon Nanowires and Nanoparticles by Arc-Discharge in Water. *Chem. Commun.* **2005**, *1*, 4690–4692.

47. Ledoux, G.; Guillois, O.; Porterat, D.; Reynaud, C.; Huisken, F.; Kohn, B.; Paillard, V. Photoluminescence Properties of Silicon Nanocrystals as A Function of Their Size. *Phys. Rev. B* **2000**, *62*, 15942–15951.
48. Kruk, M.; Jaroniec, M. Gas Adsorption Characterization of Ordered Organic-Inorganic Nanocomposite Materials. *Chem. Mater.* **2001**, *13*, 3169–3183.

Chapter 3:

Silicon Nanocrystal/Graphene Aerogel Hybrids as Anode Materials for Lithium-Ion Batteries

3.1 Introduction

The development of high-performance lithium-ion batteries (LIBs) with higher energy and power densities is of great importance for their application in portable electronics, stationary energy storage, and electric vehicles.^{1,2} To date, silicon is one of the most promising anode materials for high-performance LIBs because of its abundance, low discharge potential (0.4 V vs. Li/Li⁺), and high theoretical specific capacity (4200 mAh/g reported for Li₂₂Si₅ alloy); this is 10 times higher than that of a graphite anode (372 mAh/g) used in commercial LIBs.³⁻⁶ Unfortunately, practical applications of Si anodes are yet to become a reality due to the low electrical conductivity of Si and low lithium diffusion rate, as well as large volume changes (>300%) observed during the lithiation and delithiation processes.^{4,6} The latter results in the pulverization of Si particles and unstable solid electrolyte interphase (SEI) formation, leading to the loss of electrical contact, rapid capacity fading, and poor cyclability.^{4,6} To address these issues, one approach is to use nanoscale Si (n-Si) of various morphologies (e.g., nanoparticles,⁷ nanowires,^{8,9} nanotubes,^{10,11} hollow nanospheres,¹² and nanoporous Si^{13,14}). Nanoscale materials offer short Li diffusion distances within the electrode and exhibit improved stress/strain tolerance, which prevents the pulverization of Si anodes and improves their cycling performance.^{6,15} Another effective approach is to incorporate n-Si into conductive carbon materials,¹⁶⁻²¹ which accommodate the large volume expansion/contraction of Si particles and improve the Li diffusion rate and electrical conductivity of Si anodes.

Graphene aerogels (GAs) are nanoporous carbon-based materials exhibiting high electrical conductivity, tunable porosity, and high specific surface area.^{22,23} They are prepared commonly by chemical reduction of a graphene oxide precursor, followed by various drying procedures (e.g., freeze drying, CO₂ supercritical drying).^{24,25} Recently, n-Si/GA hybrids have been studied

as anode materials for LIBs.^{26,27} These hybrid aerogels were prepared by incorporating n-Si guests ($d \sim 100$ nm) into a graphene aerogel host using freeze drying. It has been shown that graphene aerogels prepared by CO₂ supercritical drying exhibit higher electrical conductivity (~ 100 S/m) and significantly higher specific surface area (512 m²/g) compared to freeze-dried GAs.²⁵ In addition, silicon nanocrystal (SiNC) properties (e.g., size and surface chemistry) and their effect on the electrochemical performance of the hybrid aerogels have not been explored. Furthermore, there is no report of SiNC/GA hybrids with high mass loading of functionalized SiNCs in a graphene aerogel host (~ 88 %); this could pave the way to high-performance LIBs. In this Chapter, a detailed investigation aimed at interfacing the unique properties of SiNCs (e.g., high specific capacity) with conductive mesoporous graphene aerogels is described. The impact of NC size and surface chemistry on the properties and electrochemical performance of the resultant hybrid aerogels have been investigated.

3.2 Experimental

3.2.1 Reagents and Materials

All reagents were used as received, unless otherwise indicated. A methyl isobutyl ketone solution of hydrogen silsesquioxane (HSQ, tradename Fox-17) was obtained from Dow Corning; the solvent was removed under vacuum, and the resulting white solid was used without further purification. Electronic grade hydrofluoric acid (HF, 49% aqueous solution) and L-ascorbic acid (L-AA) were purchased from J. T. Baker. 10-Undecenoic acid (98%), azobisisobutyronitrile (AIBN, 98%), lithium foil (99.9%), 1M lithium hexafluorophosphate (LiPF₆) in ethylene carbonate/diethyl carbonate (1:1 v/v), fluoroethylene carbonate (99%), *N*-methyl-2-pyrrolidone (NMP), methanol (reagent grade), ethanol (reagent grade), toluene (reagent grade), acetone (reagent grade), and hydrogen peroxide (H₂O₂, 30%) were obtained from Sigma-Aldrich. Natural

graphite flake (99.9%), carbon black (50% compressed, 99.9+%), and poly(vinylidene fluoride) (PVDF) were purchased from Alfa Aesar. Potassium permanganate (KMnO₄, reagent grade), sulfuric acid (H₂SO₄, reagent grade), phosphoric acid (H₃PO₄, reagent grade), and hydrochloric acid (HCl, 30%) were obtained from Caledon. CR2032 coin cells and stainless steel spacers were purchased from MTI Corporation. Toluene was dried using a Grubbs-type solvent purification system (Innovative Technologies, Inc.) prior to use.

3.2.2 Synthesis, Liberation, and Functionalization of SiNCs

SiNC/SiO₂ composite synthesis and SiNC liberation. A detailed procedure of silicon nanocrystal synthesis can be found elsewhere.^{28,29} Briefly, an appropriate amount of HSQ (*i.e.*, 10 g) was annealed under slightly reducing conditions (5% H₂/95% Ar) for 1 h at 1100, 1200, 1300, and 1400 °C to produce SiO₂-like composites containing silicon nanocrystals of sizes ca. 3, 5, 8, and 15 nm, respectively. Hydride-terminated silicon nanocrystals (H-SiNCs) were liberated from the silica matrix by etching SiNC/SiO₂ composites (0.9 g) in a 1:1:1 ethanol/H₂O/HF solution (30 mL) for 1 h, followed by extraction into toluene. (**Caution!** HF is extremely dangerous and must be handled with extreme care.)

Synthesis of undecanoic acid-functionalized SiNCs (*d* ~ 3, 5, 8, and 15 nm). Acid-functionalized SiNCs were synthesized using an established literature procedure for radical hydrosilylation.³⁰ After etching of SiNC/SiO₂ composites (0.9 g), H-SiNCs (*d* ~ 3, 5, 8, or 15 nm) suspended in toluene were centrifuged twice (3000 rpm, 5 min) and redispersed in dry toluene (16 mL) in a Schlenk flask equipped with a magnetic stir bar. 10-Undecenoic acid (4 g) and AIBN (200 mg) were added to the flask, and the mixture was subjected to three freeze/pump/thaw cycles using an argon charged Schlenk line. After stirring at 75 °C for 15 h,

the resulting particles were collected by centrifugation (3000 rpm, 5 min) and purified by three successive cycles of dispersion/precipitation using methanol/toluene as the solvent/antisolvent mixture. Finally, acid-functionalized SiNCs were dispersed in benzene and freeze-dried.

3.2.3 Synthesis of SiNC/Graphene Aerogel Hybrids

Synthesis of graphene oxide. Graphene oxide (GO) was prepared by oxidation of natural graphite following the Improved Hummers' method.^{31,32} Briefly, graphite flakes (3.0 g) and KMnO_4 (18.0 g) were dispersed in a 9:1 mixture of concentrated $\text{H}_2\text{SO}_4/\text{H}_3\text{PO}_4$ (360:40 mL). After stirring for 15 h at 50 °C, the green suspension turned dark purple. The mixture was cooled to room temperature and poured into an ice cold solution of water (400 mL) and 30% H_2O_2 (3 mL). The mixture was centrifuged (12000 rpm, 1 h), and the filtrate was washed successively with deionized (DI) water (200 mL \times 2), 30% HCl (200 mL \times 1), and ethanol (200 mL \times 3). After each washing, the supernatant was discarded and the unreacted graphite was removed. Finally, the brown GO precipitate was dispersed in DI water (6 mg/mL).

Synthesis of SiNC/graphene aerogel hybrids. SiNC/graphene aerogel hybrids were synthesized by incorporating functionalized SiNCs ($d \sim 3, 5, 8, \text{ or } 15 \text{ nm}$) into the GO solution, followed by GO chemical reduction and CO_2 supercritical drying. Briefly, acid-functionalized SiNCs (60 mg) were dispersed in an aqueous solution of GO (6 mg/mL, 1.25 mL), diluted to 4 mL, and vigorously stirred with a magnetic stirrer for 5 min to obtain a uniform dispersion (the feed ratio of functionalized SiNCs:GO is 8:1). L-ascorbic acid (72 mg) was added into the SiNC/GO dispersion and stirred for another 5 min. The resulting dispersion was transferred to a plastic syringe (12 \times 60 mm) and heated at 90 °C for 3 h to reduce the GO and form a hybrid hydrogel. The SiNC/graphene hydrogel was placed in a capped glass vial and rinsed with D.I. water three

times to remove any impurities. Subsequently, D.I. water was exchanged with acetone, refreshing the acetone bath every 6 h, for 1 day. The acetone-exchanged gel was placed in a home-built CO₂ supercritical dryer (See Appendix A for a detailed instruction, as well as photos of this equipment), and acetone was exchanged with liquid CO₂ over a time period of at least 12 h prior to the final drying procedure. Finally, the temperature and pressure of the dryer assembly were raised to 40°C and 8.3 MPa (above the critical point of liquid CO₂; $T_c = 31$ °C and $P_c = 7.4$ MPa), and the liquid CO₂-exchanged gel was dried for 1 h to yield a monolithic SiNC/graphene aerogel (SiNC/GA) hybrid. To study the effect of thermal processing on the electrochemical performance of the hybrid aerogels, these materials were annealed at 600 °C under argon flow for 3 h to produce annealed SiNC/GA hybrids.

3.2.4 Material Characterization

Powder samples of functionalized SiNCs and hybrid aerogels were used for characterization, unless otherwise indicated. Fourier Transform Infrared (FTIR) spectra of functionalized SiNCs were acquired using a Nicolet Magna 750 IR spectrometer. X-ray photoelectron spectroscopy (XPS) measurements were performed on a Kratos Axis Ultra instrument operating in energy spectrum mode at 210 W. The base pressure and operating chamber pressure were maintained at 10^{-7} Pa. A monochromatic Al K α source ($\lambda = 8.34$ Å) was used to irradiate the samples, and the spectra were obtained with an electron takeoff angle of 90°. CasaXPS software (VAMAS) was used to interpret spectra. All the spectra were internally calibrated to the C 1s emission (284.8 eV). After calibration, the background was subtracted using a Shirley-type background to remove most of the extrinsic loss structure. The high-resolution Si 2p region was fitted to Si 2p_{3/2} and Si 2p_{1/2} components, with spin-orbit splitting fixed at 0.6 eV, and the Si 2p_{3/2} / Si 2p_{1/2} intensity ratio set to 2/1.

Transmission electron microscopy (TEM) images were obtained using a JEOL 2010 electron microscope equipped with a LaB₆ filament and operated at an accelerating voltage of 200 kV. The TEM samples were prepared by drop-coating dilute suspensions of functionalized SiNCs or hybrid aerogels onto a holey carbon coated copper grid. Particle size distribution was calculated by counting at least 300 particles using ImageJ software (1.48v).

X-ray diffraction (XRD) analysis was performed on an AXS diffractometer (Discover 8, Bruker, Madison, WI) with Cu-K α radiation ($\lambda = 1.5406 \text{ \AA}$). The diffractometer was equipped with a Histar general-area two-dimensional detection system (GADDs) with a sample-detector distance of 22.25 cm. Raman spectra were acquired using a Renishaw inVia Raman microscope equipped with a 514 nm excitation laser and a power of 3.98 mW on the sample. Powder samples were measured on a gold-coated glass substrate.

Scanning electron microscopy (SEM) images were obtained using a Zeiss Sigma 300 VP-FESEM equipped with secondary and in-lens electron detectors and a Bruker energy dispersive X-ray (EDX) spectroscopy system operated at 10 kV. A conductive carbon coating was applied on all samples using a Leica EM SCD005 evaporative carbon coater prior to characterization.

Nitrogen adsorption-desorption isotherms were measured at 77 K using a Quantachrome ASiQwin surface area and porosimetry analyzer. Fine powders of hybrid aerogels were degassed under vacuum at 130 °C for 6 h prior to the analysis. The isotherm data were fitted using the Brunauer-Emmett-Teller (BET) theory to determine specific surface area. The average pore sizes and total pore volumes were calculated by applying the Barrett-Joyner-Halenda (BJH) model to desorption branches of the isotherms.

Thermal gravimetric analysis (TGA) was performed on a Mettler Toledo TGA/DSC 1 Star System under an argon atmosphere (25–650 °C, 10 °C/min). Carbon, hydrogen, and nitrogen

contents were measured using a Thermo Scientific Flash 2000 Organic Elemental Analyzer equipped with Eager Xperience software.

3.2.5 Electrochemical Characterization

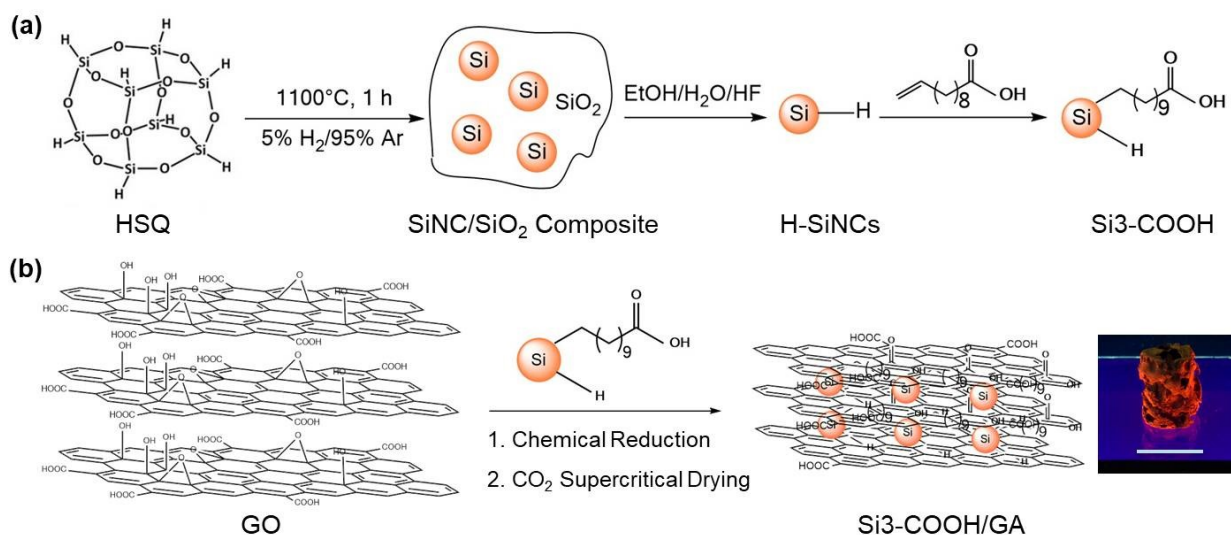
The electrochemical performance of the SiNC-based anode materials was evaluated using CR2032 coin cells. The working electrodes were prepared using a slurry method; for the functionalized SiNCs, NCs were mixed with conductive carbon black and PVDF dissolved in NMP with a mass ratio of 8:1:1 to form homogeneous slurries. For the SiNC/GA hybrids, these hybrid aerogels were mixed with PVDF dissolved in NMP with a mass ratio of 9:1. Next, the slurries were spread onto stainless steel spacers and dried overnight at 65 °C in a vacuum oven. The electrolyte was a mixture of 1M LiPF₆ in ethylene carbonate/diethyl carbonate (1:1 v/v) and fluoroethylene carbonate, with a 9:1 volume ratio. A Celgard 2325 polypropylene-polyethylene-polypropylene membrane with a porosity of 39% was used as the separator. Coin cells were assembled using the working electrode and a Li foil, as the counter electrode, in an argon-filled glove box with oxygen and moisture contents below 1 and 0.1 ppm, respectively. Galvanostatic cycling measurements were carried out using an Arbin BT2000 battery testing system at the voltage window of 0.01–2 V at 25 °C. The current densities of 200 or 400 mA/g were applied for cycle life measurements and up to 8000 mA/g for rate capability tests.

3.3 Results and Discussion

SiNC/SiO₂ composites and hydride-terminated SiNCs (H-SiNCs) were synthesized following well-established procedures developed in the Veinot laboratory.^{28,29} A SiNC/SiO₂ composite obtained from thermal annealing of hydrogen silsesquioxane (HSQ) at 1100, 1200, 1300, and 1400 °C was etched using a hydrofluoric acid solution to remove the oxide and liberate 3, 5, 8, and 15 nm SiNCs, respectively. These H-SiNCs are susceptible to oxidation, and their surfaces must be passivated to prevent undesirable oxidation reactions. Introducing long chain hydrophobic/hydrophilic groups via various hydrosilylation strategies (e.g., thermal, radical, etc.) is the most common approach to passivate H-SiNC surfaces.^{28,30,33} Since graphene oxide (GO) precursor used in graphene aerogel synthesis is dispersible in aqueous media, a radical hydrosilylation³⁰ with a polar hydrophilic group (e.g., 10-undecenoic acid) was employed to functionalize SiNCs and render them hydrophilic, compatible with the aerogel synthetic method. The procedure for the synthesis of 3 nm undecanoic acid-functionalized SiNCs (Si3-COOH) is shown in Scheme 3-1a.

The hydrophilic SiNCs ($d \sim 3, 5, 8,$ and 15 nm) were introduced to an aqueous solution of GO containing L-ascorbic acid (L-AA) as a reducing agent. Following chemical reduction of GO, hydrogels were formed and subsequently dried using a CO₂ supercritical dryer to yield monolithic aerogels. Anchoring hydrophilic groups on the surface of SiNCs resulted in ~88 % mass loading of the functionalized SiNCs in graphene aerogels. Scheme 3-1b summarizes the procedure for the synthesis of a graphene aerogel monolith containing Si3-COOH (Si3-COOH/GA), and the inset photograph qualitatively illustrates the photoluminescent response of Si3-COOH/GA upon exposure to UV light (i.e., 350 nm). This photograph indicates that the

optical properties of SiNCs were preserved after incorporation into graphene aerogel, indicating that the hydrogel formation procedure does not compromise the NC integrity.



Scheme 3-1. Synthesis of a) 3 nm undecanoic acid-functionalized SiNCs (Si3-COOH), and b) a graphene aerogel containing Si3-COOH (Si3-COOH/GA). Photograph of Si3-COOH/GA under UV light is shown as inset. The scale bar is 1 cm.

Fourier Transform Infrared (FTIR) spectroscopy provides insight into the nature of SiNC surface functionalization. Representative FTIR spectra of undecanoic acid-functionalized SiNCs ($d \sim 3, 5, 8,$ and 15 nm) show expected features corresponding to the target functional groups (Figure 3-1a). Following hydrosilylation with 10-undecenoic acid, intense absorptions corresponding to C–H and C=O stretching appeared at $2850\text{--}3000$ and $1700\text{--}1725 \text{ cm}^{-1}$, respectively (Figure 3-1a).³³ Also, broad Si–O related features at $\sim 1000\text{--}1130 \text{ cm}^{-1}$, as well as weak absorptions at $\sim 2100 \text{ cm}^{-1}$ (residual Si–H_x), are noted in the spectra of all functionalized SiNCs.²⁸

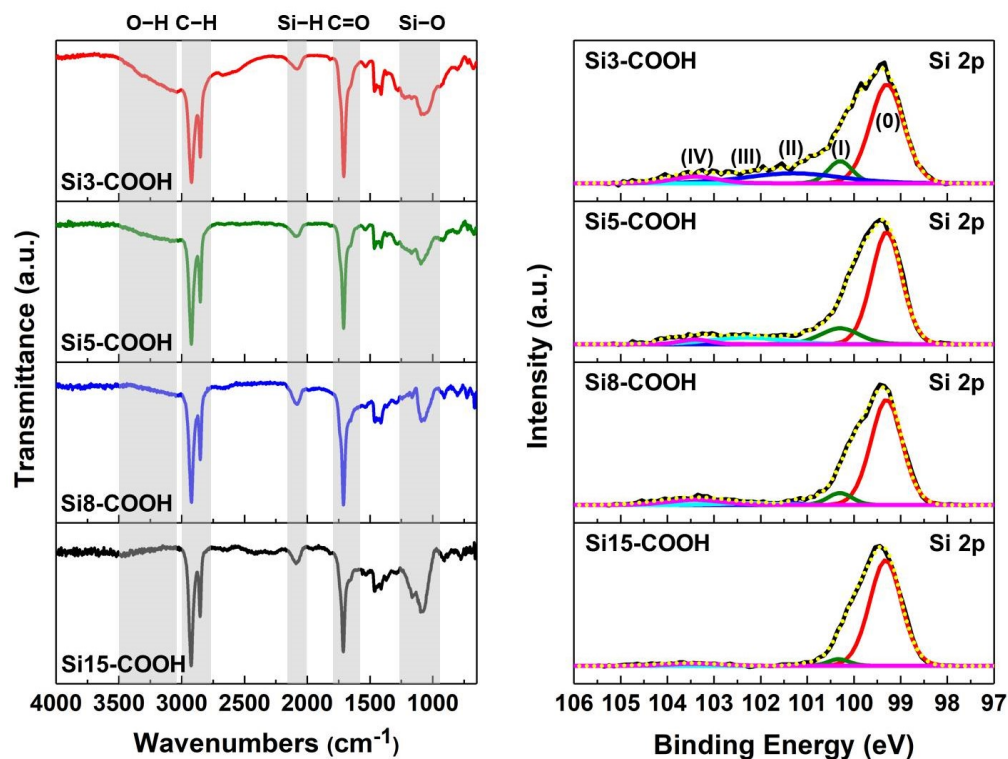


Figure 3-1. a) FTIR and b) HRXP spectra of the Si 2p region of undecanoic acid-functionalized SiNCs ($d \sim 3, 5, 8,$ and 15 nm). Please note, only Si $2p_{3/2}$ components are shown; Si $2p_{1/2}$ components are omitted for clarity.

High resolution X-ray photoelectron (HRXP) spectra of the Si 2p region of the functionalized SiNCs and their corresponding SiNC/graphene aerogel hybrids show an intense emission at 99.34 eV characteristic of the Si core (i.e., Si(0)) (Figures 3-1b and 3-2a). Higher binding energy features in this region are attributed to Si sub-oxides and surface functionalized Si atoms. A minor surface oxidation is noted in the HRXP spectra of all functionalized SiNCs (Figure 3-1a) and their corresponding hybrid aerogels (Figure 3-2a). In addition, a comparison of Figures 3-1a and 3-2a indicates an effective surface passivation for the functionalized SiNCs since the aqueous environment required for the synthesis of hybrid hydrogels does not influence SiNC surfaces.

HRXP spectra of the C 1s region of graphene oxide and SiNC/graphene aerogel hybrids are shown in Figure 3-2b. The HRXP spectrum of GO shows three emission components centered at 284.8, 287.0, and 288.2 corresponding to C–C/C=C, C–O/C–O–C, and C=O/O–C=O, respectively (Figure 3-2b: GO).³⁴ Following chemical reduction with L-AA, the peak intensities of oxygen-containing groups decreased significantly and the peak intensity of C–C/C=C increased, indicating complete removal of oxygen-containing species and successful formation of C–C/C=C during the reduction process (Figure 3-2b: Si3-COOH, Si5-COOH, Si8-COOH, and Si15-COOH).

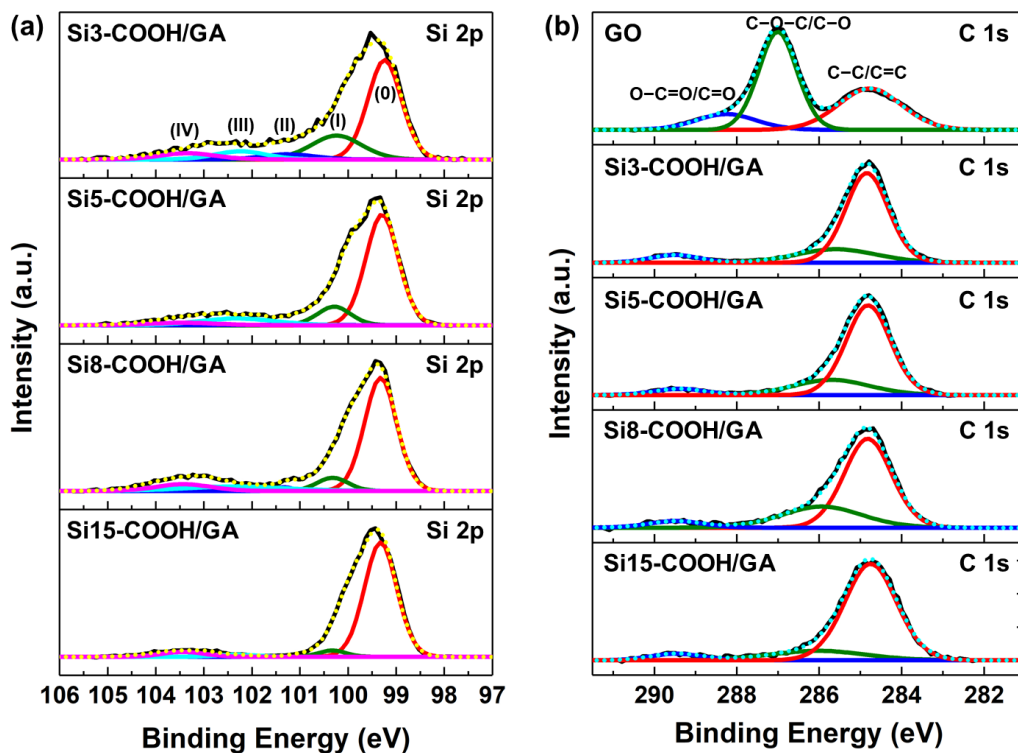


Figure 3-2. HRXP spectra of a) the Si 2p region and b) the C 1s region of graphene oxide and graphene aerogels containing undecanoic acid-functionalized SiNCs ($d \sim 3, 5, 8,$ and 15 nm). Please note, only Si 2p_{3/2} components are shown; Si 2p_{1/2} components are omitted for clarity.

Transmission electron microscopy (TEM) images of the functionalized SiNCs and their size distributions are presented in Figures 3-3a and 3-3b. The 3, 5, and 8 nm undecanoic acid-functionalized SiNCs ($d = 3.2 \pm 0.5$ nm, $d = 4.9 \pm 0.8$ nm, and $d = 7.9 \pm 1.2$ nm) are well separated, consistent with their dispersibility in polar solvents. In contrast, 15 nm undecanoic acid-functionalized SiNCs ($d = 15.3 \pm 2.8$ nm) appear as large assemblies, suggesting the poor dispersibility of these particles in polar solvents. Moreover, the TEM images of SiNC/graphene aerogel hybrids are shown in Figure 3-3c, which shows the distribution of the functionalized SiNCs on graphene aerogel sheets.

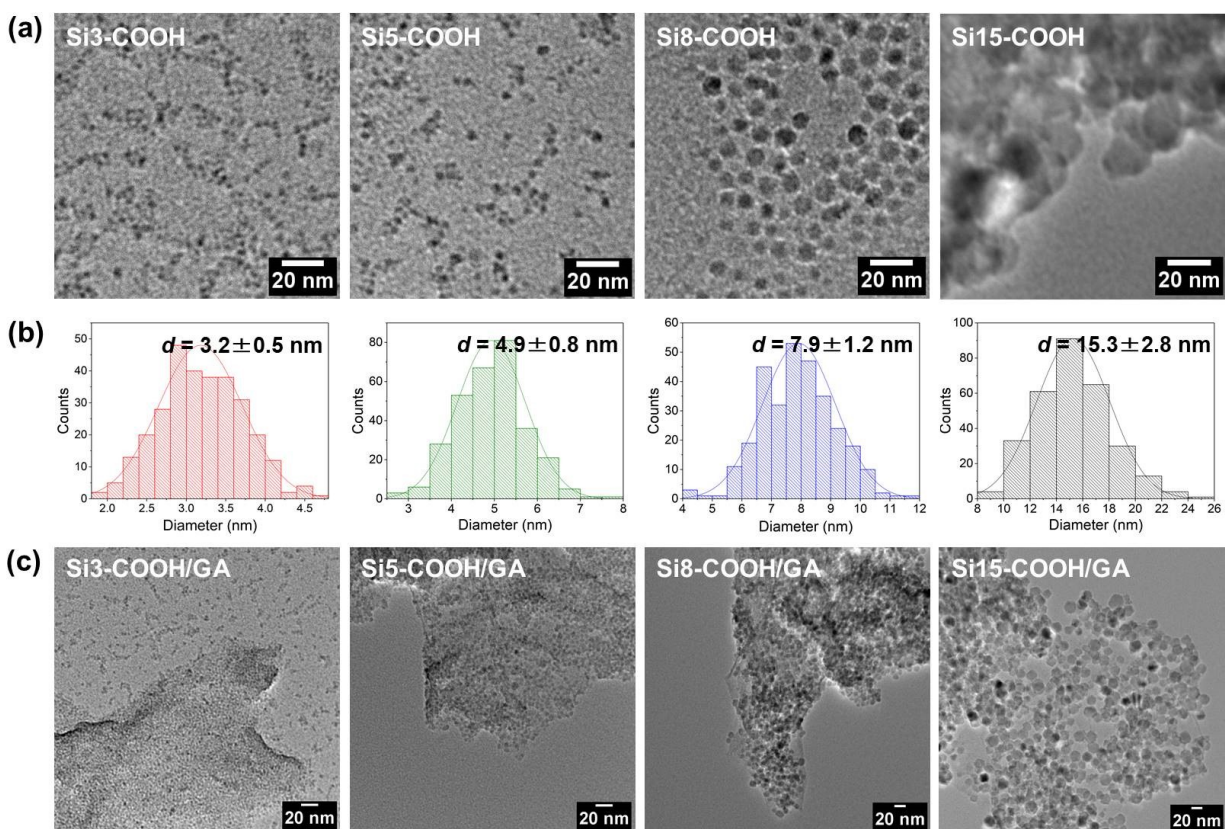


Figure 3-3. a) Bright-field TEM images of undecanoic acid-functionalized SiNCs ($d \sim 3, 5, 8,$ and 15 nm), b) their size distributions, and c) bright-field TEM images of SiNC/graphene aerogel hybrids.

X-ray diffraction (XRD) patterns of the SiNC/graphene aerogel hybrids are shown in Figure 3-4a. All XRD patterns show broad reflections at 2-theta of 28° and 47° characteristic of Si (111) and (220) lattice planes, respectively.³⁵ As the size of SiNCs increases, these reflections appear narrower and more intense due to an increase in long-range order. A broad peak at 2-theta of 20° noted in XRD patterns of 3, 5, and 8 nm SiNC/graphene aerogel hybrids corresponds to the graphene aerogel, indicating the poor ordering of graphene sheets along their stacking direction.^{36,37}

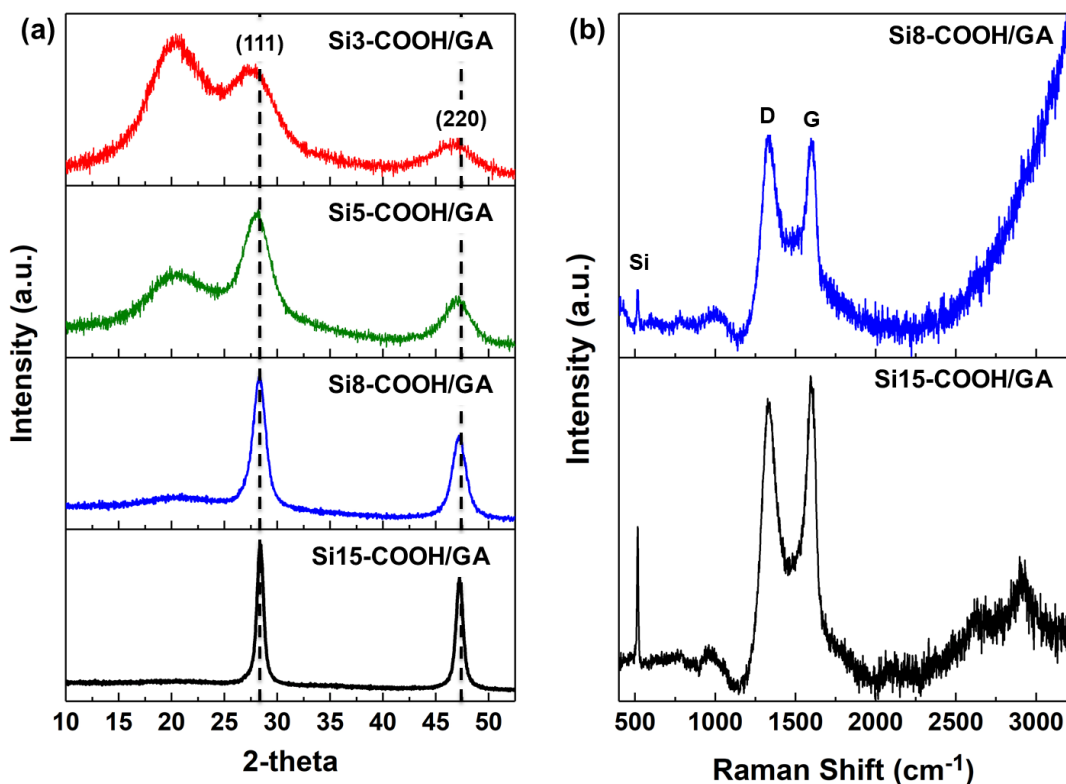


Figure 3-4. a) XRD patterns and b) Raman spectra of graphene aerogels containing undecanoic acid-functionalized SiNCs ($d \sim 3, 5, 8,$ and 15 nm).

Raman spectra of 8 and 15 nm SiNC/graphene aerogel hybrids are presented in Figure 3-4b, which further supports the crystallinity and composition of these materials. A sharp absorption

band at $\sim 516\text{ cm}^{-1}$ corresponds to crystalline Si particles, and two absorption bands at ~ 1340 and $\sim 1597\text{ cm}^{-1}$ are attributed to the D and G bands of graphene, respectively, confirming the presence of the graphene aerogel.³⁷ As the size of SiNCs decreases, the intensity of the feature appearing above 2000 cm^{-1} arising from photoluminescence of SiNCs increases (Figure 3-4b: Si8-COOH/GA), which hinders the observation of the hybrid absorption bands in Raman spectra of the 3 and 5 nm SiNC/graphene aerogel hybrids.

Secondary electron images of SiNC/graphene aerogel hybrids are shown in Figures 3-5a and 3-6a. These hybrid aerogels show a uniform morphology composed of a three-dimensional network of randomly oriented structures with broad pore size distribution (Figure 3-6a). In addition, energy dispersive X-ray (EDX) spectra and mapping of the SiNC/graphene aerogel hybrids confirm the presence of Si, C, and O (Figure 3-5b) and the uniform distribution of SiNCs throughout the graphene aerogel matrix (Figure 3-5c).

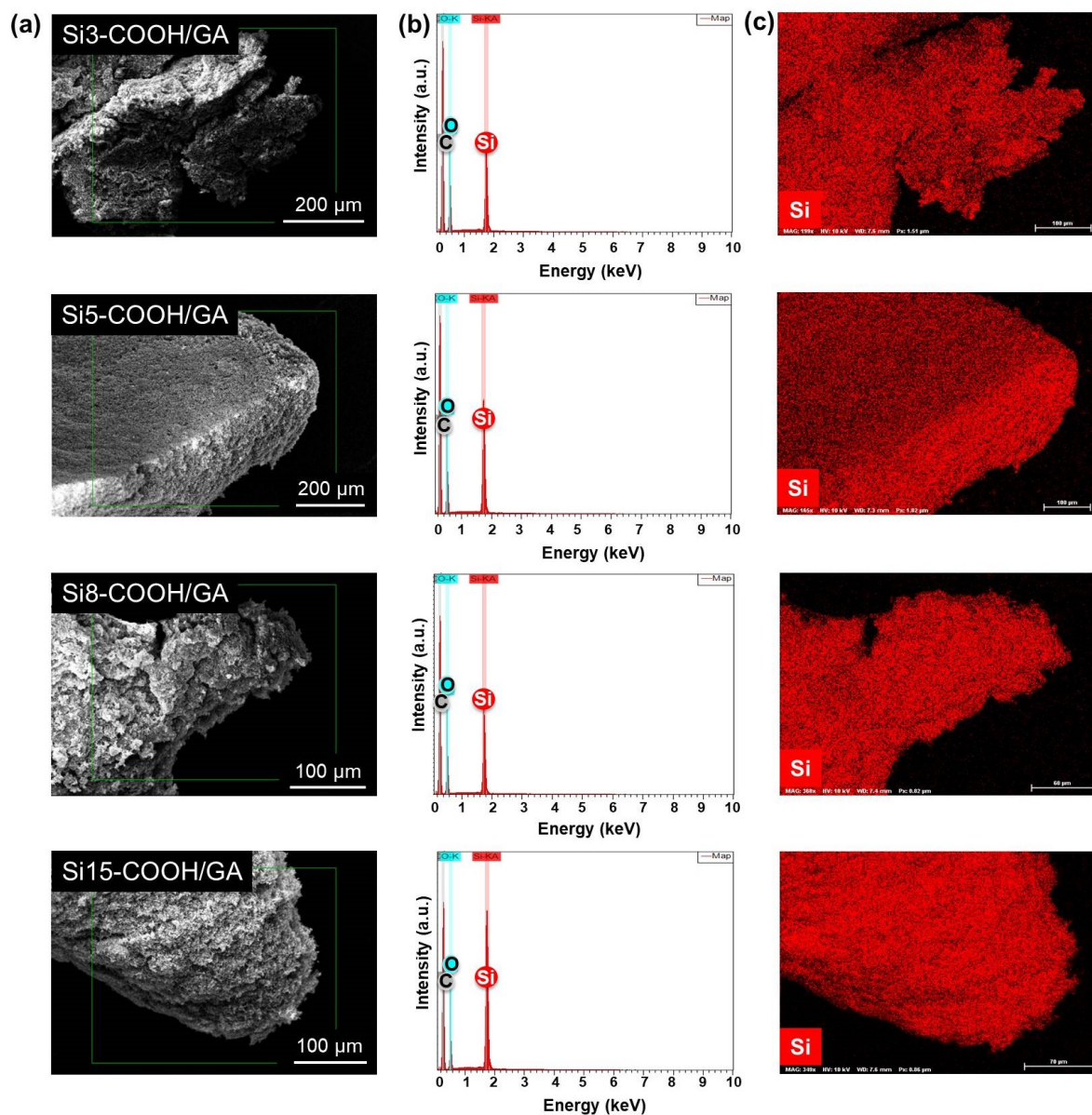


Figure 3-5. a) Secondary electron images, b) EDX spectra, and c) EDX mapping of graphene aerogels containing undecanoic acid-functionalized SiNCs ($d \sim 3, 5, 8,$ and 15 nm).

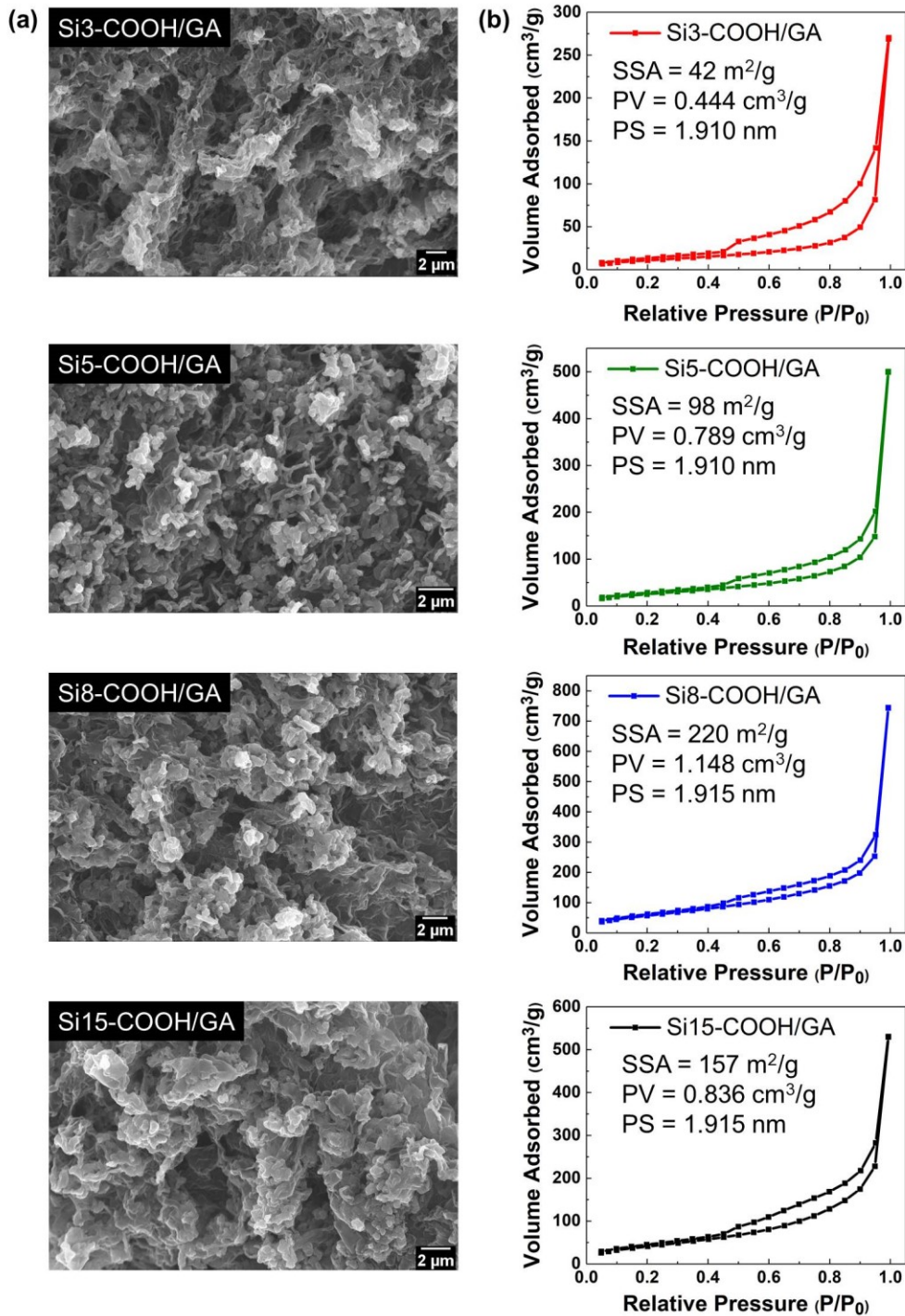


Figure 3-6. a) Secondary electron images and b) N₂ adsorption–desorption isotherms of graphene aerogels containing undecanoic acid-functionalized SiNCs ($d \sim 3, 5, 8,$ and 15 nm). The specific surface area (SSA), total pore volume (PV), and average pore size (PS) are presented as insets.

Nitrogen adsorption–desorption isotherms of SiNC/graphene aerogel hybrids are presented in Figure 3-6b. Each exhibited a Type-IV isotherm with distinct capillary condensation and evaporation steps characteristic of mesoporous materials ($d = 2\text{--}50\text{ nm}$).³⁸ It is noted that these isotherms do not level off at relative pressures close to the saturation vapor pressure (P_0), and they indicate a combination of Type-H3 and Type-H4 hysteresis loops, characterized by parallel and nearly horizontal branches, suggesting the presence of plate-like structures forming slit-like pores.³⁸

The specific surface area (SSA), total pore volume (PV), and average pore size (PS) of SiNC/graphene aerogel hybrids are presented as insets in Figure 3-6b. The SSA of hybrid aerogels was calculated using the Brunauer–Emmett–Teller (BET) model. The PV and PS values were determined using the desorption branches of the N_2 adsorption–desorption isotherms by applying the Barrett–Joyner–Halenda (BJH) model. The incorporation of 3, 5, 8, and 15 nm functionalized SiNCs into graphene aerogels results in SSA values of 42, 98, 220, and 157 m^2/g , respectively. Also, PV values of 0.444, 0.789, 1.148, and 0.836 cm^3/g were obtained for Si3-COOH/GA, Si5-COOH/GA, Si8-COOH/GA, and Si15-COOH/GA, respectively. The Si8-COOH/GA shows the highest SSA (220 m^2/g) and PV (1.148 cm^3/g) values among all hybrid aerogels; the reason for this behavior is under investigation.

The silicon content in the functionalized SiNCs and SiNC/graphene aerogel hybrids was determined using thermal gravimetric analysis (TGA) performed in an argon atmosphere (Figure 3-7). The weight loss of 3, 5, 8, and 15 nm functionalized SiNCs at 600 °C was about 38, 31, 13, and 8 %, respectively, and as a result, the Si content (remaining amount) is calculated to be 62, 69, 87, and 92 %, respectively (Figure 3-7a). As expected, the incorporation of 3, 5, 8, and 15 nm functionalized SiNCs into graphene aerogel decreased the Si content to 58, 67, 83, and 86 %, respectively.

respectively (Figure 3-7b). The weight loss of functionalized SiNCs and their corresponding hybrid aerogel is due to the decomposition of oxygen containing functional groups. As the size of SiNCs ($d = 2r$) decreases, their surface area to volume ratio ($3/r$) increases, and they experience more effective surface coverage consistent with TGA data.

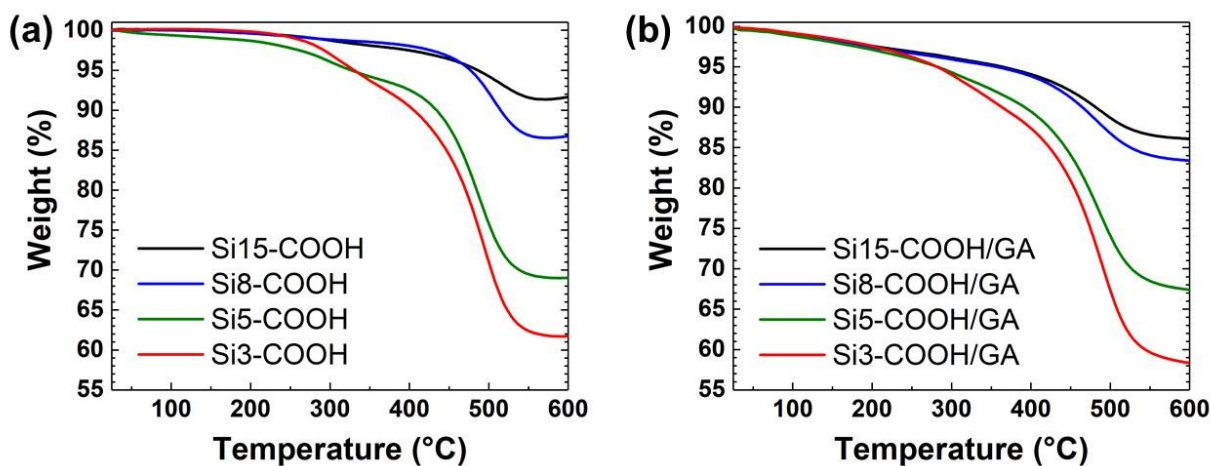


Figure 3-7. TGA of a) undecanoic acid-functionalized SiNCs ($d \sim 3, 5, 8,$ and 15 nm), and b) their corresponding SiNC/graphene aerogel hybrids.

Elemental analysis provides more accurate values for Si content, consistent with TGA data (Table 3-1). Carbon, hydrogen, and nitrogen contents were obtained from CHNS analysis, and the remaining amount assumed to be silicon, based on minimum surface oxidation observed in HRXP data (Figures 3-1b and 3-2). It is noted that CHNS analysis provided lower values for Si content compared to TGA, which indicates that the surface group is not removed completely during thermogravimetric analysis under inert atmosphere.

Table 3-1. CHNS data of undecanoic acid-functionalized SiNCs ($d \sim 3, 5, 8,$ and 15 nm) and their corresponding hybrid aerogel.

	%C	%H	%N	%Si (remaining amount)
Si3-COOH	40.57	6.91	0.66	51.86
Si3-COOH/GA	43.32	6.15	0.65	49.88
Si5-COOH	28.95	5.07	0.48	65.50
Si5-COOH/GA	34.10	4.85	0.59	60.46
Si8-COOH	19.00	3.48	0.37	77.15
Si8-COOH/GA	19.31	2.77	0.33	77.59
Si15-COOH	13.74	2.52	0.32	83.42
Si15-COOH/GA	14.85	2.06	0.27	82.82

The electrochemical performance of the functionalized SiNCs and the SiNC/GA hybrids as anode materials was tested using CR2032 coin cells, where Li foils were used as the counter electrode. Figure 3-8 shows the cycling performance of the functionalized SiNCs ($d \sim 3, 5, 8,$ and 15 nm) and their corresponding SiNC/GA hybrids at a current density of 200 mA/g. The specific capacity values were calculated based on the Si contents obtained from CHNS analysis (Table 3-1). The $5, 8,$ and 15 nm functionalized SiNCs show poor cycling stability and low specific capacity compared to that of a fully lithiated Si alloy (~ 4200 mAh/g) (Figure 3-8a). This poor performance is attributed reasonably to a substantial aggregation of SiNCs, which suggests that the conductive carbon black used for electrode preparation does not stabilize these NCs ($d < 15$ nm) and accommodate their volume changes during lithiation and delithiation cycling. Figure 3-8b shows an improved cycling stability and high specific capacity for the $5, 8,$ and 15 nm SiNC/GA hybrids, suggesting that incorporating nanoscale Si into a nanoporous graphene

aerogel stabilizes these NCs and accommodates volume changes associated with lithiation/delithiation.

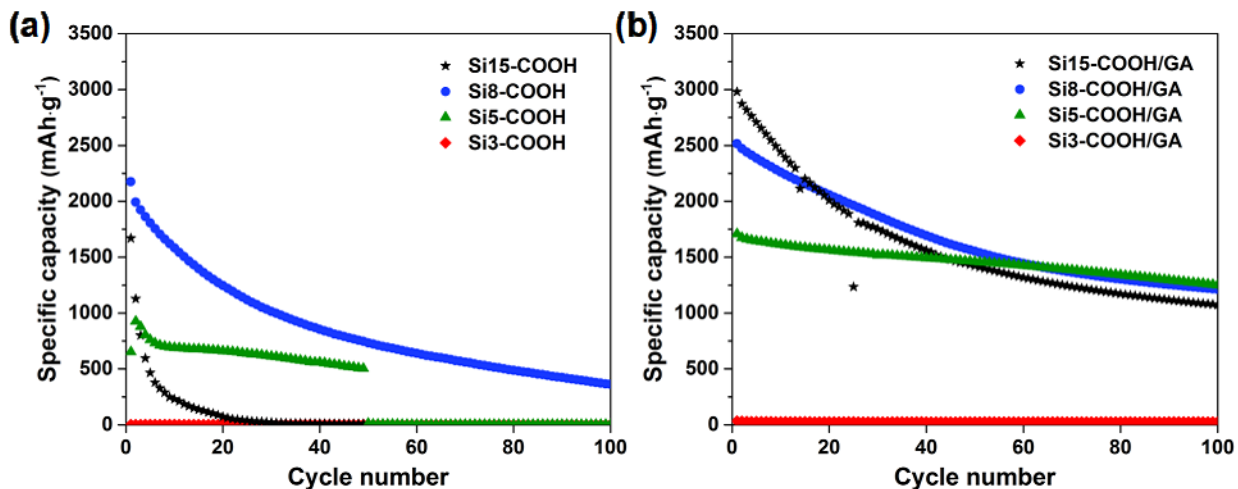


Figure 3-8. Cycling performance of a) undecanoic acid-functionalized SiNCs ($d \sim 3, 5, 8,$ and 15 nm) and b) their corresponding SiNC/graphene aerogel hybrids.

Contrary to the expectation that smaller SiNCs would provide improved electrochemical performance, neither Si3-COOH nor Si3-COOH/GA exhibit electrochemical response (Figure 3-8); this observation could be due to the large relative quantity of surface ligands on SiNCs, which leads to poor electrical conductivity and prevents Li diffusion. TGA data indicated that the functional groups decompose at $600\text{ }^{\circ}\text{C}$ under an argon atmosphere (Figure 3-7). Hence, the SiNC/GA hybrids were annealed at $600\text{ }^{\circ}\text{C}$ (3 h, Ar) to decompose the surface ligands and produce annealed SiNC/GA hybrids (i.e., Si3/GA, Si5/GA, Si8/GA, and Si15/GA). As a result, the cycling stability and specific capacity of the Si3/GA hybrid improved significantly, and a slight improvement was observed for 5, 8, and 15 nm annealed SiNC/GA hybrids (Figure 3-9a).

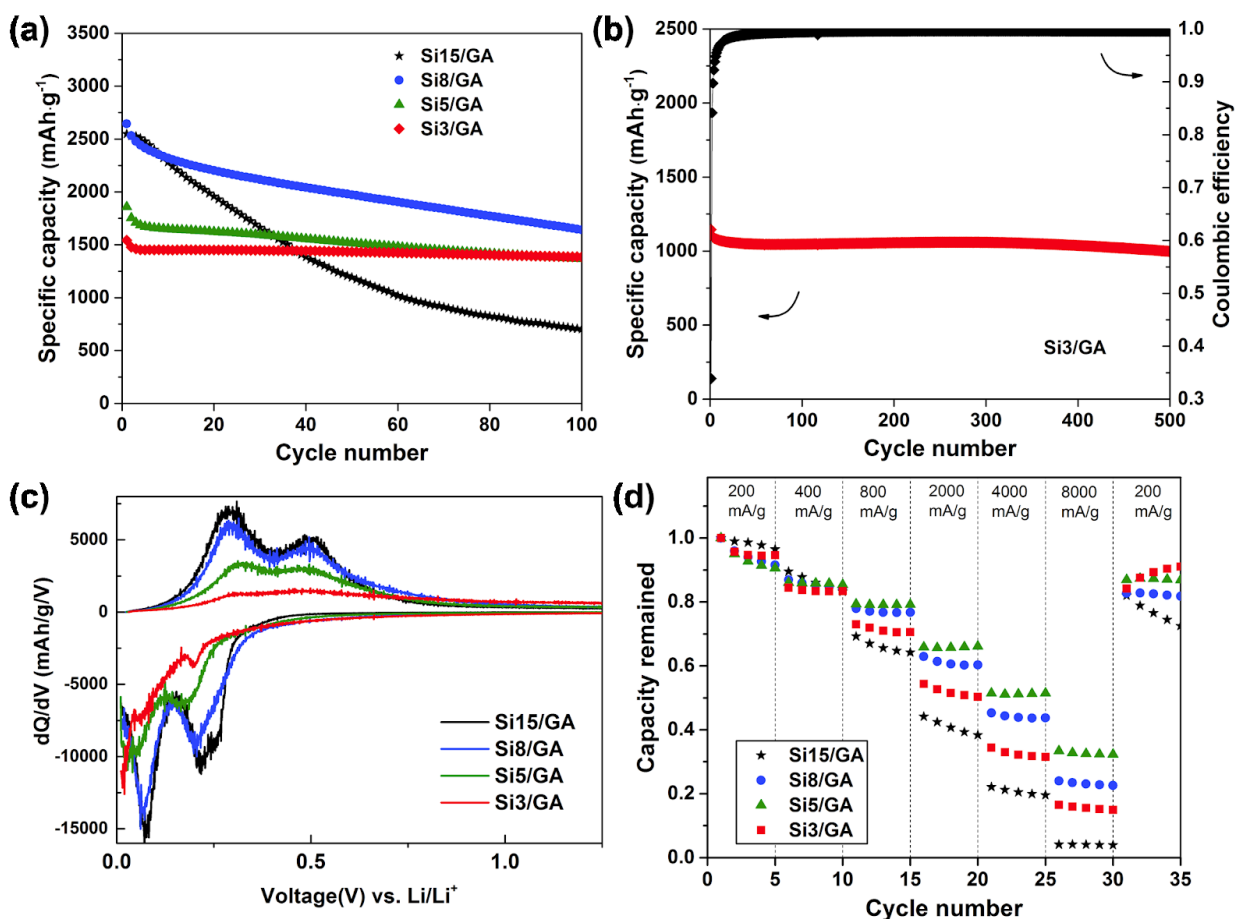


Figure 3-9. a) Cycling performance of annealed SiNC/GA hybrids at the current density of 200 mA/g, b) cycling performance and Coulombic efficiency of Si3/GA hybrid at the current density of 400 mA/g, c) differential capacity (dQ/dV) plots of annealed SiNC/GA hybrids at the second cycle, and d) capacity retention of annealed SiNC/GA hybrids at various rates ranging from 200 mA/g to 8000 mA/g.

The initial specific capacity of the 15 and 8 nm annealed SiNC/GA hybrids is ~2600 mAh/g at the current density of 200 mA/g, while the 5 and 3 nm SiNC/GA hybrids exhibit initial specific capacities of ~1900 and ~1500 mAh/g, respectively (Figure 3-9a). Also, as the size of SiNC decreased from 15 nm to 3 nm, the cycling stability improved, and Si3/GA exhibited no

detected capacity loss after 100 cycles; this is consistent with the original proposal of the size effect that decreasing the size of NCs could improve their cycling stability by shortening the Li diffusion distances and accommodating the volume changes of Si anodes.^{6,15} The prolonged cycling test of Si3/GA at a higher current density (400 mA/g) displayed a stable specific capacity of ~1100 mAh/g and capacity retention of over 90% after 500 cycles (Figure 3-9b). The initial Coulombic efficiency (CE) of Si3/GA was very low, which might be due to the initial SEI formation and Li trapping in the nanoporous structure of the graphene aerogel;²⁷ the CE increased rapidly to above 99% after a few cycles (Figure 3-9b).

The differential capacity (dQ/dV) plots of the annealed SiNC/GA hybrids at the second cycle in the voltage window of 0.01–2 V (vs. Li^+/Li) are shown in Figure 3-9c. Differential capacity plots were acquired during the lithiation and delithiation cycling and indicated two peaks at ~0.19 and 0.09 V in the lithiation branch and two peaks at ~0.35 and 0.5 V in the delithiation branch, which are characteristic of Si anodes.³⁹

The rate capability of the SiNC/GA hybrids were evaluated at the current densities ranging from 200 to 8000 mA/g. Figure 3-9d indicates capacity retention of the annealed SiNC/GA hybrids, which is the ratio of specific capacity at a higher current density to initial specific capacity at 200 mA/g. The Si3/GA hybrid retained ~50% and ~30% of its initial specific capacity (~1500 mAh/g) at higher current densities of 2000 and 4000 mA/g, respectively. Also, it retained ~90% of its initial specific capacity when the current density decreased to 200 mA/g after having been cycled at higher current densities, indicating a very good cycling stability for this hybrid material.

3.4 Conclusions

SiNC-based anode materials composed of hydrophilic SiNCs ($d \sim 3, 5, 8$ or 15 nm) and conductive graphene aerogels have been prepared by chemical reduction of a graphene oxide precursor followed by CO_2 supercritical drying. The resulting hybrid materials are mesoporous and provide nanoscale pores to accommodate the volume changes of nanoscale Si during the lithiation and delithiation cycling. Hence, the SiNC/GA hybrids show improved cycling stability and high specific capacity compared to the functionalized SiNCs. To further improve the electrical conductivity and electrochemical performance of these hybrid materials, the SiNC/GA hybrids were processed thermally to produce annealed SiNC/GA hybrids. The resulting Si3/GA hybrid indicated a stable specific capacity of ~ 1500 mAh/g after 100 cycles at the current density of 200 mA/g; this SiNC-based anode material also indicated a high specific capacity with minor capacity loss up to 500 cycles and could open the door to high-performance LIBs.

3.5 References

1. Bruce, P. G.; Scrosati, B.; Tarascon, J. M. Nanomaterials for Rechargeable Lithium Batteries. *Angew. Chemie - Int. Ed.* **2008**, *47* (16), 2930–2946.
2. Teki, R.; Krishnan, R.; Parker, T. C.; Lu, T. M.; Datta, M. K.; Kumta, P. N.; Koratkar, N. Nanostructured Silicon Anodes for Lithium Ion Rechargeable Batteries. *Small* **2009**, *5* (20), 2236–2242.
3. Kasavajjula, U.; Wang, C.; Appleby, A. J. Nano- and Bulk-Silicon-Based Insertion Anodes for Lithium-Ion Secondary Cells. *J. Power Sources* **2007**, *163* (2), 1003–1039.
4. Wu, H.; Cui, Y. Designing Nanostructured Si Anodes for High Energy Lithium Ion Batteries. *Nano Today* **2012**, *7* (5), 414–429.
5. Zamfir, M. R.; Nguyen, H. T.; Moyon, E.; Lee, Y. H.; Pribat, D. Silicon Nanowires for Li-Based Battery Anodes: A Review. *J. Mater. Chem. A* **2013**, *1* (34), 9566.
6. Su, X.; Wu, Q.; Li, J.; Xiao, X.; Lott, A.; Lu, W.; Sheldon, B. W.; Wu, J. Silicon-Based Nanomaterials for Lithium-Ion Batteries: A Review. *Adv. Energy Mater.* **2014**, *4*, 1300882.
7. Liu, X. H.; Zhong, L.; Huang, S.; Mao, S. X.; Zhu, T.; Huang, J. Y. Size-Dependent Fracture of Silicon Nanoparticles during Lithiation. *ACS Nano* **2012**, *6* (2), 1522–1531.
8. Chockla, A. M.; Harris, J. T.; Akhavan, V. A.; Bogart, T. D.; Holmberg, V. C.; Steinhagen, C.; Mullins, C. B.; Stevenson, K. J.; Korgel, B. A. Silicon Nanowire Fabric as a Lithium Ion Battery Electrode Material. *J. Am. Chem. Soc.* **2011**, *133* (51), 20914–20921.
9. Nguyen, H. T.; Yao, F.; Zamfir, M. R.; Biswas, C.; So, K. P.; Lee, Y. H.; Kim, S. M.; Cha, S. N.; Kim, J. M.; Pribat, D. Highly Interconnected Si Nanowires for Improved Stability Li-Ion Battery Anodes. *Adv. Energy Mater.* **2011**, *1* (6), 1154–1161.
10. Park, M.; Kim, M. G.; Joo, J.; Kim, K.; Kim, J.; Ahn, S.; Cui, Y.; Cho, J. Silicon Nanotube Battery Anodes. *Nano Lett.* **2009**, *9* (11), 3844–3847.
11. Wu, H.; Chan, G.; Choi, J. W.; Ryu, I.; Yao, Y.; McDowell, M. T.; Lee, S. W.; Jackson, A.; Yang, Y.; Hu, L.; et al. Stable Cycling of Double-Walled Silicon Nanotube Battery Anodes through Solid-Electrolyte Interphase Control. *Nat. Nanotechnol.* **2012**, *7* (5), 310–315.
12. Yao, Y.; McDowell, M. T.; Ryu, I.; Wu, H.; Liu, N.; Hu, L.; Nix, W. D.; Cui, Y. Interconnected Silicon Hollow Nanospheres for Lithium-Ion Battery Anodes with Long Cycle Life. *Nano Lett.* **2011**, *11* (7), 2949–2954.

13. Zhao, Y.; Liu, X.; Li, H.; Zhai, T.; Zhou, H. Hierarchical Micro/nano Porous Silicon Li-Ion Battery Anodes. *Chem. Commun.* **2012**, 48 (42), 5079.
14. Zhu, J.; Gladden, C.; Liu, N.; Cui, Y.; Zhang, X. Nanoporous Silicon Networks as Anodes for Lithium Ion Batteries. *Phys. Chem. Chem. Phys.* **2013**, 15 (2), 440–443.
15. Szczech, J. R.; Jin, S. Nanostructured Silicon for High Capacity Lithium Battery Anodes. *Energy Environ. Sci.* **2011**, 4 (1), 56–72.
16. Wang, B.; Li, X.; Zhang, X.; Luo, B.; Jin, M.; Liang, M.; Dayeh, S. A.; Picraux, S. T.; Zhi, L. Adaptable Silicon-Carbon Nanocables Sandwiched between Reduced Graphene Oxide Sheets as Lithium Ion Battery Anodes. *ACS Nano* **2013**, 7 (2), 1437–1445.
17. Liu, N.; Lu, Z.; Zhao, J.; McDowell, M. T.; Lee, H. W.; Zhao, W.; Cui, Y. A Pomegranate-Inspired Nanoscale Design for Large-Volume-Change Lithium Battery Anodes. *Nat. Nanotechnol.* **2014**, 9 (3), 187–192.
18. Chang, J.; Huang, X.; Zhou, G.; Cui, S.; Hallac, P. B.; Jiang, J.; Hurley, P. T.; Chen, J. Multilayered Si Nanoparticle/reduced Graphene Oxide Hybrid as a High-Performance Lithium-Ion Battery Anode. *Adv. Mater.* **2014**, 26 (5), 758–764.
19. Lu, Z.; Liu, N.; Lee, H. W.; Zhao, J.; Li, W.; Li, Y.; Cui, Y. Nonfilling Carbon Coating of Porous Silicon Micrometer-Sized Particles for High-Performance Lithium Battery Anodes. *ACS Nano* **2015**, 9 (3), 2540–2547.
20. Xu, Q.; Li, J. Y.; Sun, J. K.; Yin, Y. X.; Wan, L. J.; Guo, Y. G. Watermelon-Inspired Si/C Microspheres with Hierarchical Buffer Structures for Densely Compacted Lithium-Ion Battery Anodes. *Adv. Energy Mater.* **2017**, 7 (3), 1–6.
21. Chen, S.; Shen, L.; van Aken, P. A.; Maier, J.; Yu, Y. Dual-Functionalized Double Carbon Shells Coated Silicon Nanoparticles for High Performance Lithium-Ion Batteries. *Adv. Mater.* **2017**, 29 (21).
22. Gorgolis, G.; Galiotis, C. Graphene Aerogels: A Review. *2D Mater.* **2017**, 4 (3).
23. Ma, Y.; Chen, Y. Three-Dimensional Graphene Networks: Synthesis, Properties and Applications. *Natl. Sci. Rev.* **2015**, 2 (1), 40–53.
24. Chen, W.; Yan, L. In Situ Self-Assembly of Mild Chemical Reduction Graphene for Three-Dimensional Architectures. *Nanoscale* **2011**, 3 (8), 3132.
25. Zhang, X.; Sui, Z.; Xu, B.; Yue, S.; Luo, Y.; Zhan, W.; Liu, B. Mechanically Strong and

- Highly Conductive Graphene Aerogel and Its Use as Electrodes for Electrochemical Power Sources. *J. Mater. Chem.* **2011**, *21* (18), 6494.
26. Xu, B.; Wu, H.; Lin, C. X.; Wang, B.; Zhang, Z.; Zhao, X. S. Stabilization of Silicon Nanoparticles in Graphene Aerogel Framework for Lithium Ion Storage. *RSC Adv.* **2015**, *5* (39), 30624–30630.
27. Hu, X.; Jin, Y.; Zhu, B.; Tan, Y.; Zhang, S.; Zong, L.; Lu, Z.; Zhu, J. Free-Standing Graphene-Encapsulated Silicon Nanoparticle Aerogel as an Anode for Lithium Ion Batteries. *ChemNanoMat* **2016**, *2* (7), 671–674.
28. Hessel, C. M.; Henderson, E. J.; Veinot, J. G. C. Hydrogen Silsesquioxane: A Molecular Precursor for Nanocrystalline Si-SiO₂ Composites and Freestanding Hydride-Surface-Terminated Silicon Nanoparticles. *Chem. Mater.* **2006**, *18* (26), 6139–6146.
29. Clark, R. J.; Aghajamali, M.; Gonzalez, C. M.; Hadidi, L.; Islam, M. A.; Javadi, M.; Mobarak, M. H.; Purkait, T. K.; Robidillo, C. J. T.; Sinelnikov, R.; et al. From Hydrogen Silsesquioxane to Functionalized Silicon Nanocrystals. *Chem. Mater.* **2016**, *29* (1), 80–89.
30. Yang, Z.; Gonzalez, C. M.; Purkait, T. K.; Iqbal, M.; Meldrum, A.; Veinot, J. G. C. Radical Initiated Hydrosilylation on Silicon Nanocrystal Surfaces: An Evaluation of Functional Group Tolerance and Mechanistic Study. *Langmuir* **2015**, *31* (38), 10540–10548.
31. Marcano, D. C.; Kosynkin, D. V.; Berlin, J. M.; Sinitskii, A.; Sun, Z. Z.; Slesarev, A.; Alemany, L. B.; Lu, W.; Tour, J. M. Improved Synthesis of Graphene Oxide. *ACS Nano* **2010**, *4* (8), 4806–4814.
32. Thomas, H. R.; Day, S. P.; Woodruff, W. E.; Vallés, C.; Young, R. J.; Kinloch, I. A.; Morley, G. W.; Hanna, J. V.; Wilson, N. R.; Rourke, J. P. Deoxygenation of Graphene Oxide: Reduction or Cleaning? *Chem. Mater.* **2013**, *25* (18), 3580–3588.
33. Clark, R. J.; Dang, M. K. M.; Veinot, J. G. C. Exploration of Organic Acid Chain Length on Water-Soluble Silicon Quantum Dot Surfaces. *Langmuir* **2010**, *26* (19), 15657–15664.
34. Fan, X.; Peng, W.; Li, Y.; Li, X.; Wang, S.; Zhang, G.; Zhang, F. Deoxygenation of Exfoliated Graphite Oxide under Alkaline Conditions: A Green Route to Graphene Preparation. *Adv. Mater.* **2008**, *20* (23), 4490–4493.
35. Henderson, E. J.; Kelly, J. A.; Veinot, J. G. C. Influence of HSiO_{1.5} Sol–Gel Polymer Structure and Composition on the Size and Luminescent Properties of Silicon Nanocrystals.

- Chem. Mater.* **2009**, *21* (22), 5426–5434.
36. Zhang, X.; Sui, Z.; Xu, B.; Yue, S.; Luo, Y.; Zhan, W.; Liu, B. Mechanically Strong and Highly Conductive Graphene Aerogel and Its Use as Electrodes for Electrochemical Power Sources. *J. Mater. Chem.* **2011**, *21* (18), 6494.
37. Wang, J. Z.; Zhong, C.; Chou, S. L.; Liu, H. K. Flexible Free-Standing Graphene-Silicon Composite Film for Lithium-Ion Batteries. *Electrochem. commun.* **2010**, *12* (11), 1467–1470.
38. Kruk, M.; Jaroniec, M. Gas Adsorption Characterization of Ordered Organic - Inorganic Nanocomposite Materials. *Chem. Mater.* **2001**, *13*, 3169–3183.
39. Li, C.; Shi, T.; Yoshitake, H.; Wang, H. Improved Performance in Micron-Sized Silicon Anodes by in Situ Polymerization of Acrylic Acid-Based Slurry. *J. Mater. Chem. A* **2016**, *4* (43), 16982–16991.

Chapter 4:

**Water-Assisted Transfer Patterning of
Nanomaterials**

4.1 Introduction

Patterned transfer of nanomaterials (NMs) onto solid substrates is of great importance in the development of large-scale functional devices (e.g., displays, sensor arrays, etc.).^{1,2} Despite impressive advances,³⁻¹⁵ there is no single approach that allows NM patterning on all substrates, and every method brings with it process-specific challenges/limitations. Of the many methods available for patterning NMs, Transfer Printing (TP) and PMMA-Mediated Transfer (PMT) are the ones most widely employed.^{3,4,7,9,10,14} TP utilizes a structured elastomeric poly (dimethylsiloxane) (PDMS) stamp to achieve NM patterning; while effective, it can be complicated by the necessity to control the adhesion forces at the many interfaces involved.³ PMT uses a thin poly (methyl methacrylate) (PMMA) film to transfer NM patterns; unfortunately, high temperatures (e.g., 300 °C) are required when peeling the PMMA film from the source substrate and removing the PMMA residues from the target substrate.⁴

In this Chapter, a straightforward and cost-effective water-assisted method for NM transfer is reported. It is inspired by water transfer printing that is commonly used to transfer decorative patterns on three-dimensional objects.¹⁶ Water-assisted transfer patterning of nanomaterials uses an inexpensive water-soluble polymer film (e.g., poly (vinyl alcohol) (PVA)) as a sacrificial NM pattern carrier. This film is floated on the water surface where it dissolves leaving an intact NM pattern. The floating NM pattern is transferred subsequently to diverse planar and non-planar substrates.

4.2 Experimental

4.2.1 Reagents and Materials

All reagents were used as received unless otherwise indicated. Gold(III) chloride trihydrate (ACS reagent, $\geq 49.0\%$), tetraoctylammonium bromide (98%), 1-dodecanethiol (purum, $\geq 97.0\%$ (GC)), poly (vinyl alcohol) ($M_w \sim 13,000\text{--}23,000$, 98% hydrolyzed), toluene (reagent grade), and ethanol (reagent grade) were obtained from Sigma-Aldrich. Sodium borohydride (99%) and diethyl succinate (99%) were purchased from Fluka and Anachemia, respectively.

4.2.2 Fabrication of Line-Patterned Silicon Substrates (Microplates)

Line-patterned silicon substrates (2×2 cm) displaying different micron-sized widths (W) and pitches (P) were fabricated at the UofA nanoFAB facilities. Briefly, a p-type silicon wafer ($d \sim 150$ mm) was cleaned in piranha etchant (3:1 $\text{H}_2\text{SO}_4\text{:H}_2\text{O}_2$) for 15 min. The pattern was designed and written onto a photoresist using direct-write laser lithography (Heidelberg DWL-200) following hexamethyldisilazane (HMDS) vapor prime and spin-coating of a positive-tone photoresist (~ 1.2 μm Fujifilm HPR 504). The pattern was etched to a depth of ~ 30 μm using a high-rate Bosch process (Oxford Instruments PlasmaPro 100 Estrelas). The photoresist was removed using oxygen plasma, and the dies were singulated using a dicing saw (Disco DAD 321). The details for microplate fabrication were provided by the UofA nanoFAB staff.

4.2.3 Synthesis and Functionalization of Nanomaterials

Synthesis of dodecyl-functionalized SiNCs ($d \sim 3$ nm). Dodecyl-functionalized silicon nanocrystals (SiNCs) were synthesized using an established literature procedure for thermal hydrosilylation.^{17,18} The detailed procedures of SiNC/ SiO_2 composite synthesis, SiNC liberation, and 3 nm dodecyl-functionalized SiNC synthesis can be found in Chapter 2.

Synthesis of dodecanethiol-capped AuNPs ($d \sim 3$ nm). A detailed procedure for gold nanoparticle (AuNP) synthesis can be found elsewhere.¹⁹ Briefly, an aqueous solution of gold(III) chloride trihydrate (0.03 M, 10.0 mL) and a solution of tetraoctylammonium bromide in toluene (0.05 M, 26.6 mL) were mixed in a beaker and stirred vigorously for 5 min. The tetrachloroaurate was transferred into toluene, and the hydrophobic layer was separated using a separatory funnel. Subsequently, 1-dodecanethiol (67 μ L) and a freshly prepared aqueous solution of sodium borohydride (0.40 M, 8.3 mL) were added to the hydrophobic layer, sequentially, and the mixture was stirred vigorously for 3 h. The resulting dark brown hydrophobic layer was separated using a separatory funnel and mixed with 400 mL ethanol to remove excess thiol. The mixture was stored in a refrigerator (~ 4 °C) overnight, and the precipitate was collected by centrifugation (3000 rpm, 5 min). The dark brown NPs were purified using toluene/ethanol as the solvent/antisolvent mixture and separated by centrifugation (12000 rpm, 25 min). Dodecanethiol-capped AuNPs were dissolved in toluene and filtered through a 0.45- μ m PTFE syringe filter.

4.2.4 Water-Assisted Transfer Patterning (WTP) of Nanomaterials

WTP of dodecyl-functionalized SiNCs ($d \sim 3$ nm). A solution of SiNCs in toluene (~ 10 mg/mL, 10 μ L) was drop-coated onto a pattern area (1 \times 1.5 cm) of a commercially available stainless steel plate (Konad M Series, M57). The patterned plate was placed in a Petri dish (Fisherbrand®, 60 \times 15 mm). A PVA solution (0.1 g/mL, 3 mL) was added onto the plate to cover the entire area uniformly, and the solution was dried overnight to form a uniform PVA film (thickness ~ 40 – 50 μ m). The PVA film patterned with SiNCs was peeled from the stainless steel plate and immediately framed with Scotch® Tape with the patterned side facing upwards. Then,

the SiNC pattern was transferred from the PVA film onto a non-planar quartz substrate, as illustrated in Figure 4-1. The stainless steel plate was cleaned using toluene, acetone, and water, sequentially, to remove the remaining amounts of SiNCs and PVA.

WTP of dodecanethiol-capped AuNPs ($d \sim 3$ nm). A solution of AuNPs in toluene (~ 5 , 10, or 20 mg/mL, 50 μ L) was drop-coated or spin-coated (500, 1000, or 2000 rpm, 1 min) onto a line-patterned silicon microplate (2 \times 2 cm). The microplate was placed in a Petri dish (Fisherbrand®, 60 \times 15 mm) and a PVA film (thickness ~ 40 –50 μ m) was formed on the microplate, as described for SiNC patterning. Next, the AuNP pattern was transferred from the PVA film onto an aluminum stub, as illustrated in Figure 4-1a. The microplate was cleaned using toluene, acetone, and water, sequentially, to remove the remaining amounts of AuNPs and PVA.

4.2.5 Material Characterization

X-ray photoelectron spectroscopy (XPS) measurements were performed on a Kratos Axis Ultra instrument operating in energy spectrum mode at 210 W. Samples were prepared by drop-casting toluene solutions of nanomaterials onto a copper foil substrate. The base pressure and operating chamber pressure were maintained at 10^{-7} Pa. A monochromatic Al K α source ($\lambda = 8.34$ Å) was used to irradiate the samples, and the spectra were obtained with an electron takeoff angle of 90°. CasaXPS software (VAMAS) was used to interpret spectra. All the spectra were internally calibrated to the C 1s emission (284.8 eV). After calibration, the background was subtracted using a Shirley-type background to remove most of the extrinsic loss structure.

The photoluminescence (PL) spectrum of functionalized SiNCs was recorded by exciting the toluene solution of SiNCs with a 405 nm LED light source equipped with a 500 nm long pass

interference filter. The emitted photons were collected using an optic fiber connected to an Ocean Optics USB2000 spectrometer that was normalized by a black body radiator.

Transmission electron microscopy (TEM) images were obtained using a JEOL-2010 electron microscope equipped with a LaB₆ filament and operated at an accelerating voltage of 200 kV. The TEM samples were prepared by drop-coating dilute toluene solutions of nanomaterials onto a holey carbon coated copper grid. Particle size distribution was calculated by counting at least 300 particles using ImageJ software (1.48v).

Scanning electron microscopy (SEM) images were acquired using a Zeiss Sigma 300 VP-FESEM equipped with a backscattered electron detector and a Bruker energy dispersive X-ray (EDX) spectroscopy system operated at 10 kV. To prepare SEM samples of patterned target substrates, AuNPs were transferred directly onto aluminum stubs. For patterned PVA films, the film was adhered to a double-sided carbon tape attached onto an aluminum stub with the pattern side facing up. The conductive carbon coatings were deposited on all samples using a Leica EM SCD005 evaporative carbon coater prior to SEM characterization. The thickness of PVA films was measured using a digital micrometer (Mitutoyo, 0.001 mm).

4.3 Results and Discussion

The general procedure for WTP of nanomaterials is illustrated in Figure 4-1a, and Figure 4-1b shows the stages of the process for silicon nanocrystals: A PVA film (thickness $\sim 40\text{--}50\ \mu\text{m}$) is formed on a pattern of hydrophobic nanomaterials (e.g., SiNCs) predeposited on a freshly cleaned, patterned source substrate (e.g., stainless steel) (Figure 4-1a, i); the film is peeled from the source substrate, intact, bearing the patterned NMs, and immediately framed with standard Scotch® Tape (Figure 4-1a, ii); the PVA film is attached to a transfer vessel partially filled with warm water (ca. $30\ \text{°C}$) with the NM pattern side facing up (Figure 4-1a, iii); more warm water is added slowly to bring the water surface into contact with the bottom of the PVA film (Figure 4-1a, iv) – this facilitates PVA dissolution and formation of a stable floating NM pattern at the water/air interface; finally, a target substrate is immersed into the water to capture the pattern (Figure 4-1a, v).

Silicon nanocrystals are a sub-class of heavy-metal-free quantum dots (QDs) whose optical response may be tuned through the variations of NC size and surface chemistry.^{20,21} Producing QD patterns is of particular importance if they are to find applications in light-emitting diodes and full-color displays.^{22–24} For the present study, we chose to employ hydrophobic dodecyl-functionalized SiNCs ($d \sim 3\ \text{nm}$) synthesized following well-established procedures developed in the Veinot laboratory^{17,18} as the first test case (for material characterization see Chapter 2). These NCs are appealing for this study because they show strong visible red photoluminescence (PL) (Figure 4-2) that allows for straightforward tracking throughout the WTP process using a standard UV lamp ($\lambda \sim 350\ \text{nm}$), as shown in Figure 4-1b. In addition, the established susceptibility of SiNCs to water oxidation highlights the versatility of this process.^{25,26}

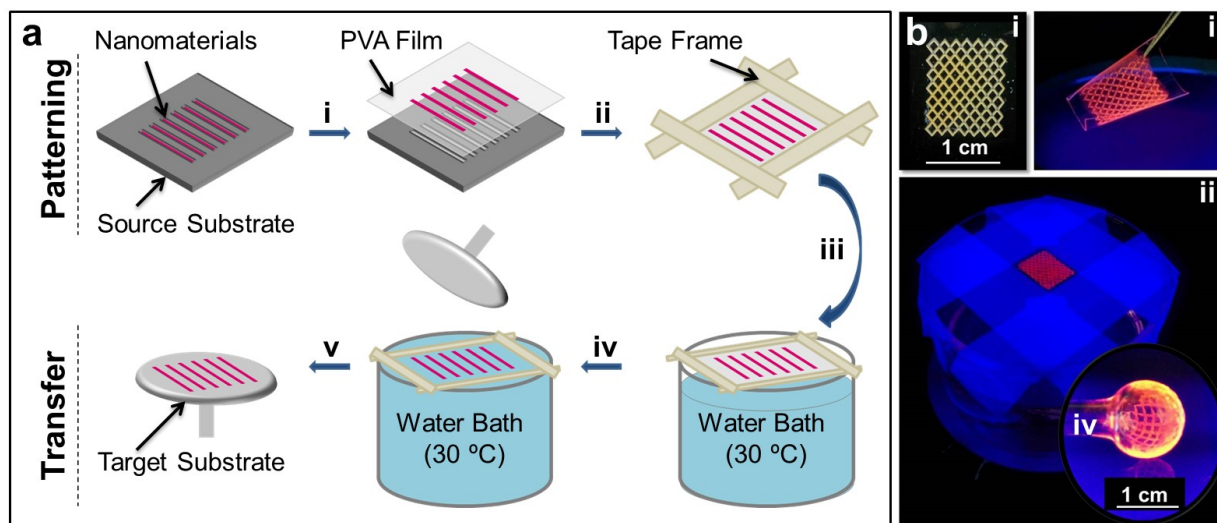


Figure 4-1. (a) An illustration of WTP of nanomaterials: (i) A poly (vinyl alcohol) film is formed on a substrate bearing a preformed nanomaterial pattern. (ii) The patterned film is peeled from the source substrate and framed with tape. (iii) The tape-framed film is attached to a transfer vessel partially filled with water. (iv) The water level is raised to expose the film to water and dissolve it. (v) A target substrate is immersed into the water to transfer the pattern. (b) WTP of dodecyl-functionalized SiNCs ($d \sim 3$ nm). Photographs of (i) SiNCs deposited on a commercial patterned stainless steel substrate under ambient light. (ii) A PVA film patterned with SiNCs under UV light. (iii) A tape-framed PVA film bearing a SiNC pattern attached to a transfer vessel under UV light. (iv) A non-planar quartz substrate patterned with photoluminescent SiNCs under UV light.

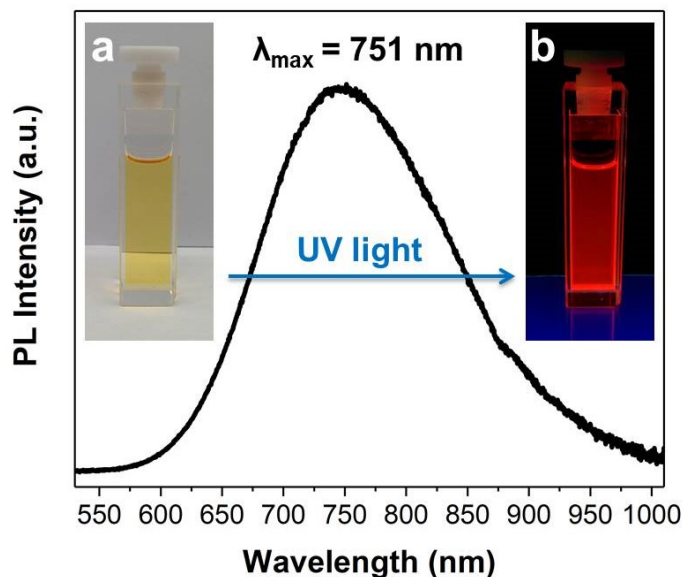


Figure 4-2. PL spectrum of a toluene solution containing dodecyl-functionalized SiNCs ($d \sim 3$ nm) upon excitation at 405 nm. The insets show a SiNC solution (a) before and (b) after exposure to UV light ($\lambda \sim 350$ nm).

While the PL response of SiNCs provides a rapid screening of the WTP process, additional characterization of SiNC patterns using standard methods (i.e., SEM) is challenging because the low atomic number (Z) of Si leads to a low Z -contrast in scanning electron microscopy. In this context, to further explore the scope of WTP process, we turned our attention to hydrophobic gold nanoparticles (AuNPs). Dodecanethiol-capped AuNPs ($d \sim 3$ nm) were synthesized according to the well-established Brust method.¹⁹ High-resolution X-ray photoelectron (HRXP) spectra of Au 4f region and S 2p region of dodecanethiol-capped AuNPs are shown in Figures 4-3a and 4-3b, respectively. The HRXP spectrum of the Au 4f region indicates the Au 4f_{7/2} and Au 4f_{5/2} doublet with binding energies of 83.8 and 87.5 eV, respectively, characteristic of Au(0) (Figure 4-3a). The HRXP spectrum of the S 2p region shows the S 2p_{3/2} and S 2p_{1/2} doublet with

binding energies of 162.0 and 163.2 eV, respectively, as expected for a monolayer of thiolates on gold (Figure 4-3b).²⁷ The bright-field TEM image and size distribution of hydrophobic AuNPs show average sizes of 3.0 ± 1.0 for these NPs (Figures 4-3c and 4-3d).

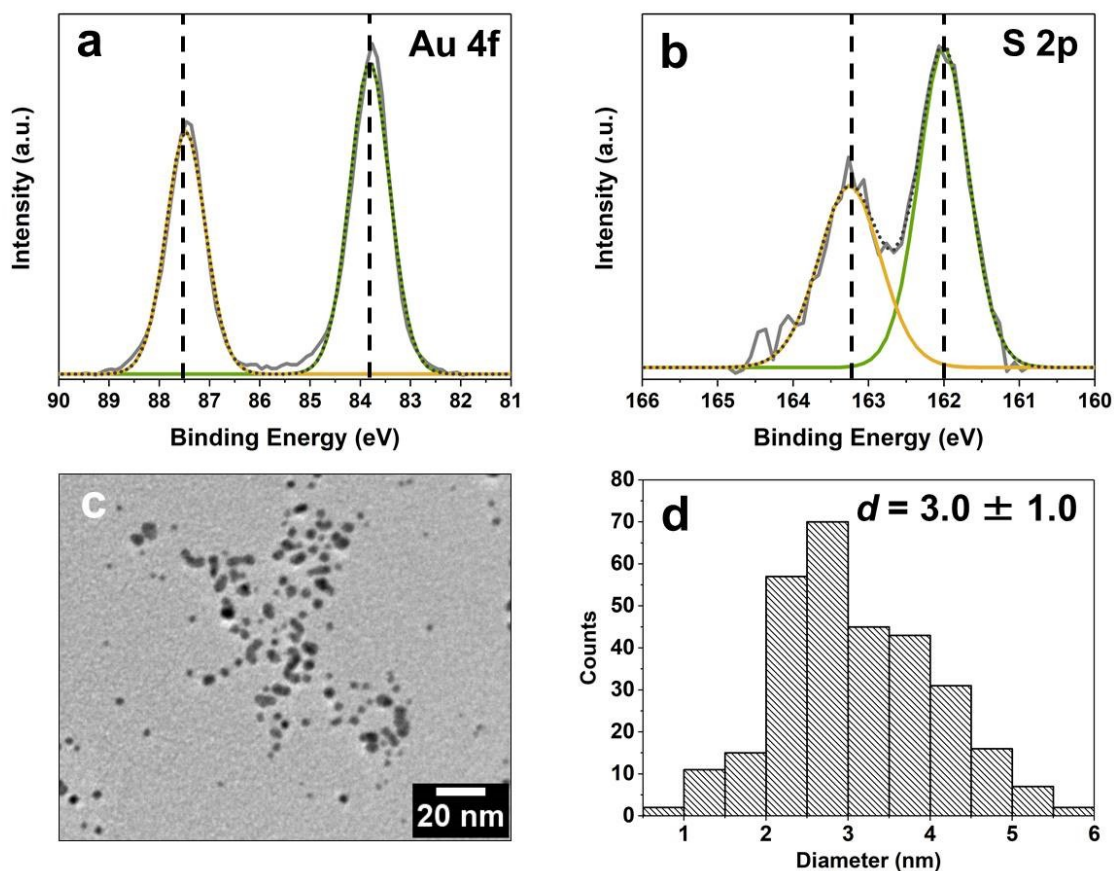


Figure 4-3. Characterization of dodecanethiol-capped AuNPs (a) HRXP spectrum of Au 4f region, (b) HRXP spectrum of S 2p region, (c) bright-field TEM image, and (d) size distribution.

Gold nanoparticles were patterned using a series of silicon substrates (i.e., microplates) bearing micron-scale line patterns (i.e., widths ($W2\mu$)-itches ($P50\mu$); Table 4-1) that were designed to give insight into WTP fidelity (Figure 4-4). Depositing AuNPs on patterned silicon substrates required optimization. Although AuNPs assembled in the troughs of microplates due

to the capillary effect, drop-coating resulted in non-uniform deposition; hence, spin-coating was explored. AuNPs were spin-coated onto the W10 μ -P100 μ microplate at 500, 1000, and 2000 rpm, and the patterns were transferred to PVA films. Figure 4-5 shows backscattered electron (BSE) images of the PVA films (FW10 μ -P100 μ) with bright AuNP patterns acquired using a scanning electron microscope equipped with a backscattered electron detector. The most well-defined pattern was obtained when AuNPs were spin-coated at 500 rpm (Figure 4-5a). Interestingly, under these conditions the AuNPs deposited on the area between the troughs rather than in the features (Figure 4-5), which produced a negative image of the original line pattern. This might be due to the immediate evaporation of the solvent (i.e., toluene) from the microplate, which does not give enough time for NPs to deposit in the troughs.

Table 4-1. Widths (W) and pitches (P) of line-patterned silicon substrates (microplates).

W (μ m)	2	10	50	100	200
P (μ m)	50	100	200	400	600

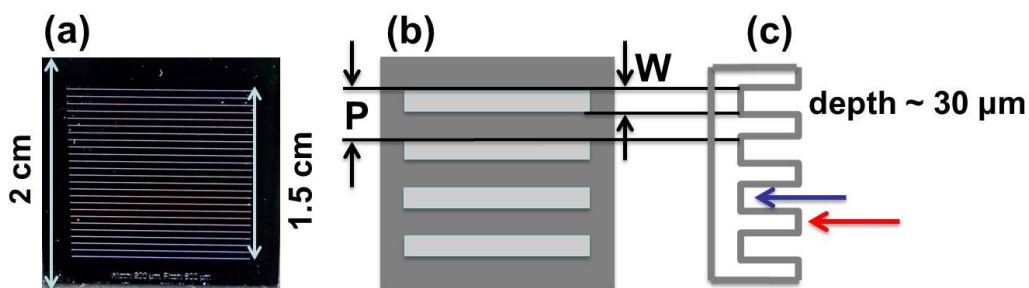


Figure 4-4. (a) Photograph of a 2 \times 2 cm line-patterned silicon substrate (i.e., W200 μ -P600 μ). (b,c) Schematic representation of a microplate defining width (W) and pitch (P); (b) top view and (c) cross-sectional view (blue arrow for when NPs deposit in the troughs and red arrow for when they are on the area between the troughs).

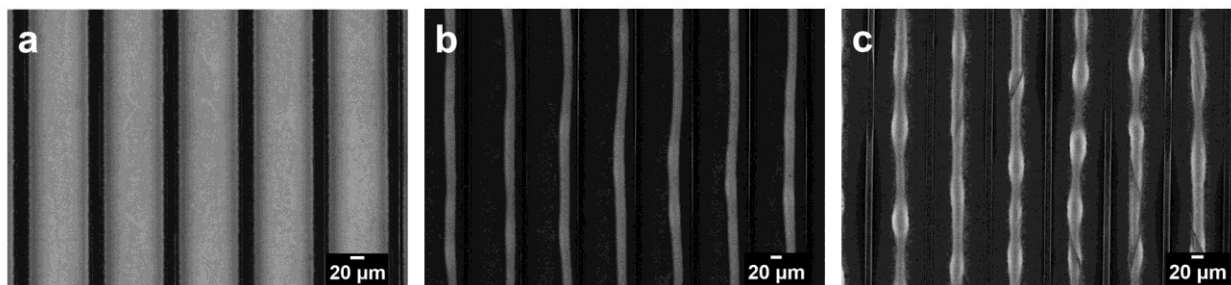


Figure 4-5. BSE images of AuNPs on PVA films (FW10 μ -P100 μ) obtained from AuNP depositions at (a) 500, (b) 1000, and (c) 2000 rpm. The brighter areas correspond to AuNPs.

Having established that spin-coating provides uniform deposition, AuNPs were deposited onto the W2 μ -P50 μ microplate at 500 rpm, a PVA film was formed, and the pattern was transferred to an aluminum substrate (Figure 4-6). The target pattern formed; however, most NPs stuck to the microplate and did not transfer to the PVA film. To address this issue, a hydrophobic plasticizer (e.g., diethyl succinate (DES)) was added to the AuNP solution. The hydrophobic plasticizer is a liquid with low volatility that sticks to NPs after evaporation of the solvent (i.e., toluene) and softens the pattern. Therefore, it can facilitate NP transfer from the microplate to the PVA carrier and improve the pattern intactness after the dissolution of the PVA film.

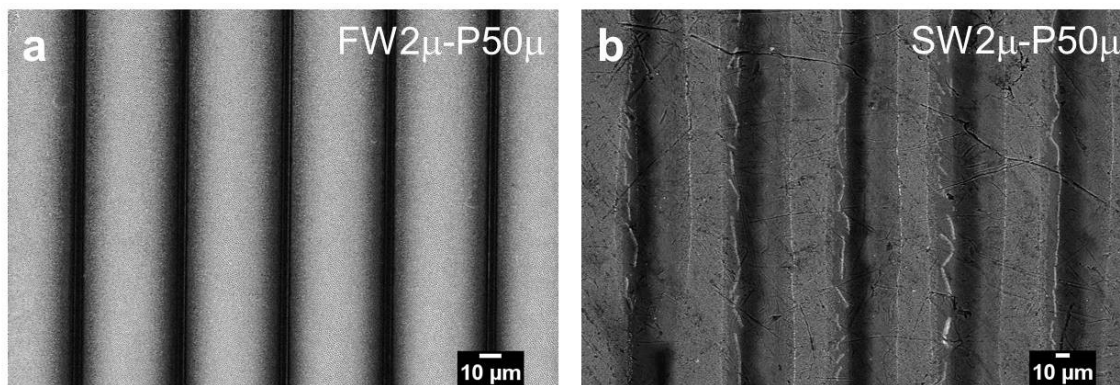


Figure 4-6. BSE images of AuNPs on (a) PVA film (FW2 μ -P50 μ) and (b) aluminum substrate (SW2 μ -P50 μ). The brighter areas correspond to AuNPs.

To explore the effect of plasticizer addition, AuNP suspensions of predefined concentrations (i.e., 5, 10, and 20 mg/mL) containing a known concentration of DES (0.6 M) were spin-coated onto the W10 μ -P100 μ microplate at 500 rpm, transferred to PVA films (FW10 μ -P100 μ), and evaluated with BSE imaging (Figure 4-7). Under these conditions, AuNPs deposit in the microplate troughs and, after transfer to the PVA film, provide a replica of the original W10 μ -P100 μ pattern. Also, an optimum concentration of 10 mg/mL is observed for AuNPs, enough to fully fill the microplate troughs without forming any unwanted features (Figure 4-7b). It is noteworthy that there is no need to add a hydrophobic plasticizer to dodecyl-functionalized SiNCs ($d \sim 3$ nm) prepared using thermal hydrosilylation. It is reasonable to attribute this difference in behavior with that of AuNPs to the presence of surface bonded oligomers on SiNCs that can retain some toluene after initial deposition on the microplates.²⁸ This residual toluene could take on the role of a plasticizer.

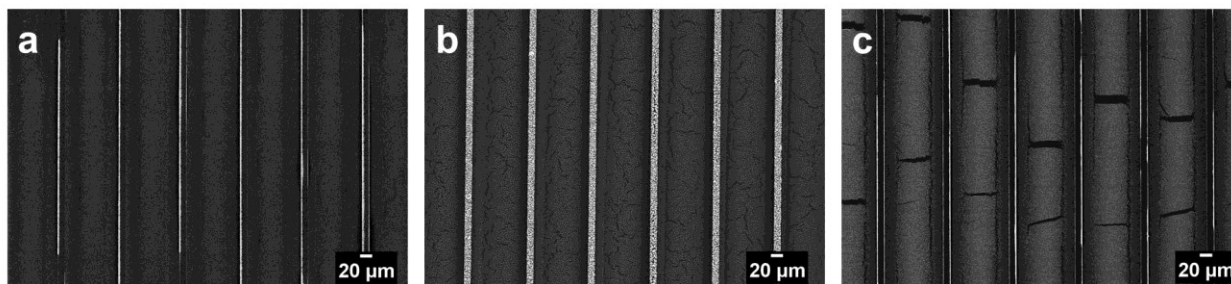


Figure 4-7. BSE images of AuNPs on PVA films (FW10 μ -100 μ) obtained from AuNP suspensions of concentrations (a) 5, (b) 10, and (c) 20 mg/mL containing 0.6 M diethyl succinate. The brighter areas correspond to AuNPs.

Having identified the optimum patterning conditions, a 10 mg/mL AuNP solution containing DES (0.6 M) was spin-coated onto a series of microplates (i.e., W2 μ -P50 μ), transferred onto PVA films (i.e., FW2 μ -P50 μ), and finally transferred onto aluminum substrates (i.e., SW2 μ -

P50 μ). BSE images of the patterns on PVA films (Figure 4-8a) and corresponding WTP patterns on aluminum substrates (Figure 4-8b) show assemblies of AuNPs as bright features. Mapping (Figure 4-8c) and line scans (Figure 4-8d) of AuNPs on aluminum substrates acquired using a scanning electron microscope equipped with an energy dispersive X-ray (EDX) spectroscopy further confirms the presence of AuNPs.

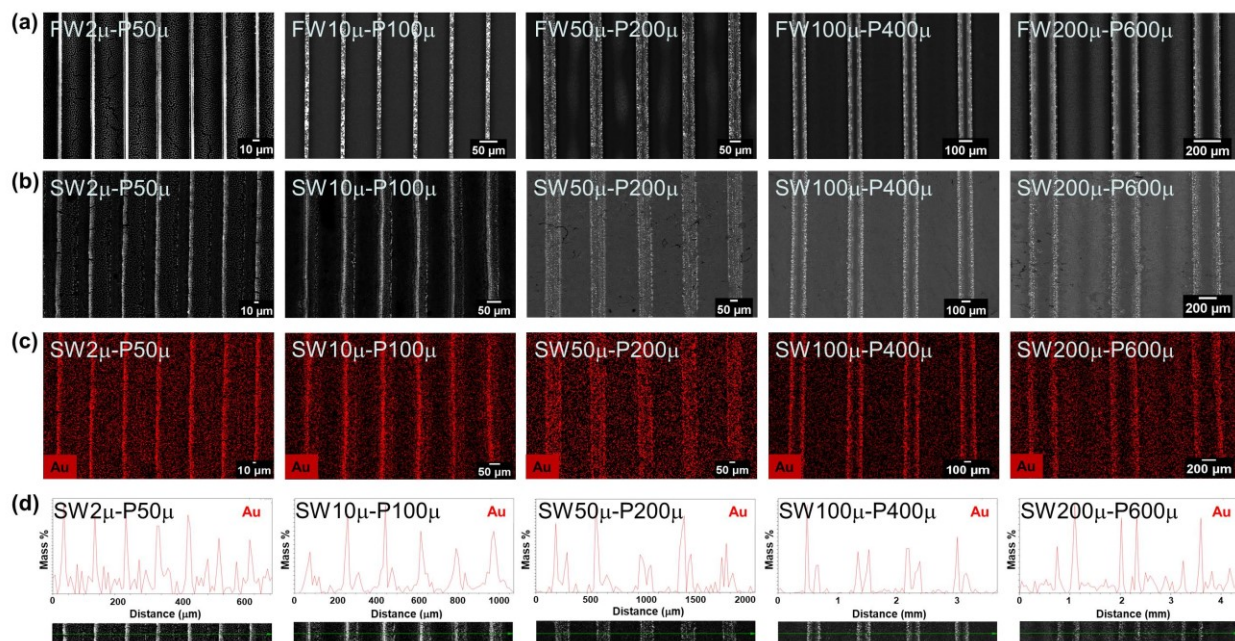


Figure 4-8. (a) BSE images of AuNPs on PVA films, (b) BSE images of AuNPs on aluminum substrates, (c) EDX mapping of AuNPs on aluminum substrates, and (d) EDX line scans of AuNPs on aluminum substrates.

Figure 4-8a shows the transfer of AuNPs onto PVA films. For microplates with widths less than or equal to 50 μ m, NPs fill the troughs, while for microplates with widths greater than 50 μ m, NPs deposit in the edges of the troughs (Figure 4-8a). NPs prefer to deposit in the edges of the troughs due to capillary forces, and as the width of the microplates decreases they fill the troughs. Figures 4-8b and 4-8c show that the patterns deposited on the PVA films are effectively

transferred via WTP to aluminum substrates. High quality transfer is obtained for all patterns as NP patterns on PVA films reproduced on the aluminum substrates; however, some minor variations are noted when feature widths are less than 10 μm . It is reasonable that these variations result from movement of the water surface and could be improved with better isolation from vibration and air currents. In addition, a comparison of Figures 4-8a and 4-8b indicates that a slight expansion in NP patterns occurs as a result of water transfer; this is more evident in small features. We propose that this expansion of the pattern relates to PVA film dissolution, which involves shrinking and expansion of the PVA film and may be addressed through application of more advanced polymers.

4.4 Conclusions

In summary, water-assisted transfer patterning of nanomaterials provides a straightforward and cost-effective approach for transfer of nanomaterial patterns onto a variety of substrates including non-planar surfaces. We believe that this method can be extended to other hydrophobic nanostructures (e.g., quantum dots, metallic nanoparticles, carbon nanotubes, and graphene) and irregular shape substrates (e.g., optical fibers, microspheres) and could open the door to a variety of new applications (e.g., flexible sensor arrays, curved displays, and optoelectronic structures).

4.5 References

1. Carlson, A.; Bowen, A. M.; Huang, Y.; Nuzzo, R. G.; Rogers, J. A. Transfer Printing Techniques for Materials Assembly and Micro/nanodevice Fabrication. *Adv. Mater.* **2012**, *24* (39), 5284–5318.
2. Choi, S.; Lee, H.; Ghaffari, R.; Hyeon, T.; Kim, D. H. Recent Advances in Flexible and Stretchable Bio-Electronic Devices Integrated with Nanomaterials. *Adv. Mater.* **2016**, *28* (22), 4203–4218.
3. Meitl, M. A.; Zhu, Z.-T.; Kumar, V.; Lee, K. J.; Feng, X.; Huang, Y. Y.; Adesida, I.; Nuzzo, R. G.; Rogers, J. A. Transfer Printing by Kinetic Control of Adhesion to an Elastomeric Stamp. *Nat. Mater.* **2006**, *5* (1), 33–38.
4. Jiao, L.; Fan, B.; Xian, X.; Wu, Z.; Zhang, J.; Liu, Z. Creation of Nanostructures with Poly (Methyl Methacrylate)-Mediated Nanotransfer Printing. *J. Am. Chem. Soc.* **2008**, *130* (38), 12612–12613.
5. Reina, A., Jia, X., Ho, J., Nezich, D., Son, H., Bulovic, V., Dresselhaus, M. S.; Kong, J. Large Area, Few-Layer Graphene Films on Arbitrary Substrates by Chemical Vapor Deposition. *Nano Lett.* **2008**, *9* (1), 30–35.
6. Xu, Q.; Rioux, R. M.; Dickey, M. D.; Whitesides, G. M. Nanoskiving: A New Method to Produce Arrays of Nanostructures. *Acc. Chem. Res.* **2008**, *41* (12), 1566–1577.
7. Allen, M. J.; Tung, V. C.; Gomez, L.; Xu, Z.; Chen, L. M.; Nelson, K. S.; Zhou, C.; Kaner, R. B.; Yang, Y. Soft Transfer Printing of Chemically Converted Graphene. *Adv. Mater.* **2009**, *21* (20), 2098–2102.
8. Schneider, G. F.; Calado, V. E.; Zandbergen, H.; Vandersypen, L. M. K.; Dekker, C. Wedging Transfer of Nanostructures. *Nano Lett.* **2010**, *10* (5), 1912–1916.
9. Liu, Y.; Cheng, R.; Liao, L.; Zhou, H.; Bai, J.; Liu, G.; Liu, L.; Huang, Y.; Duan, X. Plasmon Resonance Enhanced Multicolour Photodetection by Graphene. *Nat. Commun.* **2011**, *2* (1), 577–579.
10. Suk, J. W.; Kitt, A.; Magnuson, C. W.; Hao, Y.; Ahmed, S.; An, J.; Swan, A. K.; Goldberg, B. B.; Ruoff, R. S. Transfer of CVD-Grown Monolayer Graphene onto Arbitrary Substrates. *ACS Nano* **2011**, *5* (9), 6916–6924.
11. Lee, C. H.; Kim, D. R.; Cho, I. S.; William, N.; Wang, Q.; Zheng, X. Peel-and-Stick:

- Fabricating Thin Film Solar Cell on Universal Substrates. *Sci. Rep.* **2012**, *2*, 2–5.
12. Li, H.; Wu, J.; Huang, X.; Yin, Z.; Liu, J.; Zhang, H. A Universal, Rapid Method for Clean Transfer of Nanostructures onto Various Substrates. *ACS Nano* **2014**, *8* (7), 6563–6570.
 13. Choi, M. K.; Yang, J.; Kang, K.; Kim, D. C.; Choi, C.; Park, C.; Kim, S. J.; Chae, S. I.; Kim, T. H.; Kim, J. H.; et al. Wearable Red-Green-Blue Quantum Dot Light-Emitting Diode Array Using High-Resolution Intaglio Transfer Printing. *Nat. Commun.* **2015**, *6* (May), 1–8.
 14. Kim, B. H.; Nam, S.; Oh, N.; Cho, S. Y.; Yu, K. J.; Lee, C. H.; Zhang, J.; Deshpande, K.; Trefonas, P.; Kim, J. H.; et al. Multilayer Transfer Printing for Pixelated, Multicolor Quantum Dot Light-Emitting Diodes. *ACS Nano* **2016**, *10* (5), 4920–4925.
 15. Ma, X.; Liu, Q.; Xu, D.; Zhu, Y.; Kim, S.; Cui, Y.; Zhong, L.; Liu, M. Capillary-Force-Assisted Clean-Stamp Transfer of Two-Dimensional Materials. *Nano Lett.* **2017**, *17* (11), 6961–6967.
 16. Arai, E.; Kamei, K.; Kawasaki, A.; Takagi, F.; Shirai, K.; Orihara, Y. Patent US 4229239, 1980.
 17. Hessel, C. M.; Henderson, E. J.; Veinot, J. G. C. Hydrogen Silsesquioxane: A Molecular Precursor for Nanocrystalline Si-SiO₂ Composites and Freestanding Hydride-Surface-Terminated Silicon Nanoparticles. *Chem. Mater.* **2006**, *18* (26), 6139–6146.
 18. Clark, R. J.; Aghajamali, M.; Gonzalez, C. M.; Hadidi, L.; Islam, M. A.; Javadi, M.; Mobarok, M. H.; Purkait, T. K.; Robidillo, C. J. T.; Sinelnikov, R.; et al. From Hydrogen Silsesquioxane to Functionalized Silicon Nanocrystals. *Chem. Mater.* **2017**, *29* (1), 80–89.
 19. Brust, M.; Walker, M.; Bethell, D.; Schiffrin, D. J.; Whyman, R. Synthesis of Thiol-Derivatized Gold Nanoparticles in. *J. Chem. Soc. Chem. Commun.* **1994**, 801–802.
 20. Veinot, J. G. C. Synthesis, Surface Functionalization, and Properties of Freestanding Silicon Nanocrystals. *Chem. Commun.* **2006**, *40*, 4160.
 21. Dasog, M.; De Los Reyes, G. B.; Titova, L. V.; Hegmann, F. A.; Veinot, J. G. C. Size vs Surface: Tuning the Photoluminescence of Freestanding Silicon Nanocrystals Across the Visible Spectrum via Surface Groups. *ACS Nano* **2014**, *8* (9), 9636–9648.
 22. Kim, T. H.; Cho, K. S.; Lee, E. K.; Lee, S. J.; Chae, J.; Kim, J. W.; Kim, D. H.; Kwon, J. Y.; Amaratunga, G.; Lee, S. Y.; et al. Full-Colour Quantum Dot Displays Fabricated by Transfer Printing. *Nat. Photonics* **2011**, *5* (3), 176–182.

23. Shirasaki, Y.; Supran, G. J.; Bawendi, M. G.; Bulović, V. Emergence of Colloidal Quantum-Dot Light-Emitting Technologies. *Nat. Photonics* **2013**, *7* (1), 13–23.
24. Dai, X.; Deng, Y.; Peng, X.; Jin, Y. Quantum-Dot Light-Emitting Diodes for Large-Area Displays: Towards the Dawn of Commercialization. *Adv. Mater.* **2017**, *29* (14).
25. Rastgar, N.; Rowe, D. J.; Anthony, R. J.; Merritt, B. A.; Kortshagen, U. R.; Aydil, E. S. Effects of Water Adsorption and Surface Oxidation on the Electrical Conductivity of Silicon Nanocrystal Films. *J. Phys. Chem. C* **2013**, *117* (8), 4211–4218.
26. McVey, B. F. P.; Tilley, R. D. Solution Synthesis, Optical Properties, and Bioimaging Applications of Silicon Nanocrystals. *Acc. Chem. Res.* **2014**, *47* (10), 3045–3051.
27. Heister, K.; Zharnikov, M.; Grunze, M.; Johansson, L. S. O. Adsorption of Alkanethiols and Biphenylthiols on Au and Ag Substrates: A High-Resolution X-Ray Photoelectron Spectroscopy Study. *J. Phys. Chem. B* **2001**, *105* (19), 4058–4061.
28. Yang, Z.; Iqbal, M.; Dobbie, A. R.; Veinot, J. G. C. Surface-Induced Alkene Oligomerization: Does Thermal Hydrosilylation Really Lead to Monolayer Protected Silicon Nanocrystals? *J. Am. Chem. Soc.* **2013**, *135* (46), 17595–17601.

Chapter 5:

Conclusions

5.1 Conclusions

Over the last three decades, the synthetic approaches, surface functionalization methods, and fundamental understanding of SiNCs have advanced dramatically.^{1,2} These nanomaterials have been investigated for potential optical (e.g., LEDs, sensors) and energy (e.g., LIBs) applications.³⁻⁶ To access the unique optoelectronic properties of SiNCs and facilitate their practical applications, they must be transferred from solutions to functional structures (e.g., optical materials, conductive matrices, patterned substrates).

This thesis focuses on two approaches to transfer SiNCs from solutions to solid states: one approach involves their incorporation into aerogel hosts (Chapters 2 and 3), and another approach is the patterned transfer of SiNCs onto solid substrates (Chapter 4).

In Chapter 2, SiNCs were transferred from solutions to silica aerogel hosts. Silica aerogels are prepared by sol–gel processing of silicon alkoxide precursors, followed by CO₂ supercritical drying. Silicon alkoxide precursors, such as tetramethyl orthosilicate (TMOS) used in silica aerogel synthesis, are soluble in polar solvents. Hence, hydrophilic SiNCs of various sizes ($d \sim 3$ and 8 nm) and surface groups (*i.e.*, polymer-coated alkyl (C12/P), carboxylic acid (COOH), and polyethylene glycol (PEG)) that photoluminesce throughout the visible and NIR spectral regions were synthesized and incorporated into a TMOS containing solution to produce luminescent silica aerogels of varied transparency (**Figure 5-1**). Photoluminescence spectroscopy performed on solutions and aerogel monoliths containing SiNCs revealed that the optical properties of SiNCs are dependent on their size and surface chemistry. Furthermore, the incorporation of SiNCs into silica aerogels did not influence their PL response. Nitrogen adsorption–desorption measurements indicated that the physical properties of silica aerogels may be tailored by

changing the SiNC size and surface chemistry. Adding to the appeal of this work, PL quenching of a SiNC-loaded silica aerogel occurred upon exposure to nitrobenzene; this confirms the chemical accessibility of the SiNCs within these high surface area optical materials and could open the door to advanced sensing applications.

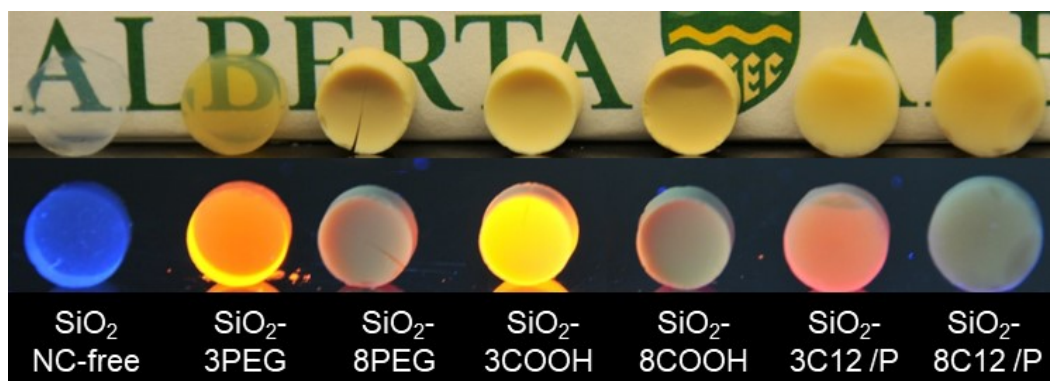


Figure 5-1. Photographs of NC-free and SiNC-containing silica aerogels with indicated sizes and surface groups under ambient (top) and UV (bottom) light (for details see Chapter 2).

In Chapter 3, SiNCs were incorporated into conductive graphene aerogel hosts and tested as anode materials for LIBs. Graphene aerogels (GAs) are prepared commonly by reducing a graphene oxide (GO) precursor, followed by different drying techniques (i.e., CO₂ supercritical drying, freeze drying). GO is hydrophilic and dispersible in water; hence, hydrophilic SiNCs of various sizes ($d \sim 3, 5, 8,$ and 15 nm) were synthesized and incorporated into a GO containing aqueous solution to prepare SiNC/GA hybrids. High resolution X-ray photoelectron spectroscopy performed on the functionalized SiNCs and their corresponding SiNC/GA hybrids indicated a small amount of surface oxidation on these materials. Nitrogen adsorption–desorption measurements revealed that the SiNC/GA hybrids are mesoporous ($d = 2\text{--}50$ nm), with plate-like structures, and could provide empty spaces to accommodate the volume changes

of SiNCs during the lithiation and delithiation cycling. The electrochemical characterization performed on the functionalized SiNCs and their corresponding SiNC/GA hybrids indicated improved cycling stabilities and high specific capacities for the hybrid aerogels compared to those of the functionalized SiNCs after 100 cycles. Moreover, the cycling performance of the hybrid aerogels improved significantly as the size of SiNCs decreased. To improve the electrical conductivity of hybrid aerogels, SiNC/GA hybrids were processed thermally at 600 °C under an argon atmosphere; the annealed 3 nm SiNC/GA hybrid indicated a stable specific capacity of ~1100 mAh/g and a capacity retention of over 90% after 500 cycles when tested at the current density of 400 mA/g (Figure 5-2).

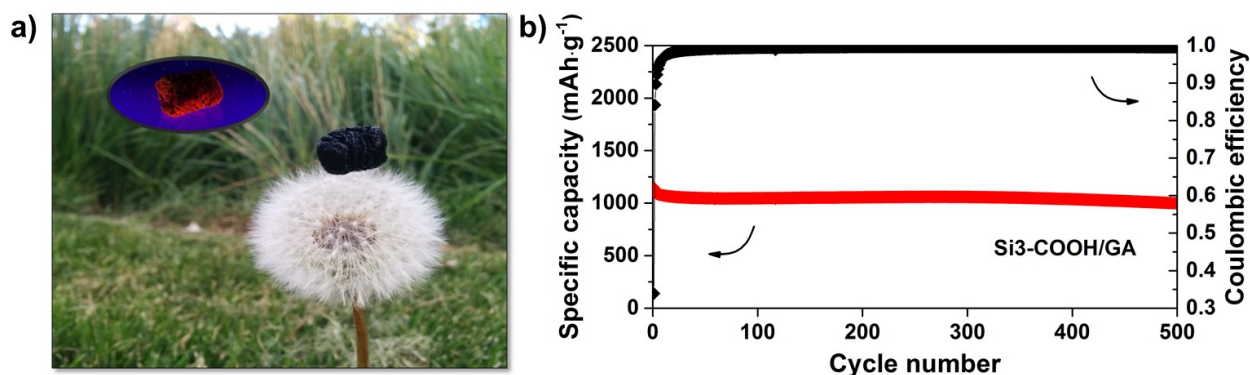


Figure 5-2. a) Photographs of a graphene aerogel containing 3 nm undecanoic acid-functionalized SiNCs under ambient and UV light and b) cycling performance of an annealed 3 nm SiNC/graphene aerogel hybrid at the current density of 400 mA/g (for details see Chapter 3).

In Chapter 4, a straightforward and cost-effective water-assisted transfer technique was developed to transfer patterns of nanomaterials from solutions to solid substrates at low temperatures (~30 °C). This transfer method relies on the hydrophobic effect and utilizes a water-soluble polymer film (e.g., poly (vinyl alcohol), PVA) as a sacrificial carrier to transfer

hydrophobic nanomaterials (e.g., SiNCs, gold nanoparticles (AuNPs)) onto surfaces of various shapes (i.e., non-planar, planar) and compositions (e.g., quartz, aluminum stub) (**Figure 5-3**). Using this approach, nanomaterial patterns on PVA films were reproduced on solid substrates with good fidelity. The water-assisted transfer patterning method can be extended to other hydrophobic nanostructures (e.g., quantum dots, metallic nanoparticles, carbon nanotubes, and graphene) and irregular shape substrates (e.g., optical fibers, microspheres) and could open the door to a variety of new applications (e.g., flexible sensor arrays, curved displays, etc.).

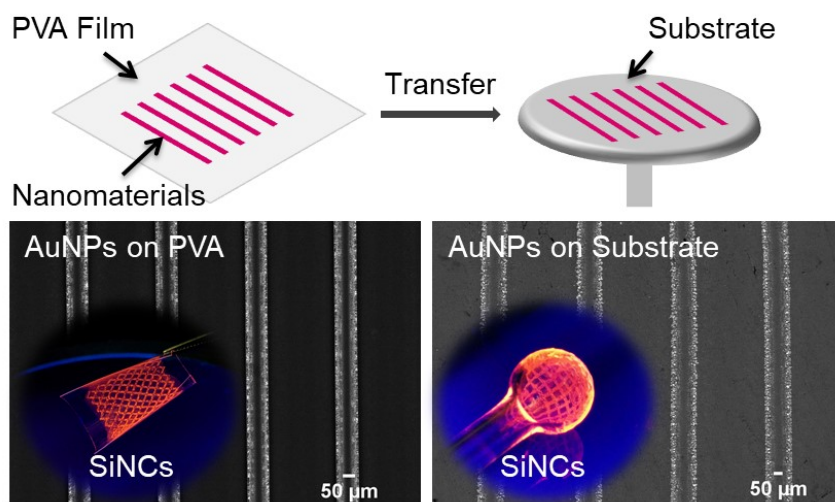


Figure 5-3. A simplified illustration and examples of patterned transfer of nanomaterials (e.g., SiNCs, AuNPs) from PVA films onto solid substrates (for details see Chapter 4).

5.2 Future Directions

5.2.1 SiNC/Silica Aerogel Hybrid Materials

The incorporation of luminescent SiNCs into silica aerogels could prevent their surface oxidation and improve their thermal stability since silica aerogels are good barriers against oxygen/moisture and possess very low thermal conductivity. One approach to synthesize SiNC-SiO₂ aerogel hybrids is to incorporate *hydrophilic* SiNCs into a *hydrophilic* silicon alkoxide-containing solution, as discussed in Chapter 2. However, most surface-functionalized SiNCs exhibiting PL emission colors covering the visible spectrum are *hydrophobic*.⁷ Hence, *hydrophobic* silicon-containing precursors must be explored if SiNC-SiO₂ aerogels exhibiting full PL emission colors appropriate for optoelectronic applications are required.

Hydrogen silsesquioxane (HSQ), the precursor used in the synthesis of SiNCs, is a hydrophobic silicon-containing precursor and can be used for this purpose. The HSQ monomer has a cage structure with a Si-H at each corner, bridged by oxygen.⁸ The monomer cages could cross-link into a network structure by forming additional bonds between cages; this cross-linking may involve reactions with water vapor to produce OH groups on the Si-H corners, which subsequently react to form Si-O-Si bridges.⁹ Following the incorporation of *hydrophobic* SiNCs into a *hydrophobic* HSQ solution, transparent luminescent SiNC-SiO₂ gels/aerogels could be synthesized.

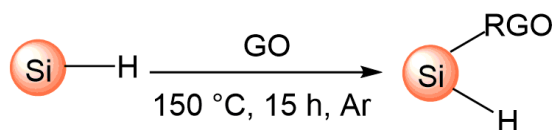
The SiNC-SiO₂ aerogel hybrids combine the optical properties of SiNCs with the transparency and low thermal conductivity of silica aerogels, opening the door to optoelectronic applications. It has been shown that the incorporation of Cd-based QDs into a silica matrix results in highly luminescent and photostable QD/silica hybrids for LED applications.¹⁰ However, Cd-based QDs are toxic and regionally restricted. Hence, it would be beneficial to

fabricate LED devices based on non-toxic SiNC-SiO₂ aerogel hybrids and investigate their performance.

5.2.2 Development of SiNC/Carbon-Based Anode Materials

As discussed earlier, SiNCs are promising anode materials for LIBs, and their incorporation into conductive porous carbon materials is an effective strategy to solve the issues facing Si electrodes (i.e., large volume changes, low electrical conductivity). In Chapter 3, hydrophilic SiNCs were synthesized and incorporated into graphene aerogels following chemical reduction of GO using L-ascorbic acid and CO₂ supercritical drying; this resulted in hybrid materials with stable specific capacities of >1000 mAh/g after 100 cycles. However, this is a multistep approach that requires pre-functionalization of SiNCs and additional reducing agents. It would be useful to explore alternative, straightforward approaches to produce SiNC/C hybrid materials that would be more appealing for industrial LIB production.

Reduced graphene oxide (RGO) is a graphene-like structure with residual oxygen-containing functional groups and surface defects; it can be obtained by chemical reduction of GO using mild reducing agents.¹¹ It has been shown that H-SiNCs are effective reducing agents at 150 °C;¹² hence, the one-step reaction of H-SiNCs with GO at 150 °C could functionalize SiNCs and reduce GO to RGO to produce SiNC-RGO hybrids (**Scheme 5-1**). The RGO sheets can provide empty space to accommodate the volume changes of SiNCs and improve their electrical conductivity for LIB applications.



Scheme 5-1. Synthesis of a SiNC-RGO hybrid material.

5.2.3 Water-Assisted Transfer Patterning of Nanomaterials

The water-assisted transfer patterning (WTP) uses a PVA film to transfer patterns of nanomaterials onto surfaces of various shapes and compositions. It is a straightforward and cost-effective transfer method since it uses an inexpensive polymer film and the whole process is performed in water at low temperatures (~ 30 °C). Also, WTP does not require a delicate control over the adhesion forces at the interfaces or high temperatures to remove polymer residues; hence, it is a practical approach to transfer patterns of nanomaterials onto diverse substrates for a variety of applications (e.g., sensor arrays, curved displays, printed electronics, etc.). However, the shrinking and expansion of the PVA film during the water transfer influence the fidelity of transfer patterning. To improve WTP fidelity, one approach could be to replace the PVA with advanced water-soluble polymers or copolymers causing less shrinking/expansion during dissolution. Another approach could be to form a transparent protective layer (e.g., hydrophobic polymer) on top of the NM patterns, which can preserve the pattern integrity during the dissolution of the PVA film (**Figure 5-4**).

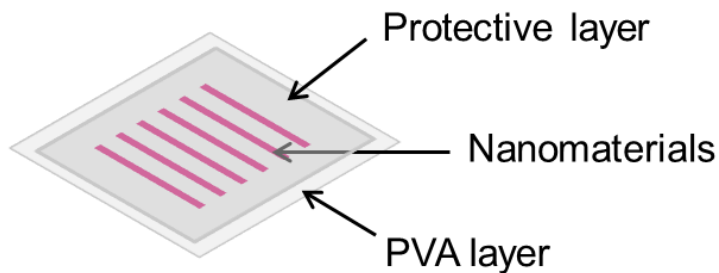


Figure 5-4. Schematic representation of a modified pattern layer; nanomaterials are sandwiched between the PVA layer and the protective layer.

5.3 References

1. Veinot, J. G. C. Synthesis, Surface Functionalization, and Properties of Freestanding Silicon Nanocrystals. *Chem. Commun.* **2006**, 4160–4168.
2. Dasog, M.; Kehrle, J.; Rieger, B.; Veinot, J. G. C. Silicon Nanocrystals and Silicon-Polymer Hybrids: Synthesis, Surface Engineering, and Applications. *Angew. Chemie Int. Ed.* **2016**, *55* (7), 2322–2339.
3. Maier-Flaig, F.; Rinck, J.; Stephan, M.; Bocksrocker, T.; Bruns, M.; Kübel, C.; Powell, A. K.; Ozin, G. A.; Lemmer, U. Multicolor Silicon Light-Emitting Diodes (SiLEDs). *Nano Lett.* **2013**, *13* (2), 475–480.
4. Liu, X. H.; Zhong, L.; Huang, S.; Mao, S. X.; Zhu, T.; Huang, J. Y. Size-Dependent Fracture of Silicon Nanoparticles during Lithiation. *ACS Nano* **2012**, *6* (2), 1522–1531.
5. Gonzalez, C. M.; Iqbal, M.; Dasog, M.; Piercey, D. G.; Lockwood, R.; Klapötke, T. M.; Veinot, J. G. C. Detection of High-Energy Compounds Using Photoluminescent Silicon Nanocrystal Paper Based Sensors. *Nanoscale* **2014**, *6* (5), 2608–2612.
6. Zhai, Y.; Dasog, M.; Snitynsky, R. B.; Purkait, T. K.; Aghajamali, M.; Hahn, A. H.; Sturdy, C. B.; Lowary, T. L.; Veinot, J. G. C. Water-Soluble Photoluminescent D-Mannose and L-Alanine Functionalized Silicon Nanocrystals and Their Application to Cancer Cell Imaging. *J. Mater. Chem. B* **2014**, *2*, 8427–8433.
7. Dasog, M.; De Los Reyes, G. B.; Titova, L. V.; Hegmann, F. A.; Veinot, J. G. C. Size vs Surface: Tuning the Photoluminescence of Freestanding Silicon Nanocrystals Across the Visible Spectrum via Surface Groups. *ACS Nano* **2014**, *8* (9), 9636–9648.
8. Cordes, D. B.; Lickiss, P. D.; Rataboul, F. Recent Developments in the Chemistry of Cubic Polyhedral.pdf. *Chem. Rev.* **2010**, *110*, 2081–2173.
9. Caster, A. G.; Kowarik, S.; Schwartzberg, A. M.; Nicolet, O.; Lim, S. H.; Leone, S. R. Observing Hydrogen Silsesquioxane Cross-Linking with Broadband CARS. *J. Raman Spectrosc.* **2009**, *40* (7), 770–774.

10. Jun, S.; Lee, J.; Jang, E. Highly Luminescent and Photostable Quantum Dot-Silica Monolith and Its Application to Light-Emitting Diodes. *ACS Nano* **2013**, *7* (2), 1472–1477.
11. Abdolhosseinzadeh, S.; Asgharzadeh, H.; Kim, H. S. Fast and Fully-Scalable Synthesis of Reduced Graphene Oxide. *Sci. Rep.* **2015**, *5*, 1–7.
12. Dasog, M.; Kraus, S.; Sinelnikov, R.; Veinot, J. G. C.; Rieger, B. CO₂ to Methanol Conversion Using Hydride Terminated Porous Silicon Nanoparticles. *Chem. Commun.* **2017**, *53* (21), 3114–3117.

Bibliography

1. Kroto, H. W.; Heath, J. R.; O'brien, S. C.; Curl, R. F.; Smalley R. E. C60: Buckminsterfullerene. *Nature* **1985**, *318*, 162–163.
2. Schmid, G. Large Clusters and Colloids. Metals in the Embryonic State. *Chem. Rev.* **1992**, *92* (8), 1709–1727.
3. Lu, Z.; Yin, Y. Colloidal Nanoparticle Clusters: Functional Materials by Design. *Chem. Soc. Rev.* **2012**, *41* (21), 6874.
4. www.hc-sc.gc.ca/sr-sr/pubs/nano/pol-eng.php (accessed April 1, 2018)
5. Alivisatos, A. P. Perspectives on the Physical Chemistry of Semiconductor Nanocrystals. *J. Phys. Chem.* **1996**, *100* (31), 13226–13239.
6. Eustis, S.; El-Sayed, M. A. Why Gold Nanoparticles Are More Precious than Pretty Gold: Noble Metal Surface Plasmon Resonance and Its Enhancement of the Radiative and Nonradiative Properties of Nanocrystals of Different Shapes. *Chem. Soc. Rev.* **2006**, *35* (3), 209–217.
7. Henglein, A. Small-Particle Research: Physicochemical Properties of Extremely Small Colloidal Metal and Semiconductor Particles. *Chem. Rev.* **1989**, *89* (8), 1861–1873.
8. Zhang, G.; Li, B. Impacts of Doping on Thermal and Thermoelectric Properties of Nanomaterials. *Nanoscale* **2010**, *2* (7), 1058–68.
9. G. Cao, *Nanostructures and Nanomaterials*, Imperial College Press, London, UK, 2004.
10. Reed, M. A.; Randall, J. N.; Aggarwal, R. J.; Matyi, R. J.; Moore, T. M.; Wetsel, A. E. Observation of Discrete Electronic States in A Zero-Dimensional Semiconductor Nanostructure. *Phys. Rev. Lett.* **1988**, *60* (6), 535–537.
11. Lim, S. J.; Zahid, M. U.; Le, P.; Ma, L.; Entenberg, D.; Harney, A. S.; Condeelis, J.; Smith, A. M. Brightness-Equalized Quantum Dots. *Nat. Commun.* **2015**, *6*, 1–10.
12. Yang, Z.; Voznyy, O.; Liu, M.; Yuan, M.; Ip, A. H.; Ahmed, O. S.; Levina, L.; Kinge, S.; Hoogland, S.; Sargent, E. H. All-Quantum-Dot Infrared Light-Emitting Diodes. *ACS Nano* **2015**, *9* (12), 12327–12333.
13. Jeong, K. S.; Guyot-Sionnest, P. Mid-Infrared Photoluminescence of CdS and CdSe

- Colloidal Quantum Dots. *ACS Nano* **2016**, *10* (2), 2225–2231.
14. Rogach, B. A. L.; Talapin, D. V.; Shevchenko, E. V.; Kornowski, A.; Haase, M.; Weller, H. Organization of Matter on Different Size Scales: Monodisperse Nanocrystals and Their Superstructures. *Adv.Funct. Mater.* **2002**, *12* (10), 653–664.
 15. Talapin, D. V.; Lee, J.; Kovalenko, M. V.; Shevchenko, E. V. Prospects of Colloidal Nanocrystals for Electronic and Optoelectronic Applications. *Chem. Rev.* **2010**, *110* (1), **2010**, 389–458.
 16. Lim, X. The nanolight revolution is coming *Nature* **2016**, *531*, 26–28.
 17. Murray, C. B.; Norris, D. J.; Bawendi, M. G. Synthesis and Characterization of Nearly Monodisperse CdE (E = S, Se, Te) Semiconductor Nanocrystallites. *J. Am. Chem. Soc.* **1993**, *115* (19), 8706–8715.
 18. Jun, Y.; Choi, C.-S.; Cheon, J. Size and Shape Controlled ZnTe Nanocrystals with Quantum Confinement Effect. *Chem. Commun.* **2001**, 5769 (1), 101–102.
 19. Shim, M.; Guyot-Sionnest, P. Organic-Capped ZnO Nanocrystals: Synthesis and N-Type Character. *J. Am. Chem. Soc.* **2001**, *123* (47), 11651–11654.
 20. Yang, Y. A.; Wu, H.; Williams, K. R.; Cao, Y. C. Synthesis of CdSe and CdTe Nanocrystals without Precursor Injection. *Angew. Chemie - Int. Ed.* **2005**, *44* (41), 6712–6715.
 21. Battaglia, D.; Peng, X. Formation of High Quality InP and InAs Nanocrystals in a Noncoordinating Solvent. *Nano Lett.* **2002**, *2* (9), 1027–1030.
 22. Xie, R.; Battaglia, D.; Peng, X. Colloidal InP Nanocrystals as Efficient Emitters Covering Blue to near-Infrared. *J. Am. Chem. Soc.* **2007**, *129* (50), 15432–15433.
 23. Harris, D. K.; Bawendi, M. G. Improved Precursor Chemistry for the Synthesis of III-V Quantum Dots. *J. Am. Chem. Soc.* **2012**, *134* (50), 20211–20213.
 24. Marzin, J.-Y.; Gérard, J.-M.; Izraël, A.; Barrier, D.; Bastard, G. Photoluminescence of Single InAs Quantum Dots Obtained by Self-Organized Growth on GaAs. *Phys. Rev. Lett.* **1994**, *73*, 716–719.

25. Mičić, O. I.; Ahrenkiel, S. P.; Bertram, D.; Nozik, A. J. Synthesis, Structure, and Optical Properties of Colloidal GaN Quantum Dots. *Appl. Phys. Lett.* **1999**, *75* (4), 478–480.
26. Coe, S.; Woo, M.; Bawendi, W. K.; Bulović, V. Electroluminescence from Single Monolayers of Nanocrystals in Molecular Organic Devices. *Nature* **2002**, *420*, 800–803.
27. Rogach, A. L.; Gaponik, N.; Lupton, J. M.; Bertoni, C.; Gallardo, D. E.; Dunn, S.; Li Pira, N.; Paderi, M.; Repetto, P.; Romanov, S. G.; et al. Light-Emitting Diodes with Semiconductor Nanocrystals. *Angew. Chemie - Int. Ed.* **2008**, *47* (35), 6538–6549.
28. Chuang, C.-H. M.; Brown, P. R.; Bulović, V.; Bawendi, M. G. Improved Performance and Stability in Quantum Dot Solar Cells through Band Alignment Engineering. *Nat. Mater.* **2014**, *13* (8), 796–801.
29. Carey, G. H.; Abdelhady, A. L.; Ning, Z.; Thon, S. M.; Bakr, O. M.; Sargent, E. H. Colloidal Quantum Dot Solar Cells. *Chem. Rev.* **2015**, *115* (23), 12732–12763.
30. Medintz, I. L.; Uyeda, H. T.; Goldman, E. R.; Mattoussi, H. Quantum Dot Bioconjugates for Imaging, Labelling and Sensing. *Nat. Mater.* **2005**, *4* (6), 435–446.
31. Freeman, R.; Willner, I. Optical Molecular Sensing with Semiconductor Quantum Dots (QDs). *Chem. Soc. Rev.* **2012**, *41* (10), 4067.
32. Huffaker, D. L.; Park, G.; Zou, Z.; Shchekin, O. B.; Deppe, D. G. 1.3 Mm Room-Temperature GaAs-Based Quantum-Dot Laser. *Appl. Phys. Lett.* **1998**, *73* (18), 2564–2566.
33. Bimberg, D.; Grundmann, M.; Heinrichsdorff, F.; Ledentsov, N. N.; Ustinov, V. M.; Zhukov, A. E.; Kovsh, A. R.; Maximov, M. V.; Shernyakov, Y. M.; Volovik, B. V.; et al. Quantum Dot Lasers: Breakthrough in Optoelectronics. *Thin Solid Films* **2000**, *367* (1–2), 235–249.
34. Michalet, X.; Pinaud, F. F.; Bentolila, L. A.; Tsay, J. M.; Doose, S.; Li, J. J.; Sundaresan, G.; Wu, A. M.; Gambhir, S. S.; Weiss, S. Quantum Dots for Live Cells, in Vivo Imaging, and Diagnostics. *Science* **2005**, *307*, 538–544.
35. Wegner, K. D.; Hildebrandt, N. Quantum Dots: Bright and Versatile in Vitro and in Vivo Fluorescence Imaging Biosensors. *Chem. Soc. Rev.* **2015**, *44*, 4792–4834.

36. Graeme, K.; Pollack, C. Heavy Metal Toxicity, Part 1: Arsenic and Mercury. *J. Emerg. Med.* **1998**, *16* (1), 46–56.
37. Houston, M. C. The Role of Mercury and Cadmium Heavy Metals in Vascular Disease, Hypertension, Coronary Heart Disease, and Myocardial Infarction. *Altern. Ther. Health Med.* **2007**, *13* (2), 128–33.
38. Gordon, R. B.; Bertram, M.; Graedel, T. E. Metal Stocks and Sustainability. *Proc. Natl. Acad. Sci.* **2006**, *103* (5), 1209–1214.
39. Dasog, M.; Kehrle, J.; Rieger, B.; Veinot, J. G. C. Silicon Nanocrystals and Silicon-Polymer Hybrids: Synthesis, Surface Engineering, and Applications. *Angew. Chemie Int. Ed.* **2016**, *55* (7), 2322–2339.
40. Veinot, J. G. C. Synthesis, Surface Functionalization, and Properties of Freestanding Silicon Nanocrystals. *Chem. Commun.* **2006**, 4160–4168.
41. Cheng, X.; Lowe, S. B.; Reece, P. J.; Gooding, J. J. Colloidal Silicon Quantum Dots: From Preparation to the Modification of Self-Assembled Monolayers (SAMs) for Bio-Applications. *Chem. Soc. Rev.* **2014**, *43* (8), 2680–2700.
42. Hessel, C. M.; Henderson, E. J.; Veinot, J. G. C. Hydrogen Silsesquioxane: A Molecular Precursor for Nanocrystalline Si-SiO₂ Composites and Freestanding Hydride-Surface-Terminated Silicon Nanoparticles. *Chem. Mater.* **2006**, *18* (26), 6139–6146.
43. Dasog, M.; De Los Reyes, G. B.; Titova, L. V.; Hegmann, F. A.; Veinot, J. G. C. Size vs Surface: Tuning the Photoluminescence of Freestanding Silicon Nanocrystals Across the Visible Spectrum via Surface Groups. *ACS Nano* **2014**, *8* (9), 9636–9648.
44. Maier-Flaig, F.; Rinck, J.; Stephan, M.; Bocksrocker, T.; Bruns, M.; Kübel, C.; Powell, A. K.; Ozin, G. A.; Lemmer, U. Multicolor Silicon Light-Emitting Diodes (SiLEDs). *Nano Lett.* **2013**, *13* (2), 475–480.
45. Liu, X. H.; Zhong, L.; Huang, S.; Mao, S. X.; Zhu, T.; Huang, J. Y. Size-Dependent Fracture of Silicon Nanoparticles during Lithiation. *ACS Nano* **2012**, *6* (2), 1522–1531.
46. Liu, C.-Y.; Holman, Z. C.; Kortshagen, U. R. Hybrid Solar Cells from P3HT and Silicon

- Nanocrystals. *Nano Lett.* **2009**, *9* (1), 449–452.
47. Gonzalez, C. M.; Iqbal, M.; Dasog, M.; Piercey, D. G.; Lockwood, R.; Klapötke, T. M.; Veinot, J. G. C. Detection of High-Energy Compounds Using Photoluminescent Silicon Nanocrystal Paper Based Sensors. *Nanoscale* **2014**, *6* (5), 2608–2612.
 48. Erogbogbo, F.; Yong, K.-T.; Roy, I.; Hu, R.; Law, W.-C.; Zhao, W.; Ding, H.; Wu, F.; Kumar, R.; Swihart, M. T.; Prasad, P. N. *In Vivo* Targeted Cancer Imaging, Sentinel Lymph Node Mapping and Multi-Channel Imaging with Biocompatible Silicon Nanocrystals. *ACS Nano* **2011**, *5* (1), 413–423.
 49. Canham, L. T. Silicon Quantum Wire Array Fabrication by Electrochemical and Chemical Dissolution of Wafers. *Appl. Phys. Lett.* **1990**, *57*, 1046–48.
 50. Cullis, A. G.; Canham, L. T. Visible Light Emission due to Quantum Size Effects in Highly Porous Crystalline Silicon. *Nature* **1991**, *353*, 335–338.
 51. Ghosh, B.; Shirahata, N. Colloidal Silicon Quantum Dots: Synthesis and Luminescence Tuning from the near-UV to the near-IR Range. *Sci. Technol. Adv. Mater.* **2014**, *15* (1), 14207.
 52. Heintz, A. S.; Fink, M. J.; Mitchell, B. S. Mechanochemical Synthesis of Blue Luminescent Alkyl/alkenyl-Passivated Silicon Nanoparticles. *Adv. Mater.* **2007**, *19* (22), 3984–3988.
 53. Chaudhary, A.-L.; Sheppard, D. A.; Paskevicius, M.; Saunders, M.; Buckley, C. E. Mechanochemical Synthesis of Amorphous Silicon Nanoparticles. *RSC Adv.* **2014**, *4* (42), 21979–21983.
 54. Kelly, M. T.; Chun, J. K. M.; Bocarsly, A. B. High Efficiency Chemical Etchant for the Formation of Luminescent Porous Silicon. *Appl. Phys. Lett.* **1994**, *64* (13), 1693–1695.
 55. Sato, K.; Tsuji, H.; Hirakuri, K.; Fukata, N.; Yamauchi, Y. Controlled Chemical Etching for Silicon Nanocrystals with Wavelength-Tunable Photoluminescence. *Chem. Commun.* **2009**, No. 25, 3759–3761.
 56. Bley, R. A.; Kauzlarich, S. M.; Davis, J. E.; Lee, H. W. H. Characterization of Silicon Nanoparticles Prepared from Porous Silicon. *Chem. Mater.* **1996**, *8* (8), 1881–1888.

57. Anglin, E. J.; Cheng, L.; Freeman, W. R.; Sailor, M. J. Porous Silicon in Drug Delivery Devices and Materials. *Adv. Drug Deliv. Rev.* **2008**, *60* (11), 1266–1277.
58. Okada, R.; Iijima, S. Oxidation Property of Silicon Small Particles. *Appl. Phys. Lett.* **1991**, *58* (15), 1662–1663.
59. Shirahata, N.; Linford, M. R.; Furumi, S.; Pei, L.; Sakka, Y.; Gates, R. J.; Asplund, M. C. Laser-Derived One-Pot Synthesis of Silicon Nanocrystals Terminated with Organic Monolayers. *Chem. Commun.* **2009**, No. 31, 4684–4686.
60. Heath, J. R. A Liquid-Solution-Phase Synthesis of Crystalline Silicon. *Science* **1992**, *258*, 1131–1133.
61. Arul Dhas, N.; Raj, C. P.; Gedanken, A. Preparation of Luminescent Silicon Nanoparticles: A Novel Sonochemical Approach. *Chem. Mater.* **1998**, *10* (11), 3278–3281.
62. Warner, J. H.; Hoshino, A.; Yamamoto, K.; Tilley, R. D. Water-Soluble Photoluminescent Silicon Quantum Dots. *Angew. Chemie - Int. Ed.* **2005**, *44* (29), 4550–4554.
63. Shavel, A.; Guerrini, L.; Alvarez-Puebla, R. A. Colloidal Synthesis of Silicon Nanoparticles in Molten Salts. *Nanoscale* **2017**, *9* (24), 8157–8163.
64. Bley, R. A.; Kauzlarich, S. M. A Low-Temperature Solution Phase Route for the Synthesis of Silicon Nanoclusters. *J. Am. Chem. Soc.* **1996**, *118* (49), 12461–12462.
65. Yang, C. S.; Bley, R. A.; Kauzlarich, S. M.; Lee, H. W. H.; Delgado, G. R. Synthesis of Alkyl-Terminated Silicon Nanoclusters by a Solution Route. *J. Am. Chem. Soc.* **1999**, *121* (22), 5191–5195.
66. Wang, L.; Lin, N.; Zhou, J.; Zhu, Y.; Qian, Y. Silicon Nanoparticles Obtained via a Low Temperature Chemical “metathesis” Synthesis Route and Their Lithium-Ion Battery Properties. *Chem. Commun.* **2015**, *51* (12), 2345–2348.
67. Huisken, F.; Kohn, B.; Paillard, V. Structured Films of Light-Emitting Silicon Nanoparticles Produced by Cluster Beam Deposition. *Appl. Phys. Lett.* **1999**, *74* (25), 3776–3778.
68. Li, X.; He, Y.; Talukdar, S. S.; Swihart, M. T. Process for Preparing Macroscopic Quantities of Brightly Photoluminescent Silicon Nanoparticles with Emission Spanning the Visible

- Spectrum. *Langmuir* **2003**, *19* (20), 8490–8496.
69. Hua, F.; Swihart, M. T.; Ruckenstein, E. Efficient Surface Grafting of Luminescent Silicon Quantum Dots by Photoinitiated Hydrosilylation. *Langmuir* **2005**, *21* (13), 6054–6062.
 70. Mangolini, L.; Thimsen, E.; Kortshagen, U. High-Yield Plasma Synthesis of Luminescent Silicon Nanocrystals. *Nano Lett.* **2005**, *5* (4), 655–659.
 71. Holmes, J. D.; Ziegler, K. J.; Doty, R. C.; Pell, L. E.; Johnston, K. P.; Korgel, B. A. Highly Luminescent Silicon Nanocrystals with Discrete Optical Transitions. *J. Am. Chem. Soc.* **2001**, *123* (16), 3743–3748.
 72. Hessel, C. M.; Henderson, E. J.; Veinot, J. G. C. An Investigation of the Formation and Growth of Oxide-Embedded Silicon Nanocrystals in Hydrogen Silsesquioxane-Derived Nanocomposites. *J. Phys. Chem. C* **2007**, *111* (19), 6956–6961.
 73. Hessel, C. M.; Reid, D.; Panthani, M. G.; Rasch, M. R.; Goodfellow, B. W.; Wei, J.; Fujii, H.; Akhavan, V.; Korgel, B. A. Synthesis of Ligand-Stabilized Silicon Nanocrystals with Size-Dependent Photoluminescence Spanning Visible to near-Infrared Wavelengths. *Chem. Mater.* **2012**, *24* (2), 393–401.
 74. Mastronardi, M. L.; Hennrich, F.; Henderson, E. J.; Maier-Flaig, F.; Blum, C.; Reichenbach, J.; Lemmer, U.; Kübel, C.; Wang, D.; Kappes, M. M.; et al. Preparation of Monodisperse Silicon Nanocrystals Using Density Gradient Ultracentrifugation. *J. Am. Chem. Soc.* **2011**, *133* (31), 11928–11931.
 75. Sun, W.; Qian, C.; Cui, X. S.; Wang, L.; Wei, M.; Casillas, G.; Helmy, A. S.; Ozin, G. A. Silicon Monoxide – a Convenient Precursor for Large Scale Synthesis of near Infrared Emitting Monodisperse Silicon Nanocrystals. *Nanoscale* **2016**, *8* (6), 3678–3684.
 76. Buriak, J. M. Illuminating Silicon Surface Hydrosilylation: An Unexpected Plurality of Mechanisms. *Chem. Mater.* **2014**, *26* (1), 763–772.
 77. Yang, Z.; Iqbal, M.; Dobbie, A. R.; Veinot, J. G. C. Surface-Induced Alkene Oligomerization: Does Thermal Hydrosilylation Really Lead to Monolayer Protected Silicon Nanocrystals? *J. Am. Chem. Soc.* **2013**, *135* (46), 17595–17601.

78. Yang, Z.; Dasog, M.; Dobbie, A. R.; Lockwood, R.; Zhi, Y.; Meldrum, A.; Veinot, J. G. C. Highly Luminescent Covalently Linked Silicon Nanocrystal/polystyrene Hybrid Functional Materials: Synthesis, Properties, and Processability. *Adv. Funct. Mater.* **2014**, *24* (10), 1345–1353.
79. Kehrle, J.; Höhle, I. M. D.; Yang, Z.; Jochem, A. R.; Helbich, T.; Kraus, T.; Veinot, J. G. C.; Rieger, B. Thermoresponsive and Photoluminescent Hybrid Silicon Nanoparticles by Surface-Initiated Group Transfer Polymerization of Diethyl Vinylphosphonate. *Angew. Chemie. Int. Ed.* **2014**, *53*, 12494–12497.
80. Yang, Z.; Gonzalez, C. M.; Purkait, T. K.; Iqbal, M.; Meldrum, A.; Veinot, J. G. C. Radical Initiated Hydrosilylation on Silicon Nanocrystal Surfaces: An Evaluation of Functional Group Tolerance and Mechanistic Study. *Langmuir* **2015**, *31*, 10540–10548.
81. Kelly, J. A.; Shukaliak, A. M.; Fleischauer, M. D.; Veinot, J. G. C. Size-Dependent Reactivity in Hydrosilylation of Silicon Nanocrystals. *J. Am. Chem. Soc.* **2011**, *133* (24), 9564–9571.
82. Purkait, T. K.; Iqbal, M.; Wahl, M. H.; Gottschling, K.; Gonzalez, C. M.; Islam, M. A.; Veinot, J. G. C. Borane-Catalyzed Room-Temperature Hydrosilylation of Alkenes/alkynes on Silicon Nanocrystal Surfaces. *J. Am. Chem. Soc.* **2014**, *136* (52), 17914–17917.
83. Mobarok, M. H.; Purkait, T. K.; Islam, M. A.; Miskolzie, M.; Veinot, J. G. C. Instantaneous Functionalization of Chemically Etched Silicon Nanocrystal Surfaces. *Angew. Chemie - Int. Ed.* **2017**, *56* (22), 6073–6077.
84. Islam, M. A.; Mobarok, M. H.; Sinelnikov, R.; Purkait, T. K.; Veinot, J. G. C. Phosphorus Pentachloride Initiated Functionalization of Silicon Nanocrystals. *Langmuir* **2017**, *33* (35), 8766–8773.
85. Thissen, P.; Seitz, O.; Chabal, Y. J. Wet Chemical Surface Functionalization of Oxide-Free Silicon. *Prog. Surf. Sci.* **2012**, *87* (9–12), 272–290.
86. Hirschman, K. D.; Tsybeskov, L.; Dutta Gupta, S. P.; Fauchet, P. M. Silicon-Based Visible Light-Emitting Devices Integrated into Microelectronic Circuits. *Nature* **1996**, *384*, 338–341.

87. Clemens, J. T. Silicon Microelectronics Technology. *Bell Labs Tech. J.* **2002**, 2 (4), 76–102.
88. Liang, D.; Bowers, J. E. Recent Progress in Lasers on Silicon. *Nat. Photonics* **2010**, 4, 511–517.
89. Hill, N. A.; Whaley, K. B. A Theoretical Study of Light Emission from Nanoscale Silicon. *J. Electron. Mater.* **1996**, 25 (2), 269–285.
90. Daldosso, N.; Pavesi, L. Nanosilicon Photonics. *Laser Photonics Rev.* **2009**, 3 (6), 508–534.
91. Hybertsen, M. S. Absorption and Emission of Light in Nanoscale Silicon Structures. *Phys. Rev. Lett.* **1994**, 72 (10), 1514–1517.
92. Wolkin, M. V.; Jorne, J.; Fauchet, P. M.; Allan, G.; Delerue, C. Electronic States and Luminescence in Porous Silicon Quantum Dots: The Role of Oxygen. *Phys. Rev. Lett.* **1999**, 82 (1), 197–200.
93. Godefroo, S.; Hayne, M.; Jivanescu, M.; Stesmans, A.; Zacharias, M.; Lebedev, O. I.; Van Tendeloo, G.; Moshchalkov, V. V. Classification and Control of the Origin of Photoluminescence from Si Nanocrystals. *Nat. Nanotechnol.* **2008**, 3 (3), 174–178.
94. Sun, W.; Qian, C.; Chen, K. K.; Ozin, G. A. Silicon Nanocrystals: It's Simply a Matter of Size. *ChemNanoMat* **2016**, 2 (9), 847–855.
95. Sinelnikov, R.; Dasog, M.; Beamish, J.; Meldrum, A.; Veinot, J. G. C. Revisiting an Ongoing Debate: What Role Do Surface Groups Play in Silicon Nanocrystal Photoluminescence? *ACS Photonics* **2017**, 4 (8), 1920–1929.
96. Bruce, P. G.; Scrosati, B.; Tarascon, J. M. Nanomaterials for Rechargeable Lithium Batteries. *Angew. Chemie - Int. Ed.* **2008**, 47 (16), 2930–2946.
97. Teki, R.; Krishnan, R.; Parker, T. C.; Lu, T. M.; Datta, M. K.; Kumta, P. N.; Koratkar, N. Nanostructured Silicon Anodes for Lithium Ion Rechargeable Batteries. *Small* **2009**, 5 (20), 2236–2242.
98. Su, X.; Wu, Q.; Li, J.; Xiao, X.; Lott, A.; Lu, W.; Sheldon, B. W.; Wu, J. Silicon-Based Nanomaterials for Lithium-Ion Batteries: A Review. *Adv. Energy Mater.* **2014**, 4, 1300882.
99. Kasavajjula, U.; Wang, C.; Appleby, A. J. Nano- and Bulk-Silicon-Based Insertion Anodes

- for Lithium-Ion Secondary Cells. *J. Power Sources* **2007**, *163* (2), 1003–1039.
100. Wu, H.; Cui, Y. Designing Nanostructured Si Anodes for High Energy Lithium Ion Batteries. *Nano Today* **2012**, *7* (5), 414–429.
101. Zamfir, M. R.; Nguyen, H. T.; Moyen, E.; Lee, Y. H.; Pribat, D. Silicon Nanowires for Li-Based Battery Anodes: A Review. *J. Mater. Chem. A* **2013**, *1* (34), 9566.
102. Bruce, P. G.; Freunberger, S. A.; Hardwick, L. J.; Tarascon, J.-M. Li–O₂ and Li–S Batteries with High Energy Storage. *Nat. Mater.* **2012**, *11* (1), 19–29.
103. Christensen, J.; Albertus, P.; Sanchez-Carrera, R. S.; Lohmann, T.; Kozinsky, B.; Liedtke, R.; Ahmed, J.; Kojic, A. A Critical Review of Li/Air Batteries. *J. Electrochem. Soc.* **2012**, *159* (2), R1.
104. Park, C.-M.; Kim, J.-H.; Kim, H.; Sohn, H.-J. Li-Alloy Based Anode Materials for Li Secondary Batteries. *Chem. Soc. Rev.* **2010**, *39* (8), 3115.
105. Zhang, W. J. A Review of the Electrochemical Performance of Alloy Anodes for Lithium-Ion Batteries. *J. Power Sources* **2011**, *196* (1), 13–24.
106. Boukamp, B. A.; Lesh, G. C.; Huggins, R. A. All-Solid Lithium Electrodes with Mixed-Conductor Matrix. *J. Electrochem. Soc.* **1981**, *128* (4), 725–729.
107. Kulova, T. L.; Skundin, A. M.; Pleskov, Y. V.; Terukov, E. I.; Kon'kov, O. I. Lithium Insertion into Amorphous Silicon Thin-Film Electrodes. *J. Electroanal. Chem.* **2007**, *600* (1), 217–225.
108. Pollak, E.; Salitra, G.; Baranchugov, V.; Aurbach, D. In Situ Conductivity, Impedance Spectroscopy, and Ex Situ Raman Spectra of Amorphous Silicon during the Insertion/extraction of Lithium. *J. Phys. Chem. C* **2007**, *111* (30), 11437–11444.
109. Szczech, J. R.; Jin, S. Nanostructured Silicon for High Capacity Lithium Battery Anodes. *Energy Environ. Sci.* **2011**, *4* (1), 56–72.
110. Liu, X. H.; Zhong, L.; Huang, S.; Mao, S. X.; Zhu, T.; Huang, J. Y. Size-Dependent Fracture of Silicon Nanoparticles during Lithiation. *ACS Nano* **2012**, *6* (2), 1522–1531.
111. Chockla, A. M.; Harris, J. T.; Akhavan, V. A.; Bogart, T. D.; Holmberg, V. C.; Steinhausen,

- C.; Mullins, C. B.; Stevenson, K. J.; Korgel, B. A. Silicon Nanowire Fabric as a Lithium Ion Battery Electrode Material. *J. Am. Chem. Soc.* **2011**, *133* (51), 20914–20921.
112. Nguyen, H. T.; Yao, F.; Zamfir, M. R.; Biswas, C.; So, K. P.; Lee, Y. H.; Kim, S. M.; Cha, S. N.; Kim, J. M.; Pribat, D. Highly Interconnected Si Nanowires for Improved Stability Li-Ion Battery Anodes. *Adv. Energy Mater.* **2011**, *1* (6), 1154–1161.
113. Park, M.; Kim, M. G.; Joo, J.; Kim, K.; Kim, J.; Ahn, S.; Cui, Y.; Cho, J. Silicon Nanotube Battery Anodes. *Nano Lett.* **2009**, *9* (11), 3844–3847.
114. Wu, H.; Chan, G.; Choi, J. W.; Ryu, I.; Yao, Y.; McDowell, M. T.; Lee, S. W.; Jackson, A.; Yang, Y.; Hu, L.; et al. Stable Cycling of Double-Walled Silicon Nanotube Battery Anodes through Solid-Electrolyte Interphase Control. *Nat. Nanotechnol.* **2012**, *7* (5), 310–315.
115. Yao, Y.; McDowell, M. T.; Ryu, I.; Wu, H.; Liu, N.; Hu, L.; Nix, W. D.; Cui, Y. Interconnected Silicon Hollow Nanospheres for Lithium-Ion Battery Anodes with Long Cycle Life. *Nano Lett.* **2011**, *11* (7), 2949–2954.
116. Zhao, Y.; Liu, X.; Li, H.; Zhai, T.; Zhou, H. Hierarchical Micro/nano Porous Silicon Li-Ion Battery Anodes. *Chem. Commun.* **2012**, *48* (42), 5079.
117. Zhu, J.; Gladden, C.; Liu, N.; Cui, Y.; Zhang, X. Nanoporous Silicon Networks as Anodes for Lithium Ion Batteries. *Phys. Chem. Chem. Phys.* **2013**, *15* (2), 440–443.
118. Wang, B.; Li, X.; Zhang, X.; Luo, B.; Jin, M.; Liang, M.; Dayeh, S. A.; Picraux, S. T.; Zhi, L. Adaptable Silicon-Carbon Nanocables Sandwiched between Reduced Graphene Oxide Sheets as Lithium Ion Battery Anodes. *ACS Nano* **2013**, *7* (2), 1437–1445.
119. Liu, N.; Lu, Z.; Zhao, J.; McDowell, M. T.; Lee, H. W.; Zhao, W.; Cui, Y. A Pomegranate-Inspired Nanoscale Design for Large-Volume-Change Lithium Battery Anodes. *Nat. Nanotechnol.* **2014**, *9* (3), 187–192.
120. Chang, J.; Huang, X.; Zhou, G.; Cui, S.; Hallac, P. B.; Jiang, J.; Hurley, P. T.; Chen, J. Multilayered Si Nanoparticle/reduced Graphene Oxide Hybrid as a High-Performance Lithium-Ion Battery Anode. *Adv. Mater.* **2014**, *26* (5), 758–764.
121. Lu, Z.; Liu, N.; Lee, H. W.; Zhao, J.; Li, W.; Li, Y.; Cui, Y. Nonfilling Carbon Coating of

- Porous Silicon Micrometer-Sized Particles for High-Performance Lithium Battery Anodes. *ACS Nano* **2015**, *9* (3), 2540–2547.
122. Xu, Q.; Li, J. Y.; Sun, J. K.; Yin, Y. X.; Wan, L. J.; Guo, Y. G. Watermelon-Inspired Si/C Microspheres with Hierarchical Buffer Structures for Densely Compacted Lithium-Ion Battery Anodes. *Adv. Energy Mater.* **2017**, *7* (3), 1–6.
123. Chen, S.; Shen, L.; van Aken, P. A.; Maier, J.; Yu, Y. Dual-Functionalized Double Carbon Shells Coated Silicon Nanoparticles for High Performance Lithium-Ion Batteries. *Adv. Mater.* **2017**, *29* (21).
124. Heinrich, T.; Klett, U.; Fricke, J. Aerogels-Nanoporous Materials Part I: Sol-Gel Process and Drying of Gels. *J. Porous Mater.* **1995**, *1* (1), 7–17.
125. Fricke, J. Aerogels — Highly Tenuous Solids with Fascinating Properties. *J. Non. Cryst. Solids* **1988**, *100* (1–3), 169–173.
126. Hu, Z.; Srinivasan, M. P.; Ni, Y. Preparation of Mesoporous High-Surface-Area Activated Carbon. *Adv. Mater.* **2000**, *12* (1), 62–65.
127. Kistler, S. S. Coherent Expanded-Aerogels. *J. Phys. Chem.* **1931**, *36* (1), 52–64.
128. Teichner, S. J.; Nicolaon, G. A.; Vicarini, M. A.; Gardes, G. E. E. Inorganic Oxide Aerogels. *Adv. Colloid Interface Sci.* **1976**, *5* (3), 245–273.
129. Du, A.; Zhou, B.; Zhang, Z.; Shen, J. A Special Material or a New State of Matter: A Review and Reconsideration of the Aerogel. *Materials* **2013**, *6* (3), 941–968.
130. Soleimani Dorcheh, A.; Abbasi, M. H. Silica Aerogel; Synthesis, Properties and Characterization. *J. Mater. Process. Technol.* **2008**, *199* (1–3), 10–26.
131. Gurav, J. L.; Jung, I.-K.; Park, H.-H.; Kang, E. S.; Nadargi, D. Y. Silica Aerogel: Synthesis and Applications. *J. Nanomater.* **2010**, *2010*, 1–11.
132. Schmidt, M.; Schwertfeger, F. Applications for Silica Aerogel Products. *J. Non. Cryst. Solids* **1998**, *225*, 364–368.
133. Pajonk, G. M. Some Applications of Silica Aerogels. *Colloid Polym. Sci.* **2003**, *281* (7), 637–651.

134. Maleki, H.; Durães, L.; Portugal, A. An Overview on Silica Aerogels Synthesis and Different Mechanical Reinforcing Strategies. *J. Non. Cryst. Solids* **2014**, *385*, 55–74.
135. Pierre, A. C.; Pajonk, G. M. Chemistry of Aerogels and Their Applications. *Chem. Rev.* **2002**, *102*, 4243–4265.
136. Lofgreen, J. E.; Ozin, G. A. Controlling Morphology and Porosity to Improve Performance of Molecularly Imprinted Sol–gel Silica. *Chem. Soc. Rev.* **2014**, *43* (3), 911–933.
137. Schubert, U.; Hüsing, N. *Synthesis of Inorganic Materials*, Second, Revised and Updated Edition. Wiley-VCH: Germany, 2005, 205–206.
138. Bisson, A.; Rigacci, A.; Lecomte, D.; Rodier, E.; Achard, P. Drying of Silica Gels to Obtain Aerogels: Phenomenology and Basic Techniques. *Dry. Technol.* **2003**, *21* (4), 593–628.
139. Tewari, P. H.; Hunt, A. J.; Lofftus, K. D. Ambient-Temperature Supercritical Drying of Transparent Silica Aerogels. *Mater. Lett.* **1985**, *3* (9–10), 363–367.
140. Scherer, G. W. Freezing Gels. *J. Non. Cryst. Solids* **1993**, *155* (1), 1–25.
141. Kalinin, S. V.; Kheifets, L. I.; Mamchik, A. I.; Knot'ko, A. G.; Vertegel, A. A. Influence of the Drying Technique on the Structure of Silica Gels. *J. Sol-Gel Sci. Technol.* **1999**, *15* (1), 31–35.
142. Hrubesh, L. W.; Pekala, R. W. Thermal Properties of Organic and Inorganic Aerogels. *J. Mater. Res.* **1994**, *9* (3), 731–738.
143. Yoldas, B. E.; Annen, M. J.; Bostaph, J. Chemical Engineering of Aerogel Morphology Formed under Nonsupercritical Conditions for Thermal Insulation. *Chem. Mater.* **2000**, *12* (8), 2475–2484.
144. Thapliyal, P. C.; Singh, K. Aerogels as Promising Thermal Insulating Materials: An Overview. *J. Mater.* **2014**, *2014*, 10.
145. Nardecchia, S.; Carriazo, D.; Ferrer, M. L.; Gutiérrez, M. C.; del Monte, F. Three Dimensional Macroporous Architectures and Aerogels Built of Carbon Nanotubes and/or Graphene: Synthesis and Applications. *Chem. Soc. Rev.* **2013**, *42* (2), 794–830.
146. Ma, Y.; Chen, Y. Three-Dimensional Graphene Networks: Synthesis, Properties and

- Applications. *Natl. Sci. Rev.* **2015**, *2* (1), 40–53.
147. Gorgolis, G.; Galiotis, C. Graphene Aerogels: A Review. *2D Mater.* **2017**, *4* (3), 032001.
148. Mao, J.; Iocozzia, J.; Huang, J.; Meng, K.; Lai, Y.; Lin, Z. Graphene Aerogels for Efficient Energy Storage and Conversion. *Energy Environ. Sci.* **2018**, *11*, 772–799.
149. Chen, Z.; Li, H.; Tian, R.; Duan, H.; Guo, Y.; Chen, Y.; Zhou, J.; Zhang, C.; Dugnani, R.; Liu, H. Three Dimensional Graphene Aerogels as Binder-Less, Freestanding, Elastic and High-Performance Electrodes for Lithium-Ion Batteries. *Sci. Rep.* **2016**, *6*, 1–9.
150. Yu, Z.; McInnis, M.; Calderon, J.; Seal, S.; Zhai, L.; Thomas, J. Functionalized Graphene Aerogel Composites for High-Performance Asymmetric Supercapacitors. *Nano Energy* **2015**, *11*, 611–620.
151. Zhu, C.; Liu, T.; Qian, F.; Han, T. Y. J.; Duoss, E. B.; Kuntz, J. D.; Spadaccini, C. M.; Worsley, M. A.; Li, Y. Supercapacitors Based on Three-Dimensional Hierarchical Graphene Aerogels with Periodic Macropores. *Nano Lett.* **2016**, *16* (6), 3448–3456.
152. Ren, L.; Hui, K. S.; Hui, K. N. Self-Assembled Free-Standing Three-Dimensional Nickel Nanoparticle/graphene Aerogel for Direct Ethanol Fuel Cells. *J. Mater. Chem. A* **2013**, *1* (18), 5689.
153. Bi, H.; Xie, X.; Yin, K.; Zhou, Y.; Wan, S.; He, L.; Xu, F.; Banhart, F.; Sun, L.; Ruoff, R. S. Spongy Graphene as a Highly Efficient and Recyclable Sorbent for Oils and Organic Solvents. *Adv. Funct. Mater.* **2012**, *22* (21), 4421–4425.
154. Wu, Z.; Yang, S.; Sun, Y.; Parvez, K.; Feng, X.; Müllen, K. 3D Nitrogen-Doped Graphene Aerogel-Supported Fe₃O₄ Nanoparticles as Efficient Electrocatalysts for the Oxygen Reduction Reaction. *J. Am. Chem. Soc.* **2012**, *134* (22), 9082–9085.
155. Yin, H.; Zhang, C.; Liu, F.; Hou, Y. Hybrid of Iron Nitride and Nitrogen-Doped Graphene Aerogel as Synergistic Catalyst for Oxygen Reduction Reaction. *Adv. Funct. Mater.* **2014**, *24* (20), 2930–2937.
156. Wang, J.; Ellsworth, M. W. Graphene Aerogels. *ECS Trans.* **2009**, *19* (5), 241–247.
157. Sheng, K. X.; Xu, Y. X.; Li, C.; Shi, G. Q. High-Performance Self-Assembled Graphene

- Hydrogels Prepared by Chemical Reduction of Graphene Oxide. *New Carbon Mater.* **2011**, *26* (1), 9–15.
158. Chen, W.; Yan, L. In Situ Self-Assembly of Mild Chemical Reduction Graphene for Three-Dimensional Architectures. *Nanoscale* **2011**, *3* (8), 3132.
159. Sheng, K.; Sun, Y.; Li, C.; Yuan, W.; Shi, G. Ultrahigh-Rate Supercapacitors Based on Electrochemically Reduced Graphene Oxide for AC Line-Filtering. *Sci. Rep.* **2012**, *2*, 3–7.
160. Li, Y.; Sheng, K.; Yuan, W.; Shi, G. A High-Performance Flexible Fibre-Shaped Electrochemical Capacitor Based on Electrochemically Reduced Graphene Oxide. *Chem. Commun.* **2013**, *49* (3), 291–293.
161. Yuxi Xu, Kaixuan Sheng, C. L.; Shi, G. Self-Assembled Graphene Hydrogel. *ACS Nano* **2010**, *4* (7), 4324–4330.
162. Han, Z.; Tang, Z.; Li, P.; Yang, G.; Zheng, Q.; Yang, J. Ammonia Solution Strengthened Three-Dimensional Macro-Porous Graphene Aerogel. *Nanoscale* **2013**, *5* (12), 5462.
163. Choi, B. G.; Yang, M.; Hong, W. H.; Choi, J. W.; Huh, Y. S. 3D Macroporous Graphene Frameworks for Supercapacitors with High Energy and Power Densities. *ACS Nano* **2012**, *6* (5), 4020–4028.
164. Wang, Z.; Shen, X.; Han, N. M.; Liu, X.; Wu, Y.; Ye, W.; Kim, J. K. Ultralow Electrical Percolation in Graphene Aerogel/Epoxy Composites. *Chem. Mater.* **2016**, *28* (18), 6731–6741.
165. Hu, H.; Zhao, Z.; Wan, W.; Gogotsi, Y.; Qiu, J. Ultralight and Highly Compressible Graphene Aerogels. *Adv. Mater.* **2013**, *25* (15), 2219–2223.
166. Cong, H. P.; Ren, X. C.; Wang, P.; Yu, S. H. Macroscopic Multifunctional Graphene-Based Hydrogels and Aerogels by a Metal Ion Induced Self-Assembly Process. *ACS Nano* **2012**, *6* (3), 2693–2703.
167. Worsley, M. a; Pauzauskie, P. J.; Olson, T. Y.; Biener, J.; Satcher Jr., J. H.; Baumann, T. F. Synthesis of Graphene Aerogel with High Electrical Conductivity. *J. Am. Chem. Soc.* **2010**, *132*, 14067–14069.

168. Hummers, W. S.; Offeman, R. E. Preparation of Graphitic Oxide. *J. Am. Chem. Soc.* **1958**, *80* (6), 1339.
169. Dreyer, D. R.; Park, S.; Bielawski, C. W.; Ruoff, R. S. Graphite Oxide. *Chem. Soc. Rev.* **2010**, *39* (1), 228–240.
170. Marcano, D. C.; Kosynkin, D. V.; Berlin, J. M.; Sinitskii, A.; Sun, Z. Z.; Slesarev, A.; Alemany, L. B.; Lu, W.; Tour, J. M. Improved Synthesis of Graphene Oxide. *ACS Nano* **2010**, *4* (8), 4806–4814.
171. Zhang, X.; Sui, Z.; Xu, B.; Yue, S.; Luo, Y.; Zhan, W.; Liu, B. Mechanically Strong and Highly Conductive Graphene Aerogel and Its Use as Electrodes for Electrochemical Power Sources. *J. Mater. Chem.* **2011**, *21* (18), 6494.
172. **a)** Carlson, A.; Bowen, A. M.; Huang, Y.; Nuzzo, R. G.; Rogers, J. A. Transfer Printing Techniques for Materials Assembly and Micro/Nanodevice Fabrication. *Adv. Mater.* **2012**, *24* (39), 5284–5318. **b)** Cao, Q.; Kim, H. S.; Pimparkar, N.; Kulkarni, J. P.; Wang, C.; Shim, M.; Roy, K.; Alam, M. A.; Rogers, J. A. Medium-Scale Carbon Nanotube Thin-Film Integrated Circuits on Flexible Plastic Substrates. *Nature* **2008**, *454* (7203), 495–500. **c)** Kim, T. H.; Cho, K. S.; Lee, E. K.; Lee, S. J.; Chae, J.; Kim, J. W.; Kim, D. H.; Kwon, J. Y.; Amaratunga, G.; Lee, S. Y.; et al. Full-Colour Quantum Dot Displays Fabricated by Transfer Printing. *Nat. Photonics* **2011**, *5* (3), 176–182. **d)** Kim, H.; Brueckner, E.; Song, J.; Li, Y.; Kim, S.; Lu, C.; Sulkin, J.; Choquette, K.; Huang, Y.; Nuzzo, R. G.; Rogers, J. A. Unusual Strategies for Using Indium Gallium Nitride Grown on Silicon (111) for Solid-State Lighting. *Proc. Natl. Acad. Sci.* **2011**, *108* (25), 10072.
173. Meitl, M. A.; Zhu, Z.-T.; Kumar, V.; Lee, K. J.; Feng, X.; Huang, Y. Y.; Adesida, I.; Nuzzo, R. G.; Rogers, J. A. Transfer Printing by Kinetic Control of Adhesion to an Elastomeric Stamp. *Nat. Mater.* **2006**, *5* (1), 33–38.
174. Allen, M. J.; Tung, V. C.; Gomez, L.; Xu, Z.; Chen, L. M.; Nelson, K. S.; Zhou, C.; Kaner, R. B.; Yang, Y. Soft Transfer Printing of Chemically Converted Graphene. *Adv. Mater.* **2009**, *21* (20), 2098–2102.
175. Kim, B. H.; Nam, S.; Oh, N.; Cho, S. Y.; Yu, K. J.; Lee, C. H.; Zhang, J.; Deshpande, K.;

- Trefonas, P.; Kim, J. H.; et al. Multilayer Transfer Printing for Pixelated, Multicolor Quantum Dot Light-Emitting Diodes. *ACS Nano* **2016**, *10* (5), 4920–4925.
176. Jiao, L.; Fan, B.; Xian, X.; Wu, Z.; Zhang, J.; Liu, Z. Creation of Nanostructures with Poly(methyl Methacrylate)-Mediated Nanotransfer Printing. *J. Am. Chem. Soc.* **2008**, *130* (38), 12612–12613.
177. Suk, J. W.; Kitt, A.; Magnuson, C. W.; Hao, Y.; Ahmed, S.; An, J.; Swan, A. K.; Goldberg, B. B.; Ruoff, R. S. Transfer of CVD-Grown Monolayer Graphene onto Arbitrary Substrates. *ACS Nano* **2011**, *5* (9), 6916–6924.
178. Liu, Y.; Cheng, R.; Liao, L.; Zhou, H.; Bai, J.; Liu, G.; Liu, L.; Huang, Y.; Duan, X. Plasmon Resonance Enhanced Multicolour Photodetection by Graphene. *Nat. Commun.* **2011**, *2* (1), 577–579.
179. Xu, Q.; Rioux, R. M.; Dickey, M. D.; Whitesides, G. M. Nanoskiving: A New Method to Produce Arrays of Nanostructures. *Acc. Chem. Res.* **2008**, *41* (12), 1566–1577.
180. Reina, A.; Son, H.; Jiao, L.; Fan, B.; Dresselhaus, M. S.; Liu, Z.; Kong, J. Transferring and Identification of Single- and Few-Layer Graphene on Arbitrary Substrates. *J. Phys. Chem. C* **2008**, *112* (46), 17741–17744.
181. Reina, A., Jia, X., Ho, J., Nezich, D., Son, H., Bulovic, V., Dresselhaus, M.S. and Kong, J. Large Area, Few-Layer Graphene Films on Arbitrary Substrates by Chemical Vapor Deposition. *Nano Lett.* **2008**, *9* (1), 30–35.
182. Schneider, G. F.; Calado, V. E.; Zandbergen, H.; Vandersypen, L. M. K.; Dekker, C. Wedging Transfer of Nanostructures. *Nano Lett.* **2010**, *10* (5), 1912–1916.
183. Lee, C. H.; Kim, D. R.; Cho, I. S.; William, N.; Wang, Q.; Zheng, X. Peel-and-Stick: Fabricating Thin Film Solar Cell on Universal Substrates. *Sci. Rep.* **2012**, *2*, 2–5.
184. Li, H.; Wu, J.; Huang, X.; Yin, Z.; Liu, J.; Zhang, H. A Universal, Rapid Method for Clean Transfer of Nanostructures onto Various Substrates. *ACS Nano* **2014**, *8* (7), 6563–6570.
185. Choi, M. K.; Yang, J.; Kang, K.; Kim, D. C.; Choi, C.; Park, C.; Kim, S. J.; Chae, S. I.; Kim, T. H.; Kim, J. H.; et al. Wearable Red-Green-Blue Quantum Dot Light-Emitting Diode

- Array Using High-Resolution Intaglio Transfer Printing. *Nat. Commun.* **2015**, *6*, 1–8.
186. Ma, X.; Liu, Q.; Xu, D.; Zhu, Y.; Kim, S.; Cui, Y.; Zhong, L.; Liu, M. Capillary-Force-Assisted Clean-Stamp Transfer of Two-Dimensional Materials. *Nano Lett.* **2017**, *17* (11), 6961–6967.
187. Arai, E.; Kamei, K.; Kawasaki, A.; Takagi, F.; Shirai, K.; Orihara, Y. Patent US 4229239, 1980.
188. Water Transfer Printing Films - DIC Corporation
http://www.dic-global.com/us/en/products/decorative_materials/transcript.html.
189. <http://www.liquidcustoms.ca/gallery>
1. Hüsing, N.; Schubert, U. Aerogels—Airy Materials: Chemistry, Structure, and Properties. *Angew. Chem. Int. Ed.* **1998**, *37*, 22–45.
 2. Pierre, A. C.; Pajonk, G. M. Chemistry of Aerogels and Their Applications. *Chem. Rev.* **2002**, *102*, 4243–4265.
 3. Hrubesh, L. W. Aerogel Applications. *J. Non. Cryst. Solids* **1998**, *225*, 335–342.
 4. Schmidt, M.; Schwertfeger, F. Applications for Silica Aerogel Products. *J. Non. Cryst. Solids* **1998**, *225*, 364–368.
 5. Melde, B. J.; Johnson, B. J.; Charles, P. T. Mesoporous Silicate Materials in Sensing. *Sensors* **2008**, *8*, 5202–5228.
 6. Pajonk, G. M. Aerogel Catalysts. *Appl. Catal.* **1991**, *72*, 217–266.
 7. Pajonk, G. M. Catalytic Aerogels. *Catal. Today* **1997**, *35*, 319–337.
 8. Rolison, D. R. Catalytic Nanoarchitectures: the Importance of Nothing and the Unimportance of Periodicity. *Science* **2003**, *299*, 1698–1701.
 9. Wu, Z.; Yang, S.; Sun, Y.; Parvez, K.; Feng, X.; Müllen, K. 3D Nitrogen-Doped Graphene Aerogel-Supported Fe₃O₄ Nanoparticles as Efficient Electrocatalysts for the Oxygen Reduction Reaction. *J. Am. Chem. Soc.* **2012**, *134*, 9082–9085.
 10. Hrubesh, L. W.; Poco, J. F. Thin Aerogel Films for Optical, Thermal, Acoustic and Electronic Applications. *J. Non. Cryst. Solids* **1995**, *188*, 46–53.
 11. Fricke, J.; Tillotson, T. Aerogels: Production, Characterization, and Applications. *Thin Solid Films* **1997**, *297*, 212–223.

12. Akimov, Y. K. Fields of Application of Aerogels (Review). *Instrum. Exp. Tech.* **2003**, *46* (3), 287–299.
13. Frackowiak, E.; Béguin, F. Carbon Materials for the Electrochemical Storage of Energy in Capacitors. *Carbon* **2001**, *39*, 937–950.
14. Rolison, D. R.; Long, J. W.; Lytle, J. C.; Fischer, A. E.; Rhodes, C. P.; McEvoy, T. M.; Bourg, M. E.; Lubers, A. M. Multifunctional 3D Nanoarchitectures for Energy Storage and Conversion. *Chem. Soc. Rev.* **2009**, *38*, 226–252.
15. Teichner, S. J.; Nicolaon, G. A.; Vicarini, M. A.; Gardes, G. E. E. Inorganic Oxide Aerogels. *Adv. Colloid Interface Sci.* **1976**, *5*, 245–273.
16. Soleimani Dorcheh, A.; Abbasi, M. H. Silica Aerogel; Synthesis, Properties and Characterization. *J. Mater. Process. Technol.* **2008**, *199*, 10–26.
17. Fricke, J. Aerogels—Highly Tenuous Solids with Fascinating Properties. *J. Non. Cryst. Solids* **1988**, *100*, 169–173.
18. Morris, C. A.; Anderson, M. L.; Stroud, R. M.; Merzbacher, C. I.; Rolison, D. R. Silica Sol as A Nanoglue: Flexible Synthesis of Composite Aerogels. *Science* **1999**, *284*, 622–624.
19. Kim, J.; Nakanishi, H.; Pollanen, J.; Smoukov, S.; Halperin, W. P.; Grzybowski, B. A. Nanoparticle–Loaded Aerogels and Layered Aerogels Cast from Sol–Gel Mixtures. *Small* **2011**, *7* (18), 2568–2572.
20. Veinot, J. G. C. Synthesis, Surface Functionalization, and Properties of Freestanding Silicon Nanocrystals. *Chem. Commun.* **2006**, *40*, 4160–4168.
21. Dasog, M.; Reyes, G. B. D. L.; Titova, L. V.; Hegmann, F. A.; Veinot, J. G. C. Size vs Surface: Tuning the Photoluminescence of Freestanding Silicon Nanocrystals Across the Visible Spectrum *via* Surface Groups. *ACS Nano* **2014**, *8* (9), 9636–9648.
22. Park, J. H.; Gu, L.; von Maltzahn, G.; Ruoslahti, E.; Bhatia, S. N.; Sailor, M. J. Biodegradable Luminescent Porous Silicon Nanoparticles for *In Vivo* Applications. *Nat. Mater.* **2009**, *8* (4), 331–336.
23. Erogbogbo, F.; Yong, K. -T.; Roy, I.; Xu, G.; Prasad, P. N.; Swihart, M. T. Synthesis and Enhanced Light-Emission of Si Nanocrystals Embedded in Silicon Oxide Nanowires. *ACS Nano* **2008**, *2* (5), 873–878.

24. Gonzalez, C. M.; Iqbal, M.; Dasog, M.; Piercey, D. G.; Lockwood, R.; Klapötke, T. M.; Veinot, J. G. C. Detection of High-Energy Compounds Using Photoluminescent Silicon Nanocrystal Paper Based Sensors. *Nanoscale* **2014**, *6*, 2608–2612.
25. Lockwood, R.; Veinot, J. G. C.; Meldrum, A. Sensing Water and Alcohol Vapors with Freestanding Silicon Quantum Dots. *Sens. Lett.* **2013**, *11*, 1535–1540.
26. Kim, H.; Seo, M.; Park, M. H.; Cho, J. A Critical Size of Silicon Nano-Anodes for Lithium Rechargeable Batteries. *Angew. Chem. Int. Ed.* **2010**, *49*, 2146–2149.
27. Graetz, J.; Ahn, C. C.; Yazami, R.; Fultz, B. Highly Reversible Lithium Storage in Nanostructured Silicon. *Electrochem. Solid-State Lett.* **2003**, *6* (9), A194-A197.
28. Zhai, Y.; Dasog, M.; Snitynsky, R. B.; Purkait, T. K.; Aghajamali, M.; Hahn, A. H.; Sturdy, C. B.; Lowary, T. L.; Veinot, J. G. C. Water-Soluble Photoluminescent D-Mannose and L-Alanine Functionalized Silicon Nanocrystals and Their Application to Cancer Cell Imaging. *J. Mater. Chem. B* **2014**, *2*, 8427–8433.
29. Zhong, Y.; Peng, F.; Bao, F.; Wang, S.; Ji, X.; Yang, L.; Su, Y.; Lee, S. T.; He, Y. Large-Scale Aqueous Synthesis of Fluorescent and Biocompatible Silicon Nanoparticles and Their Use as Highly Photostable Biological Probes. *J. Am. Chem. Soc.* **2013**, *135*, 8350–8356.
30. Xu, Z.; Wang, D.; Guan, M.; Liu, X.; Yang, Y.; Wei, D.; Zhao, C.; Zhang, H. Photoluminescent Silicon Nanocrystal-Based Multifunctional Carrier for pH-Regulated Drug Delivery. *ACS Appl. Mater. Interfaces* **2012**, *4*, 3424 – 3431.
31. Kazes, M.; Lewis, D. Y.; Banin, U. Method for Preparation of Semiconductor Quantum-Rod Lasers in A Cylindrical Microcavity. *Adv. Funct. Mater.* **2004**, *14* (10), 957–962.
32. Maier-Flaig, F.; Rinck, J.; Stephan, M.; Bocksrocker, T.; Bruns, M.; Kübel, C.; Powell, A. K.; Ozin, G. A.; Lemmer, U. Multicolor Silicon Light-Emitting Diodes (SiLEDs). *Nano Lett.* **2013**, *13*, 475–480.
33. Conibeer, G.; Green, M.; Corkish, R.; Cho, Y.; Cho, E. C.; Jiang, C. W.; Fangsuwannarak, T.; Pink, E.; Huang, Y.; Puzzer, T.; Trupke, T.; Richards, B.; Shalav, A.; Lin, K. L. Silicon Nanostructures for Third Generation Photovoltaic Solar Cells. *Thin Solid Films* **2006**, *511-512*, 654–662.
34. Priolo, F.; Gregorkiewicz, T.; Galli, M.; Krauss, T. F. Silicon Nanostructures for Photonics and Photovoltaics. *Nat. Nanotechnol.* **2014**, *9*, 19–32.

35. Perez-Wurfl, I.; Hao, X.; Gentle, A.; Kim, D. H.; Conibeer, G.; Green, M. A. Si Nanocrystal p-i-n Diodes Fabricated on Quartz Substrates for Third Generation Solar Cell Applications. *Appl. Phys. Lett.* **2009**, *95*, 153506-3.
36. Borsella, E.; Falconieri, M.; Botti, S.; Martelli, S.; Bignoli, F.; Costa, L.; Grandi, S.; Sangaletti, L.; Allieri, B.; Depero, L. Optical and Morphological Characterization of Si Nanocrystals/Silica Composites Prepared by Sol–Gel Processing. *Mater. Sci. Eng. B* **2001**, *79*, 55–62.
37. Amonkosolpan, J.; Wolverson, D.; Goller, B.; Polisski, S.; Kovalev, D.; Rollings, M.; Grogan, M. D. W.; Birks, T. A. Porous Silicon Nanocrystals in A Silica Aerogel Matrix. *Nanoscale Res. Lett.* **2012**, *7*, 397-403.
38. Karlash, A. Y.; Skryshevsky, V. A.; Kuznetsov, G. V.; Kladko, V. P. Evolution of Visible Photoluminescence of Si Quantum Dots Embedded in Silicon Oxide Matrix. *J. Alloys Compd.* **2013**, *577*, 283–287.
39. Hessel, C. M.; Henderson, E. J.; Veinot, J. G. C. Hydrogen Silsesquioxane: A Molecular Precursor for Nanocrystalline Si-SiO₂ Composites and Freestanding Hydride-Surface-Terminated Silicon Nanoparticles. *Chem. Mater.* **2006**, *1*, 6139–6146.
40. Yang, Z.; Iqbal, M.; Dobbie, A. R.; Veinot, J. G. C. Surface-Induced Alkene Oligomerization: Does Thermal Hydrosilylation Really Lead to Monolayer Protected Silicon Nanocrystals?. *J. Am. Chem. Soc.* **2013**, *135*, 17595–17601.
41. Hessel, C. M.; Rasch, M. R.; Hueso, J. L.; Goodfellow, B. W.; Akhavan, V. A.; Puvanakrishnan, P.; Tunnel, J. W.; Korgel, B. A. Alkyl Passivation and Amphiphilic Polymer Coating of Silicon Nanocrystals for Diagnostic Imaging. *Small* **2010**, *6* (18), 2026–2034.
42. Lin, C. A. J.; Sperling, R. A.; Li, J. K.; Yang, T. Y.; Li, P. Y.; Zanella, M.; Chang, W. H.; Parak, W. J. Design of An Amphiphilic Polymer for Nanoparticle Coating and Functionalization. *Small* **2008**, *4* (3), 334–341.
43. Anderson, M. L.; Morris, C. A.; Stroud, R. M.; Merzbacher, C. I.; Rolison, D. R. Colloidal Gold Aerogels: Preparation, Properties, and Characterization. *Langmuir* **1999**, *15* (3), 674–681.

44. Russo, R. E.; Hunt, A. J. Comparison of Ethyl versus Methyl Sol-Gels for Silica Aerogels Using Polar Nephelometry. *J. Non-Cryst. Solids* **1986**, *86*, 219–230.
45. Purkait, T. K.; Iqbal, M.; Wahl, M. H.; Gottschling, K.; Gonzalez, C. M.; Islam, M. A.; Veinot, J. G. C. Borane-Catalyzed Room Temperature Hydrosilylation of Alkenes/Alkynes on Silicon Nanocrystal Surfaces. *J. Am. Chem. Soc.* **2014**, *136*, 17914–17917.
46. Liu, S.; Kobayashi, M.; Sato, S.; Kimura, K. Synthesis of Silicon Nanowires and Nanoparticles by Arc-Discharge in Water. *Chem. Commun.* **2005**, *1*, 4690–4692.
47. Ledoux, G.; Guillois, O.; Porterat, D.; Reynaud, C.; Huisken, F.; Kohn, B.; Paillard, V. Photoluminescence Properties of Silicon Nanocrystals as A Function of Their Size. *Phys. Rev. B* **2000**, *62*, 15942–15951.
48. Kruk, M.; Jaroniec, M. Gas Adsorption Characterization of Ordered Organic-Inorganic Nanocomposite Materials. *Chem. Mater.* **2001**, *13*, 3169–3183.
1. Bruce, P. G.; Scrosati, B.; Tarascon, J. M. Nanomaterials for Rechargeable Lithium Batteries. *Angew. Chemie - Int. Ed.* **2008**, *47* (16), 2930–2946.
2. Teki, R.; Krishnan, R.; Parker, T. C.; Lu, T. M.; Datta, M. K.; Kumta, P. N.; Koratkar, N. Nanostructured Silicon Anodes for Lithium Ion Rechargeable Batteries. *Small* **2009**, *5* (20), 2236–2242.
3. Kasavajjula, U.; Wang, C.; Appleby, A. J. Nano- and Bulk-Silicon-Based Insertion Anodes for Lithium-Ion Secondary Cells. *J. Power Sources* **2007**, *163* (2), 1003–1039.
4. Wu, H.; Cui, Y. Designing Nanostructured Si Anodes for High Energy Lithium Ion Batteries. *Nano Today* **2012**, *7* (5), 414–429.
5. Zamfir, M. R.; Nguyen, H. T.; Moyen, E.; Lee, Y. H.; Pribat, D. Silicon Nanowires for Li-Based Battery Anodes: A Review. *J. Mater. Chem. A* **2013**, *1* (34), 9566.
6. Su, X.; Wu, Q.; Li, J.; Xiao, X.; Lott, A.; Lu, W.; Sheldon, B. W.; Wu, J. Silicon-Based Nanomaterials for Lithium-Ion Batteries: A Review. *Adv. Energy Mater.* **2014**, *4*, 1300882.
7. Liu, X. H.; Zhong, L.; Huang, S.; Mao, S. X.; Zhu, T.; Huang, J. Y. Size-Dependent Fracture of Silicon Nanoparticles during Lithiation. *ACS Nano* **2012**, *6* (2), 1522–1531.
8. Chockla, A. M.; Harris, J. T.; Akhavan, V. A.; Bogart, T. D.; Holmberg, V. C.; Steinhagen, C.; Mullins, C. B.; Stevenson, K. J.; Korgel, B. A. Silicon Nanowire Fabric as a Lithium Ion Battery Electrode Material. *J. Am. Chem. Soc.* **2011**, *133* (51), 20914–20921.

9. Nguyen, H. T.; Yao, F.; Zamfir, M. R.; Biswas, C.; So, K. P.; Lee, Y. H.; Kim, S. M.; Cha, S. N.; Kim, J. M.; Pribat, D. Highly Interconnected Si Nanowires for Improved Stability Li-Ion Battery Anodes. *Adv. Energy Mater.* **2011**, *1* (6), 1154–1161.
10. Park, M.; Kim, M. G.; Joo, J.; Kim, K.; Kim, J.; Ahn, S.; Cui, Y.; Cho, J. Silicon Nanotube Battery Anodes. *Nano Lett.* **2009**, *9* (11), 3844–3847.
11. Wu, H.; Chan, G.; Choi, J. W.; Ryu, I.; Yao, Y.; McDowell, M. T.; Lee, S. W.; Jackson, A.; Yang, Y.; Hu, L.; et al. Stable Cycling of Double-Walled Silicon Nanotube Battery Anodes through Solid-Electrolyte Interphase Control. *Nat. Nanotechnol.* **2012**, *7* (5), 310–315.
12. Yao, Y.; McDowell, M. T.; Ryu, I.; Wu, H.; Liu, N.; Hu, L.; Nix, W. D.; Cui, Y. Interconnected Silicon Hollow Nanospheres for Lithium-Ion Battery Anodes with Long Cycle Life. *Nano Lett.* **2011**, *11* (7), 2949–2954.
13. Zhao, Y.; Liu, X.; Li, H.; Zhai, T.; Zhou, H. Hierarchical Micro/nano Porous Silicon Li-Ion Battery Anodes. *Chem. Commun.* **2012**, *48* (42), 5079.
14. Zhu, J.; Gladden, C.; Liu, N.; Cui, Y.; Zhang, X. Nanoporous Silicon Networks as Anodes for Lithium Ion Batteries. *Phys. Chem. Chem. Phys.* **2013**, *15* (2), 440–443.
15. Szczech, J. R.; Jin, S. Nanostructured Silicon for High Capacity Lithium Battery Anodes. *Energy Environ. Sci.* **2011**, *4* (1), 56–72.
16. Wang, B.; Li, X.; Zhang, X.; Luo, B.; Jin, M.; Liang, M.; Dayeh, S. A.; Picraux, S. T.; Zhi, L. Adaptable Silicon-Carbon Nanocables Sandwiched between Reduced Graphene Oxide Sheets as Lithium Ion Battery Anodes. *ACS Nano* **2013**, *7* (2), 1437–1445.
17. Liu, N.; Lu, Z.; Zhao, J.; McDowell, M. T.; Lee, H. W.; Zhao, W.; Cui, Y. A Pomegranate-Inspired Nanoscale Design for Large-Volume-Change Lithium Battery Anodes. *Nat. Nanotechnol.* **2014**, *9* (3), 187–192.
18. Chang, J.; Huang, X.; Zhou, G.; Cui, S.; Hallac, P. B.; Jiang, J.; Hurley, P. T.; Chen, J. Multilayered Si Nanoparticle/reduced Graphene Oxide Hybrid as a High-Performance Lithium-Ion Battery Anode. *Adv. Mater.* **2014**, *26* (5), 758–764.
19. Lu, Z.; Liu, N.; Lee, H. W.; Zhao, J.; Li, W.; Li, Y.; Cui, Y. Nonfilling Carbon Coating of Porous Silicon Micrometer-Sized Particles for High-Performance Lithium Battery Anodes. *ACS Nano* **2015**, *9* (3), 2540–2547.
20. Xu, Q.; Li, J. Y.; Sun, J. K.; Yin, Y. X.; Wan, L. J.; Guo, Y. G. Watermelon-Inspired Si/C

- Microspheres with Hierarchical Buffer Structures for Densely Compacted Lithium-Ion Battery Anodes. *Adv. Energy Mater.* **2017**, 7 (3), 1–6.
21. Chen, S.; Shen, L.; van Aken, P. A.; Maier, J.; Yu, Y. Dual-Functionalized Double Carbon Shells Coated Silicon Nanoparticles for High Performance Lithium-Ion Batteries. *Adv. Mater.* **2017**, 29 (21).
 22. Gorgolis, G.; Galiotis, C. Graphene Aerogels: A Review. *2D Mater.* **2017**, 4 (3).
 23. Ma, Y.; Chen, Y. Three-Dimensional Graphene Networks: Synthesis, Properties and Applications. *Natl. Sci. Rev.* **2015**, 2 (1), 40–53.
 24. Chen, W.; Yan, L. In Situ Self-Assembly of Mild Chemical Reduction Graphene for Three-Dimensional Architectures. *Nanoscale* **2011**, 3 (8), 3132.
 25. Zhang, X.; Sui, Z.; Xu, B.; Yue, S.; Luo, Y.; Zhan, W.; Liu, B. Mechanically Strong and Highly Conductive Graphene Aerogel and Its Use as Electrodes for Electrochemical Power Sources. *J. Mater. Chem.* **2011**, 21 (18), 6494.
 26. Xu, B.; Wu, H.; Lin, C. X.; Wang, B.; Zhang, Z.; Zhao, X. S. Stabilization of Silicon Nanoparticles in Graphene Aerogel Framework for Lithium Ion Storage. *RSC Adv.* **2015**, 5 (39), 30624–30630.
 27. Hu, X.; Jin, Y.; Zhu, B.; Tan, Y.; Zhang, S.; Zong, L.; Lu, Z.; Zhu, J. Free-Standing Graphene-Encapsulated Silicon Nanoparticle Aerogel as an Anode for Lithium Ion Batteries. *ChemNanoMat* **2016**, 2 (7), 671–674.
 28. Hessel, C. M.; Henderson, E. J.; Veinot, J. G. C. Hydrogen Silsesquioxane: A Molecular Precursor for Nanocrystalline Si-SiO₂ Composites and Freestanding Hydride-Surface-Terminated Silicon Nanoparticles. *Chem. Mater.* **2006**, 18 (26), 6139–6146.
 29. Clark, R. J.; Aghajamali, M.; Gonzalez, C. M.; Hadidi, L.; Islam, M. A.; Javadi, M.; Mobarok, M. H.; Purkait, T. K.; Robidillo, C. J. T.; Sineelnikov, R.; et al. From Hydrogen Silsesquioxane to Functionalized Silicon Nanocrystals. *Chem. Mater.* **2017**, 29 (1), 80–89.
 30. Yang, Z.; Gonzalez, C. M.; Purkait, T. K.; Iqbal, M.; Meldrum, A.; Veinot, J. G. C. Radical Initiated Hydrosilylation on Silicon Nanocrystal Surfaces: An Evaluation of Functional Group Tolerance and Mechanistic Study. *Langmuir* **2015**, 31 (38), 10540–10548.
 31. Marcano, D. C.; Kosynkin, D. V.; Berlin, J. M.; Sinitskii, A.; Sun, Z. Z.; Slesarev, A.; Alemany, L. B.; Lu, W.; Tour, J. M. Improved Synthesis of Graphene Oxide. *ACS Nano*

- 2010**, 4 (8), 4806–4814.
32. Thomas, H. R.; Day, S. P.; Woodruff, W. E.; Vallés, C.; Young, R. J.; Kinloch, I. A.; Morley, G. W.; Hanna, J. V.; Wilson, N. R.; Rourke, J. P. Deoxygenation of Graphene Oxide: Reduction or Cleaning? *Chem. Mater.* **2013**, 25 (18), 3580–3588.
 33. Clark, R. J.; Dang, M. K. M.; Veinot, J. G. C. Exploration of Organic Acid Chain Length on Water-Soluble Silicon Quantum Dot Surfaces. *Langmuir* **2010**, 26 (19), 15657–15664.
 34. Fan, X.; Peng, W.; Li, Y.; Li, X.; Wang, S.; Zhang, G.; Zhang, F. Deoxygenation of Exfoliated Graphite Oxide under Alkaline Conditions: A Green Route to Graphene Preparation. *Adv. Mater.* **2008**, 20 (23), 4490–4493.
 35. Henderson, E. J.; Kelly, J. A.; Veinot, J. G. C. Influence of HSiO_{1.5} Sol–Gel Polymer Structure and Composition on the Size and Luminescent Properties of Silicon Nanocrystals. *Chem. Mater.* **2009**, 21 (22), 5426–5434.
 36. Zhang, X.; Sui, Z.; Xu, B.; Yue, S.; Luo, Y.; Zhan, W.; Liu, B. Mechanically Strong and Highly Conductive Graphene Aerogel and Its Use as Electrodes for Electrochemical Power Sources. *J. Mater. Chem.* **2011**, 21 (18), 6494.
 37. Wang, J. Z.; Zhong, C.; Chou, S. L.; Liu, H. K. Flexible Free-Standing Graphene-Silicon Composite Film for Lithium-Ion Batteries. *Electrochem. commun.* **2010**, 12 (11), 1467–1470.
 38. Kruk, M.; Jaroniec, M. Gas Adsorption Characterization of Ordered Organic - Inorganic Nanocomposite Materials. *Chem. Mater.* **2001**, 13, 3169–3183.
 39. Li, C.; Shi, T.; Yoshitake, H.; Wang, H. Improved Performance in Micron-Sized Silicon Anodes by in Situ Polymerization of Acrylic Acid-Based Slurry. *J. Mater. Chem. A* **2016**, 4 (43), 16982–16991.
 1. Carlson, A.; Bowen, A. M.; Huang, Y.; Nuzzo, R. G.; Rogers, J. A. Transfer Printing Techniques for Materials Assembly and Micro/nanodevice Fabrication. *Adv. Mater.* **2012**, 24 (39), 5284–5318.
 2. Choi, S.; Lee, H.; Ghaffari, R.; Hyeon, T.; Kim, D. H. Recent Advances in Flexible and Stretchable Bio-Electronic Devices Integrated with Nanomaterials. *Adv. Mater.* **2016**, 28 (22), 4203–4218.
 3. Meitl, M. A.; Zhu, Z.-T.; Kumar, V.; Lee, K. J.; Feng, X.; Huang, Y. Y.; Adesida, I.; Nuzzo, R. G.; Rogers, J. A. Transfer Printing by Kinetic Control of Adhesion to an Elastomeric

- Stamp. *Nat. Mater.* **2006**, *5* (1), 33–38.
4. Jiao, L.; Fan, B.; Xian, X.; Wu, Z.; Zhang, J.; Liu, Z. Creation of Nanostructures with Poly (Methyl Methacrylate)-Mediated Nanotransfer Printing. *J. Am. Chem. Soc.* **2008**, *130* (38), 12612–12613.
 5. Reina, A., Jia, X., Ho, J., Nezich, D., Son, H., Bulovic, V., Dresselhaus, M. S.; Kong, J. Large Area, Few-Layer Graphene Films on Arbitrary Substrates by Chemical Vapor Deposition. *Nano Lett.* **2008**, *9* (1), 30–35.
 6. Xu, Q.; Rioux, R. M.; Dickey, M. D.; Whitesides, G. M. Nanoskiving: A New Method to Produce Arrays of Nanostructures. *Acc. Chem. Res.* **2008**, *41* (12), 1566–1577.
 7. Allen, M. J.; Tung, V. C.; Gomez, L.; Xu, Z.; Chen, L. M.; Nelson, K. S.; Zhou, C.; Kaner, R. B.; Yang, Y. Soft Transfer Printing of Chemically Converted Graphene. *Adv. Mater.* **2009**, *21* (20), 2098–2102.
 8. Schneider, G. F.; Calado, V. E.; Zandbergen, H.; Vandersypen, L. M. K.; Dekker, C. Wedging Transfer of Nanostructures. *Nano Lett.* **2010**, *10* (5), 1912–1916.
 9. Liu, Y.; Cheng, R.; Liao, L.; Zhou, H.; Bai, J.; Liu, G.; Liu, L.; Huang, Y.; Duan, X. Plasmon Resonance Enhanced Multicolour Photodetection by Graphene. *Nat. Commun.* **2011**, *2* (1), 577–579.
 10. Suk, J. W.; Kitt, A.; Magnuson, C. W.; Hao, Y.; Ahmed, S.; An, J.; Swan, A. K.; Goldberg, B. B.; Ruoff, R. S. Transfer of CVD-Grown Monolayer Graphene onto Arbitrary Substrates. *ACS Nano* **2011**, *5* (9), 6916–6924.
 11. Lee, C. H.; Kim, D. R.; Cho, I. S.; William, N.; Wang, Q.; Zheng, X. Peel-and-Stick: Fabricating Thin Film Solar Cell on Universal Substrates. *Sci. Rep.* **2012**, *2*, 2–5.
 12. Li, H.; Wu, J.; Huang, X.; Yin, Z.; Liu, J.; Zhang, H. A Universal, Rapid Method for Clean Transfer of Nanostructures onto Various Substrates. *ACS Nano* **2014**, *8* (7), 6563–6570.
 13. Choi, M. K.; Yang, J.; Kang, K.; Kim, D. C.; Choi, C.; Park, C.; Kim, S. J.; Chae, S. I.; Kim, T. H.; Kim, J. H.; et al. Wearable Red-Green-Blue Quantum Dot Light-Emitting Diode Array Using High-Resolution Intaglio Transfer Printing. *Nat. Commun.* **2015**, *6* (May), 1–8.
 14. Kim, B. H.; Nam, S.; Oh, N.; Cho, S. Y.; Yu, K. J.; Lee, C. H.; Zhang, J.; Deshpande, K.; Trefonas, P.; Kim, J. H.; et al. Multilayer Transfer Printing for Pixelated, Multicolor Quantum Dot Light-Emitting Diodes. *ACS Nano* **2016**, *10* (5), 4920–4925.

15. Ma, X.; Liu, Q.; Xu, D.; Zhu, Y.; Kim, S.; Cui, Y.; Zhong, L.; Liu, M. Capillary-Force-Assisted Clean-Stamp Transfer of Two-Dimensional Materials. *Nano Lett.* **2017**, *17* (11), 6961–6967.
16. Arai, E.; Kamei, K.; Kawasaki, A.; Takagi, F.; Shirai, K.; Orihara, Y. Patent US 4229239, 1980.
17. Hessel, C. M.; Henderson, E. J.; Veinot, J. G. C. Hydrogen Silsesquioxane: A Molecular Precursor for Nanocrystalline Si-SiO₂ Composites and Freestanding Hydride-Surface-Terminated Silicon Nanoparticles. *Chem. Mater.* **2006**, *18* (26), 6139–6146.
18. Clark, R. J.; Aghajamali, M.; Gonzalez, C. M.; Hadidi, L.; Islam, M. A.; Javadi, M.; Mobarok, M. H.; Purkait, T. K.; Robidillo, C. J. T.; Sinelnikov, R.; et al. From Hydrogen Silsesquioxane to Functionalized Silicon Nanocrystals. *Chem. Mater.* **2017**, *29* (1), 80–89.
19. Brust, M.; Walker, M.; Bethell, D.; Schiffrin, D. J.; Whyman, R. Synthesis of Thiol-Derivatised Gold Nanoparticles in. *J. Chem. Soc. Chem. Commun.* **1994**, 801–802.
20. Veinot, J. G. C. Synthesis, Surface Functionalization, and Properties of Freestanding Silicon Nanocrystals. *Chem. Commun.* **2006**, *40*, 4160.
21. Dasog, M.; De Los Reyes, G. B.; Titova, L. V.; Hegmann, F. A.; Veinot, J. G. C. Size vs Surface: Tuning the Photoluminescence of Freestanding Silicon Nanocrystals Across the Visible Spectrum via Surface Groups. *ACS Nano* **2014**, *8* (9), 9636–9648.
22. Kim, T. H.; Cho, K. S.; Lee, E. K.; Lee, S. J.; Chae, J.; Kim, J. W.; Kim, D. H.; Kwon, J. Y.; Amaratunga, G.; Lee, S. Y.; et al. Full-Colour Quantum Dot Displays Fabricated by Transfer Printing. *Nat. Photonics* **2011**, *5* (3), 176–182.
23. Shirasaki, Y.; Supran, G. J.; Bawendi, M. G.; Bulović, V. Emergence of Colloidal Quantum-Dot Light-Emitting Technologies. *Nat. Photonics* **2013**, *7* (1), 13–23.
24. Dai, X.; Deng, Y.; Peng, X.; Jin, Y. Quantum-Dot Light-Emitting Diodes for Large-Area Displays: Towards the Dawn of Commercialization. *Adv. Mater.* **2017**, *29* (14).
25. Rastgar, N.; Rowe, D. J.; Anthony, R. J.; Merritt, B. A.; Kortshagen, U. R.; Aydil, E. S. Effects of Water Adsorption and Surface Oxidation on the Electrical Conductivity of Silicon Nanocrystal Films. *J. Phys. Chem. C* **2013**, *117* (8), 4211–4218.
26. McVey, B. F. P.; Tilley, R. D. Solution Synthesis, Optical Properties, and Bioimaging Applications of Silicon Nanocrystals. *Acc. Chem. Res.* **2014**, *47* (10), 3045–3051.

27. Heister, K.; Zharnikov, M.; Grunze, M.; Johansson, L. S. O. Adsorption of Alkanethiols and Biphenylthiols on Au and Ag Substrates: A High-Resolution X-Ray Photoelectron Spectroscopy Study. *J. Phys. Chem. B* **2001**, *105* (19), 4058–4061.
28. Yang, Z.; Iqbal, M.; Dobbie, A. R.; Veinot, J. G. C. Surface-Induced Alkene Oligomerization: Does Thermal Hydrosilylation Really Lead to Monolayer Protected Silicon Nanocrystals? *J. Am. Chem. Soc.* **2013**, *135* (46), 17595–17601.
1. Veinot, J. G. C. Synthesis, Surface Functionalization, and Properties of Freestanding Silicon Nanocrystals. *Chem. Commun.* **2006**, 4160–4168.
 2. Dasog, M.; Kehrle, J.; Rieger, B.; Veinot, J. G. C. Silicon Nanocrystals and Silicon-Polymer Hybrids: Synthesis, Surface Engineering, and Applications. *Angew. Chemie Int. Ed.* **2016**, *55* (7), 2322–2339.
 3. Maier-Flaig, F.; Rinck, J.; Stephan, M.; Bocksrocker, T.; Bruns, M.; Kübel, C.; Powell, A. K.; Ozin, G. A.; Lemmer, U. Multicolor Silicon Light-Emitting Diodes (SiLEDs). *Nano Lett.* **2013**, *13* (2), 475–480.
 4. Liu, X. H.; Zhong, L.; Huang, S.; Mao, S. X.; Zhu, T.; Huang, J. Y. Size-Dependent Fracture of Silicon Nanoparticles during Lithiation. *ACS Nano* **2012**, *6* (2), 1522–1531.
 5. Gonzalez, C. M.; Iqbal, M.; Dasog, M.; Piercey, D. G.; Lockwood, R.; Klapötke, T. M.; Veinot, J. G. C. Detection of High-Energy Compounds Using Photoluminescent Silicon Nanocrystal Paper Based Sensors. *Nanoscale* **2014**, *6* (5), 2608–2612.
 6. Zhai, Y.; Dasog, M.; Snitynsky, R. B.; Purkait, T. K.; Aghajamali, M.; Hahn, A. H.; Sturdy, C. B.; Lowary, T. L.; Veinot, J. G. C. Water-Soluble Photoluminescent D-Mannose and L-Alanine Functionalized Silicon Nanocrystals and Their Application to Cancer Cell Imaging. *J. Mater. Chem. B* **2014**, *2*, 8427–8433.
 7. Dasog, M.; De Los Reyes, G. B.; Titova, L. V.; Hegmann, F. A.; Veinot, J. G. C. Size vs Surface: Tuning the Photoluminescence of Freestanding Silicon Nanocrystals Across the Visible Spectrum via Surface Groups. *ACS Nano* **2014**, *8* (9), 9636–9648.
 8. Cordes, D. B.; Lickiss, P. D.; Rataboul, F. Recent Developments in the Chemistry of Cubic Polyhedral.pdf. *Chem. Rev.* **2010**, *110*, 2081–2173.

9. Caster, A. G.; Kowarik, S.; Schwartzberg, A. M.; Nicolet, O.; Lim, S. H.; Leone, S. R. Observing Hydrogen Silsesquioxane Cross-Linking with Broadband CARS. *J. Raman Spectrosc.* **2009**, *40* (7), 770–774.
10. Jun, S.; Lee, J.; Jang, E. Highly Luminescent and Photostable Quantum Dot-Silica Monolith and Its Application to Light-Emitting Diodes. *ACS Nano* **2013**, *7* (2), 1472–1477.
11. Abdolhosseinzadeh, S.; Asgharzadeh, H.; Kim, H. S. Fast and Fully-Scalable Synthesis of Reduced Graphene Oxide. *Sci. Rep.* **2015**, *5*, 1–7.
12. Dasog, M.; Kraus, S.; Sinelnikov, R.; Veinot, J. G. C.; Rieger, B. CO₂ to Methanol Conversion Using Hydride Terminated Porous Silicon Nanoparticles. *Chem. Commun.* **2017**, *53* (21), 3114–3117.

Appendices

Appendix A: A Detailed Procedure of CO₂ Supercritical Drying Presented in Experimental Sections of Chapters 2 and 3

In the studies described in Chapters 2 and 3, a home-built CO₂ supercritical dryer was used to dry the gels and obtain aerogels. A detailed process of building a CO₂ supercritical dryer can be found elsewhere.^{1,2} To build a CO₂ supercritical dryer with a 1-inch (2.5 cm) diameter opening, the manulave parts were ordered from McMaster-Carr and assembled with the assistance of the staff at the Design and Manufacturing Centre, Department of Chemistry, University of Alberta (Figure A-1).

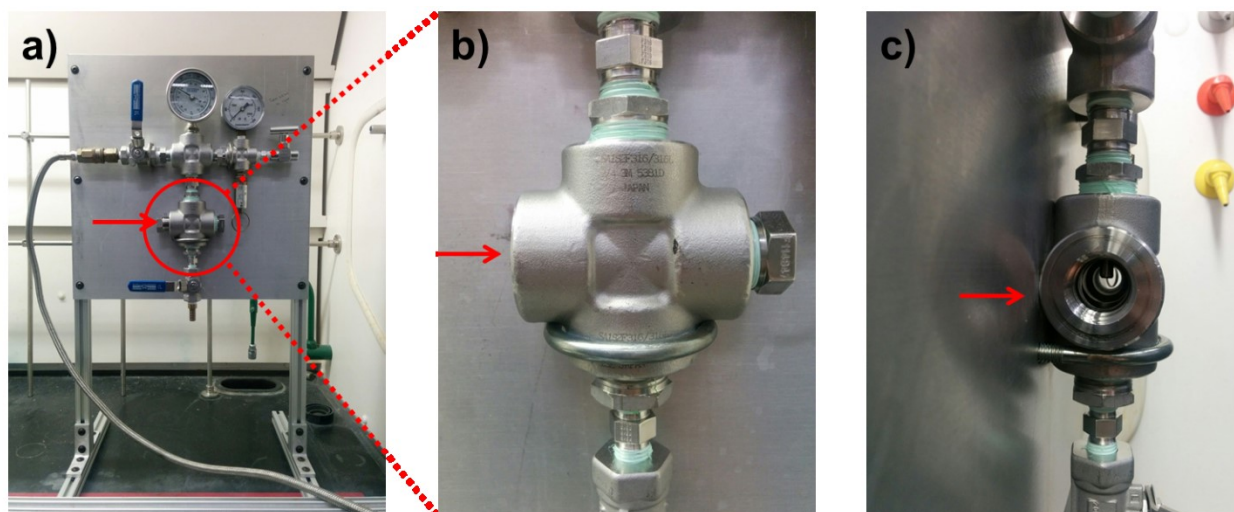


Figure A-1. Photographs of **a)** a home-built CO₂ supercritical dryer with a 1-inch diameter opening, **b)** the front view, and **c)** the side view.

Drying a gel using a home-built CO₂ supercritical dryer involves three steps: i) loading the gel (~1 h), ii) solvent exchange with liquid CO₂ (~1 day), and iii) CO₂ supercritical drying and depressurizing (~1 h).

Loading the gel is an important step; it must be handled with extreme care and patience to prevent the collapse of the gel structure. To avoid cracking the gel, the vessel was filled with a solvent compatible with the gel (i.e., acetone) (**Figure A-2a**). Next, the gel was transferred into the vessel using a pre-fabricated aluminum (Al) container (**Figure A-2b**). When the gel was loaded into the vessel, the pipe plug was tightened to close the opening (**Figure A-2c**). A poly (tetrafluoroethylene) (PTFE) tape was used to wrap the pipe plug before tightening. After closing the pipe plug and all the valves (i.e., intake valve, pressure release valve), the temperature of the vessel was decreased to 10 °C using crushed ice obtained from an ice machine (Hoshizaki™). Finally, the liquid CO₂ tank (CARBON DIOXIDE 29KG 64LB K Type Cylinder, Praxair Inc.) and intake valves were opened sequentially and slowly to siphon liquid CO₂ into the vessel. After ~5 min, the solvent was drained using the drain valve. Next, the vessel was cooled down to 10 °C and refilled with liquid CO₂.

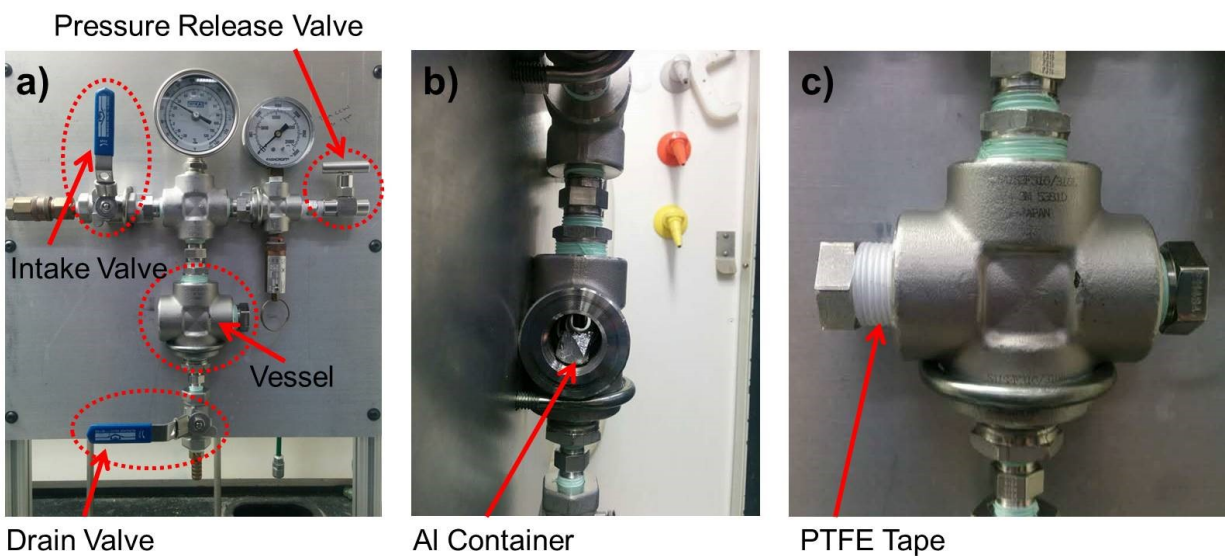


Figure A-2. Photographs of **a**) a CO₂ supercritical dryer indicating main components, **b**) loading a gel, and **c**) tightening the pipe plug.

After an overnight solvent exchange with liquid CO₂ (~15 h), the remaining solvent was drained using the drain valve, and fresh liquid CO₂ was transferred into the vessel after decreasing the temperature of the vessel to 10 °C.

The gel was left in liquid CO₂ for at least 2 h. Next, all the valves (i.e., intake valve, liquid CO₂ tank valve) were closed to increase the temperature and pressure of the vessel and carry out CO₂ supercritical drying. A heat gun was used to heat the vessel and increase the temperature and pressure above the critical point of liquid CO₂ (31 °C, 1100 psi). To obtain an aerogel, a two-step heating profile was used; first, the temperature and pressure of the vessel were increased to 40 °C and 1200 psi, respectively, and the gel was kept under these conditions for 30 min. Next, the temperature and pressure was raised to 50–60 °C and 1300–1400 psi, respectively, and kept under these conditions for another 30 min. Finally, the vessel was depressurized slowly using the pressure release valve, and the aerogel was unloaded from the vessel after opening the pipe plug. A more detailed instruction of CO₂ supercritical drying can be found elsewhere.^{3,4}

References:

1. <http://www.aerogel.org/?cat=33> (accessed on April 29, 2018)
2. <http://www.aerogel.org/?p=667> (accessed on April 29, 2018)
3. <http://www.aerogel.org/?p=1340> (accessed on April 29, 2018)
4. <http://www.aerogel.org/?p=1344> (accessed on April 29, 2018)